UNIVERSITY OF BIRMINGHAM

Enhancing Thermal Performance of Heat Pipe Based Solar Thermal Collector

By

Ahmed Ali Ghulfus Alammar

A T**hesis Submitted to the University of Birmingham for the Degree of Doctor of Philosophy**

School of Engineering

Department of Mechanical Engineering

The University of Birmingham

Edgbaston, Birmingham, UK

Abstract

Enhancement of energy conversion devices has become an important task to reduce size and cost, and to design efficient systems. Recently, heat pipes have attracted more attention to enhance their thermal performance due to their use in different heat transfer applications. The main features of heat pipes are low-temperature difference, employing a small quantity of liquid, compact and working as a thermal diode, hence are utilised in different applications such as heat exchangers, electronics cooling, and solar thermal collectors.

In this work, a new CFD model has been developed to simulate the phase-change processes inside a Two-Phase Closed Thermosyphon (TPCT) using Fluent software (ANSYS 15). The effect of the inclination and fill ratio (volume of liquid to the volume of evaporator) on the performance of the TPCT has been investigated using the developed model. Also, this model was used for the first time to visualise the boiling characteristics in an inclined thermosyphon and vertical TPCT with different fill ratios. Results from the CFD model were compared to published experimental data showing a good agreement.

In addition, the vapour condensation process on a plain surface and surfaces with different contact angle has been simulated and results have been compared with published experimental data to validate the CFD solution. Validated solution showed that the maximum enhancement in the heat flux has been achieved at a contact angle of 140^{o}. The model has also been employed to investigate the thermal performance of a thermosyphon heat pipe and to visualise the phase-change characteristics at different heat inputs using contact angles of 140^{o} and 40^{o} in the condenser and evaporator, respectively. The TPCT CFD model can visualise different shapes of droplet based on contact angles of 90^{o} and 140^{o} in the condenser, and various boiling regimes, convection, bubbly and slug regimes based on contact angles of 90^{o} and 40^{o} in the evaporator.

An experimental study was also conducted to examine comprehensively several parameters affecting the geyser boiling characteristics inside a TPCT charged with water. The occurrence and period of the geysering were tested under the impact of different angles of inclination and liquid charges at a broad range of heat loads. The study revealed that the fill ratio and inclination affected significantly the geyser boiling occurrence and period at the tested range of heat inputs. Subsequently, the influence of geysering on the TPCT thermal performance was extensively investigated at the same parameters and operating conditions. Results showed that geyser phenomena can be beneficial at certain operating conditions in terms of improving the TPCT thermal ressistance and its temperature distribution. Likewise, it can have deteremental effects on the TPCT performance under certain operating conditions. The result from this work allows the user to identify the range of operating conditions that can either improve the TPCT performance or to avoid the conditions that lead to the opposite effect.

Furthermore, enhancement of heat transfer performance of a TPCT has been investigated by making an internal surface roughness employing an advanced machining technique (Electrical Discharge Machining (EDM)). The experimental work has been carried out at two initial sub-atmospheric pressures (3 and 30 kPa), heat input range of (90-160W) and a fill ratio of 50%. The results revealed that using internal wall roughness on the TPCT's wall can enhance its thermal performance by reducing the evaporator wall temperature.

Acknowledgement

I would like to express my sincere gratitude to my supervisor **Dr. Raya Al-Dadah** for the continuous support, patience, revision and sharing knowledge throughout my Ph.D study. Her guidance helped me in all the time of research and writing of this thesis.

My sincere thanks also extend to **Dr. Saad Mahmoud** for his precious suggestions and ideas, support and revision of my work. I would like to thank Mr Simon Rowan for helping in constructing of my experimental rigs and solving any technical issue. My thanks also go to Dr. R. Hood for helping in making and measuring the surface roughness.

I also would like to thank my colleague Mr. Fadhel Al-Mousawi for his kind help in manufacturing of heat pipes. Also, I would like to thank all my colleagues who I know during my postgraduate years.

My deep and sincere gratitude to my family, especially my father and my mother for their upbringing, love and supports that enable me to reach this status. I truly cannot find the words to thank my wonderful wife and my children for their patience and praying during my study. I thank them for all sacrifices over this long and arduous period.

Finally, I gratefully acknowledge the Iraqi Government for supporting financially my Ph.D. study. Also, I take this opportunity to thank all the staff in the Iraqi cultural attaché in London for their continuous support.

Ahmed Alammar

Unversity of Birmingham

Dedication

To my beloved Father and Mother,

To my wife and children,

And all my loved ones.

Table of Contents

LIST OF FIGURES

LIST OF TABLES

NOMENCLATURE

cp	Specific heat (J/kg K)
D	Outside diameter of thermosiphon (m)
d_b	Bubble diameter (m)
E	Total energy per unit mass (J/kg)
F_S	Continuum surface force ($Kg/m^2 s^2$)
g	Acceleration gravity (m/s^2)
h	Heat transfer coefficient ($W/m^2 K$)
h_{fg}	Latent heat (J/kg)
I	Electrical current (A)
k	Thermal conductivity (W/m K)
K_C	Surface curvature
L	Height (m)
l_b	Bubble scale length (μm)
M	Molecular weight (Kg/Kgmol)
n_w	Wall normal vector
P	Pressure
Pr	Prantel number
Q	Heat input (W)
Q_{cond}	Heat removed from condenser (W)
q	Heat flux (W/m2)
R	Universal gas constant (J/mol.K)
Ra	Arithmetical mean roughness (μm)
R_{th}	Thermal Resistance (K/W)

Rz	Mean roughness depth (µm)
S_q	Energy source term (J/m^{3}s)
S_{am}	Mass source term (kg/m^3 s)
$S_{\bar{x}}$	Standard deviation of the mean
T	Temperature (K)
t	Time (s)
$t_{n-1,95\%}$	Student distribution factor
t_w	Wall tangential vector
U	Uncertainty
u	Velocity
V	Electrical Voltage (v)

Greek symbols

α	Volume fraction
µ	Dynamic viscosity (Pa. s)
ρ	Density (Kg/m^3)
σ	Surface tension (N/m)
θ_w	Contact angle (o)
β	Accommodation coefficient (1/s)
Δ	Partial derivatives
π	Pi

Subscripts

av	Average
c	Condenser

cond	Condenser
conv	Convection
cw,av	Condenser wall, average
c-f	Curve fitting
DL	Data logger
e	Evaporator
EXP	Experimental
F	Flow meter
i	Inside
in	Inlet
l	Liquid
mix	Mixture
o	Outside
out	Outlet
ov	Overall
r	Riser
rand	Random
s	Solid
Sat	Saturation
st	Standard
sys	Systematic
t	total
T	Thermocouple
v	Vapour
VC	Volume collection

w	Wall

Abbreviations

CFD	Computational Fluid Dynamic
CHF	Critical Heat Flux
CHTC	Condensation Heat Transfer Coefficient
CSF	Continuum Surface Force
DHW	Domestic Hot Water
EDM	Electrical Discharge Machining
FR	Fill Ratio
NCG	Non-Condensable Gas
RHP	Rotating Heat Pipe
RSS	Root Sum Squared
RTD	Resistance Temperature Detector
SED	Spark Erosion Machining
TPCT	Two-Phase Closed Thermosiphon
VOF	Volume of Fluid

LIST OF PUBLICATIONS

JOURNAL PUBLICATIONS

1) Alammar, A.A., Al-Dadah, R.K. & Mahmoud, S.M., 2016. Numerical investigation of effect of fill ratio and inclination angle on a thermosiphon heat pipe thermal performance. **Applied Thermal Engineering**, 108, pp.1055–1065.
2) Alammar, A.A., Al-Dadah, R.K. & Mahmoud, S.M., 2018. Effect of inclination angle and fill ratio on geyser boiling phenomena in a two-phase closed thermosiphon – Experimental investigation. **Energy Conversion and Management**, 156 (October 2017), pp.150–166.
3) Alammar, A.A., Al-Dadah, R.K. & Mahmoud, S.M., 2017. Experimental investigation of the influence of the geyser boiling phenomenon on the thermal performance of a two-phase closed thermosyphon. **Journal of Cleaner Production**, 172, pp.2531–2543.
4) A. A. Alammar, F. N. Al-Mousawi, R. K. Al-Dadah, S. M. Mahmoud, and R. Hood, "Enhancing Thermal performance of a Two-phase Closed Thermosyphon With an Internal Surface Roughness," **Journal of Cleaner Production**., 2018.

CONFERENCES PAPERS

1) Alammar, A.A., Al-Dadah, R.K. & Mahmoud, S.M., 2016. Effect of fill ratio on thermosiphon heat-pipe performance: a numerical investigation. In **Heat Powered Cycles 2016**. University of Nottingham, p. 35.
2) Alammar, A.A., Al-Dadah, R.K. & Mahmoud, S.M., 2017. Effect of hydrophobicity on enhancement of condensation heat transfer-numerical investigation. In 2016 **International Conference for Students on Applied Engineering**, ICSAE 2016.

Chapter 1

1. Introduction

Solar thermal system has been proven as a cost-effective technology and has offered a substantial worldwide market potential. Its installed capacity has increased by a factor of 7.4 between year 2000 and 2016 (from about 62 to 465 GW_{th}, see Figure 1.1). This is equivalent to a reduction in oil consumption of 40.3 million tons and CO_2 emissions of 130 million tons [1]. Solar thermal systems have been effectively used for decades worldwide to produce hot water, provide space heating and cooling and to deliver the heat required for industrial processes. Most of these systems are utilised for domestic use where the hot water consumption represents the major thermal energy demand [2] (91% worldwide, (63%) small DHW systems and (28%) large DHW systems) [1], [3], [4].

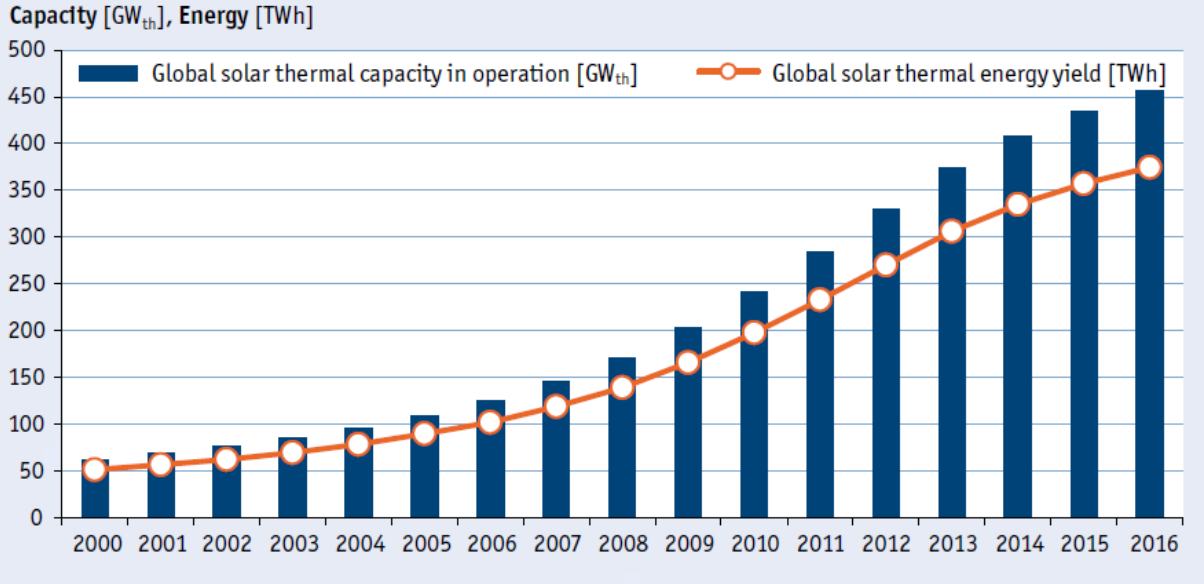

Figure 1.1 Worldwide solar thermal installed capacity between year 2000 and 2016 [1]

The key element in the solar water heater is the solar collector. Consequently, the solar collector efficiency represents the most important parameter affecting the thermal characteristics of the solar hot water system [5], [6]. The conventional solar collectors which depend on working fluid circulation suffer from many drawbacks such as low thermal

performance, corrosion problems, freezing in a cold climate, inner surface fouling, reverse heat flow at night and others related to space and weight [7], [8]. Using a heat pipe as an energy converter in the solar collector can eliminate most of these disadvantages [9], [10]. In addition, heat pipes are characterised by an isothermal surface due to a uniform temperature distribution [11]. This uniform distribution in the wall temperature of heat pipes play a significant role in improving the performance of the solar water collector, especially with the flat plate type where the uniform surface temperature reduces the heat losses significantly; thereby increasing the heat gain and thermal efficiency of the collector [12], [13]. Figure 1.2 shows the difference between the efficiency of solar collector with and without heat pipe [2]. Consequently, improvement of the performance of solar collectors by utilising the advantages of heat pipes has a significant effect on domestic energy consumption by reducing the reliance on the fossil fuel [2]. This conserves natural resources, reduces environmental pollution and provides sustainable, secure and clean energy [14], [15].

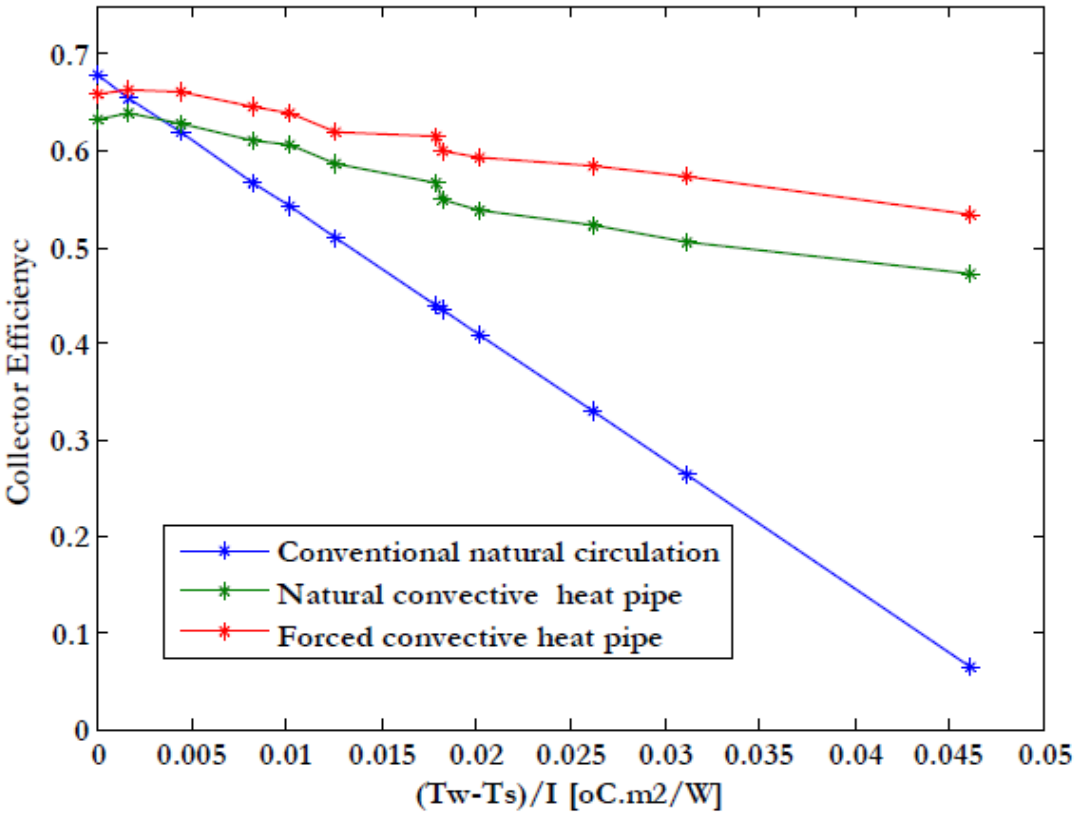

Figure 1.2 Efficiency of solar collector with and without heat pipe

1.1 Background of Heat Pipes

Heat pipes are efficient two-phase devices utilising the latent heat of fluids to transfer energy from one place to another by means of evaporation and condensation in a sealed vessel [2]. The heat pipe as an idea was firstly proposed by Gaugler in 1942. Then, Grover in 1960's reported the heat pipe as a device that has important potential properties, and efforts to develop such a device have begun [16].

Wick heat pipe includes a wick on its internal surface where the evaporation and condensation processes take place inside the wick structure. In such a heat pipe, the wick is essential to return the condensed liquid back to the evaporator where the evaporator is located at the top, while the condenser is placed at the bottom as shown in Figure 1.3a [16]. If the evaporator is placed at the bottom, the gravity will assist the wick in returning the condensate to the evaporator. However, many applications do not need such an arrangement, so there is no need to insert a wick structure on the wall of the heat pipe. In this case, the heat pipe is called a wickless heat pipe or thermosyphon heat pipe as shown in Figure 1.3b [16]. The device is evacuated from the air and charged with a small amount of liquid. This liquid saturates the wick structure in the case of the wick heat pipe, whereas it forms a liquid pool at the bottom in the case of the thermosyphon.

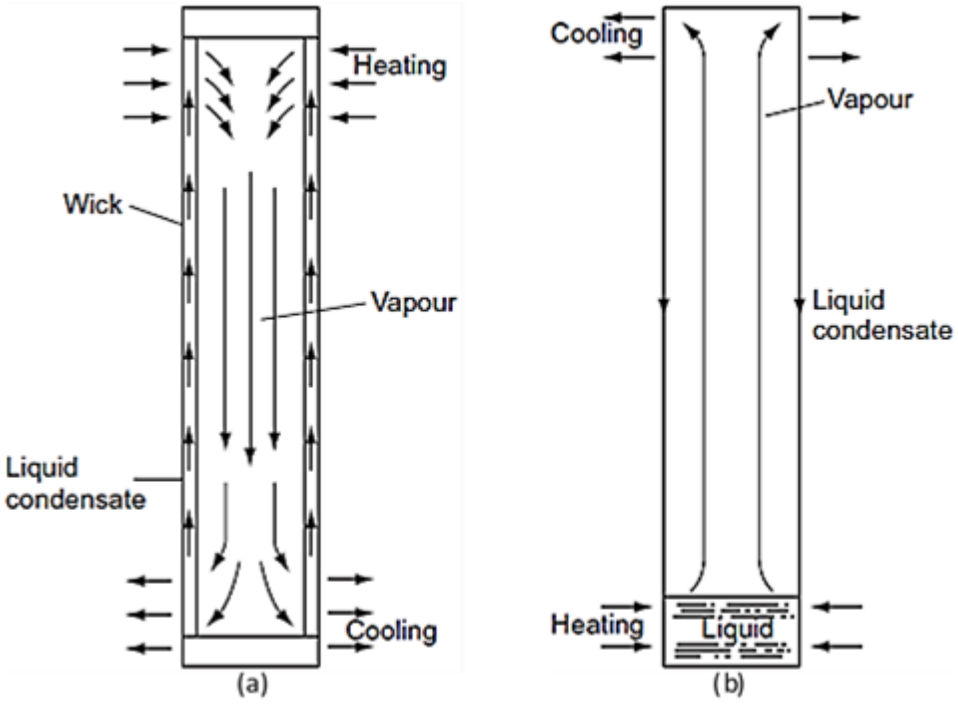

Figure 1.3: (a)- heat pipe and (b)- Thermosyphon [16]

Due to their various advantages of the relatively low-temperature difference between the heat source and heat sink, compact, low thermal response time and employing a small amount of working fluid, they can be used in various applications such as heat exchangers [17]–[19], cooling of electronics [20], [21], and solar systems [22], [23]. Because of simplicity in construction and cost-effectiveness of wickless heat pipes, a substantial attention has been paid to investigate their thermal performance to make them suitable for certain applications [8].

1.2 Working Principles of Heat Pipes

Heat pipes consist of two main sections: the evaporator where heat is absorbed by the working fluid; and the condenser in which heat is rejected. After heat is added to the evaporator section, the liquid reaches its saturation temperature and evaporates generating vapour. Due to the vapour pressure difference between the condenser and evaporator (in the case of thermosyphon), it rises to the condenser (with the assistance of the buoyancy forces) where it condenses delivering its latent heat to the coolant at the condenser [2]. At that time, the

vapour condenses due to a lower temperature in the condenser and returns to the evaporator by gravity, if the heat pipe is wickless (thermosiphon), or by capillary force, if a wick heat pipe is used [24] as shown in Figure 1.3 [8].

1.3 Research Gap

Although numerous applications have utilised the wickless heat pipe, limited CFD research have been carried out to investigate their thermal performance. These investigations have been employed to model the evaporation and condensation processes inside the TPCT, thereby its thermal performance. However, CFD modelling of important parameters such as fill ratio and inclination angle that affect the performance of the TPCT was not found in literature, especially, the visualisation of the phase-change process of the inclined TPCT and visualisation of different fill ratios. In addition, CFD modelling was not utilised to investigate the effect of the contact angle which reflects the influence of the surface wettability on the thermal characteristics of the TPCT, nor, to visualise the phase-change characteristics under influence of different contact angles.

Regarding the experimental work, according to the latest review [25] of research on the TPCT, there are still challenges related to phase change processes and the operating limit predictions inside the TPCT which need to be considered. Accordingly, limited research have reported the occurrence of the geyser boiling and its characteristics in the thermosyphon heat pipe. Also, previous investigations about the geyser boiling in the TPCT did not cover all parameters at a wide range of heat input, so, their conclusion remains limited only to the investigated parameters [8]. In addition, all investigations about geyser boiling have only focused on the effect of different operating conditions on this boiling phenomenon. Thus, the effect of geyser boiling on the thermal characteristics of the TPCT has not been reported [2].

Different means have been implemented experimentally to increase the capability of heat transfer and to improve the performance of heat pipes. There have been two different methods

employed in TPCT, using nanofluids as a working fluid and modifying the surface characteristics of internal walls of heat pipes. However, the preparation and using of nanofluids would be complex and suffer from instability and agglomeration of the nanoparticles. In addition, application of surface coatings can be a difficult process, making additional conduction thermal resistance, and being time-consuming and expensive, whereas making micro-grooves may reduce the heat transfer limit of heat pipes which needs more investigations.

1.4 Aim and Objectives

The solar thermal collector main element is the receiver which is preferred to be a heat pipe. This research aims to investigate experimentally and numerically using CFD different parameters affecting the TPCT's thermal performance such as fill ratio, inclination angle and geyser boiling as well as employing an advanced machining technique to enhance the thermal performance of the thermosyphon heat pipe by producing a roughness in the internal wall of the TPCT through the following objectives:

1. Extensive review of heat pipes under different categories: heat pipe based solar collectors, experimental investigations of heat pipes, CFD modelling of heat pipes, experimental investigations of the geyser phenomena inside the heat pipe and means of enhancing the performance of heat pipes.
2. Develop a CFD model to simulate the phase change process in the heat pipe and investigate and visualise the effect of fill ratio and inclination angle on the thermal performance of the heat pipe using Ansys-Fluent.
3. Develop a CFD model to investigate the effect of different surface wettabilities in terms of the contact angle on the enhancement of condensation and boiling heat transfer process inside the TPCT [26].

4. Develop a test rig to investigate different fill ratios, inclinations, coolant flow rate and coolant inlet temperature at a broad range of heat inputs on the characteristics of the geyser boiling phenomena inside the TPCT [8].
5. Investigate the effect of geyser boiling on the thermal characteristics of the TPCT for different orientations and fill ratios at a wide range of heat loads [2].
6. Develop a heat pipe with an internal roughness and investigate experimentally the effect of changing surface features on the heat transfer performance of the heat pipe.

1.5 Thesis Outlines

This thesis comprises six chapters. **Chapter one** highlights the importance of integrating heat pipes into solar collectors, heat pipes background, research gap, aim and objectives and the thesis framework.

Chapter two provides a detailed literature review of research regarding the heat pipe based solar collector and experimental and CFD numerical studies about various parameters affecting the operation and the performance of heat pipes.

Chapter three firstly provides a general description of the CFD mathematical method used to model the multiphase flows in Ansys Fluent. Then, section one interduces a CFD model to simulate the phase-change processes and the resulting temperature distribution and thermal resistance of a TPCT where the CFD solution is compared with experimental data found in the literature to validate the model. This model was also used to investigate the effect of the fill ratio and inclination on the performance of the TPCT and to visualise the phase-change process in an inclined TPCT and of different amount of the working fluid. Section two in this chapter models the effect of the contact angle on the two-phase flow for a flat plate in order to validate the CFD solution with and without the effect of the contact angle and find the optimum contact angle. Then, a CFD model for the TPCT is developed to investigate the effect of the contact angle on the thermal characteristics of the TPCT and to visualise and

compare the phase change phenomena between the plain TPCT and the TPCT with a certain contact angle.

Chapter four is divided into two sections. Section one describes the experimental apparatus and the calibration of different measuring instruments used in the test. This section also reports and explains in detail the temperature oscillation, occurrence and period of geyser boiling phenomena inside the TPCT under the influence of different fill ratios and inclinations at a wide range of heat loads and different inlet temperatures and flow rates of the cooling water. Then, section two compares and explains the thermal performance of the TPCT before and after the occurrence of the geyser boiling for different fill ratios and orientations at a broad range of heat inputs [2].

Chapter five describes the test rig which is developed to investigate the thermal performance enhancement of a TPCT with an internal wall roughness compared to the plain TPCT. This chapter compares the temperature distribution, thermal resistance and the evaporator heat transfer coefficient between the two TPCTs at two different pressures and various heat inputs.

Chapter six reports the main findings from the CFD modelling and experimental studies of the thermal performance of heat pipes at different parameters. This chapter also suggests some recommendations for future work to further enhance the performance of the TPCT.

Chapter 2

2. Literature Review

2.1 Introduction

Heat pipes are two-phase devices which can transfer high amount of heat at a relatively low-temperature gradient between two points employing the latent heat of a working fluid in a closed container by utilising evaporation and condensation processes. Due to their various advantages of the relatively low-temperature difference, compact and employing a small amount of working fluid, they can be used in various applications. The evaporator and condenser represent the heat pipe main sections in which the heat is absorbed by working fluid in the evaporator and is rejected in the condenser. The vapour provides its latent heat to the coolant at condenser section to condense and flow back to the evaporator by gravity, if the heat pipe is wickless (Thermosyphon) or by capillary force, if a wicked heat pipe is used. As a result of simplicity in construction and cost-effectiveness of wickless heat pipes [8], significant investigations have been conducted to study their thermal characteristics to make them suitable for a specific application [2], [16], [24]. This chapter provides a detailed literature review of the published work related to heat pipes (especially wickless heat pipe or thermosyphon). Firstly, it presents a review of the heat pipe based solar collectors to report the importance of integrating the heat pipe with the solar collector. Then, different studies investigating the thermal performance of the heat pipe are reviewed under different categories, namely CFD modelling, experimental investigation, geyser boiling phenomena, and the enhancement of condensation and evaporation processes by employing different techniques.

2.2 Heat Pipe Based Solar Collector

Integrating heat pipes into solar collector systems has received significant attention in recent decades due to the increase in the energy demands for different applications. The importance of utilising heat pipes in solar collectors is to improve energy conversion capability of solar collectors. This is due to their high heat transport capacity and approximately isothermal surface which represent the most important features for efficient solar collectors. Therefore, numerous research studies have been performed to study the characteristics of integrating heat pipes into the solar collector arrangements [27]–[30].

Joudi and Al-Tabbakh [31] analysed theoretically using numerical simulation a domestic solar water system operating with a two-phase thermosyphon employing R-11 as a refrigerant. This was the first attempt for studying numerically the whole components of the hot water solar system operating under phase-change process to investigate the effect of the presence of the two-phase thermosyphon on the efficiency and other parameters of such a system. The study also included the effect of the temperature on the physical properties of R-11 and compared the results of the two-phase system with those of single phase. They reported a continuous increase in the saturation temperature and pressure for the two-phase system during the day depending on the tank temperature. Thus, unlike the single-phase system, the efficiency of the two-phase system was not affected by the tank load. The study also concluded that using the two-phase thermosyphon increased the collector efficiency (useful heat collected in the tank divided by the amount of incident heat over the collector) significantly compared with the single-phase system as shown in Figure 2.1. A similar theoretical and experimental study was carried out by Hussein et al. [6], but with different flat plate solar collector configuration and water as a working fluid. They compared the numerical results with their experimental data and a good agreement was reported. However, the temperature of load tank and the amount of the load was not taken into account.

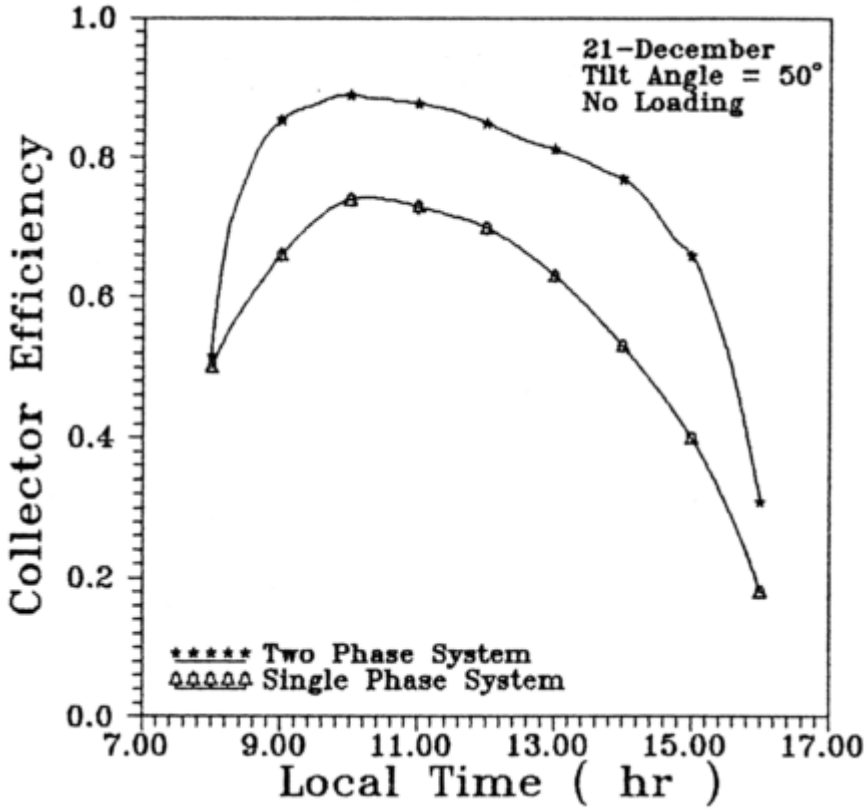

Figure 2.1 Comparison of collector efficiency between two-phase and single-phase systems [31]

The thermal characteristics of a heat pipe based solar water heater was studied theoretically and experimentally by Mathioulakis and Belessiotis [32] using ethanol as a working fluid. The study reported the thermal behaviour of various sections of the system employing a loop thermosyphon heat pipe, namely the collector, evaporator, condenser and the tank. In addition, the theoretical results were compared with the experimental data. It was concluded that integrating thermosyphon heat pipe into solar hot water systems can increase the system efficiency up to a maximum of 60%, widen the range of the operating temperature and the system can operate effectively under low-temperature gradient between the receiver and the tank.

Riffat et al. [10] investigated theoretically the performance of a heat pipe solar water collector. They developed a theoretical model to investigate the heat transfer mechanism in the different parts of the system, namely, absorber, glass cover and the condenser heat

exchanger as shown in Figure 2.2. A collector efficiency of 40-70% was obtained from the experimental data and compared with results predicted by the theoretical model (35-65%).

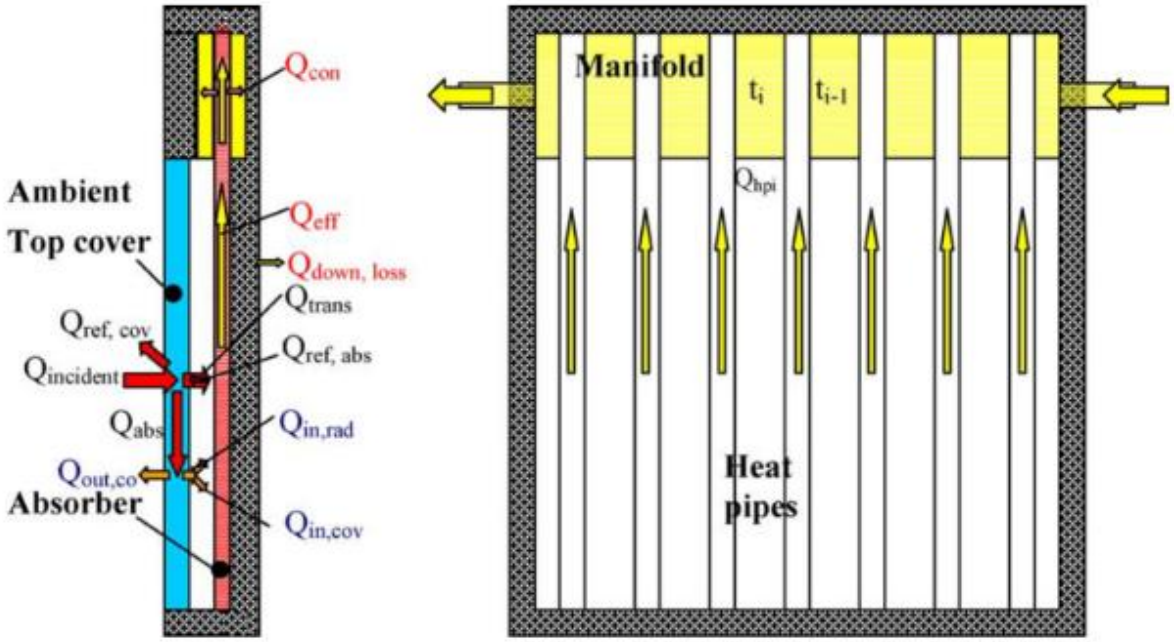

Figure 2.2 Schematic diagram of heat balance of heat pipe solar collector [10]

Hussein et al. [33] modified the computer program developed by [34] to study theoretically a flat plate solar collector employing thermosyphon heat pipes charged with water and a cross flow heat exchanger in the condenser. They analysed numerically the effect of the number of heat pipes, configuration of the condenser heat exchanger (cross flow heat exchanger), coolant flow rate and coolant inlet temperature on the performance of the solar collector. The study also tested the system experimentally by building a flat plate solar collector with 14 thermosyphon heat pipes as shown in Figure 2.3 and compared the numerical results with the experimental data. An optimum coolant flow rate was identified which provides the highest thermal performance of the TPCT solar collector and agrees well with ASHRAE standard for such system. In addition, a number of 12 heat pipes was found to be the optimum number offering the best collector efficiency at a constant pitch distance between them.

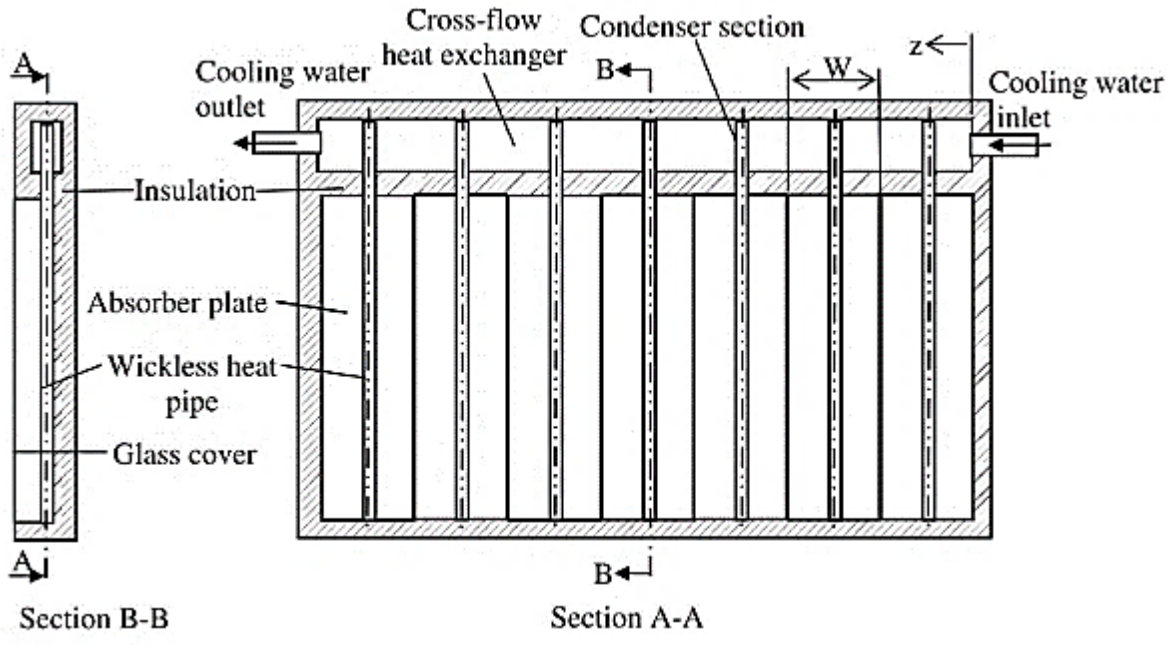

Figure 2.3 TPCT based solar collector employing cross flow in the condenser [33]

A theoretical and experimental study was conducted to investigate the thermal performance of a flat plate solar collector with a gravity-assisted heat pipe as a receiver [35]. A numerical model was developed to evaluate various parameters influencing the thermal behaviour of the gravity-assisted heat pipe solar hot water system. In addition, a new configuration of the heat exchanger in the condenser section was tested as shown in Figure 2.4. The study concluded that the model is capable to predict the thermal characteristics of the system where the model results agreed well with the experimental work.

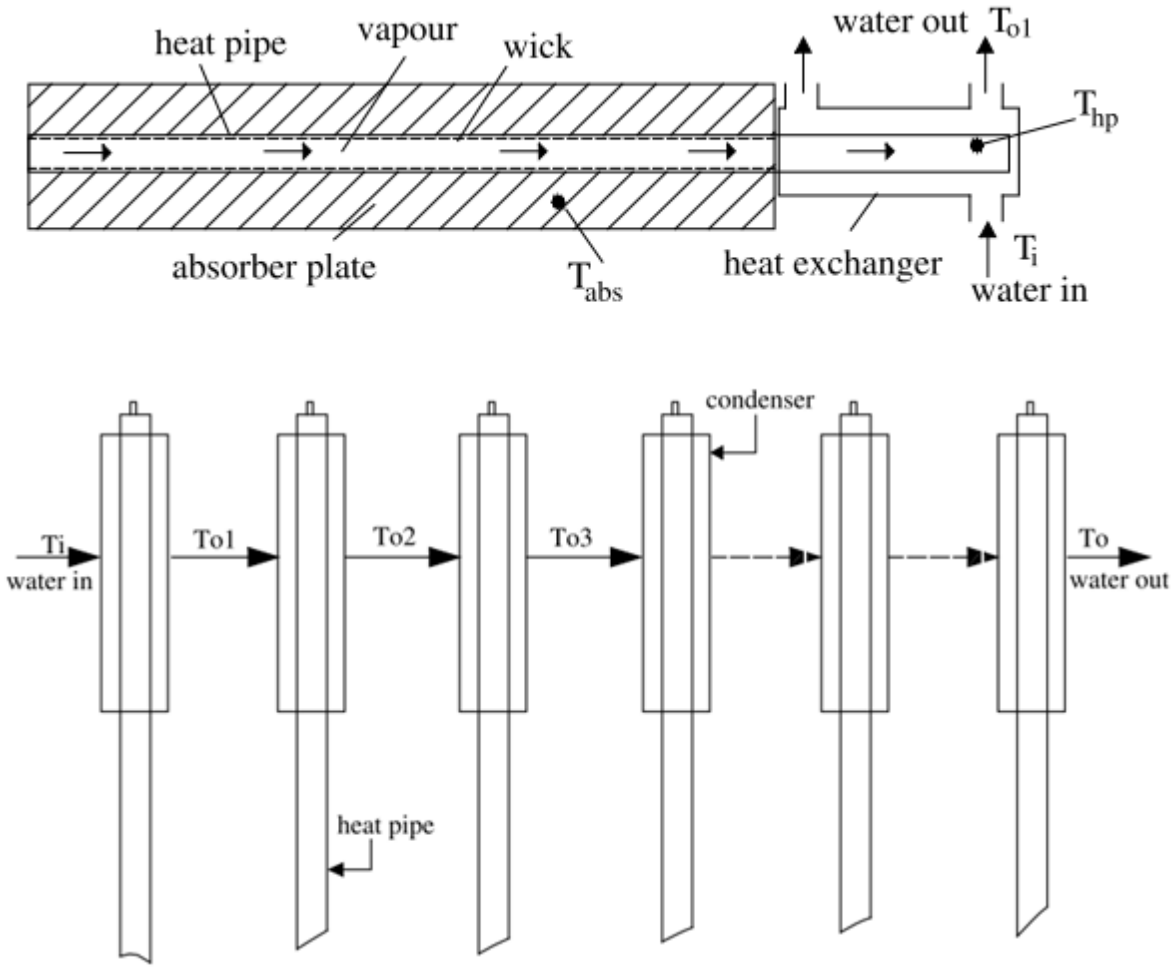

Figure 2.4 Condenser heat exchanger configuration and fluid flow in condenser of TPCT solar collector [35]

Zhao et al. [36] developed a model to analyse the performance of a novel loop-heat pipe solar water collector under influence of different operating conditions. They also built a prototype for the proposed system and compared the model results with the experimental data obtained. The system is presented in Figure 2.5. Results showed that the operating temperature of the heat pipe has a significant influence on the particular system efficiency and the optimum operating temperature of 72^{o}C provides the highest system efficiency. In addition, using loop-heat pipe makes the collected energy transferring regardless of the difference in height between the heat exchanger and the absorber.

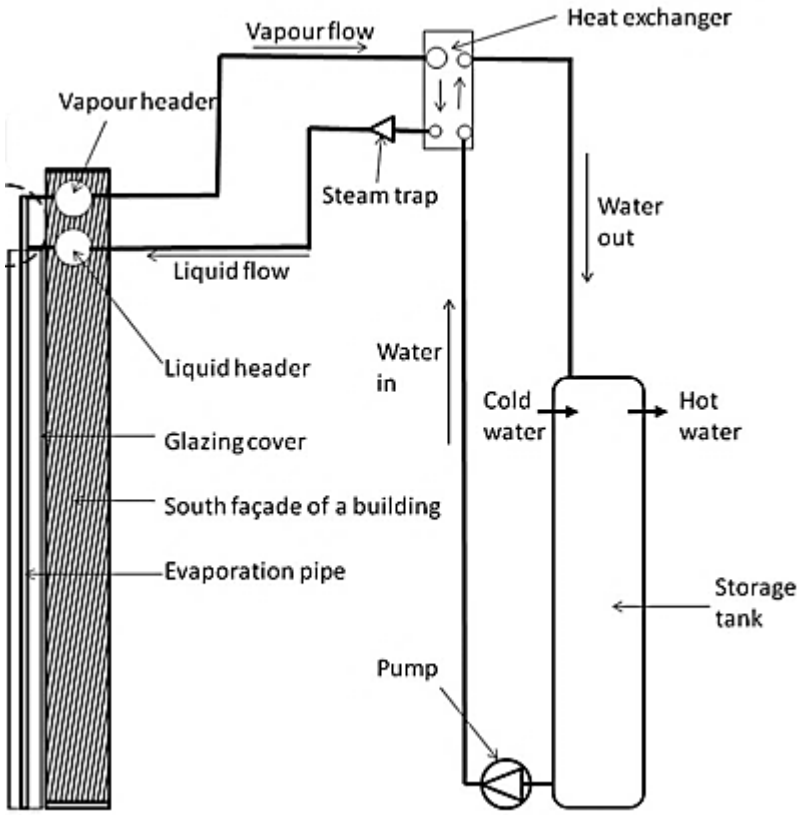

Figure 2.5 Solar water collector with loop-heat pipe [36]

Abebe and Endalew [12] carried out a numerical and experimental study to compare the performance of a heat pipe solar water collector with a conventional solar collector for forced and natural convection at the condenser heat exchanger. The study showed that the solar collector with a heat pipe and the forced convective heat pipe condenser provide higher collector efficiency compared with the conventional solar collector and the natural convective condenser, respectively as shown in Figure 2.6. A similar conclusion has been reported by Ong et al. [37] and [38].

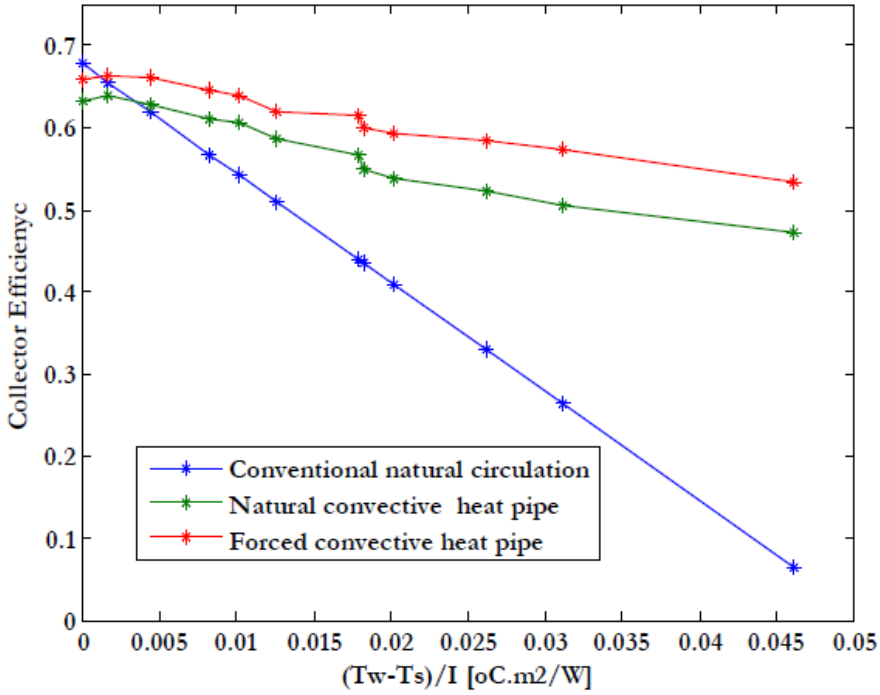

Figure 2.6 Comparison of collector efficiency [12]

Arab et al. [39] studied experimentally the performance of a single-phase thermosyphon solar collector and extra-long pulsating heat pipe solar collector at three different fill ratios (liquid volume to the volume of the evaporator) 30%, 50% and 70% and compared their performance. They found that a solar collector employing heat pipe with fill ratio 70% was more stable and exhibited a higher efficiency (about 54%) than the conventional solar collector (31-36%).

A heat pipe PV/T solar collector was developed and analysed numerically and experimentally to investigate its thermal and electrical efficiencies and to report the annual thermal and electrical gains in three different cities in China under influence of different parameters [40]–[42]. They concluded that PV/T collector integrated with heat pipe can be used in cold climate areas without the freezing issue related to traditional system PV/T. Also, higher efficiency was obtained using higher water flow rate, smaller space between heat pipes, higher cell covering factor and using a selective coating. However, the electrical gain decreases when the selective coating was used. Figure 2.7 shows the developed heat pipe PV/T solar collector.

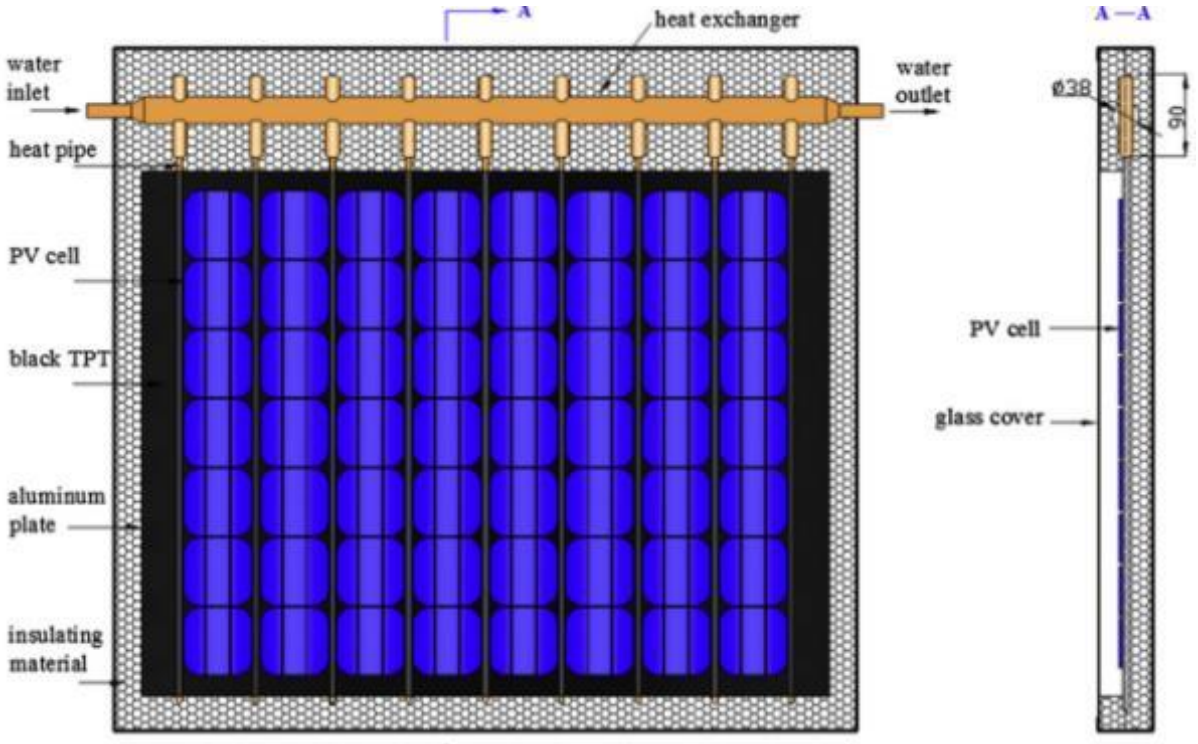

Figure 2.7 heat pipe PV/T solar collector [41]

Islam et al. [43], Chen et al. [44] and Samanci and Berber [45] compared the thermal performance of a single-phase solar water collector and a two-phase solar collector experimentally for different working fluids. They reported that the thermal efficiency of the two-phase thermosyphon solar collectors is significantly higher than that for the single-phase solar collectors. Figure 2.8 shows a comparison of thermal efficiency between the TPCT (Proposed system) and four single-phase collectors, one evacuated tube (system A) and three flat plate collectors with different geometrical parameters (system B, system C and system D) [44].

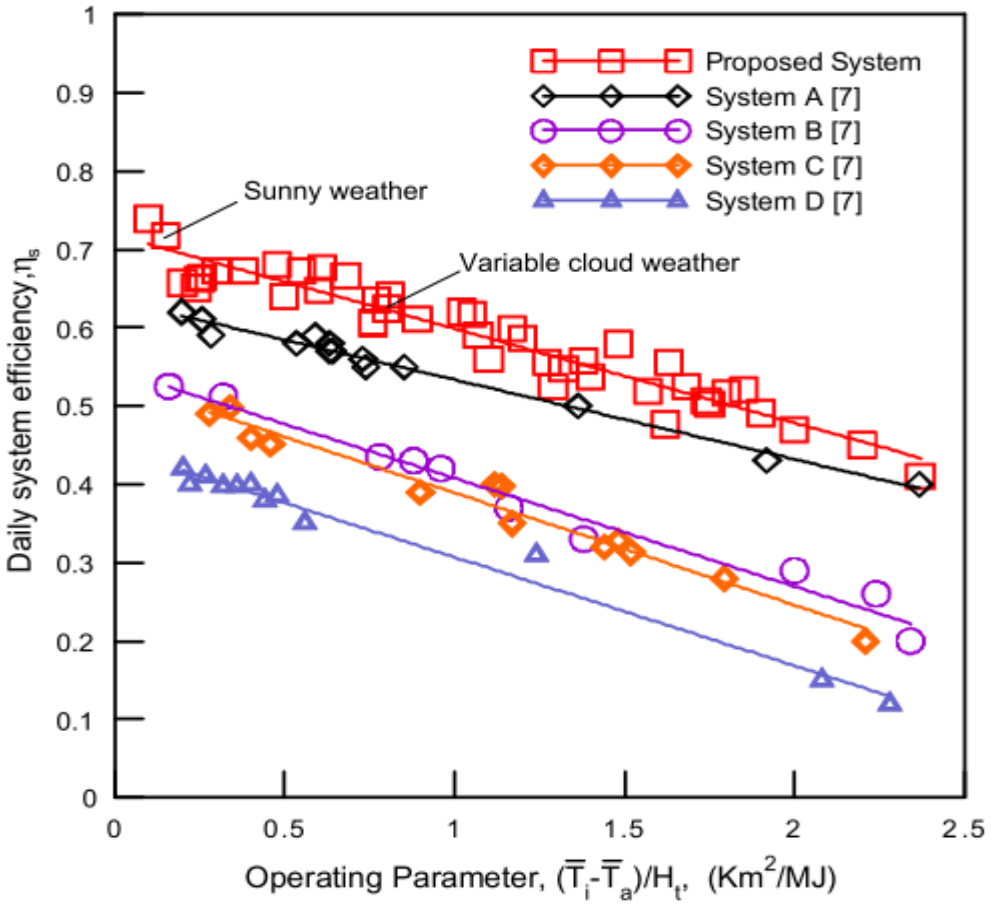

Figure 2.8 Comparison of system efficiency between two-phase closed thermosyphon and single-phase collector [44]

Aung and Li [46] studied numerically the effect of the riser size (vapour channel) and orientation on the performance of a loop-thermosyphon heat pipe solar hot water collector at various operating conditions. They reported an optimum range of inclination of 24-44^o corresponding to a riser diameter range of 1.25-2.5 cm, which provides the highest system efficiency as shown in Figure 2.9 where D_r is the riser diameter.

The influence of the working fluid properties on the effectiveness performance of a solar water heating system with a vacuum tube heat pipe has been investigated by Arab and Abbas [47]. Different working fluids have been used, namely, water, ethanol, ammonia, acetone, and pentane. It was concluded that water exhibited the highest performance compared with other working fluids. Then three hypothetical fluids have been designed to provide a higher performance than water where 82% higher system performance was achieved using the

proposed fluid compared with water leading to reducing the cost of the solar water heater by 50%.

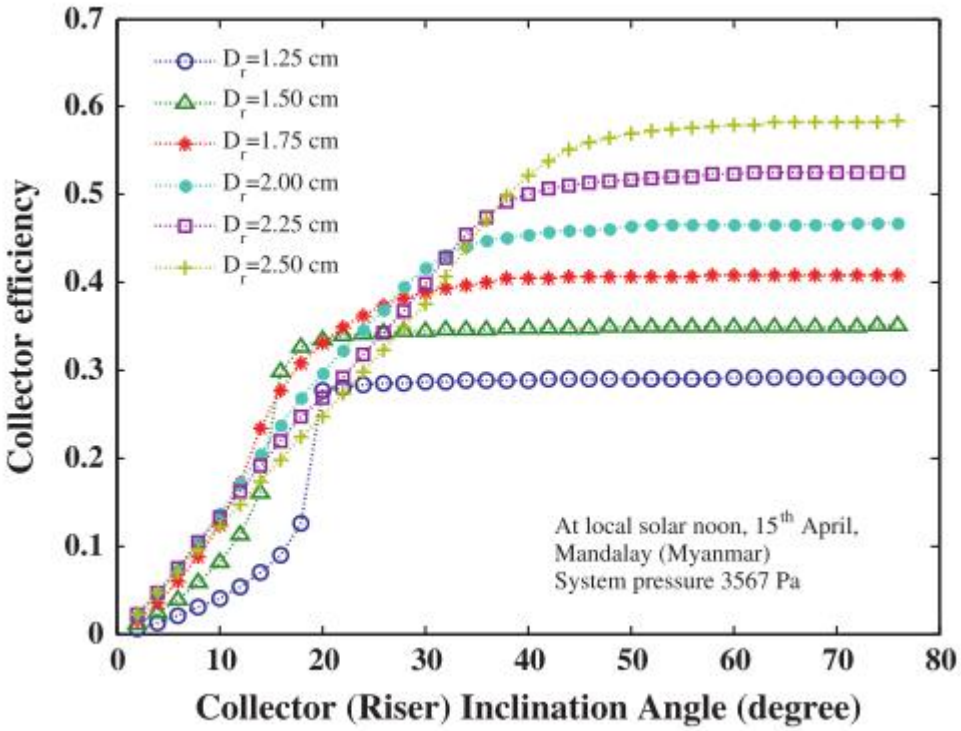

Figure 2.9 Collector efficiency versus riser diameter and inclination [47]

Wei et al. [48] developed a new configuration of a TPCT based flat plate solar collector consisting of a number of vertical tubes connected to upper and lower headers, and one returning liquid vertical tube as shown in Figure 2.10. They performed an experimental and theoretical study to investigate the performance of the new solar collector. The study revealed that employing the new TPCT solar water heater, a collector efficiency of 66% can be reached and an increase of 25 K in water tank temperature was obtained. They also reported that using an evacuated collector can provide a further increase in the collector efficiency compared with non-evacuated collector as illustrated in Figure 2.11.

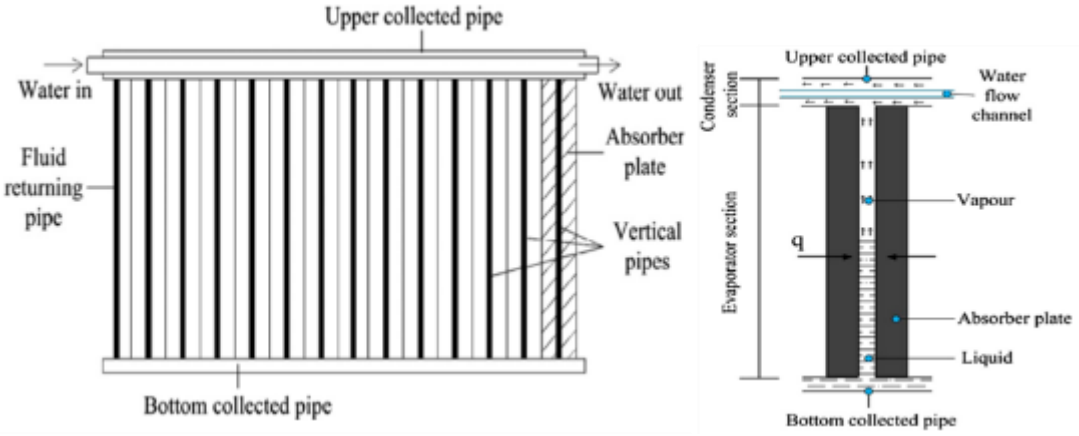

Figure 2.10 Developed wickless heat pipe solar collector [48]

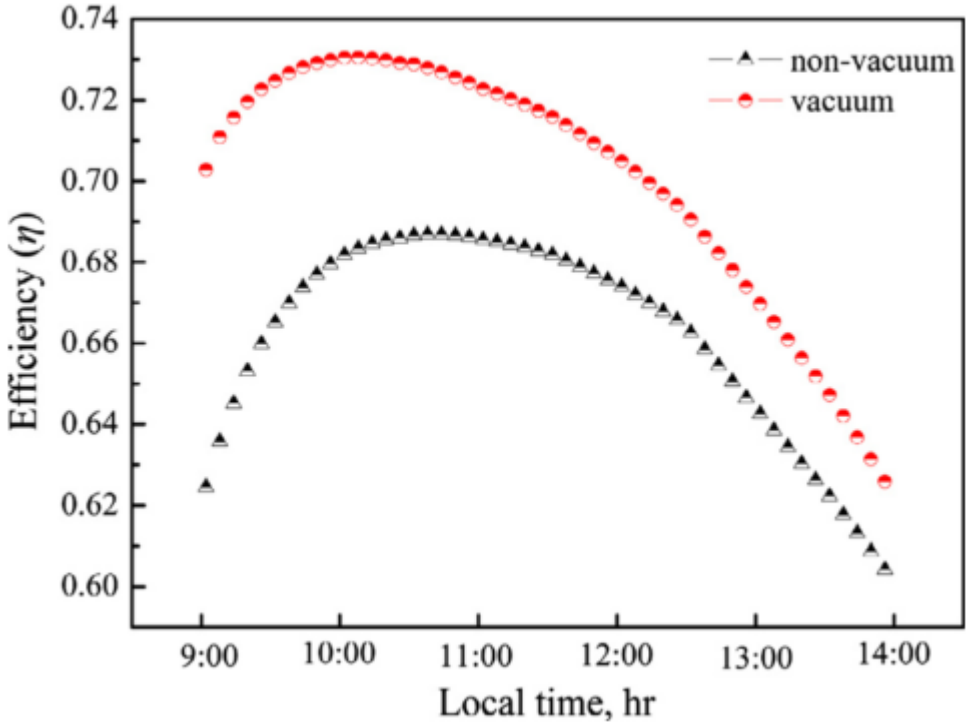

Figure 2.11 Comparison of collector efficiency between evacuated and non-evacuated collectors [48]

Li et al. [49] investigated experimentally a new insert-type loop-thermosyphon heat pipe to reduce the cost and facilitate the maintenance of the solar water heater at different fill ratios and heat inputs. They concluded that fill ratio has a significant influence on thermal performance, start-up temperature and a start-up time of the proposed heat pipe. Also, the heating speed of the solar water heater with this new type of loop-heat pipe is 2 times that

with conventional thermosyphon. Figure 2.12 shows the arrangement of the new insert-type loop-thermosyphon heat pipe.

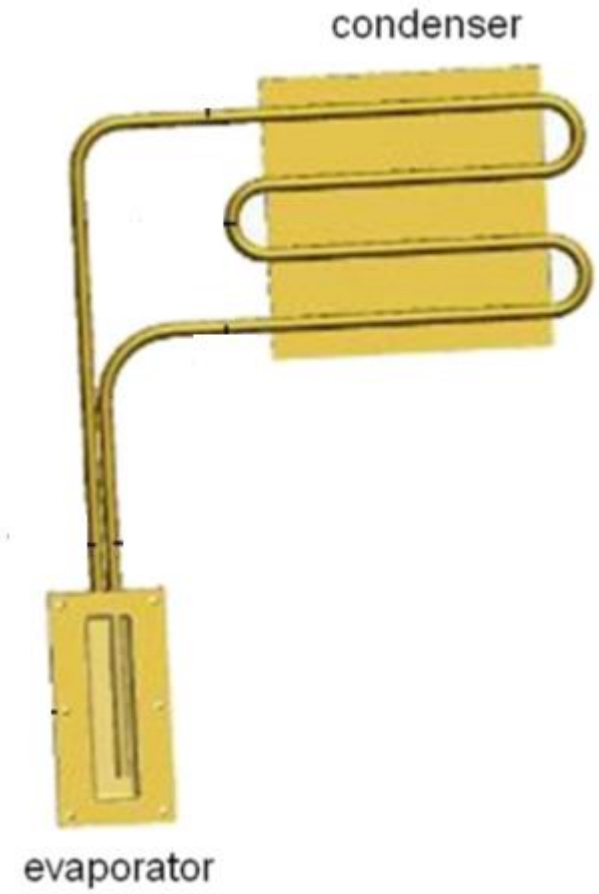

Figure 2.12 Loop-thermosyphon heat pipe [49]

Jahanbakhsh et al [50] tested the use of an ethanol-water solution in a heat pipe as a working fluid for different solution concentrations and inclinations to investigate their effect on the performance of the heat pipe. They found that the highest performance was obtained at concentrations of 50% and 75% and an angle of 35^{o} which provide an efficiency of 52%. Then, the performance of a solar hot water collector was investigated using the heat pipe with the highest performance. Results showed that using evacuated glass cover and changing the flow rate have a small influence on the collector performance.

Ersoz [51] compared the thermal performance of six thermosyphon heat pipe based evacuated tube air solar collectors charged with six different working fluids, namely, methanol, acetone, ethanol, chloroform, petroleum ether and hexane. The tests carried out at three different air

velocities 2, 3 and 4 m/s showed that the lowest efficiency was achieved using hexane for the three air velocities, while the highest efficiency was obtained when acetone at 2 and 3 m/s and chloroform at 4 m/s were used.

Kabeel et al. [52] designed, manufactured and tested a vacuum tube solar collector employing coaxial heat pipes and compared its performance with a conventional evacuated tube solar collector at different air flow rates and fill ratios. The annulus between the two coaxial tubes represents the heat pipe which was charged with two different refrigerants R22 and R134a, while the heat removal fluid (air) passes through the inner tube as shown in Figure 2.13. It was shown that optimum fill ratio was 30% at air flow rates of 0.0051 and 0.0062 kg/s, and it was 40% at 0.007 and 0.009 kg/s. Also, a maximum enhancement in system efficiency of 67% was achieved compared with conventional evacuated collector as illustrated in Figure 2.14.

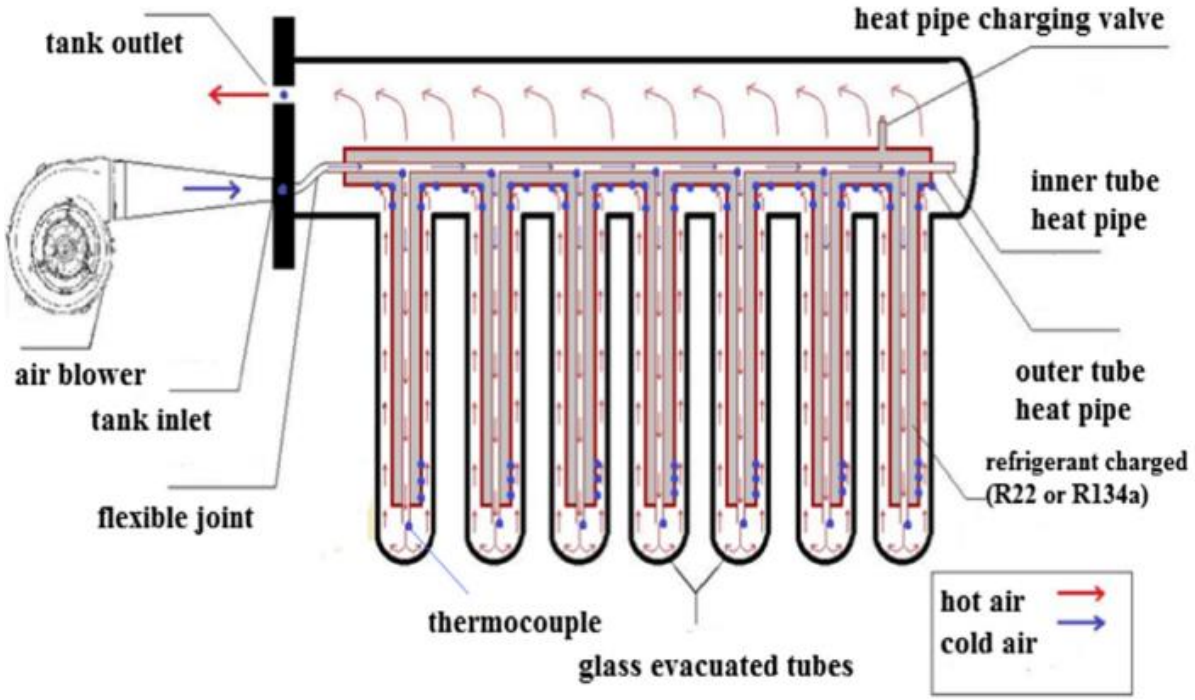

Figure 2.13 Coaxial heat pipe solar collector [52]

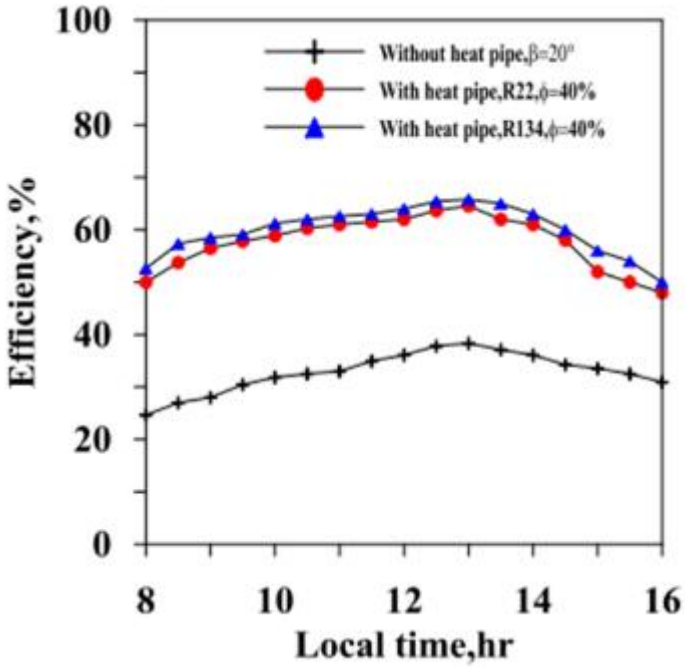

Figure 2.14 Comparison of collector efficiency with and without heat pie [52]

Zhang et al. [5] employed a steady state numerical finite difference method to investigate the effect of different geometrical parameters on the thermal characteristics of a heat pipe based flat plate solar water collector. The thermal resistance network was used to represent the physical model of the thermosyphon heat pipe. Effect of parameters such as solar insolation, evaporator length, heat pipe diameter, inclination and the thickness of absorber plate on the heat gain and efficiency of the system were reported. It was concluded that the highest heat gain and efficiency were obtained at a heat pipe diameter of 12 mm. Also, the heat gain was higher for higher evaporator length and higher absorber plate thickness, while the instant efficiency was higher for lower evaporator length and higher absorber plate thickness. In addition, the highest performance was achieved at inclination range of 30-45^{o} for the specified geographical location.

2.2.1 Summary

The above literature showed that integrating heat pipes with solar water heaters can greatly increase their thermal performance by reducing heat losses, and increasing efficiency and heat

gain of solar collectors as well as many general advantages of employing heat pipes in solar hot water systems. That means improving the thermal performance of the heat pipe can result in improving the heat transfer capability of solar collectors. Therefore, the next literature review will concentrate on the various studies investigating heat pipes thermal performance under influence of different operating and geometrical parameters. In addition, various means employed to enhance the condensation and evaporation processes inside heat pipes will be also reviewed.

2.3 CFD Numerical Studies

2.3.1 Numerical Studies of Multiphase Flows

Understanding of multiphase flows is an important task to solve numerous problems related to different engineering applications. Thus, a significant attention has been paid to investigate various flow patterns and phase-change characteristics in multiphase flows. Also, many researchers have employed numerical techniques to investigate the characteristics of the multiphase process as illustrated in Table 2.1.

Table 2.1 CFD modelling of multiphase flows

Ref.	**Working fluid**	**Investigated parameters**	**Agreement with experimental results and Findings**
[53]	Water	Gas-liquid flow in pipes	Acceptable agreement (deviation 10%), the CFD model can successfully predict the two-phase flow patterns
[54],[55]	R141B	Boiling process	The model can predict the phase-change process, high-temperature area corresponds to the vapour region
[56]	Water	Two-phase flow regimes	The CFD modelling can be used to simulate different gas/liquid flow regimes

[57]	Water	Mass and heat transfer during phase-change process	The CFD modelling can be employed to model the boiling process.
[58]	Water	Boiling phenomena during the vapour-venting process	The developed model would be used to design and optimize heat exchangers with vapour venting
[59]	Water	Vapour-liquid two-phase flows	Agree well with the analytical solutions (maximum deviation 5%), the model would be used to solve heat transfer and two-phase flow problems
[60]	R134a	Condensation process at different vapour mass fluxes	Good agreement (error of 8.1%) was achieved when the model results were compared with empirical correlations available in the open literature.
[61]	Water vapour	Condensation process of a vapour with non-condensable gases	The model predicts accurately the heat transfer rate of condensation of vapour with non-condensable gases.
[62]	Water vapour	Condensation process of a pure water vapour and vapour with different non-condensable gases	No effect was observed of vapour velocity and degree of superheat on the heat transfer coefficient, while it increased sharply as the saturation temperature increased, the mass transfer decreased at the interface when the non-condensable gas concentration increased

[63]	Water vapour	Condensation of vapour with non-condensable gas	The interfacial axial velocity cannot be neglected at a low fraction of non-condensable gases

All of the above studies have used CFD tool employing the Volume Of Fluid (VOF) approach in Fluent to model the multiphase flows. These studies concluded that using such a technique can predict well the experimental results and analytical solutions in the literature. They also reported that CFD modelling can simulate different gas/liquid flow regimes and boiling and condensation with mass and heat transfer during the phase-change processes.

2.3.2 Numerical Studies of Heat Pipes

There have been limited published CFD research work conducted to analyse thermal characteristics of TPCT heat pipes despite their numerous applications [64]. The following sections present various numerical studies according to different categories:

2.3.2.1 Numerical Technique Used

Different numerical methods were used to investigate flow patterns, phase-change processes and the thermal performance of heat pipes. Zhang et al. [65] developed a numerical 2-dimension mass and heat transfer model to investigate the thermal characteristics of a flat TPCT (see Figure 2.15). The study assumed that the flow inside the TPCT is a single-phase vapour flow and the phase change only occurs at the vapour-liquid interface. They compared the numerical solution with experimental work showing good agreement. The study also reported the temperature and velocity distribution inside the thermosyphon heat pipe.

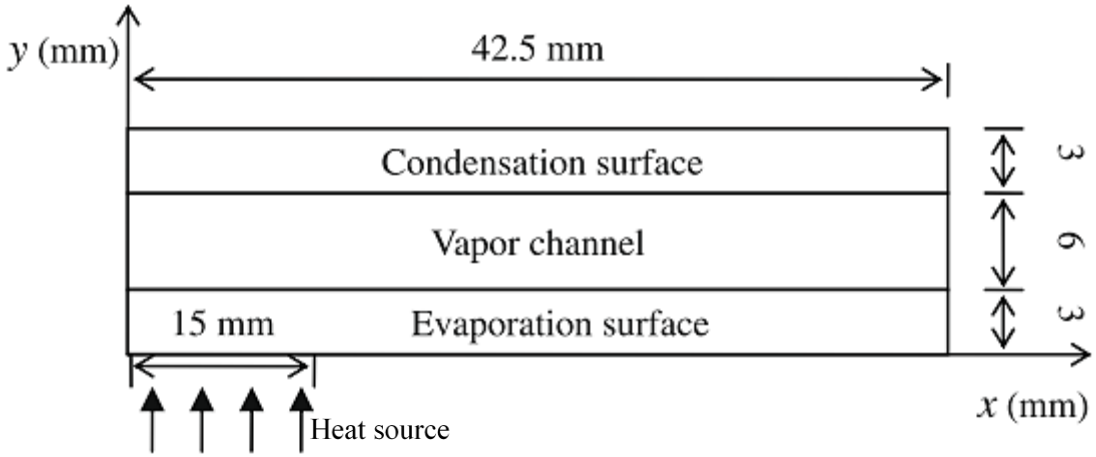

Figure 2.15 Dimensions and model of flat TPCT [65]

Alizadhdakel et al [66] tested the effect of input energy and liquid charge amount on the performance of a TPCT. They have also carried out a CFD simulation employing the VOF model in Fluent to investigate the phase-change process with the effect of non-condensable gases throughout the thermosiphon heat pipe, and compared the results of the experiment and CFD model. They concluded that the CFD simulation is beneficial in modelling and explaining the complex phase-change phenomenon. Also, an optimum value for fill ratio of 50% was identified for the studied thermosiphon heat pipe and heat input range.

Kafeel and Turan [67] developed a steady state axi-symmetric CFD model of a vertical TPCT employing the Eulerian multiphase technique in Fluent 13.0. The model included the effect of heat and mass transfer at the interface, condensation and evaporation throughout the computational domain. The water jacket at the condenser section was modelled to investigate the effect of heat transfer between the TPCT's wall and the cooling liquid. Effects of different evaporation mass transfer relaxation factors and heat inputs were investigated on thermal performance of the TPCT. They reported the validity of the model by comparing the CFD solution with experimental data in the literature. They found that the model is useful to use in simulation of the two-phase process and can be applied for different types of heat pipes. A similar study was carried out by Kafeel and Turan [68].

Huminic and Huminic [69] performed a three dimension CFD simulation based on VOF approach to model the effect of different concentrations of nanoparticles in water in a TPCT. The study investigated the effect of different operating temperatures and iron oxide nanoparticles concentrations on thermal performance of the TPCT. The study revealed that the CFD solution agreed well with the experimental data. It was shown that the concentration of nanoparticles in water had a considerable influence on the heat transfer characteristics of the TPCT.

Nair and Balaji [70] developed a steady state numerical model in Matlab, and a CFD code with the VOF model to investigate the effect of internal fins inside the condenser section on the performance of a TPCT. They compared results of the two numerical models with experimental data in published literature. The study concluded that the lumped parameter model agreed with experimental results better than the CFD model, but it does not have the capability to visualise the temperature distribution and volume fraction as the CFD simulation has as shown in Figure 2.16.

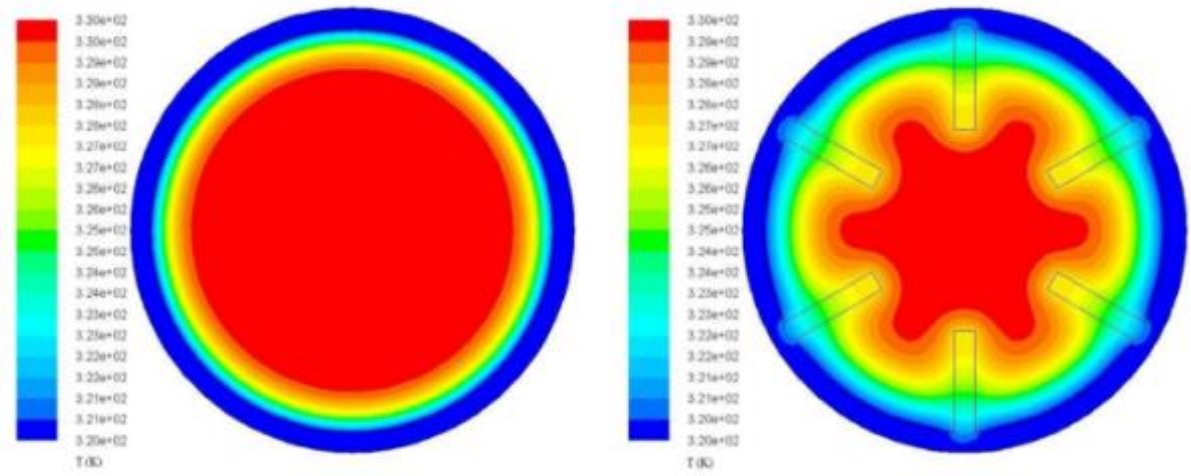

Figure 2.16 Temperature contours with and without fins [70]

Shabgard et al. [71] developed a numerical model to study the effect of various liquid charge amounts on the heat transfer performance of a TPCT using finite volume method and validated the model with experimental data of [72] and [73]. They found that the model can

predict the optimum fill ratio depending on the liquid film in the evaporator and condenser. It was also concluded that the thermosyphon with optimum fill ratio exhibits the lowest thermal resistance and shortest time response, while over-filled and under-filled TPCTs may cause flooding and dry-out conditions, respectively. In addition, in the case of optimum fill ratio, the study recommended adding a small amount of the working fluid to avoid the liquid film breakdown.

2.3.2.2 Working Fluid Used

Fadhl et al [64] developed a CFD model using the VOF method in Fluent to simulate condensation and evaporation processes inside a TPCT charged with water. CFD results were compared with experimental data at different heat inputs. They found that the numerical solution can effectively model the two-phase flow and heat transfer inside the TPCT and visualise the complex phase-change processes. They also found that the thermal performance of the thermosiphon heat pipe was improved by increasing heat input over 172 W.

Kuang et al. [74] modelled the boiling characteristics in the evaporator section of a vertical TPCT for application in a nuclear reactor employing CFD simulation based on VOF model in Fluent. Different regimes and boiling flow behaviours were visualised, namely bubbly flow, slug flow and churn bubbly flow for ammonia as a working fluid. They found that different phase-change characteristics were obtained between large and small pipe diameters. Based on heat transfer coefficient figures, it was concluded that the dominant mechanism is the nucleate boiling for large pipes and low heat and mass fluxes. Also, mass flux had less influence on the heat transfer coefficient for large pipes and low heat flux.

Fadhl et al [75] carried out a CFD modelling of a TPCT charged with R134a and R404a, and results were compared with published experimental data in terms of the wall temperature distribution. They found that phase-change characteristics of both fluids inside the thermosiphon differ significantly from that of water.

Jouhara et al [76] performed a three-dimensional CFD modelling with the VOF method to visualise the boiling and condensation processes in a TPCT charged with water and R134a. The study also simulated the water jacket to investigate the characteristics of the cooling process in the condenser. They validated the numerical results experimentally using glass thermosyphon and concluded that the CFD simulation can successfully model the transient characteristics of the boiling process and the condensate liquid film. They found that the boiling characteristics of the two fluids were different where smaller bubbles were observed using R134a compared with those using water [8].

2.3.2.4 Effect of Inclination Angle and Fill Ratio

A number of CFD studies have been conducted to examine the influence of fill ratio and tilt angle on the thermal characteristics of heat pipes. Abdullahi [77] performed CFD and experimental studies to examine the effect of coolant flow rate, input energy and orientation on thermal performance of a TPCT. They reported that the thermal performance of the TPCT increases as inclination and input energy increase.

Lian et al. [78] developed a numerical CFD simulation based on the VOF technique in Fluent to model the phase-change thermal characteristics in a Rotating Heat Pipe (RHP) as shown in Figure 2.17. They modified the model developed by Sun et al. [59] to be used to simulate the heat and mass transfer during the phase-change process in the evaporator and condenser. This model has been employed to investigate the effect of heat input, rotational speed and the fill ratio on the two-phase thermal characteristics of the RHP. The study concluded that the new model can capture well the thermal characteristics of the phase-change processes during the operation of the RHP. It was also reported that the performance of the RHP increased as the rotational speed increased, whereas it decreased when the fill ratio increased.

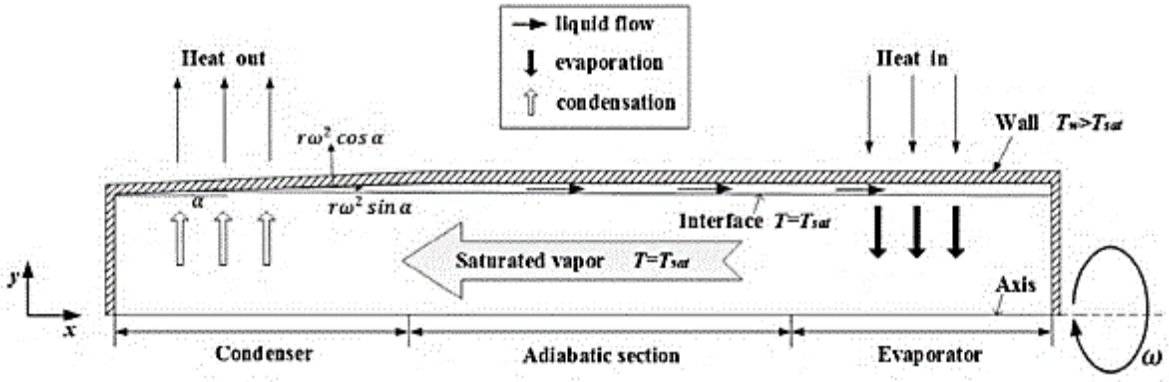

Figure 2.17 Working principles and physical domain of RHP [78]

Xu et al. [79] developed a CFD model employing the VOF technique in Fluent software to simulate the effect of different inclination angles and evaporator wettability in terms of contact angle on thermal characteristics of a TPCT. The numerical model was validated by carrying out an experimental work and comparing the results where a good agreement was reported. The study visualised different hydrophobic and hydrophilic evaporator surfaces, and different orientations from the vertical to near horizontal. Also, the thermal performance of the TPCT for various surface wettabilities and inclinations was reported. The study concluded that the highest and lowest thermal resistance was found at angles of 10^o and 90^o, respectively. This is due to detachment of bubbles away from the surface as the inclination increases with respect to the horizontal. A similar study was conducted by Xu et al. [80], but for different fill ratios besides the evaporator wettability. They found that the optimum fill ratio is between 20% and 30% which provides the lowest thermal resistance, while fill ratios of 12% and 40% exhibit a higher thermal resistance.

2.3.2.4 Effect of Evaporation and Condensation Time Relaxation Factors

Kim et al [81] implemented a CFD simulation to study the effect of the condensation time relaxation factor on the thermal characteristics of a TPCT. The study concluded that the condensation relaxation factor should be considered as $0.1\times(\rho l/\rho v)$ to accurately simulate the mass transfer process during condensation and evaporation phenomena.

Xu et al. [82] developed a CFD model based on the VOF method in Fluent with a variable time relaxation parameter to model the phase-change processes in a TPCT. The model calculates the new relaxation parameter for the condensation and evaporation and processes at every time step depending on old values to become variable rather than a constant. They found that the relative errors in temperature distribution and thermal resistance are greatly reduced using variable time relaxation parameter compared with constant time relaxation parameter. This was proved by comparing CFD results with experimental data available in the literature.

2.3.2.5 Enhancing Thermal Performance

Xia et al. [83] performed a numerical CFD simulation using the VOF model in Fluent to investigate the two-phase flow and phase-change processes in a TPCT integrated into a cooling system of a heavy duty extrusion pelleting line as shown in Figure 2.18. The study reported that the model predicted well the experimental data. Thus, the CFD solution can represent the phase-change processes for the proposed cooling system.

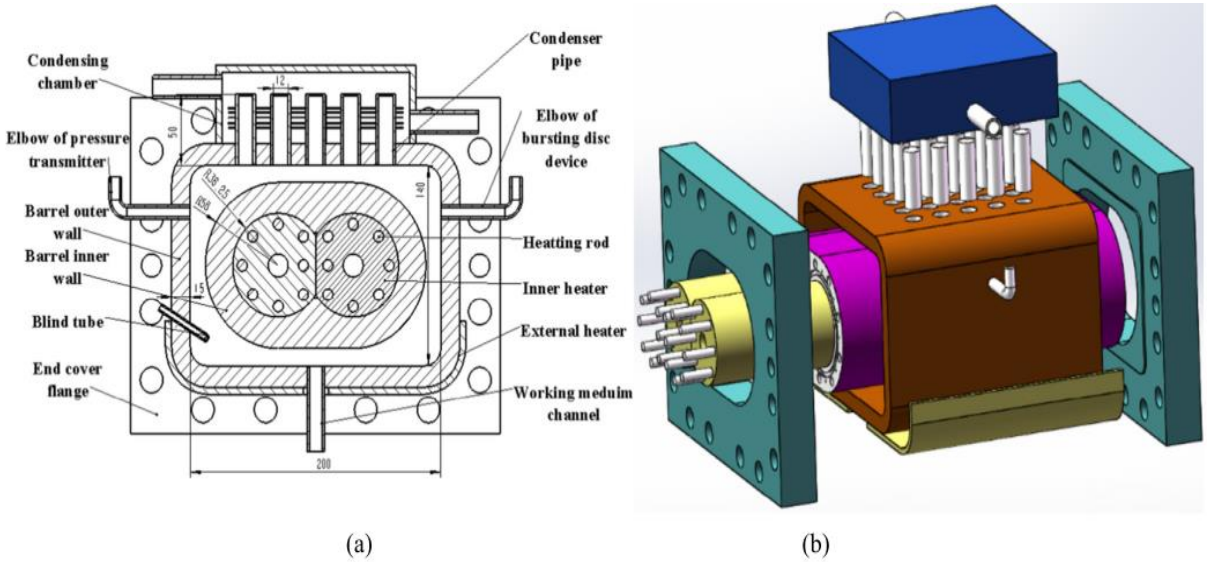

Figure 2.18 Thermosyphon heat pipe integrating to cooling system of a heavy-duty extruder [83]

Fertahi et al. [84] carried out a CFD simulation with the VOF multiphase technique in Fluent to model the phase-change characteristics of a TPCT. They used the work of Fadhl et al. [64] to validate their CFD solution. Then, they used the validated numerical solution to compare the performance of two TPCTs, one with a smooth condenser and another TPCT with inclined fins emerged with the vapour zone as shown in Figure 2.19. The model solution visualised the liquid pool, a liquid film in the condenser, temperature contours and vertical velocity contours. The study reported an increase of 16.05% in the efficiency of the TPCT with finned condenser compared with the TPCT of the smooth condenser.

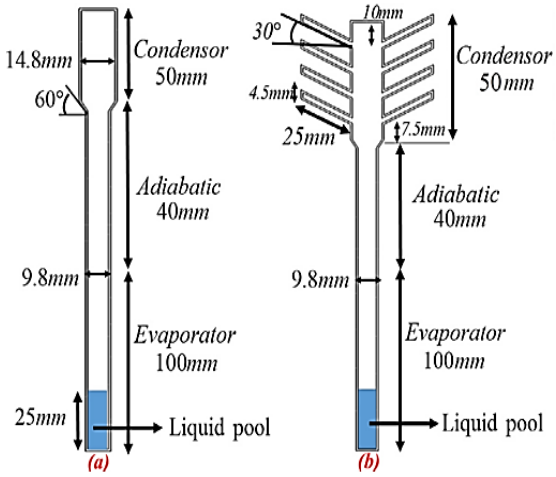

Figure 2.19 The proposed thermosyphon: (a) plain condenser and (b) finned condenser [84]

2.3.3 Summary

From reviewing of various numerical investigations about heat pipes, different numerical methods were used, CFD in Fluent, finite volume method and lamped parameter models using Matlab. The most effective tool was the CFD modelling using Fluent. For CFD in Fluent, the three multiphase approaches; namely Eulerian, Mixture and VOF were used to model the two-phase flows. Most of these studies proved that the VOF technique can simulate the flow patterns and phase change processes inside heat pipes by facilitating the tracking of the interface effectively due to solving one set of equations only. On the other hand, the effect of using different working fluids was investigated using CFD modelling where different boiling characteristics of these fluids were observed compared with water. In addition, the effect of

the evaporation and condensation time relaxation factors on the performance of heat pipes were studied using CFD simulation showing the capability of using CFD Fluent in reproducing the flow fields and phase-change processes inside heat pipes. While very limited CFD modelling studies were carried out to investigate effects of important parameters such as fill ratio, inclination angle, liquid charge ratio and surface wettability (contact angle) on the performance of the TPCT.

2.4 Experimental Studies of heat pipes

A number of experimental investigations have been carried out to examine the impact of different parameters such as working fluid, fill ratio, aspect ratio and inclination angle on the thermal characteristics of various heat pipes at different operating conditions.

2.4.1 Effect of Fill ratio

Fill ratio is an important parameter affecting the performance of heat pipes, so various experimental investigations were conducted to identify the optimum fill ratio which provides the best thermal performance. Emami et al. [85] investigated the thermal performance of an inclined TPCT charged with water at different fill and aspect ratios. They reported the effect of these parameters on heat transfer performance, heat transfer coefficient in the condenser and the temperature distribution. The study revealed that for all aspect ratios, an angle of 60^{o} and a fill charge of 45% exhibited the best heat transfer rate, whereas the highest condensation heat transfer coefficient was obtained between angles of 30 and 40^{o}.

Jiao et al [86] developed a steady-state analytical model to investigate the influence of the amount of the charged liquid on the thermal characteristics of a vertical wickless heat pipe and compared the results with their experimental work. They found that the fill ratio depends on geometrical parameters, operating pressure and heat input. They also reported that their model does not consider unstable boiling phenomena which has a considerable influence on the thermal characteristics of the TPCT.

Sukchana and Jaiboonma [87] examined the effect of the liquid charge and length of adiabatic section on the performance of a heat pipe charged with R-134a. They found that the liquid charge amount has a higher effect on the tested heat pipe performance than the adiabatic length. They also reported that 5.92 kW/m^2 and 15% are the optimal heat flux and fill ratio for the shorter adiabatic section, respectively.

Chehade et al [88] investigated the influence of charged water liquid amount, coolant flow rate and inlet temperature on the thermal characteristics of a loop TPCT. They found that the fastest startup was obtained at the optimal fill ratio which was between 7% and 10%. The study also found that the best thermal performance was achieved at a coolant inlet temperature and flow rate of 5^{o}C and 0.7 l/min, respectively.

Chen and Chou [89] carried out an experimental study to examine the performance of a flat plate heat pipe employing three different fill ratios of acetone. They reported that the optimum charging liquid volume for the tested heat pipe was 25%. Yin et al [90] analysed theoretically the maximum liquid filled to start up an oscillating heat pipe and concluded that the maximum amount of liquid charge depends on the type of liquid and the operating temperature.

Lataoui and Jemni [91] tested the thermal performance of a stainless steel TPCT using ethanol, water and acetone as working fluids. The test carried out for three charge fills, underfilled, optimally filled and overfilled conditions and different condenser coolant inlet temperatures at various heat loads. They concluded that the coolant inlet temperature has a similar effect as the heat load on the evaporator-condenser temperature difference. They also found that a fill ratio of 10% (underfilled) exhibited the highest evaporator temperature which caused a dry-out condition, while the lowest evaporator temperature was obtained using a fill ratio of 20% (optimum). Almost a same evaporator temperature was observed for a fill ratio 35% (overfilled), but more uniform temperature distribution was attained. In addition, the fill

ratio of 100% of evaporator volume corresponds to the highest evaporation heat transfer coefficient for all working fluids [2].

Manimaran et al [92] and [93] performed experimental studies to examine the effect of heat load, inclination and liquid amount on thermal characteristics of heat pipes using nanofluid and water as working fluids, respectively. They reported that the vertical orientation and a fill ratio of 75% exhibit the lowest thermal resistance. Also, the study concluded that at an angle of 30^{o} and a fill charge of 75%, the efficiency of the heat pipe reached its highest value for both fluids. In addition, using nanofluid reduced the thermal resistance by 62% compared with pure water.

2.4.2 Effect of Inclination Angle

Some applications such as solar collectors require inclined heat pipes, thus a number of research studies investigated the effect of inclination on the thermal performance of heat pipes. Sadeghinezhad et al. [94] and Ghanbarpour et al. [95] and [96] investigated the effect of inclination angles on the thermal characteristics of a sintered wick and screen mesh heat pipes, respectively, using different nanofluids. They reported that the orientation has a strong influence on the heat pipe performance and an angle of 60^{o} exhibits the lowest thermal resistance. Regarding nanofluid effect, they concluded that using nanofluid particles reduced the thermal resistance of the heat pipe and reduction in thermal resistance of 48.4 and 30% were reported by [94] and [96], respectively.

Xue and Qu, [97] and Senthilkurmar et al. [98], studied experimentally the influence of the inclination on the thermal characteristics of ammonia and copper nanofluid two pulsating heat pipes. They demonstrated that the thermal performance of studied heat pipes increased as the inclination angle increased. In addition, Xue and Qu [97] concluded that the best fill ratio in terms of avoiding the dry-out at the horizontal orientation was between 70% and 80%.

Nazarimanesh et al [99] tested the performance of a sintered heat pipe at various inclination angles. They found that the lowest thermal resistance for water as a working fluid was achieved at an angle of 90^o, whereas for silver nanofluid, the lowest thermal resistance was obtained at 30^o.

Sukchana and Pratinthong [100] investigated the effect of tilt angle and bending position on the thermal performance of a TPCT charged with R-134a with a flexible hose as an adiabatic section as shown in Figure 2.20. They concluded that for all inclination angles, the lowest thermal resistance was obtained at a liquid charge of 18%. Regarding bending effect, at optimum heat flux and fill ratio, the best performance was at a tilt angle of 40^o for all bending positions excluding when the bending at both lower and upper ends of the adiabatic section, the best performance was at 60^o. Also, they pointed out that the case without bending exhibited the highest performance, whereas the case with bending at both ends provided the highest thermal resistance.

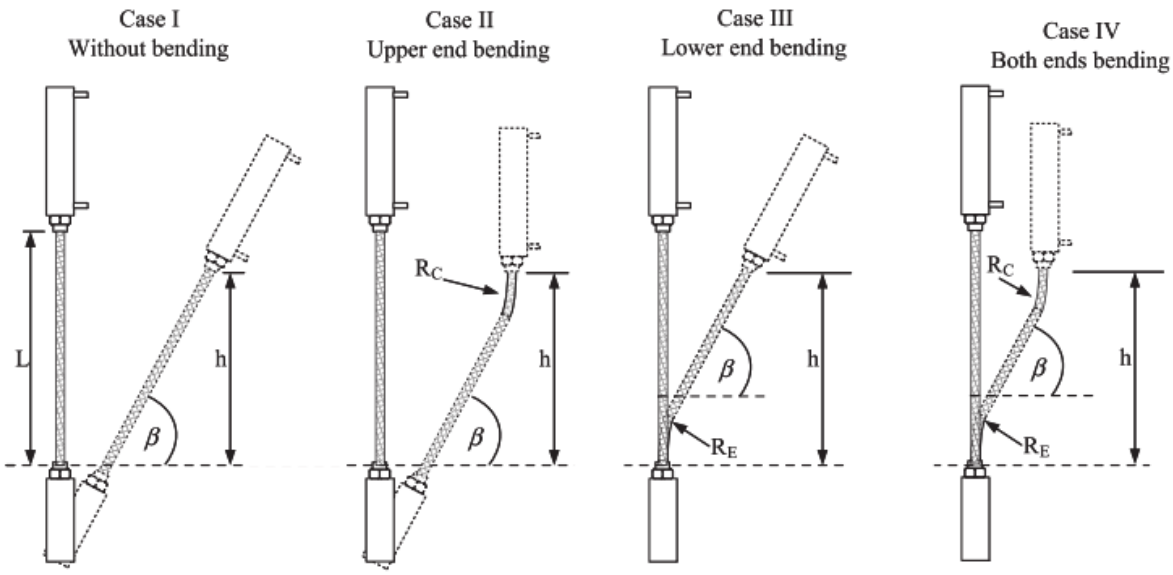

Figure 2.20 Different cases of orientations and bend positions of TPCT [100]

Gedik [101] investigated experimentally the effect of inclination angle at various operating conditions on the performance of a TPCT using water, ethanol and ethylene glycol as working fluids. Results revealed that the amount of heat released at condenser section increased as the

inclination angle increased and the inclination angle of 90° exhibited the highest heat transfer rate for all cases. They also reported that at an inclination angle of 90°, the lowest thermal resistance was achieved when ethanol was used as a working fluid for all three coolant flow rates and heat inputs. In addition, the highest heat transfer rate was obtained for water at a heat input of 200W and 10 l/h water flow rate, for ethylene glycol at 200W and 30 l/h, and for ethanol at 600W and 10 l/h making each one of them suitable for a certain application.

Tang et al. [102] investigated the effect of horizontal and inclined orientations on the performance of heat pipes with two heat sources at their both ends and the cooling section placed at different positions as shown in Figure 2.21, [102]. They concluded that a significant enhancement in the thermal performance of heat pipes was observed using such an arrangement for both inclined and horizontal orientations. They also found that the increase in the upper evaporator temperature for inclined heat pipes can be effectively controlled by mounting the cooling block close to the upper evaporator.

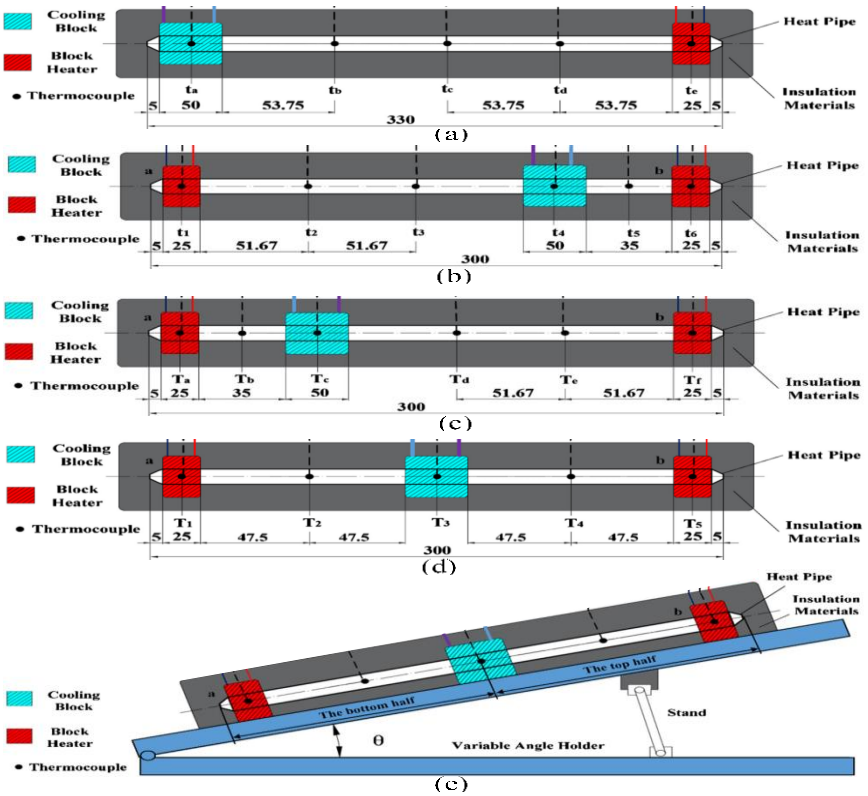

Figure 2.21 Horizontal and inclined heat pipe with different positions for cooling block: a-normal, b-right, c-left, d-middle and e-middle-inclined [102]

2.4.3 Effect of geometrical factors

Noie [103] investigated the effect of different evaporator aspect ratios (evaporator length to evaporator diameter) of 7.45, 9.8, and 11.8 on the heat transfer characteristics of the TPCT for different liquid charge amounts and a range of heat inputs. It was found that the aspect ratio had a significant effect on the evaporator wall temperature and heat transfer rate depending on the fill ratio. For example, the lowest aspect ratio (7.45) provided the lowest evaporator wall temperature and highest heat transfer rate at a fill ratio of 90%, while at the highest aspect ratio (11.8), the best fill ratio was 60%.

Amatachaya and Srimuang [104] tested the effect of two different cross-section geometries with a number of parameters on the performance of a TPCT filled with water. They concluded that circular geometry has higher heat transfer performance compared to the flat one and the heat flux increased as input energy and aspect ratio increased.

Seo and Lee [105] examined the effect of aspect ratio (total length to inside diameter) on the occurrence of the entrainment limit of a long stainless steel TPCT. They found that the aspect ratio has a considerable impact on the point at which the entrainment limit occurs which was not considered in the previous correlations. Therefore, a new correlation for the entrainment limit including the aspect ratio effect was proposed. They reported that addition of such parameter has reduced the error in the previous correlation from 40% to 5%.

2.4.4 Effect of Working Fluid

Jouhara and Robinson [73] investigated experimentally the effect of using three working fluids namely, water, FC-84 and FC-3283 at two filling ratios (100% and 50%) on the performance of a TPCT. The study revealed that the TPCT charged with FC-84 offers a better performance than that charged with water at heat loads lower than 30-40 W for the same fill ratio. However, above a heat load of 40 W, the TPCT charged with water outperforms thermosyphons charged with other fluids.

Mozumder et al [106] investigated the effect of different working fluids, namely acetone, methanol and water on the performance of a small size thermosiphon (10 W heat transfer capacity) at different liquid charges and heat loads. Results revealed that the TPCT charged with acetone provided the highest overall heat transfer coefficient. It was also observed that the performance of the TPCT filled with acetone increased as the fill ratio increased and a fill ratio of 100% exhibited the highest thermal performance whereas for water-filled thermosyphon, the highest thermal performance was obtained at a liquid charge of 85%.

Ersoz and Yıldız [13] investigated the effect of water, methanol and petroleum ether as working fluids on the thermal characteristics of a TPCT at different air velocities as a coolant at the condenser section. They reported that the highest and lowest thermal performance correspond to methanol and petroleum ether, respectively at all air velocities. Results also showed that water is more cost-effective fluid compared with petroleum ether and methanol.

Ma et al. [107] carried out an experimental work to test the effect of using eight working fluids on the performance of a TPCT with evaporator placed vertically in a constant temperature water bath as shown in Figure 2.22 [107]. The experimental data were compared with some correlations available in the literature. They concluded that the highest thermal performance was achieved using R245fa/R152a and the performance of R600a and R1234ze was close to that of R134a.

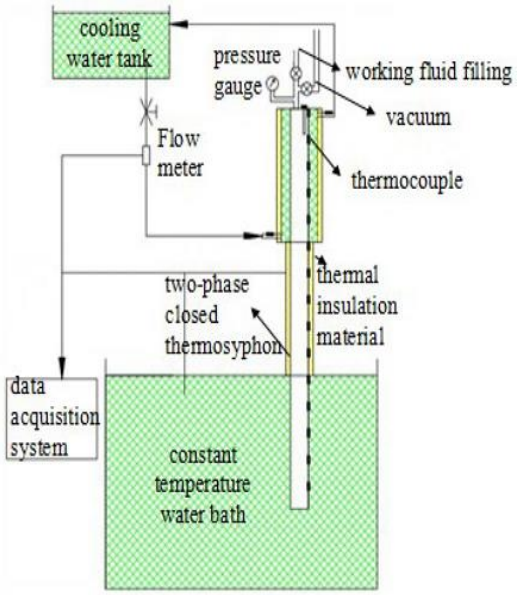

Figure 2.22 Thermosyphon test rig [107]

Jouhara et al [108] tested the use of an ethanol-water azeotrope as a working fluid in a TPCT with an inclined condenser by an angle of 12^{o} from a horizontal evaporator (as shown in Figure 2.23 [108]) and compared the TPCT's performance with another TPCT charged with water. The study examined the influence of the working fluid, evaporator inclination and the heat load on the TPCT thermal performance. They concluded that using the azeotrope can reduce the evaporator temperature, overall thermal resistance and the temperature oscillation in the evaporator at the vertical orientation and low heat inputs. They also reported that the inclined and horizontally oriented thermosyphons operate normally (the condensate returns to the evaporator without the need to a wick structure) under the proposed configuration although they are wickless.

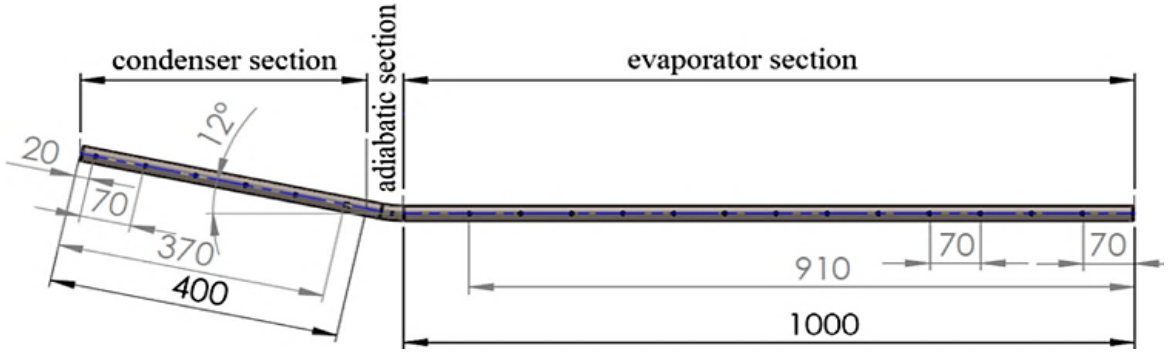

Figure 2.23 The proposed Thermosyphon [108]

2.4.5 Investigation of Phase-Change Characteristics

Liu et al. [109] visualised two-phase flow characteristics in a TPCT using Electrical Capacitance Tomography (ECT) technique with an image reconstruction algorithm. They reported that the ECT technique has the capability to measure the film thickness accurately as compared with that predicted by Nusselt theory. The study concluded that the dominant flow pattern at low heat inputs is the annulus flow, whereas at high heat inputs, the flow becomes greatly unstable due to the formation of plug flow.

Putra et al. [110] used the neutron radiography technique to visualise characteristics of the phase-change phenomena inside a heat pipe. The study also visualised and investigated the effect of different fill ratios and pressures on the change in temperature and the two-phase processes in the heat pipe. They concluded that the neutron radiography method can visualise the change in boiling and condensation processes, and hence the heat pipe's temperature due to the use of various pressures and fill ratios. They also reported that the pressure has a significant role on the phase-change characteristics inside the heat pipe. Also, the highest evaporator temperature was achieved at a fill ratio of 10%, whereas the lowest temperature is obtained at fill ratios of 50% and 70%.

Jafari et al. [111] performed an experimental study to specify the more applicable correlation for the evaporation and condensation in a TPCT filled with water under influence of different fill ratios and heat inputs. The study reported a dry-out occurrence at low fill ratios of 8% and 16%, whereas a fill ratio of 100% exhibits the highest evaporation heat transfer coefficient. The study suggested that some of the previous correlations developed for the evaporation and condensation processes in the TPCT agree with the experimental data. For example, Imura correlation showed very good agreement at fill ratios 50% and higher and good for fill ratio 35% at high and low heat loads whereas at a fill ratio of 16%, it showed very good agreement only at high heat inputs. Also, Rohsenow correlation provided very good agreement at a fill

ratio of 100% whereas combination of some correlations such as Kutateladze and Shiraishi, Labuntsov and Shiraishi, and Chowdhury and Shiraishi showed very good agreement at a fill ratio of 35%. These agreement were only reported for a large diameter of the TPCT.

2.4.6 Summary

The above experimental studies about heat pipes showed that there are optimal values for the liquid charge volume and angle of inclination which correspond to the highest thermal performance. Most investigations identified the optimum fill ratio between a small amount (causing dry-out) and large amount (causing flooding). This optimal value can differ from one heat pipe to another depending on geometrical parameters, operating pressure and heat load. However, few research studies reported that heat pipes performance increases as the liquid charge volume increases. On the other hand, identifying the best inclination has some discrepancy in the literature. Some investigations reported the vertical orientation as the best in terms of the thermal performance, while other studies concluded that other inclinations were the best. This may also depend on different parameters such as geometry, fill ratio and working fluid. Regarding the working fluid, the experimental investigations revealed that water outperformed all other working fluids, especially at relatively high heat inputs, while some other fluids provided higher performance than water at low heat inputs.

2.5 Studies of Geyser Boiling Phenomena

Geyser boiling is a phenomenon arising during the phase-change process. In a TPCT, it occurs due to a gathering of the generated vapour slightly above the bottom of the evaporator section inside the TPCT, creating a large bubble size covering the entire inside diameter. Consequently, at a certain pressure and superheat condition, the bubble bursts pushing the liquid above it up to the condenser section, which may lead to vibrating of the TPCT [112], [2] as shown in Figure 2.24 [113].

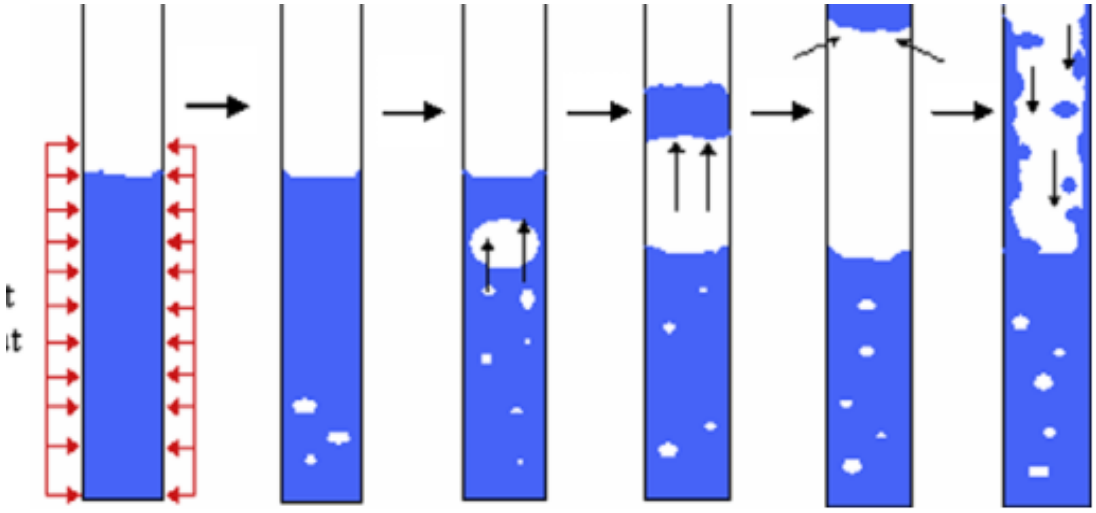

Figure 2.24 Initiation and developing of geyser boiling in TPCT [113]

There are still challenges concerning the phase-change process that limits the thermal characteristics of thermosiphon heat pipes and these need to be investigated to examine their effect on the performance and the operating limits of the TPCT [25], [2]. The following sections will categorise the investigations of geyser boiling based on different parameters:

2.5.1 Effect of Working Fluid

Different parameters affecting the geyser boiling in an annular vertical thermosiphon charged with water and ethanol was tested by Lin et al [112]. The study revealed that the occurrence of geyser boiling for ethanol was delayed to a higher heat flux than that for water. They also concluded that the geysering period was longer at a lower heat input, with a higher liquid charge and a longer length of the evaporator [2].

Negishi and Sawada [114] tested the performance of a TPCT filled with water and ethanol at different inclination angles and fill ratios, with visualisation of the unsteady behaviour of thermosiphon. The study revealed that to achieve a steady heat transfer performance, a 25-60% fill ratio and inclination angle between 20-40^{o} should be used when water is the working fluid [8]; whereas a 40-75% fill ratio and more than 5^{o} tilt angle is needed for ethanol. They reported that the amplitude and period of the geyser boiling for ethanol was smaller than those of water. Also, a uniform temperature distribution and higher heat transfer rate resulted after

the fluid in the evaporator pushes up to the condenser; they called this strange behaviour a water hammer phenomenon which occurred when the fill ratio exceeded 60%. However, the evaporator of the TPCT was fixed at a constant temperature of 85ºC, so that the effect of the heat load was not studied [2].

The mechanism of the geysering in a vertical glass TPCT filled with water and R-113 was tested by Kuncoro et al. [115]. Results showed that inducing the geyser effect can be largely related to the temperature distribution; which depends on the geometry of the TPCT, the mechanism of heat transfer and the physical properties of the charged liquid. It was also reported that even if the pressure increases during the bubble formation, the occurrence of geysering may continue when the driving force for initiating the geysering is the superheat [8].

Jouhara et al. [76] performed experimental and numerical study to visualise the geyser phenomenon in a TPCT filled with water and R134a; they used a glass TPCT to visualise the geysering experimentally. They found that the heat input has a considerable influence on initiating and disappearance of the geyser phenomenon; in which the geysering period decreases with increasing the heat input and disappears at a higher input energy [2]. They also reported that the geysering was not observed in the case of R134a due to very small bubbles generation.

Xia et al. [116] visualised experimentally the instability behaviour of the boiling process inside a flat evaporator and condenser TPCT (as shown in Figure 2.25 [116]) using water, acetone and ethanol as working fluids. The study tested the effect of the fill ratio, type of working fluid, heat flux and coolant inlet temperature on the heat transfer mode and, hence on the temperature and pressure oscillation inside the flat TPCT. They reported that the fluctuation in the heat transfer coefficient, temperature and pressure were produced mainly due to physical properties of the working fluid, behaviour of bubbles and low operating

pressure which strongly affect the boiling regime. Also, it was observed that the initiation of a large bubble is significantly affected by condensate droplets falling in the liquid pool which causes heat transfer instability, especially, in the natural convection boiling regime.

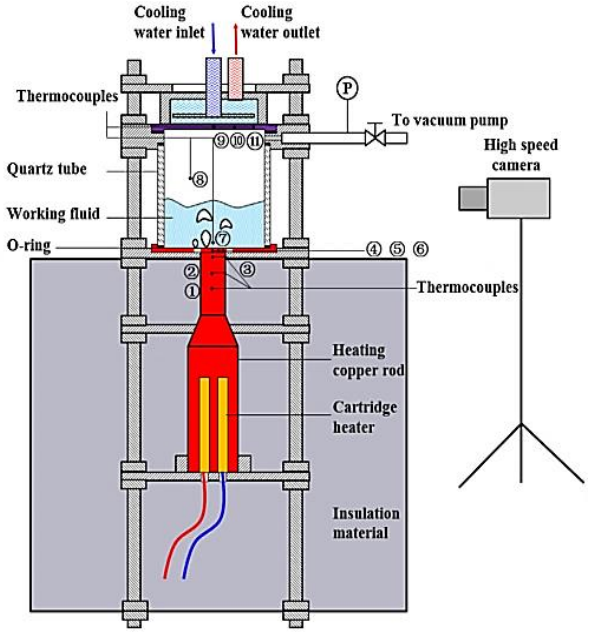

Figure 2.25 Experimental apparatus of flat TPCT [116]

It was also reported that the boiling instability is greatly affected by the fill ratio at heat flux lower than 69.6 W/cm^2, whereas the effect of the coolant inlet temperature was large when the heat flux ranged from 23.6 and 69.6 W/cm^2. In addition, very low-temperature oscillations were observed using acetone and ethanol where no intermittent boiling was noticed.

2.5.2 Effect of Fill ratio and Inclination

The influence of the tilt angle and fill ratio on the thermal characteristics of a TPCT filled with water [8] was tested by Noie et al. [117]. Results showed that the condensation heat transfer coefficient increases with the increase of the fill ratio and the highest value was obtained at 22% and 30% for the inclination angle of 30^o, whereas for the inclination angle of 45^o, it was obtained at a fill ratio of 15%. In addition, the heat transfer rate increases as the fill ratio increases; and for the three fill ratios, the highest heat transfer rate was achieved at an inclination angle between 15^o and 60^o. They also observed the occurrence of the geyser

phenomenon [2], but they did not examine its characteristics or its effect on the performance of the TPCT.

Abreu and Colle [118] studied the effect of different parameters such as fill ratio, inclination and coolant inlet temperature on the thermal performance of a TPCT with a straight evaporator and semi-circular condenser for a compact solar water heater. The study revealed that the highest thermal performance was obtained at the lowest inclination and liquid charge, but the dry-out limitation may occur at these low values. They also reported the occurrence of the geyser boiling at a low heat input during the test, but the effect of this phenomenon was not analysed [8].

Emami et al. [119] tested the effect of the liquid charge, the orientation, the inside diameter of thermosyphon and the coolant flow rate on geyser boiling in the TPCT. They reported that a shorter geyser period and lower temperature oscillation was observed at a lower fill ratio and inclination; no effect from the water mass flow rate on the geyser boiling was noticed. In addition, the geyser effect can be avoided below a fill ratio of 30% and it did not occur at an angle of 15^{o} and inside diameters of 20 and 24 mm [2].

Khazaee et al. [113] tested the effect of input energy, fill ratio, coolant flow rate and the evaporator length on the geyser phenomenon in the TPCT charged with methanol. The study showed that the period of the geysering and the amplitude of the temperature oscillation increase as the fill ratio increases; whereas the geysering disappears at a fill ratio of less than 30%. In addition, the heat input plays an important role by affecting the period and intensity of the geyser phenomenon, in which the period and intensity of the geysering decrease as the heat input increases, until it disappears completely at a higher heat input. They also observed that the period of the geyser effect increases as the coolant flow rate decreases [2].

The effect of the fill ratio on the TPCT thermal performance was investigated experimentally and numerically at a wide range of heat inputs by Jafari et al. [120]. The study revealed that

the performance of the TPCT is limited by the dry out at a small amount of liquid charge (16%) and the geyser boiling at a different range of the heat flux, depending on the fill ratio [8].

2.5.3 Effect of Operating Pressure

An experimental study was conducted to observe the geyser effect in a two-phase close thermosiphon filled with water at different values of pressure and heat flux [121]. The study showed a visualisation of the geyser phenomenon inside the TPCT and concluded that this phenomenon can occur by decreasing the pressure at a constant heat flux. Also, a relationship for the evaporator heat transfer coefficient with the pressure and heat flux was proposed [8].

Tecchio et al. [122] examined the effect of heat removal in two condensers, the fill ratio, the heat input and vapour pressure on the geyser phenomenon in a loop-thermosyphon heat pipe in terms of acceleration measurements. They reported that the geyser boiling characteristics in the loop-thermosyphon differs from that in the normal TPCT. They also observed that geysering occurred at a heat flux higher than 12500 W/m^2 and a vapour pressure less than 25 kPa for the steady state regime. On the other hand, for the transient regime, the geyser intensity was suppressed due to an increase in vapour pressure with the heat flux. Also, evaporator acceleration caused by geyser boiling was affected by the rate at which heat was removed from the condenser [2].

2.5.4 Summary

From the above literature review about the geyser boiling inside heat pipes, the occurrence of geysering using water as a working fluid occurred at a lower heat input and fill ratio compared with ethanol, acetone, methanol, R113 and R134a and the geysering period and amplitude was larger. Also, as well as the pressure, the temperature distribution, geometrical parameters and heat input played important roles in the initiation of the geysering. It was also concluded that the geysering period was shorter for higher heat input, larger fill ratio and

lower inclination angle. However, the conclusions about the fill ratio and inclination were made at a certain heat input, thus they may not be valid at at other values of heat loads. Regarding the influence of the operating pressure, the geyser boiling can be initiated by reducing the pressure at a constant heat load, while it can be suppressed by increasing the pressure at high heat input.

2.6 Studies of Enhancing Phase-Change Processes

Two types of enhancement methods have been implemented to augment the phase-change process, namely active and passive techniques. In the active type, applying an external force such as electrical field is required to accomplish the enhancement, whereas in the passive one; modifying a surface feature of materials can effectively enhance condensation and evaporation heat transfer using fluid additives or micro and nanostructures [123]. One of the most recent enhancement techniques is the use of hydrophilic and/or hydrophobic coatings to change the surface wettability [26]. They reflected the wettability of the surface where water can wet the surface if it is hydrophilic (contact angle$< 90^{o}$) whereas water cannot wet the surface if it is hydrophobic (contact angle$> 90^{o}$). Also, the surface is considered as superhydrophilic when it is completely wetted by the fluid (contact angle $< 10^{o}$), while the surface is considered as superhydrophobic when the fluid completely does not wet the surface (contact angle $> 150^{o}$).

2.6.1 Enhancing Condensation Process

Many researchers investigated the enhancement of the condensation process implementing hydrophobic, hydrophilic, superhydrophobic, superhydrophilic and hybrid or patterned surfaces (patterned or hybrid surface consists of more than one of the above mentioned surfaces). Table 2.2 illustrates some of these studies.

Table 2.2 Different studies about enhancing condensation process using various coatings

Ref.	Phase-change process	Surface type	Outcome
[124]	Condensation and boiling	Superhydrophobic or superhydrophilic	Using superhydrophilic or superhydrophobic coatings promoted nucleate boiling and dropwise condensation [125], [126].
[127]	Condensation	Hydrophobic	Compared with a hydrophilic surface, hydrophobic surface exhibited higher heat transfer rate and pressure drop [26].
[128]	Condensation	Micro/nano-size porous surfaces	Using such surfaces enhanced the nucleation rate and stimulated the dropwise condensation
[129]	Condensation	Hydrophilic, hydrophobic and hybrid patterns [26].	Hydrophobic surface provided 2.5 times enhancement in Condensation Heat Transfer Coefficient (CHTC) compared with that for hydrophilic while patterned surface provided less enhancement than hydrophobic and higher than hydrophilic surface.
[130]	Condensation	Hydrophobic, hydrophilic and patterns surface	Enhancement of 3.2-13.4 times in the condensation thermal performance was obtained using hydrophobic and patterned surfaces compared with hydrophilic surface.
[131]	Condensation	Patterns with different feature sizes and shapes	The patterned surface with a feature size of 0.25 mm exhibited the highest CHTC.
[132]	Condensation	Surface coated with SU-8 epoxy	Copper coated with SU-8 produced higher CHTC than the uncoated copper.

[133]	Condensation	Different hybrid surfaces	The highest CHTC was achieved using hybrid hydrophilic-hydrophobic and hydrophobic finned tubes for a pure vapour, while with presence of large amount of Non-Condensable Gas (NCG), the hybrid hydrophilic-superhydrophobic exhibited the highest CHTC [26].
[134]	Condensation	Hydrophobic, hydrophilic and superhydrophobic plain and finned tubes	1.53 and 1.34 times higher CHTC were achieved using tubes with superhydrophobic coating and 9 tube bundle rows at high (89%) and low (77%) amounts of NCG, respectively, compared with a single row.
[135]	Condensation	hydrophobic coating	Enhancement of 50% in CHTC was obtained using hydrophobic coating compared with smooth surface
[136]	Condensation	patterned surfaces	Using patterned surfaces can augment the condensation process by 30% despite the presence of NCG.

2.6.2 Enhancing Boiling Process

Many researchers have examined the influence of using different surface features on the characteristics of the boiling process at atmospheric pressure. Takata et al. [137] used a superhydrophilic surface (contact angle≈0^o) and reported a 200% increase in Critical Heat Flux (CHF), while another study by Takata et al. [138] concluded a negative effect for using a superhydrophobic surface (contact angle≥150^o). Betz et al. [139] tested a hybrid

superhydrophilic and superhydrophobic coating on a silicon nanostructure, whereas patterned surfaces (hydrophilic and hydrophobic) were investigated by [140]–[142]. They reported that using such surface characteristics can enhance the heat transfer coefficient by about 3 and 11 times at high and low superheat, respectively. Also, using these surfaces can increase the CHF from 200% to 350%. All these studies have been carried out to enhance the boiling process under atmospheric pressure.

However, Yamada et al. [143] examined the effect of different surface pattern arrangements (hydrophilic substrate with hydrophobic spots) in terms of spot diameters and pitches (as shown in Figure 2.26 [143]) on the pool and nucleate boiling characteristics at sub-atmospheric pressure. The study reported an enhancement of 270% in the heat transfer coefficient achieved at a pressure of 14 kPa when the surface pattern with a small spot pitch and diameter was used compared to that for a cooper with mirror-finished.

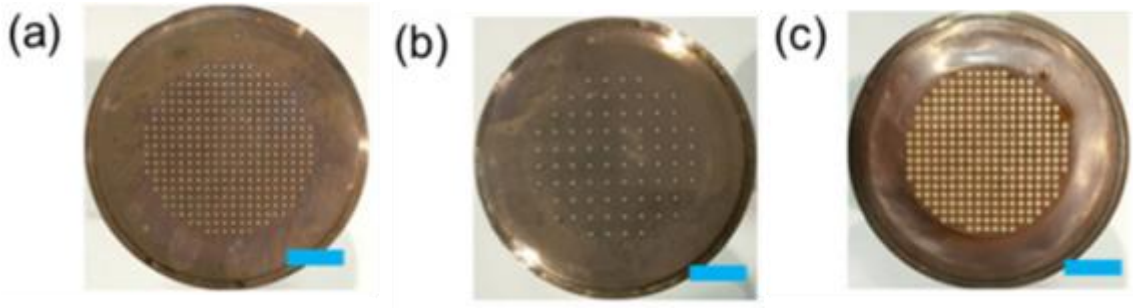

Figure 2.26 Three different hydrophilic and hydrophobic patterned surfaces with various hydrophobic spot diameters and pitches [143]

2.6.3 Summary

From the review of the above investigations about the enhancement of phase-change processes, the condensation heat transfer can be enhanced several times using hydrophobic, superhydrophobic or patterned surfaces. Results also showed that the enhancement depended on the pattern shape and size and it was higher at the higher portion of NCG. However, some studies reported that patterned surfaces provided higher enhancement than the hydrophobic or superhydrophobic surfaces, while other studies concluded the opposite. On the other hand,

regarding boiling heat transfer enhancement, using such surfaces can greatly increase the critical heat flux and the boiling heat transfer coefficient at both atmospheric and sub-atmospheric pressures. However, using superhydrophobic surface has a negative effect on the boiling heat transfer.

2.7 Studies of Enhancing Phase-Change Processes in Heat Pipes

Several research works have been conducted to investigate the enhancement in thermal performance of heat pipes using the following two different means; namely using nanofluids and modifying surface characteristics:

2.7.1 Using Nanofluids

This method employed nanoparticles to enhance the characteristics of working fluids by increasing their thermal conductivity, thereby the performance of heat pipes. Different studies investigated the effect of using various nanoparticles with water such as CuO nanoparticles [93], [144]–[146], Al_2O_3 nanoparticles [147] and [148], silver nanoparticles [149] and [95], iron oxide nanoparticles [150] and [69], graphene nanoparticles [94], multiwalled carbon nanotubes functionalized with ethyl-enediamine EDA-MWCNT nanoparticles [151]. It was found that the best nanoparticles concentration which provided the highest thermal performance was 1.0wt% [144] and [151], 0.1wt% [94], 0.06wt% [146] and 3wt% [148]. Different studies showed that using nanofluid increased the heat transfer coefficient by 46% [144] and 30.4% [148], increased CHF by 30% [144] and 79% [146], increased thermal performance [145], by 14.7% [147], 70% [149], 93% [151], 37.2% [94] and reduced the thermal resistance [152] by 62% [93], 48% [94] and 18.2% [148]. Also, It was concluded that some nanoparticles may be deposited on the heat pipe wall as a coating which results in an increase of the surface wettability [94] and [146].

2.7.2 Changing the surface Characteristics

Some researchers modified the heat pipes' surface characteristics to enhance the heat pipes thermal performance. The next two sections will review the effect of internal micro-grooves and surface wettability on the thermal characteristics of heat pipes.

2.7.2.1 Effect of micro-grooves

A number of theoretical and experimental research studies were conducted to investigate the influence of internal micro-grooves on the heat pipes performance. Han and Cho [153] tested the performance of a micro-grooved TPCT for various working fluids, number of grooves and operating temperatures. They found that the number of 60 grooves (inside diameter of 12.7 mm) correspond to the highest condensation heat transfer performance of 2.5 times higher compared to a plain TPCT. Also, the condensation heat transfer coefficients of grooved thermosyphons filled with methanol and ethanol were 1.5-2 and 1.3-1.5 times higher compared to the plain one, respectively, and water provides the highest heat transfer rate.

Han and Cho [154] also investigated the thermal characteristics of two thermosyphon heat pipes with straight and helical grooves filled with water at different inclinations, fill ratios and operating temperatures. They concluded that the fill ratio of 30% exhibited the highest heat flux. In addition, angles of 25-30^{o} and 40^{o} provided the best thermal performance for helical and straight grooves, respectively.

Jiao et al, [155] studied theoretically and experimentally the effect of thin-film evaporation in a grooved heat pipe. The study revealed that the performance of the grooved heat pipe was greatly affected by the thin film evaporation where the reduction in the evaporator temperature was considerably larger than the reduction in the condenser temperature. Also, the thin film region was enlarged by the decrease in the contact angle which increases the heat transfer performance. A similar mathematical study to [155] was carried out by Jiao et al,

[156], but the thin film region inside the groove was divided into three different regions instead of one region.

Lefèvre et al. [157] developed a numerical thermal model to predict the thermal performance of a micro-grooved flat plate heat pipe and validated the results with an experimental study. They found that the optimum dimensions of the rectangular groove were 0.36, 0.7 and 0.1 mm corresponding to groove width, height and fin width, respectively. These dimensions provided a maximum heat flux and lowest thermal resistance.

Yong et al, [158] investigated the thermal characteristics of a micro-grooved heat pipe manufactured by Extrusion–ploughing process. The study reported that the heat transfer limit for the grooved heat pipe fabricated by the new technique was larger than that for the normally grooved heat pipe, thus the low heat transfer limit for axially micro-grooved heat pipe can be resolved.

Wang et al, [159] tested the effect of internal helical microfin on the condensation heat transfer performance in a TPCT. They reported that the existence of internal helical microfin provides a better thermal response and increases the heat transfer coefficient of condensation by 116.87% at high heat load. Also, they proposed a correlation to predict the heat transfer coefficient of condensation in the TPCT.

Nair and Balaji, [70] concluded that adding 8 fins inside the condenser increased the thermal conductivity of the TPCT by about 43%. They also reported that an additional condensate mass of 22% and 32% can be produced using 8 and 12 fins, respectively, which would be helpful to avoid the dry out during the operation of the thermosyphon. A similar study to [70] was carried out experimentally by Naresh and Balaji [160], but for various fill ratios and two working fluids, water and acetone. They concluded that at low heat load, a reduction of 17% and 35.48% were obtained in the temperature and thermal resistance of TPCT, respectively, due to the additional condensate mass resulting from inserting six internal fins in the

condenser section. It was also reported that the optimum thermal performance of the TPCT is achieved at a fill ratio of 50%. In addition, acetone exhibits higher performance at low heat loads, while water provides better performance at high heat inputs.

2.7.2.2 Effect of Surface Wettability

Effect of changing surface wettability on heat pipes performance has been investigated by many researchers using different coatings. Wong et al, [161] investigated the impact of surface wettability on the evaporator performance in a mesh wick flat plate heat pipe charged with water, methanol and acetone. They concluded that the heat transfer limit decreased as the contact angle of the copper surface with water increased, while it was unaffected for methanol and acetone.

Solomon et al, [162] investigated the influence of nanoparticles coating on a screen wick heat pipe thermal performance. Results revealed that the thermal resistance of the evaporator and heat transfer coefficient reduced and increased by 40%, respectively, while the thermal performance in the condenser section decreased compared with an uncoated heat pipe. It was also reported that a reduction of 19%, 15%, and 14% were achieved at heat loads of 100, 150 and 200W respectively.

Hu et al, [163] studied the thermal characteristics of a horizontal grooved heat pipe with different surface wettability for the three parts, condenser, evaporator and adiabatic. The study revealed that a considerable decrease was achieved in the total thermal resistance due to the change in the surface characteristics to hydrophilic, gradient wettability and normal surface for the evaporator, adiabatic and condenser sections, respectively. Also, more than 42% increase in the dry-out limit of the grooved heat pipe was obtained.

Rahimi et al [164] modified the surface characteristics of the evaporator and condenser inside a TPCT to investigate their influence on the thermal performance of the TPCT filled with water. They found that the thermosyphon efficiency can be increased by 15.27%, whereas a

decrease of 2.35 times in the thermal resistance was obtained compared with the plain TPCT. Another surface modification study was conducted by Solomon et al, [165] to test the performance of an anodized Aluminium TPCT charged with acetone. Results showed that a maximum reduction in the evaporator thermal resistance and increase in heat transfer coefficient of the TPCT was 15% compared with non-anodized thermosyphon. In addition, a negligible effect of anodized TPCT was observed on the condenser thermal performance.

Hsu et al, [166] employed different surface characteristics in terms of contact angle [26] in the condenser and evaporator to investigate the thermal performance of a TPCT. Experimental results showed that when evaporator and condenser are superhydrophilic and superhydrophobic, respectively, the highest performance of the TPCT was obtained where the maximum reduction in the thermal resistance is 26.1% compared with the plain TPCT. Also, the worst thermal performance of the thermosyphon was observed when the whole inside wall of the TPCT is superhydrophilic.

Xu et al. [79] and Xu et al. [80] also reported the influence of using hydrophobic and hydrophilic evaporator surfaces on thermal performance of the tested TPCT. They concluded a reduction of 44.1% and 20.6% in the thermal resistance for the hydrophilic and hydrophobic evaporators, respectively, compared with uncoated TPCT. This is due to the increase in bubble generation density for hydrophilic and hydrophobic surfaces by 265% and 100%, respectively. They also found a decrease of 59.5% in the TPCT thermal resistance resulting from changing the angle from 15^{o} to 90^{o}.

2.7.3 Summary

From the review of above studies about changing the surface features of heat pipes, making micro-grooves on the internal wall of heat pipes can greatly enhance their thermal performance. This enhancement depends on micro-grooves' number, shape and dimensions as well as others parameters like the working fluid used. Also, the existence of micro-grooves

can widen the evaporation thin film producing a significant decrease in the evaporator temperature. It was also concluded that embedding fins in the condenser wall can considerably enhance the condensation heat transfer depending on fins number as well as the inclination and fill ratio. On the other hand, changing the surface wettability can significantly increase the heat transfer limit and reduce the thermal resistance of heat pipes. Also, enhancing each section in the heat pipe requires different surface wettabilities, so that some studies investigated the use of different coatings in the condenser, evaporator, adiabatic parts to provide different wettability characteristics. Therefore, it was reported that using superhydrophilic and superhydrophobic or hydrophilic and hydrophobic in the evaporator and condenser, respectively, enhanced greatly the performance of heat pipes. However, other studies reported a deterioration in the condenser heat transfer due to using a wettable surface such as superhydrophilic.

2.8 Conclusions

From reviewing the previous work about the heat pipe, the following conclusions would be drawn:

- Integration of heat pipes with solar water heaters can greatly increase their thermal performance by reducing heat losses and increasing efficiency and heat gain of solar collectors. Therefore, optimising of the heat pipe by investigating different geometrical and operational parameters can improve the thermal performance of such systems.
- Although many CFD studies have been carried out to model the multiphase flows, a limited CFD research has been conducted to model the TPCT. Most of these studies have concentrated on the modelling of the phase-change phenomena inside the TPCT and the resulting temperature distribution. However, CFD modelling of important parameters affecting the TPCT performance such as angle of inclination and liquid

charge have not been found in literature, especially, the visualisation of the phase-change process of the inclined TPCT and visualisation of different fill ratios.

- In addition, the effect of the surface wettability in terms of contact angle [26] has not been investigated in the literature using CFD numerical modelling of the TPCT. Therefore, it is beneficial to model the two-phase process with the contact angle to examine their influence on the thermal characteristics of the TPCT. Also, to visualise the phase-change characteristics under the influence of different contact angles.
- From experimental investigations, the best fill ratio and inclination angle depend on several geometrical and operating parameters as well as the physical properties of the working fluid. Thus, based on these parameters, the appropriate angle of inclination and charged liquid amount vary from one heat pipe to another and investigations to find the best liquid charge amount and the inclination angle are required whenever any one of these factors is changed.
- Although several experimental studies have been performed to examine the influence of different parameters affecting the performance of the thermosiphon heat pipe, challenges regarding the two-phase process still need to be considered to enhance the thermal performance and to predict the operating limits of this device [8].
- Limited research works have reported the occurrence of the geyser boiling and its characteristics in the thermosyphon heat pipe. Also, the previous investigations about the geyser boiling in the TPCT did not cover all parameters at a wide range of heat input, so, their conclusion remains limited to the few investigated parameters [8].
- All investigations about geyser boiling have only focused on the effect of different operating conditions on this boiling and the vibration caused by this phenomenon. Consequently, the effect of geyser boiling on the thermal characteristics of the TPCT was not reported [2].

- Several experimental tests have been performed to enhance the thermal performance and increase the heat transfer limit of heat pipes. This has been achieved by implementing different means namely, using nanoparticles to improve the thermal characteristics of the working fluids or changing the surface features of the wall using coatings or making micro-grooves. However, the effect of making a roughness on the internal wall of the TPCT has not been reported in the literature.

CHAPTER 3

3. Numerical CFD Modelling of the Two-Phase Closed Thermosiphon

3.1. Introduction

Numerical simulation is widely used to model different systems in various engineering applications to reduce cost and time of the experimental work. Computational Fluid Dynamic (CFD) modelling of a thermosyphon heat pipe is a powerful tool that can be used to investigate the complex physical phenomena of the evaporation and condensation phase change processes [167]. It solves a set of mathematical equations and employs a number of assumptions to simulate the phase-change processes and predict the heat transfer performance of the heat pipe. These assumptions depend on the initial and boundary conditions of the real system. In this chapter, a CFD model of the flow and phase-change processes inside a thermosyphon heat pipe is developed and employed to investigate the effect of fill ratio (liquid volume to the evaporator volume) and inclination angle on its thermal performance using Fluent (ANSYS 15). Also, the surface wettability in terms of the contact angle was investigated to report their effect on the thermal characteristics of the TPCT.

3.2. Multiphase flows

Generally, multiphase flow is a wider concept than the physical phases of matter. Thus, multiphase flow can be defined as a recognisable material class immersed in a flow and can respond in an inertial manner to the flow and interact with the potential field. For instance, solids particles for the same material with different sizes can be considered as a different phase in which the interaction of these particles with the flow depends on their sizes [168]. There are four categories of the multiphase regimes, namely liquid-solid; gas-solid; gas-liquid or liquid-liquid; and three-phase flows. The multiphase flow category related to this work is gas-liquid category and can be classified into the following regimes, Figure 3.1:

- Bubbly flow: denotes discrete bubbles or gaseous flow in a continuous liquid.
- Droplets flow: denotes the flow of discrete droplets of liquid in a continuous gas.
- Slug flow: denotes large bubbles flow in a continuous liquid [168].
- Stratified/free-surface flow: denotes immiscible fluids flow separated by well-defined interface [168].

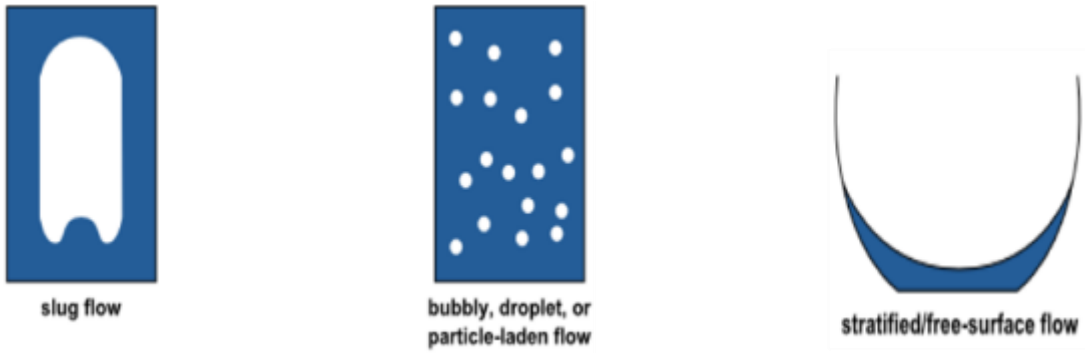

Figure 3.1 Multiphase flow regimes [168]

3.3. Multiphase modelling

Two numerical approaches are employed to model multiphase flows; the Euler-Euler and Euler-Lagrange approaches. In Euler-Lagrange approach, Navier-Stokes equations are solved for the fluid phase where it is considered as a continuum, while several numbers of particles are tracked to solve the dispersed phase. This approach cannot be used for applications where the volume fraction of the secondary phase is important and cannot be neglected. In the Euler-Euler approach, the various phases are considered mathematically as interpenetrating continua. In this approach, the volume fraction concept is important where each phase has a volume and other phases cannot occupy it [168]. Therefore, the Euler-Euler approach is adopted to model the two-phase closed thermosyphon in this work.

In Ansys Fluent, three various multiphase models can be selected using Euler-Euler approach. These models are:

a) The mixture model

b) The Eulerian model

c) The Volume Of Fluid (VOF) model

Identifying the proper multiphase regime as classified above which represents the flow needed to be modelled is the first step in modelling any multiphase problem. For example, the mixture model is used to model particle-laden flows, sedimentation, cyclone separators and bubbly flows. The Eulerian model in turn is appropriate to model applications such as fluidised beds, risers, particle suspension and bubble columns. On the other hand, the VOF model is used to model liquid-gas interface tracking (steady or transient), large bubbles motion in a liquid, free-surface flows and stratified flows. Accordingly, The VOF has been employed to model heat pipes by many researchers [53], [54], [56]–[60], [62], [64], [66], [69], [70], [74]–[80], [83], [84], [139], [169].

3.4. The VOF model

Many researchers have used Volume Of Fluid (VOF) model to solve numerically a multiphase flow because it needs less computational time compared with finite volume method. Reasons behind that in the VOF model, only one set of equations for one phase is solved then the result is shared between phases which greatly reduces the simulation time where the location of the interface between phases and physical properties at the interface vary for each computational step. Thus, solving such problems can be achieved using the VOF model by defining the motion of all phases and tracking the location of the interface accordingly [168]. Two or more immiscible fluids can be modelled using the VOF model. In the VOF model, movement of different fluids can be tracked by solving a single set of Navier-Stocks equations for the volume fraction of each fluid throughout the computational cell [168]. Therefore, the existence of a certain phase in any control volume can be easily specified from the volume fraction according to the following three cases [26]:

$\alpha_v = 1$: The cell is full of vapour

$\alpha_v = 0$: The cell is full of liquid

$0 < \alpha_v < 1$: The cell contains a mixture of liquid and vapour

The third case means

$$\alpha_l + \alpha_v = 1 \quad (3.1)$$

Where α_l and α_v are volume fractions of liquid and vapour respectively [26].

3.5. Governing Equations

In order to define the motion of the fluid inside the TPCT during evaporation and condensation processes, the governing equations of mass continuity, momentum and energy with source terms are solved using Ansys Fluent [26].

3.5.1. Continuity Equation

$$\frac{\partial}{\partial t}(\rho) + \nabla.(\rho\vec{u}) = 0 \quad (3.2)$$

where, u and ρ represent the velocity and density of the fluid.

The interface between phases can be tracked by solving eq. (3.2) for the volume fraction. Therefore, for the secondary phase (liquid phase) of VOF model, this equation can be written as follow [168]:

$$\frac{\partial}{\partial t}(\alpha_l\rho_l) + \nabla.(\alpha_l\rho_l\vec{u}) = 0 \quad (3.3)$$

where, $S_{\alpha m}$ is the mass source term that can be used to find the mass transport from one phase to another during the evaporation and condensation processes. The above equation is solved for the secondary phase (*l*) only, while the primary phase (*v*) volume fraction can be calculated using eq. (3.4) [26]:

$$\sum_{k=1}^{2} \alpha_k = 1 \quad (3.4)$$

3.5.2 Momentum Equation

$$\frac{\partial}{\partial t}(\rho_l \vec{u}) + \nabla.(\rho_l \vec{u}\vec{u}) = -\nabla p + \rho \vec{g} + \nabla.\left[\mu(\nabla \vec{u} + \nabla \vec{u}^T - \frac{2}{3}\mu \nabla.uI\right] + F_S \quad 3.5$$

where, p is the pressure, g is the acceleration of gravity, I is a unit tensor and the fluid density ρ and viscosity μ are represented by eq. (3.6) and eq. (3.7), respectively. According to the VOF model, the physical properties are determined for the mixture only based on the value of volume fractions of liquid and vapour [26].

$$\rho = \alpha_l \rho_l + \alpha_v \rho_v \quad 3.6$$

$$\mu = \alpha_l \mu_l + \alpha_v \mu_v \quad 3.7$$

In this study, the vapour velocity is modelled to vary with heat input depending on the saturation temperature at each heat input.

F_S is the Continuum Surface Force (CSF) [26] acting on the interface between two phases which was proposed by Brackbill [170] and is used in Ansys Fluent to include the effect of surface tension. This term can be expressed as [171]:

$$F_S = 2\sigma \frac{\alpha_l \rho_l kc_v \nabla \alpha_v + \alpha_v \rho_v kc_l \nabla \alpha_l}{\rho_l + \rho_v} \quad 3.8$$

Where, σ is the interfacial tension between two phases, Kc_l and Kc_v are surface curvatures of liquid and vapour respectively that can be written in the following forms [26]:

$$kc_l = \frac{\Delta \alpha_l}{|\nabla \alpha_l|} \quad 3.9$$

$$kc_v = \frac{\Delta \alpha_v}{|\nabla \alpha_v|} \quad 3.10$$

3.5.3 Energy Equation

$$\frac{\partial}{\partial t}(\rho E) + \nabla.[\vec{u}(\rho E + p)] = -\nabla.(k\nabla T) + S_q \quad 3.11$$

Where, *E* and *k* are the internal energy and thermal conductivity which can be computed using Eq. (3.12) and Eq. (3.13) respectively, again, for mixture only [26].

$$E = \frac{\alpha_l \rho_l Cp_l + \alpha_v \rho_v Cp_v}{\alpha_l \rho_l + \alpha_v \rho_v}(T - T_{sat}) \quad 3.12$$

$$k = \alpha_l k_l + \alpha_v k_v \quad 3.13$$

Where, k_v and k_l denote the thermal conductivity of vapour and liquid Cp_v and Cp_l denote the specific heat of vapour and liquid, respectively. S_q, is the energy source term which can be employed to calculate the heat transfer from one phase to another which is determined from mass source term $S_{\alpha m}$ and the latent heat (h_{fg}) as follow:

$$S_q = S_{\alpha M} h_{fg} \quad 3.14$$

Single momentum equation and energy equation will be solved for the control volume of both fluids. Accordingly, the computed velocity and temperature will be shared between the two phases [26].

3.5.4. Phase Change Equations

In order to model the transport phenomenon inside the thermosiphon heat pipe represented by mass and heat transfer from [26] one phase to another during evaporation and condensation processes, source terms proposed by De Schepper et al [57] need to be added to the continuity and energy equations used by the VOF model in Ansys Fluent [167]. As stated previously, a single volume fraction equation will be solved for each cell for secondary phase while the volume fraction for the primary phase will be obtained from eq. (3.4). Therefore, to describe

the mass transfer related to the evaporation process, two equations are needed, one for liquid phase and another for vapour phase as follow [167]:

Evaporation $T_{mix} > T_{sat}$

Liquid phase:

$$S_{\alpha M} = -0.1\alpha_l \rho_l \left| \frac{T_{mix} - T_{sat}}{T_{sat}} \right| \quad 3.15$$

Vapour phase:

$$S_{\alpha M} = 0.1\alpha_l \rho_l \left| \frac{T_{mix} - T_{sat}}{T_{sat}} \right| \quad 3.16$$

where, T_{sat} and T_{mix} represent the saturation and mixture temperature, respectively.

Similar to the evaporation process, two expressions are also required to represent the mass transfer during the condensation process. Again, one for liquid and another for vapour as follow [26]:

Condensation $T_{mix} < T_{sat}$

Liquide phase:

$$S_{\alpha M} = 0.1\alpha_v \rho_v \left| \frac{T_{mix} - T_{sat}}{T_{sat}} \right| \quad 3.17$$

Vapour phase:

$$S_{\alpha M} = -0.1\alpha_v \rho_v \left| \frac{T_{mix} - T_{sat}}{T_{sat}} \right| \quad 3.18$$

Accordingly, the energy source term S_q that needs to be added to the energy equation (eq. (3.11)) to represent the amount of heat transfer from one phase to another during the evaporation and condensation processes can be determined using eq. (3.14) as follow [167]:

Evaporation:

$$S_q = -0.1\alpha_l \rho_l \left| \frac{T_{mix} - T_{sat}}{T_{sat}} \right| h_{fg} \qquad 3.19$$

Condensation

$$S_q = 0.1\alpha_v \rho_v \left| \frac{T_{mix} - T_{sat}}{T_{sat}} \right| h_{fg} \qquad 3.20$$

Equations (3.15-3.20) are set in a sub-program and linked to the Fluent to include mass source terms (eqs.3.15-3.18) and energy source terms (eqs.3.19 and 3.20) in the mass conservation equation (3.3) and energy equation (3.11), respectively of the VOF model in order to model the phase change process [167].

3.6 Modelling of Fill Ratio and Inclination [167]

3.6.1 CFD Simulation Set up

3.6.1.1 Geometry and Mesh

Geometry of a vertical two-dimension wickless heat pipe has been generated using workbench (Ansys 15). The geometry shown in Figure 3.2 represents a copper tube with a total height of 400 mm, inner and outer diameters of 20.2 and 22 and mm, respectively. The thermosiphon is divided into two sections, evaporator and condenser with height of 200 mm each. These dimensions are chosen to be similar to the geometry of a previous experimental work by Abdullahi [77] to validate the CFD simulation [167].

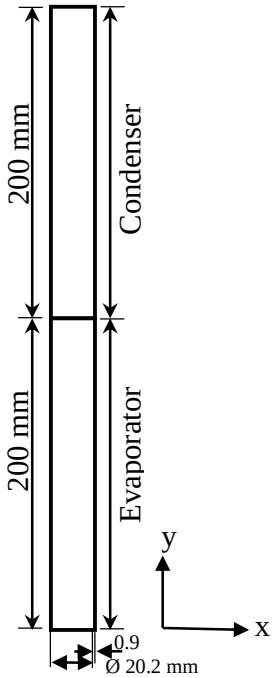

Figure 3.2 Heat pipe geometry [167]

Workbench is the design module of (Ansys 15) which can also be used to mesh the geometry where control edge sizing technique was employed to control the grid in every domain. This teqnique is also used to govern cell sizes near inner walls and inside the solid domain (walls) with bias factor of 10 used in these regions to ensure that the flow and heat transfer can be correctly captured in these areas. Three different structured mesh sizes were generated 18824, 34142 and 112884 to test the solution sensitivity to mesh size as shown in Figure 3.3 which shows the lower 20 mm part with wall mesh [167].

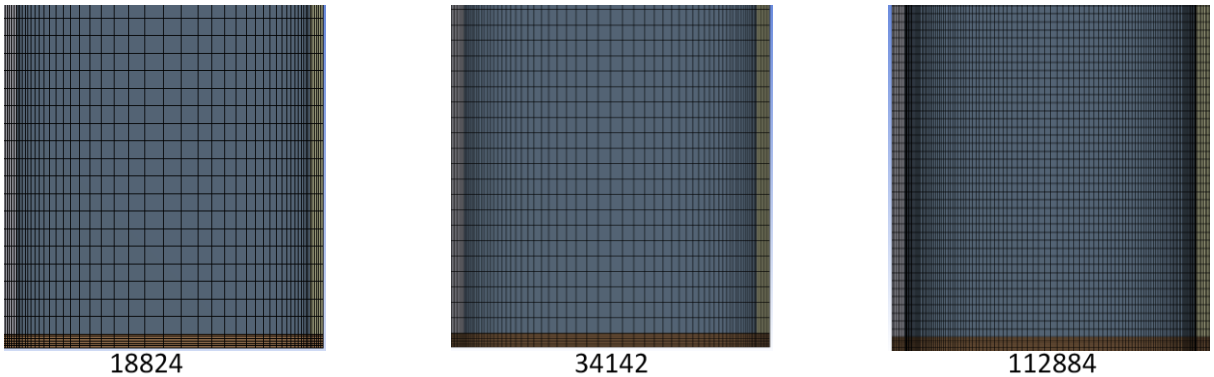

Figure 3.3 Different mesh sizes

Variation of the temperature distribution with the distance along the wall of the thermosyphon is shown in Figure 3.4 for different computational cell sizes at a heat load of 101.5W. It shows that higher evaporator temperature is obtained when a mesh size of 18824 is used, while no difference is observed in the temperature distribution between mesh sizes of 34142 and 112884. Therefore, the mesh size of 34142 is implemented in this work to reduce the solution computational time while maintaining a good accuracy.

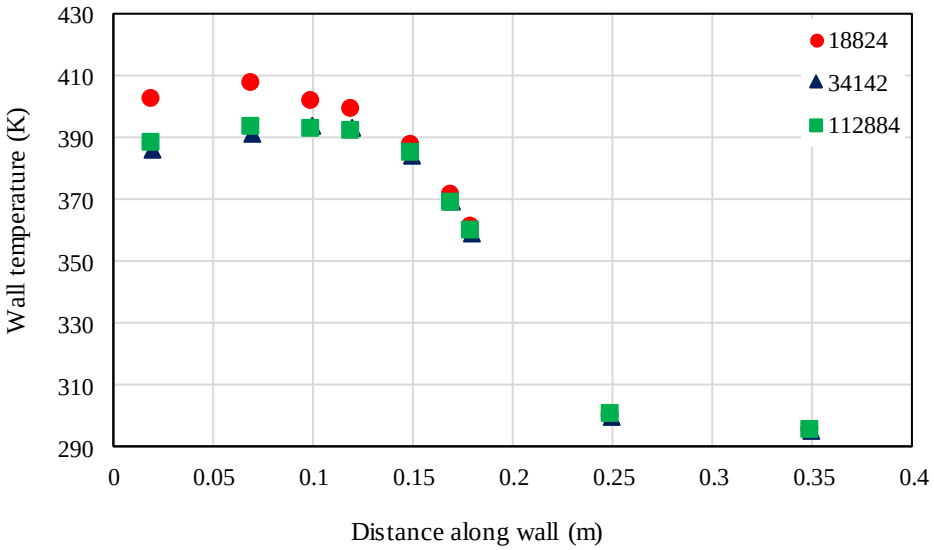

Figure 3.4 Temperature distribution versus distance along the wall of thermosyphon at heat input of 101W

3.6.1.2 Initial and Boundary Conditions

Five different filling ratios and inclination angles are used in this study namely, 25%, 35%, 65%, 80% and 100% of the evaporator volume, and 10, 30, 50, 70 and 90^{o}, respectively. To set up the fill ratio for each case, the corresponding evaporator height is initially patched with liquid while the remaining height is patched with vapour. In addition, the inclination angle is defined as the inclination of thermosiphon heat pipe from the horizontal axis and can be set up by multiplying y-component of acceleration gravity with sine of the angle and x-component with cosine as shown in Figure 3.5 [167].

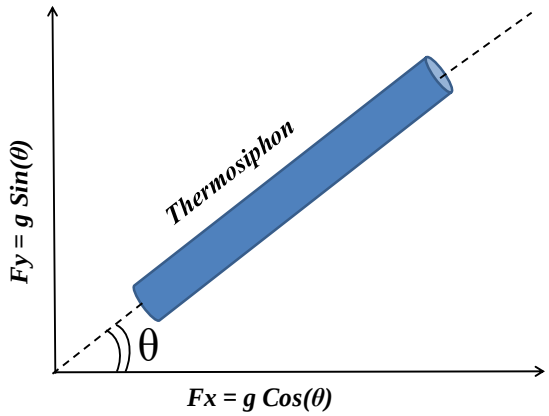

Figure 3.5 Inclination angle of thermosiphon heat pipe [167]

The initial temperature of both evaporator wall and liquid should be selected slightly above the boiling point which was chosen to be 100°C to ensure that the boiling process occurs once simulation time starts to reduce computational time [171] and the condenser wall temperature were set as 290 K (condenser cooling temperature). Operating temperature should be set to be the smallest temperature in the system (290 K) and operating density must be set as 0 kg/m^3 when ideal gas is used and as the smallest density in the system when constant gas density is used [171]. In addition, saturation temperature and operating pressure were set to be 373 K and 101325 Pa, respectively [167].

At the internal walls of the condenser and evaporator, a non-slip boundary condition was applied, while a constant heat flux was imposed at the evaporator outer wall to simulate the heat added to the thermosiphon. Three values of heat flux were employed 2858, 5910 and 7346 W/m^2 corresponding to heat transfer rates 39, 81 and 101W respectively, which were taken from [77]. The top and the bottom ends of the thermosiphon were assumed to be insulated, which means no cooling or heating effect applied at these walls. Thus, a zero-heat flux is defined at these ends. To model the heat removed from the condenser section, a convection boundary condition was applied at the outer wall of the condenser section. Thus, the heat transfer coefficient between cooling water and the condenser's wall needs to be calculated using the following equation [167]:

$$h_{conv} = \frac{Q_{cond}}{2\pi D L_{cond}(T_{cw,av} - T_m)} \quad 3.21$$

Where, h_{conv} is the convection heat transfer coefficient between the cooling water and the condenser's wall, Q_{cond} is the heat removed from the condenser section, $T_{cw,av}$ denotes the condenser average wall temperature and T_m denotes mean temperature of the cooling water. Values of Q_{cond}, and T_m were obtained from Abdallahi [77] experimental work [167].

$$T_{cw,av} = \frac{T_{25} + T_{35}}{2} \quad 3.22$$

and

$$T_m = \frac{T_{in} + T_{out_3}}{2} \quad 3.23$$

where, T_{25} and T_{35} are the condenser wall temperatures at distances of 0.25 and 0.35 m, respectively. T_{in} and T_{out} are cooling water inlet and outlet temperatures, respectively.

To include the effect of the interfacial force between liquid and vapour, the term F_s is added to the momentum equation eq. (3.5) by activating the CSF in the Fluent software. Consequently, the value of the surface tension in eq. (3.8) can be computed from the following formula [64]:

$$\sigma = 0.09805856 \; -1.845 \times 10^{-5} T - 2.3 \times 10^{-7} T^2 \quad 3.24$$

Where T is the temperature.

3.6.1.3 Solution Methods and Techniques

In this work, the VOF technique was used to model the multi-phase flow, while the gravitational acceleration of 9.81 m/s^2 was activated to include a body force term. The water liquid was chosen to be a secondary phase (liquid phase) and its density was set as a function of temperature (T) using the following relation [64]:

$$\rho_l = 859.0083 + 1.252209\, T - 0.0026429\, T^2 \quad 3.25$$

A transient solution with a time step of 0.001s was employed for all cases due to the two-phase flow dynamic behaviour [66], [57]. The SIMPLE algorithm and first-order upwind scheme for pressure-velocity coupling and calculation of the momentum and energy were used, respectively [64]. For determination of the volume fraction and pressure, Geo-Reconstruct and PRESTO discretisation were chosen, respectively [64], [66]. The solution convergence was considered when the residuals of the velocity and mass components are reduced to 10^{-4} while the residuals of the temperature dependent variables are reduced to 10^{-6} [167].

3.6.2 Results and Discussion [167]

3.6.2.1 Validation of the CFD Solution

To validate the CFD simulation, same geometry and boundary conditions as Abdullahi [77] have been adopted. Therefore, the temperature distribution along the wall and the thermal resistance of the thermosiphon for the stated three different heat inputs which were determined from CFD modelling have been compared with those obtained from Abdullahi [77] experimental work [167].

A comparison of the temperature distribution along the thermosyphon wall between the CFD modelling (current work) and the experimental work [77] is illustrated in Figure 3.6 for three input energies. Results showed that the CFD solution predicts well the experimental results. However, there is a slight deviation (maximum 4.2%) at the bottom of the evaporator and the top of the condenser where the difference becomes larger at larger heat input [167].

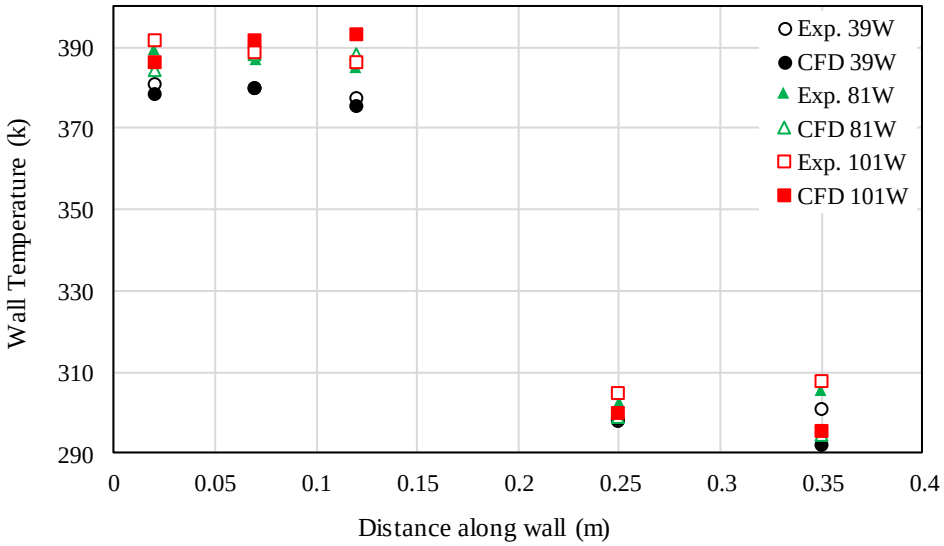

Figure 3.6 Comparison of temperature distribution along the wall of thermosiphon between experimental data and CFD results (Vertical orientation) [167]

Figure 3.7 presents a comparison of the thermal resistance between CFD simulation and experimental study [77] at different heat loads. It is shown that the CFD solution over predicts the experimental results in the worst case (at 101 W) by 8.1%. This is due to higher evaporator temperature and lower condenser temperature obtained from the CFD solution, which yield higher thermal resistance. However, the same trend was achieved in which the thermal resistance decreases as the heat load increases [167].

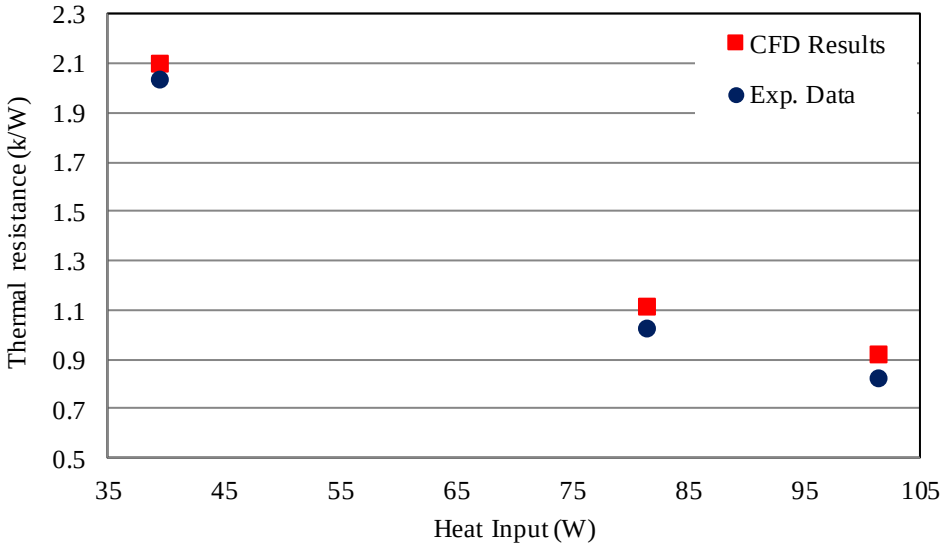

Figure 3.7 Comparison of thermal resistance versus heat load between experimental data and CFD results (Vertical orientation) [167]

Figure 3.8 shows the heat transfer process represented by temperature contours during simulation time of 60 seconds at heat input 101W, fill ratio 65% and vertical orientation. Firstly, heat is transfered from the evaporator wall to the liquid, where the working fluid starts boiling and the phase change occurs. Therefore, vapour raises up to heat the upper part of the heat pipe and the temperature increases accordingly with time until reaching the steady state [167].

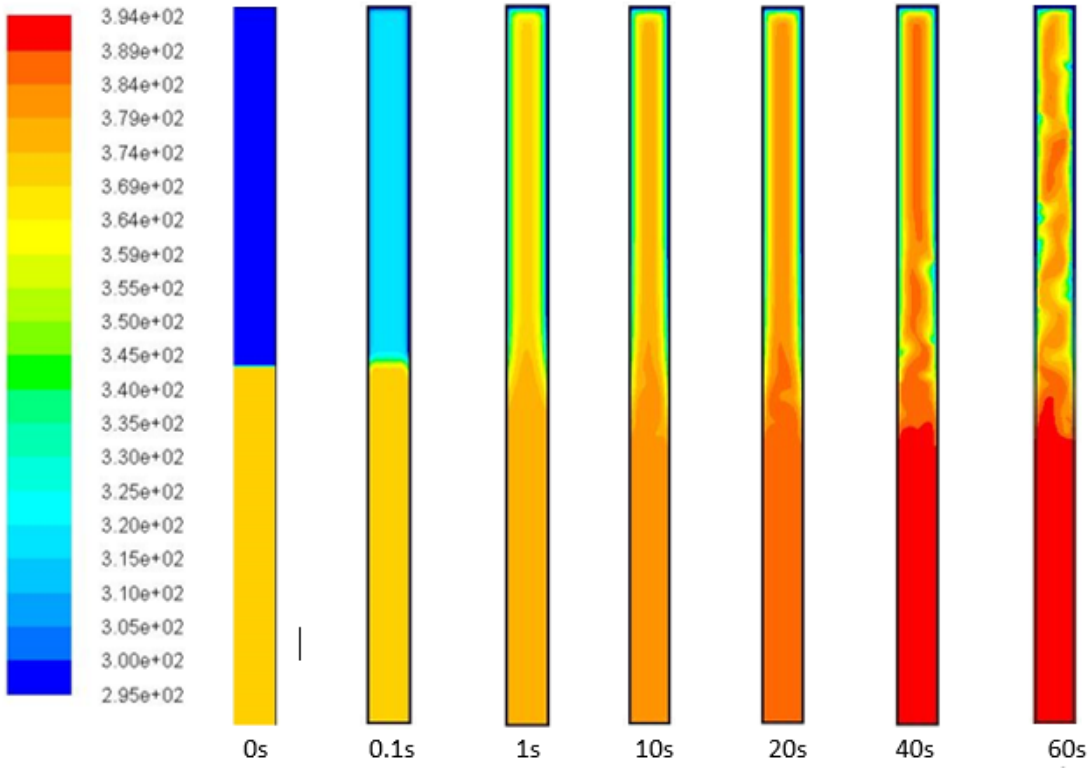

Figure 3.8 Temperature contours at various simulation times (101W, 65 % and 90º) [167]

The variation of the vapour volume fraction with simulation time is illustrated in Figure 3.9 at (101W, 65 % and 90º) in which the red colour refers to vapour phase (volume fraction=1) and the blue one refers to liquid phase (volume fraction=0). At the beginning, a very small bubble size is observed at time 0.1 second, then, bubbles size and number increase as simulation time increases due to increase in the temperature of the liquid reaching the boiling temperature and, hence, the steady state condition at time 60 seconds [167].

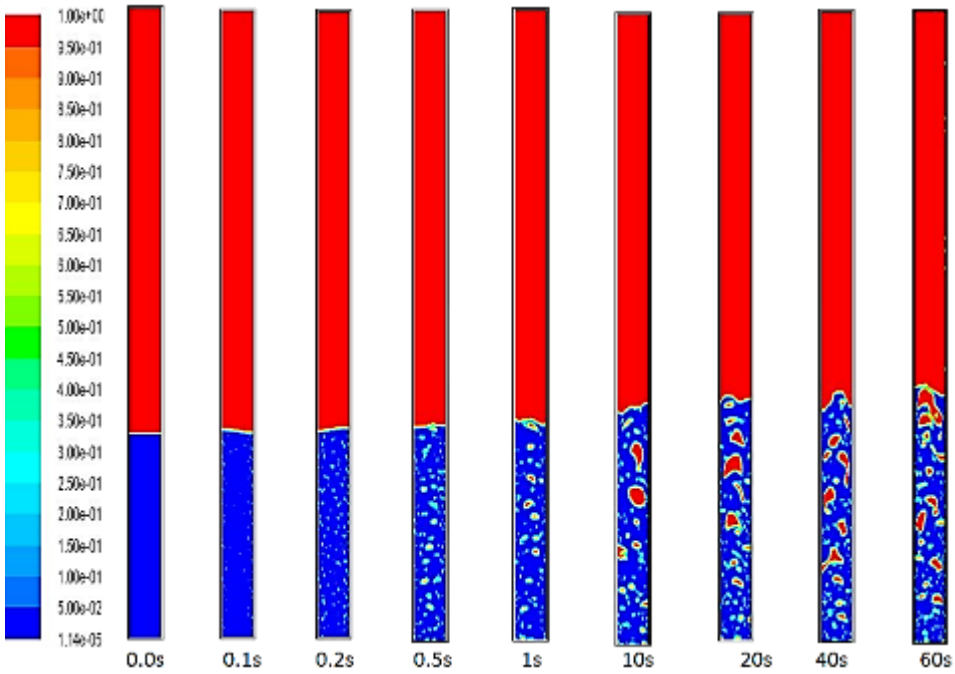

Figure 3.9 Vapour volume fraction contours at various simulation times (101W, 65 % and 90o) [167]

3.6.2.2 Fill Ratio Effect

The influence of the liquid charge volume on the TPCT thermal performance was studied by employing the CFD simulation. The temperature distribution on the outer wall of the thermosiphon for fill ratios 25%, 35%, 65%, 80% and 100% is shown in Figure 3.10 (a), (b) and (c) at heat inputs of 39, 81 and 101W respectively. Figure 3.10 (a, b and c) show similar trends in temperature distribution along the wall of thermosiphon at three heat inputs for each fill ratio [167]. It is also observed that the effect of changing fill ratio and increasing heat input on temperature profile is more significant in the evaporator section than in condenser section. In addition, a lowest wall temperature distribution is seen at fill ratio 65% for all input energies. On the other hand, a high wall temperature occurs at the mid-distance of the evaporator wall at fill ratio 25% and 35% for all heat inputs. This wall temperature increases as the heat load increases until reaching the highest value at heat input 101W and fill ratio 25%. For fill ratios 80% and 100%, a higher wall temperature in the upper part of the evaporator is observed compared with other values of fill ratio for three heat inputs. This is due to higher liquid height in the evaporator which prevents large bubbles to reach liquid

surface forming a vapour film on the evaporator inner wall and hence, increasing the wall evaporator temperature in that region. The effect of higher liquid height decreases with increasing the heat input in the case of 80% fill ratio whereas it increases in the case of 100% [167].

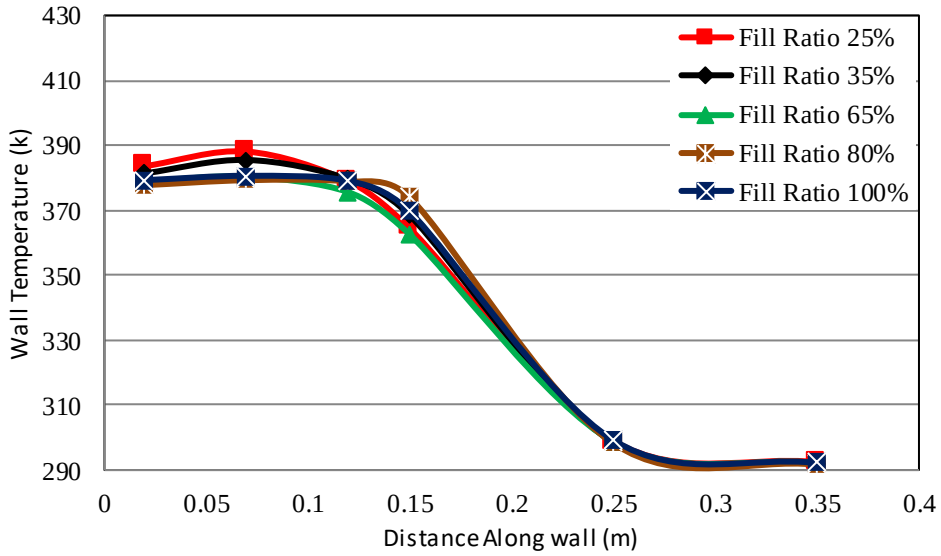

Figure 3.10a Temperature distribution on the TPCT's wall at heat input of 39 W for different fill ratios (Vertical orientation) [167]

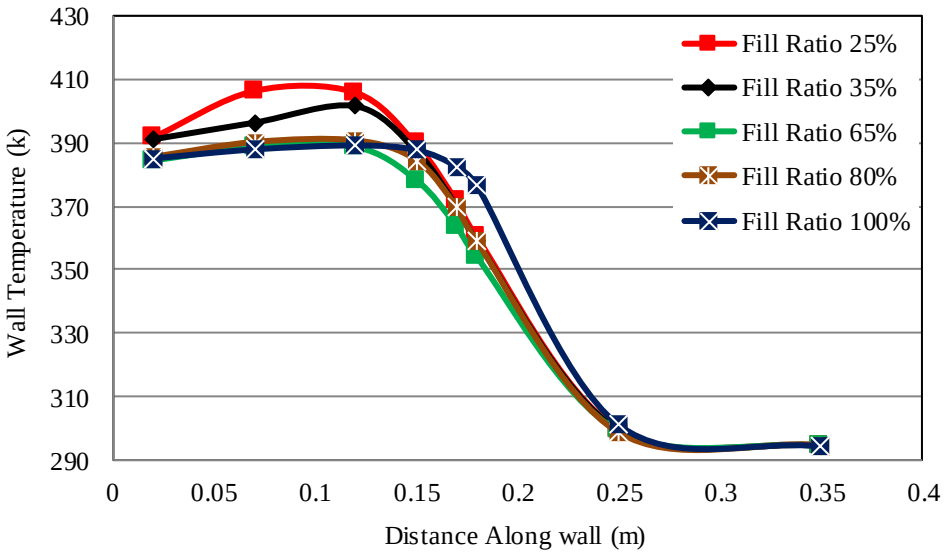

Figure 3.10b Temperature distribution on the TPCT's wall at heat input of 81 W for different fill ratios (Vertical orientation) [167]

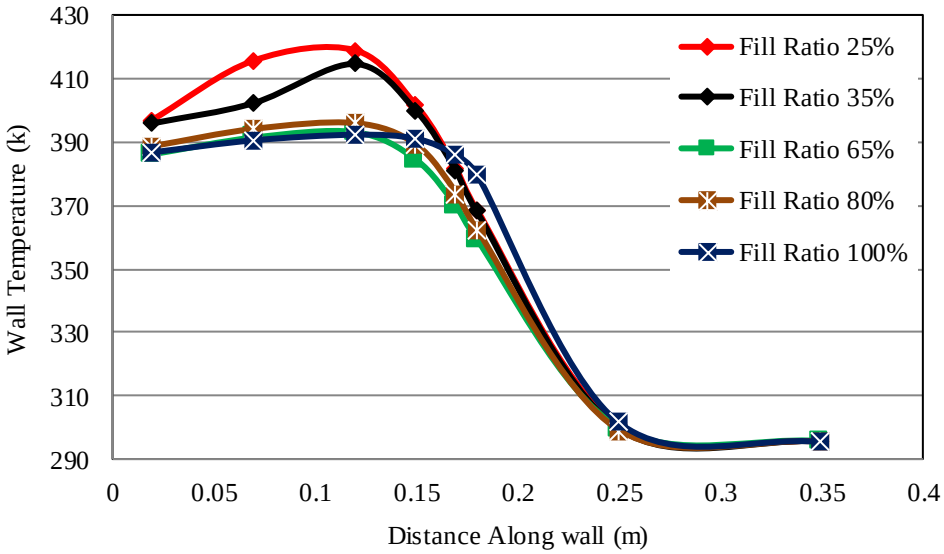

Figure 3.10c Temperature distribution on the TPCT's wall at heat input of 101 W for different fill ratios (Vertical orientation) [167]

Figure 3.11 shows the vapour volume fraction at simulation times 3 and 60 seconds for different fill ratios. Relatively small bubbles are observed for fill ratios 25% and 35% due to nearness of liquid surface from bubble sites. On the other hand, for fill ratios 80% and 100%, many large bubbles were stuck on evaporator wall before they reach liquid surface due to high height of liquid column resulting in higher evaporator temperature compared with fill ratio of 65% [167]. This can be confirmed by the last four columns in the figure (fill ratios 80% and 100%) where number of bubbles detached to the liquid pool at the lower part of the evaporator while at the top part, bubbles are noticed to reattached to the wall due to a higher liquid height compared with other fill ratios.

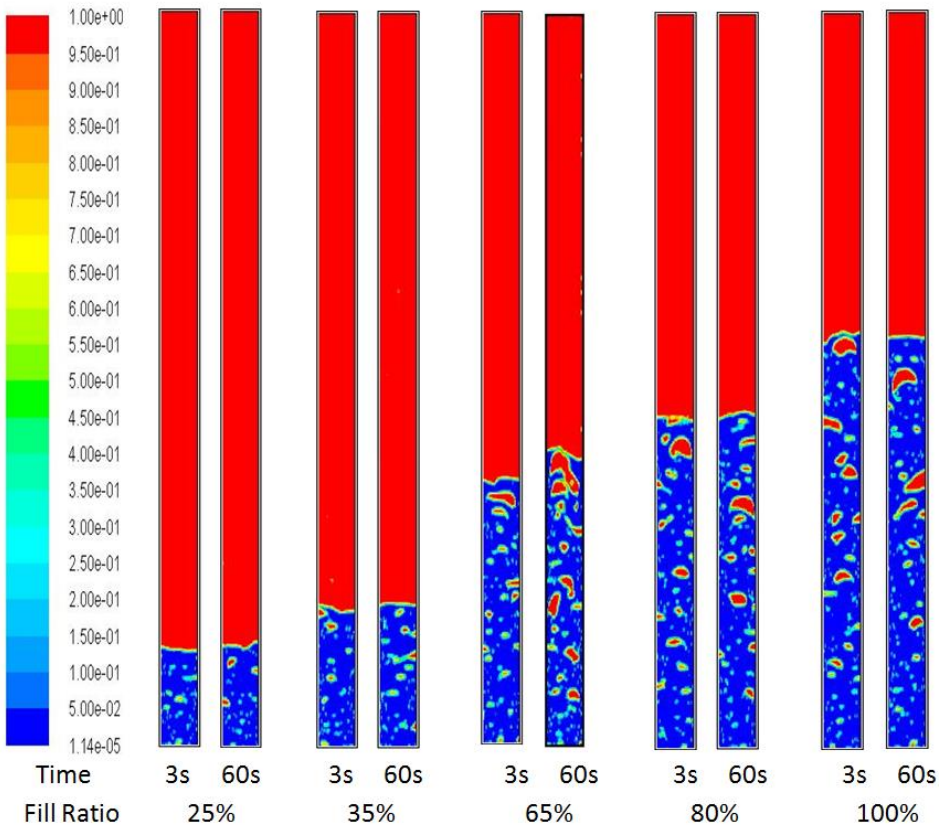

Figure 3.11 Vapour volume fraction contours at various simulation times for different fill ratios (90º)

3.12 presents the effect of the fill ratio on the average wall temperature of the evaporator for three heat inputs. It is shown that the average evaporator wall temperature decreases from its maximum value at a fill ratio of 25% to the minimum value at 65% then increases again at higher fill ratios of 80% and 100% for input energies 81and 101W (similar trend was obtained by [88] and [172]). However, at heat input 39 W, there is a slight change in evaporator wall temperature between fill ratios 25% and 35% and after fill ratio 80% the trend decreases slightly at fill ratio 100%. Therefore, the effect of fill ratio on evaporator wall temperature is clearer at relatively high input energy (81and 101W) than that at low energy (39W) [167].

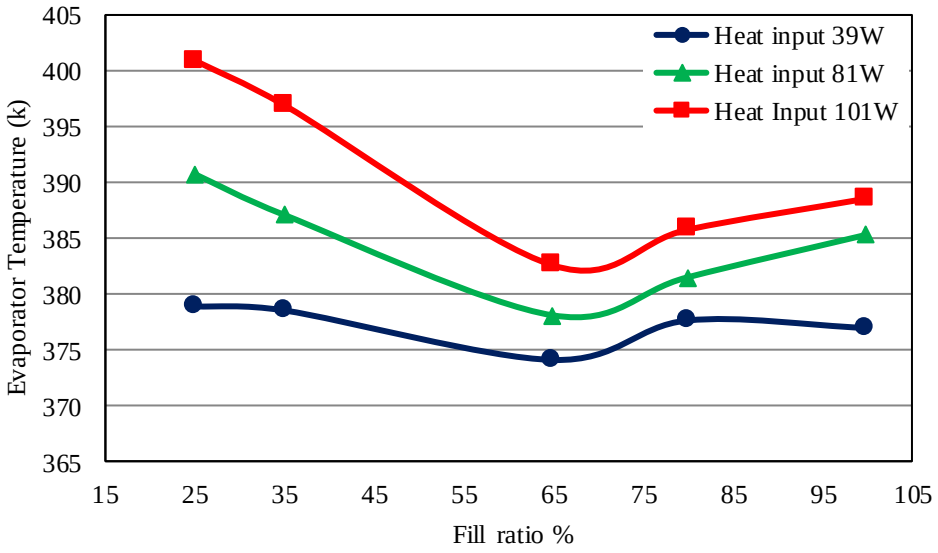

Figure 3.12 Evaporator average wall temperature versus liquid charge at various heat inputs (Vertical orientation) [167]

Thermal Resistance

The thermal resistance of the TPCT is defined as follow:

$$R_{t=}\frac{T_{ew,av}-T_{cw,av}}{Q_{in}} \qquad 3.26$$

Where R_t is the total thermal resistance of the TPCT, $T_{ew,av}$ and $T_{cw,av}$ are the average wall temperatures of the evaporator and condenser respectively, and Q_{in} is haet input.

Figure 3.13 presents the influence of heat load on thermal resistance for various fill ratios. It is noticed that the thermal resistance decreases as the heat load increases for all fill ratios. A higher thermal resistance is observed at fill ratio 25% due to a small volume of working fluid whereas a lower value at 65% for all energy inputs (similar trend was obtained by [92]). However, a lower difference in thermal resistance between the fill ratios is seen at heat input of (39W), especially, between 25% and 35% compared with that at higher energy inputs (81 and 101W) [167]. This indicates that with low fill ratios and a heat input of 101W, the heat pipe reaches its heat transfer limit leading to high temperatures at the upper part of the evaporator as shown in Figure 3.10 (b and c). In addition, the thermal resistance for fill ratio 80% is greater than that for 100% at input energy 39W compared with that at higher heat

inputs (81 and 101W). Thus, the best fill ratio is 65% and this is a similar conclusion as that made by [66] and [92]. The reason behind increasing the thermal resistance at high fill ratios (80% and 100%) is that the upper part of the evaporator is constantly covered with the hot liquid due to a higher liquid height. This prevents the relatively cold liquid dropping from the condenser to directly cooling this part as happen in the case of low fill ratios causing the thermal resistance to be higher compared with fill ratio 65% [167].

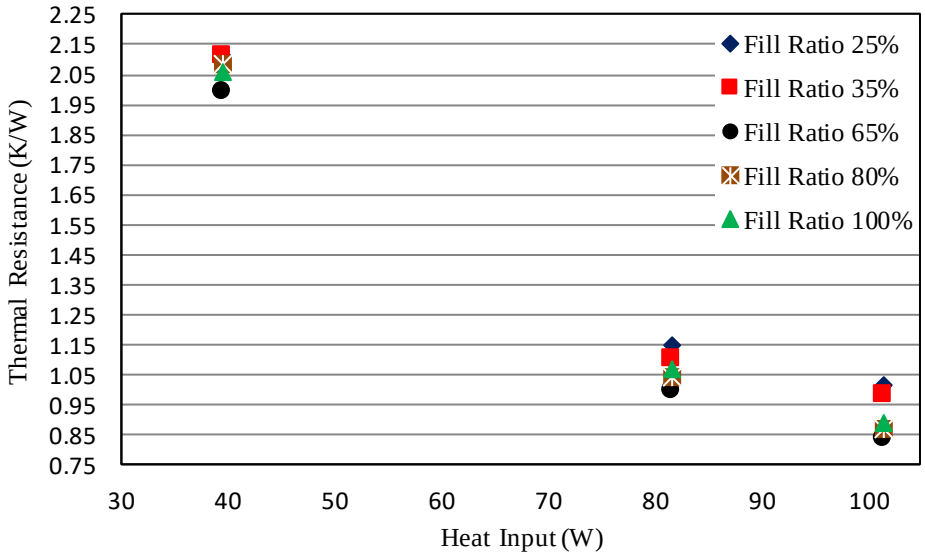

Figure 3.13 Thermal resistance versus heat input for five fill ratios (Vertical orientation) [167]

3.6.2.3 Effect of Inclination Angle

CFD simulation was employed to study the influence of inclination on the TPCT thermal performance at angles of (10, 30, 50, 70 and 90^{o}). Firstly, the numerical results were compared with the experimental work of Abdullahi [77] in terms of thermal resistance to validate the CFD solution. Figure 3.14 presents a comparison of variation of thermal resistance with inclination angle of thermosiphon at heat input of 109 W between CFD modelling and experimental work [77]. CFD results showed a good agreement with experimental data with maximum deviation of (1.3%) and produced a similar trend in which the lowest thermal resistance is attained at angles of (80 and 90^{o}) whereas the highest at (70^{o}) [167].

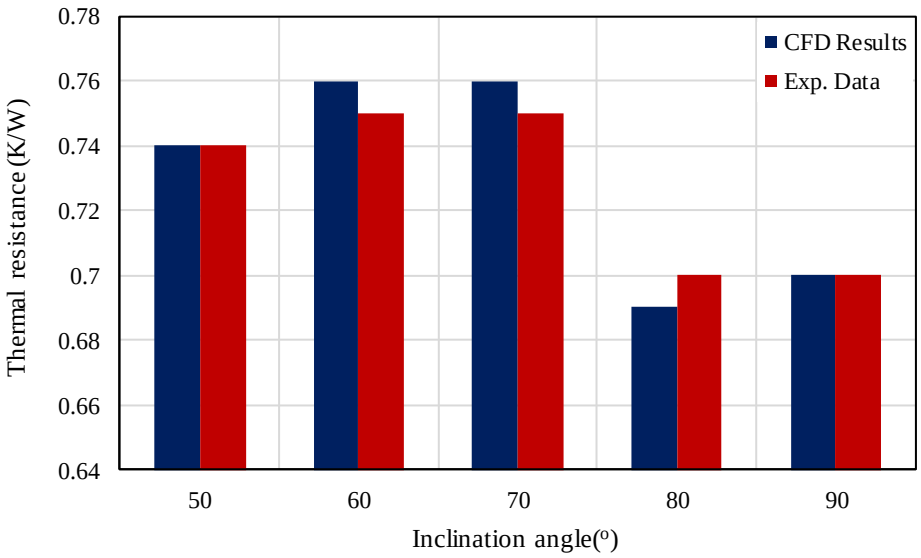

Figure 3.14 Comparison of variation of thermal resistance with inclination angle between CFD result and experimental work (109W and FR=65%) [167]

Figure 3.15 presents the variation of vapour volume fraction during flow time for inclination angle of 10°, heat input 101W and fill ratio 65%. It is clearly observed that the liquid in evaporator is not in contact at certain parts of evaporator wall due to inclination leading to the increase in the wall evaporator temperature. In addition, it is observed that the bubble size remains relatively small as time increases and this may be attributed to the nearness of liquid surface to the bubble nucleation sites because of the inclination. As a result, a vapour film forms on the upper part of the evaporator wall which leads to additional increase in evaporator wall temperature [167].

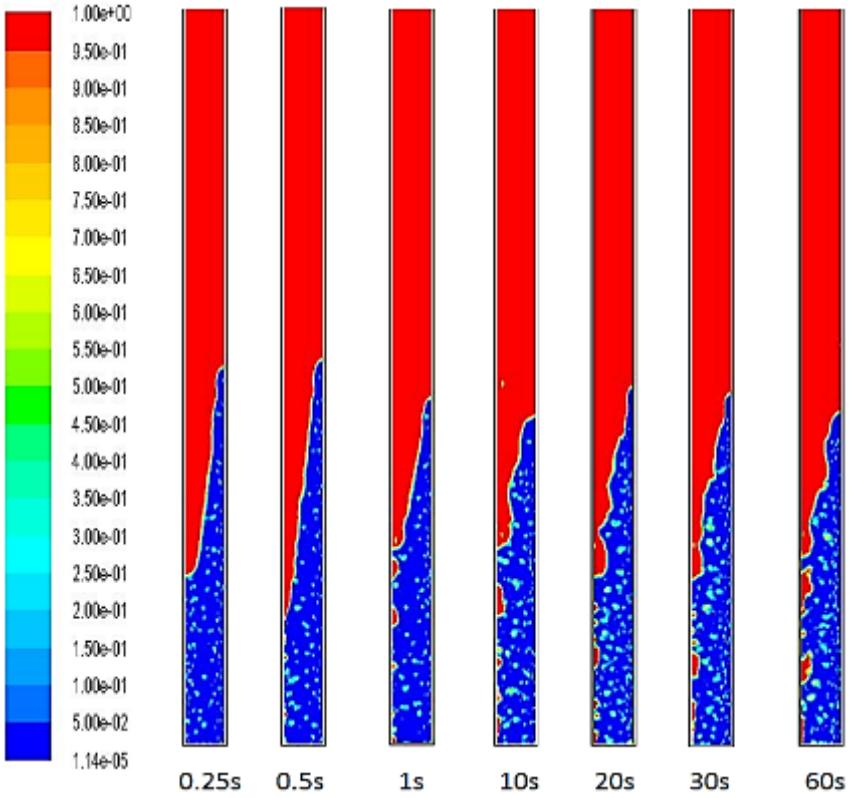

Figure 3.15 Vapour volume fraction contours at various simulation times for inclination angle 10°

Figure 3.16 (a, b and c) illustrate the variation of the wall temperature of thermosiphon with the distance along the wall for three heat inputs (39, 81 and 101W) at five inclination angles (10, 30, 50, 70 and 90) and fill ratio of 65%. They show a similar trend for three input energies in which the highest and lowest wall temperature occur at angles of 10° and 90°, respectively. These higher temperatures at low inclination angles can be attributed to the fact that some of the upper part of the evaporator section is not in contact with liquid due to inclination . It is also noticed that the inclination effect increases with heat load [167].

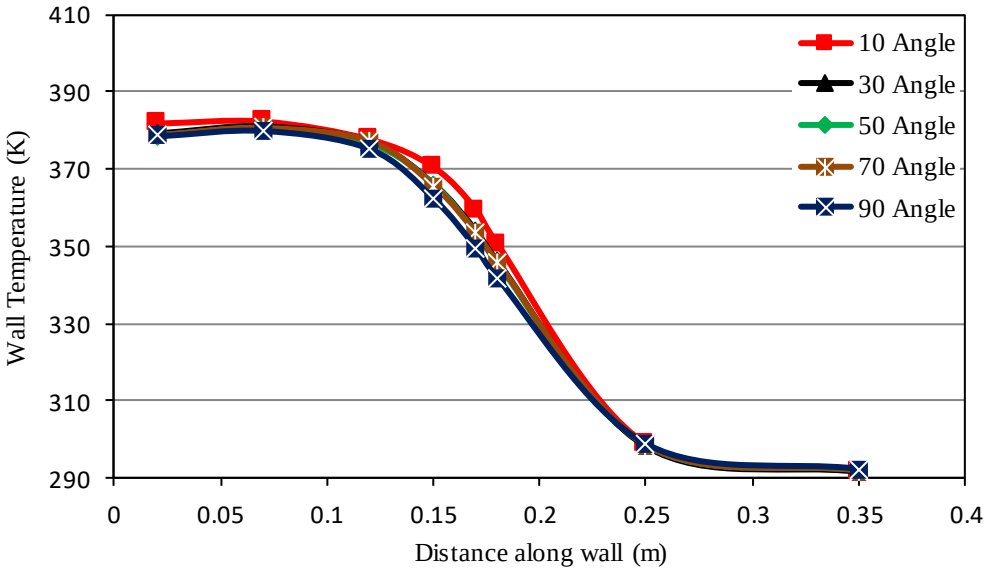

Figure 3.16a Wall temperature distribution at heat input 39W and fill ratio 65% for different inclination angles [167]

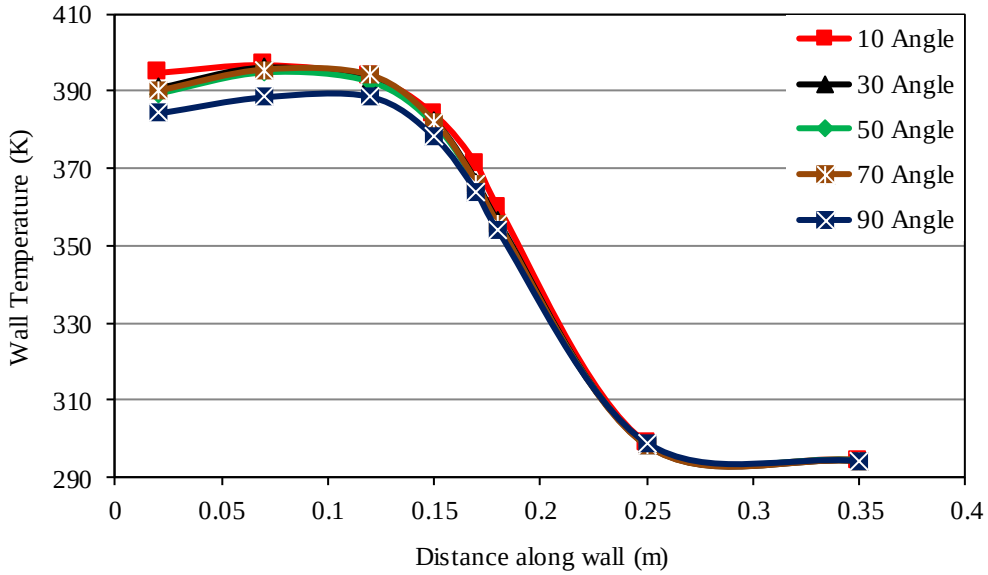

Figure 3.16b Wall temperature distribution at heat input 81W and fill ratio 65% for different inclination angles [167]

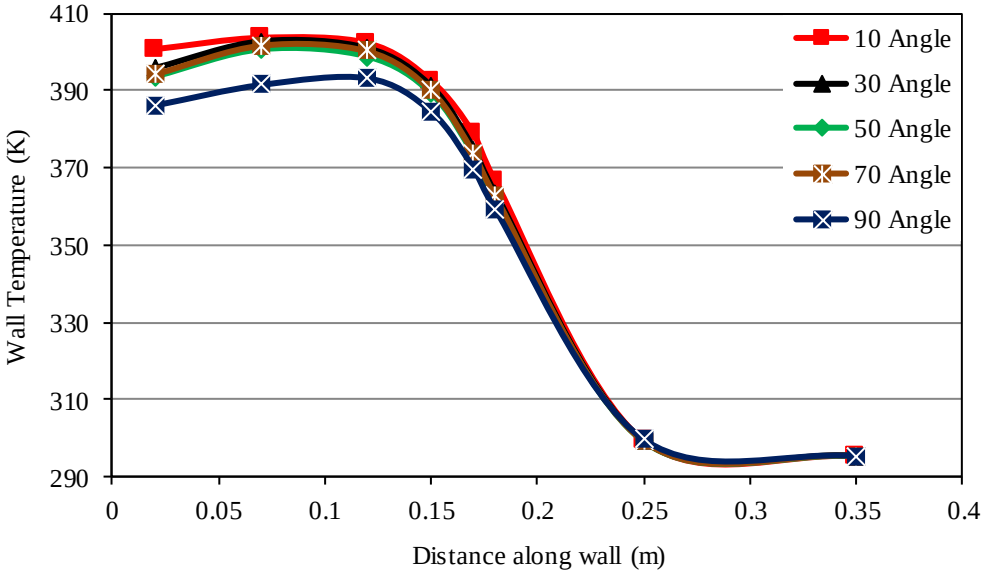

Figure 3.16c Wall temperature distribution at heat input 101W and fill ratio 65% for different inclination angles [167]

The effect of inclination on the evaporator average wall temperature at input energies of 39, 81, and 101W is illustrated in Figure 3.17. It is seen that the evaporator temperature increases as the inclination angle decreases toward the horizontal orientation for all heat inputs and this increase is higher when the heat input is higher. However, at angle of 50^{o} the value of the evaporator temperature is less than that at angle 70^{o} for all three cases, but it is still higher than the value at angle 90^{o} [167].

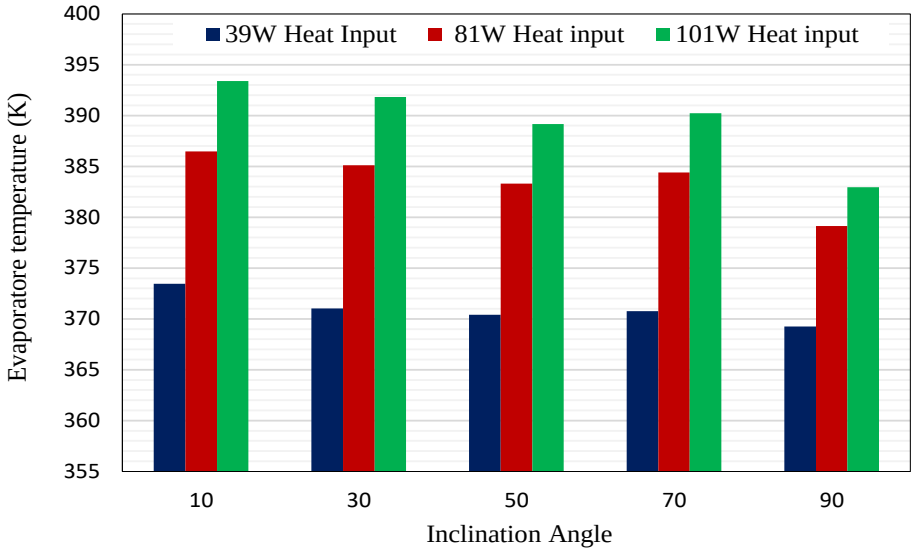

Figure 3.17 Evaporator wall temperature versus inclination at heat loads 39, 81, and 101W (FR=65%) [167]

Figure 3.18 shows the effect of inclination angle on the thermal resistance of the thermosiphon at heat loads 39, 81, and 101W. The results show that the thermal resistance decreases as the inclination angle increases and the highest and lowest thermal resistance are at inclination angle 10^o and 90^o, respectively, for all input energies. Therefore, the thermal performance of the (TPCT) for current geometry and operating conditions is better at vertical orientation (90^o) than that at other orientations (similar conclusions were reported by [92], [99] and [102]).

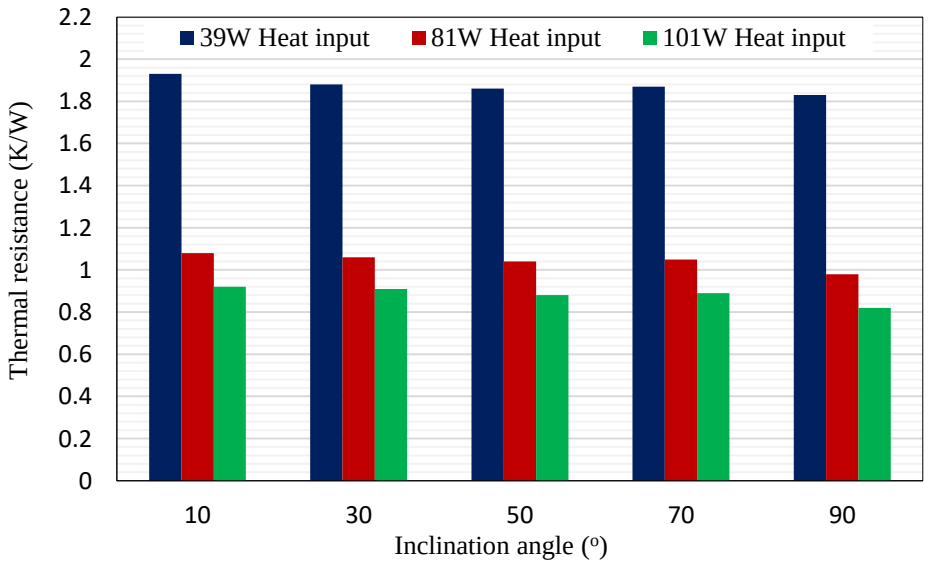

Figure 3.18 Thermal resistance varsus inclination at heat loads 39, 81, and 101W (FR= 65%) [167]

3.7 Modelling of Contact Angle

3.7.1 Introduction

Interaction of a liquid or a vapour with a solid surface depend on the contact angle. Different fluids interact in different ways with a certain surface and different surface characteristics also effect the interaction with a certain fluid. In other words, the contact angle is a measure of the surface wettability, when the contact angle is low (θ_w<<90^o), the surface is wetted by the liquid, while the liquid does not wet the surface, when the contact angle is high (θ_w>>90^o) as shown in Figure 3.19. Likewise, hydrophilic surface is indicated by a low contact angle, whereas high contact angle indicates that the surface is hydrophobic. On the other hand, the

surface tension which depends on the type of the liquid exerts a force to maintain a semi droplet or bubble shape. Thus, when the interaction between the liquid and the surface which is called the interfacial tension is stronger than the surface tension of the liquid, the droplet will spread out and that means the surface has high wetting characteristics. On the contrary, when the interfacial tension is weaker than the surface tension, the surface has low wetting features [173]. That means:

-Low contact angle = high interfacial tension.

-High contact angle = low interfacial tension.

Theoretically, the contact angle can be defined as the angle between the two tangential lines of liquid-solid and liquid-vapour interfaces (Figure 3.19) [173]. Yong's equation is used to describe the contact angle which assumes that the liquid drop on a solid substrate is in a mechanical equilibrium due to the effect of three interfacial tensions as follow [173]:

$$cos\theta_w = \frac{\sigma_{sv}-\sigma_{sl}}{\sigma_{lv}} \qquad 3.27$$

Where, σ_{sl}, σ_{lv} and σ_{sv} denote interfacial tensions of the solid-liquid, liquid-vapour and solid-vapour, respectively as shown in Figure 3.19, and θ_w denotes the contact angle.

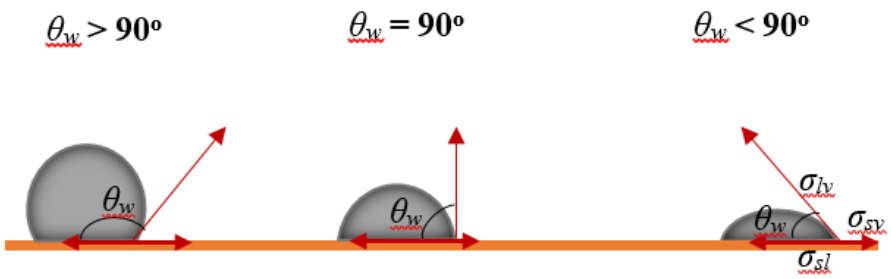

Figure 3.19 Different contact angle for different interacting with surfaces

3.7.2 Contact angle modelling

In Ansys Fluent, the surface normal local gradients at the interface are employed to compute the surface curvature Kc_l and Kc_v in eq. (3.8). The wall adhesion angle can be included in the VOF model in combination with the model of surface tension which is adopted from

Brackbill work [170] to model the contact angle of the fluid with the wall [26]. Thus, instead of applying this as a wall boundary condition, the contact angle is used to govern the surface normal in the computational cells near the wall. Therefore, the surface curvature near the wall is adjusted using so-called dynamic boundary condition. Consequently, the surface normal at the cell adjacent to the wall can be written as [168]:

$$\hat{n} = \hat{n}_w cos\theta_w + \hat{t}_w sin\theta_w \qquad 3.28$$

Where $\hat{t}_w$ and $\hat{n}_w$ denote unit vectors tangential and normal to the wall and θ is the contact angle. Accordingly, the surface local curvature can be determined by combining the above value of the contact angle with the computed surface normal for the cell next to the wall. This curvature is employed to correct the body force term in the determination of the surface tension eq. (3.8) [26].

3.7.2.1 Phase Change Model

In Ansys Fluent, multiphase VOF model, the evaporation-condensation model is used to simulate the evaporation and condensation processes represented by mass transfer from liquid to the vapour and from vapour to the liquid based on Lee model [174]. In the Lee model, the mass transfer at the liquid-vapor interface is governed by the continuity based volume fraction equation (eq.3.3). The theoretical model is built based on the kinetic theory assumptions and relates the pressure to the temperature at the saturation condition based on the Clapeyron-Clausius equation. These assumptions are [168]:

- Flat interface
- Dispersed regime with constant diameter
- Known accommodation coefficient

For the evaporation process, the model assumes vapour bubbles in a continuous liquid phase, Thus, the following mass source term is used ($T_l > T_{sat}$):

$$S_{\alpha M} = C_{coef} \times \alpha_l \rho_l \frac{(T_{sat} - T_{mix})}{T_{mix}} \quad 3.29$$

On the other hand, for the condensation process, the model considers small droplets in a continuous vapour even though the liquid is the primary phase. Accordingly, the following mass transfer expression is applied for the condensation process ($T_v < T_{sat}$):

$$S_{\alpha M} = C_{coef} \times \alpha_v \rho_v \frac{(T_{sat} - T_{mix})}{T_{mix}} \quad 3.30$$

Where, C_{coef} is the evaporation or condensation coefficient which theoretically has different values for evaporation and condensation and is expressed as [168]:

For evaporation:

$$C_{coef} = \frac{6}{d_b} \beta_e \sqrt{\frac{M}{2\pi R T_{sat}}} \times \left(\frac{\alpha_v \rho_v}{\rho_l - \rho_v} \right) \quad 3.31$$

For Condensation:

$$C_{coef} = \frac{6}{d_d} \beta_c \sqrt{\frac{M}{2\pi R T_{sat}}} \times \left(\frac{\alpha_l \rho_l}{\rho_l - \rho_v} \right) \quad 3.32$$

Where d_b and d_d are the bubble and droplet diameters, respectively, M is the molecular weight and R is the universal gas constant. β_e *and* β_c are the evaporation and condensation accommodation coefficients which represent the ratio of liquid molecules absorbed by vapour surface to the total number of molecules reaching the vapour surface and the ratio of vapour molecules absorbed by a liquid surface to the total number of molecules reaching the liquid surface, respectively.

The accommodation coefficient, bubble diameter and droplet diameter are usually not well known. Therefore, the C_{coef} must be tuned carefully to match the experimental results [168]. Accordingly, the energy source terms for evaporation and condensation processes can be calculated from (3.14), (3.29) and (3.30) as follow:

Evaporation:

$$S_q = C_{coef} \times \alpha_l \rho_l \frac{(T_{sat} - T_{mix})}{T_{mix}} h_{fg} \quad 3.33$$

Condensation:

$$S_q = C_{coef} \times \alpha_v \rho_v \frac{(T_{sat} - T_{mix})}{T_{mix}} h_{fg} \quad 3.34$$

Equations (3.29), (3.30), (3.33) and (3.34) are employed in Fluent to model the transport phenomena represented by mass and heat transfer during phase change process. This can be achieved by activating the evaporation-condensation model in Fluent to add the phase change mass and heat transfer rates to the continuity and energy equations, respectively as source terms [26].

3.7.3 **Modelling of a Flat Plate**

To simplify the CFD solution and reduce the computational time, a simple geometry of a flat plate is used to simulate the condensation process and investigate the effect of the contact angle on condensation heat transfer enhancement using Ansys Fluent. This work was published in [26].

3.7.3.1 CFD Set up and Strategy

Geometry and mesh of a vertical flat plate were generated using workbench design module (Ansys 17). The flat plate is 50 mm in height with a vapour domain depth of 10 mm as shown in Figure 3.20. These dimensions were chosen to be equal to those in a previous experimental work [175] to validate the CFD results related to contact angle.

Workbench design module (Ansys 17) was also employed in the meshing of the geometry with elements number of 100 and 300 in the horizontal and vertical directions, respectively. Thus, the total number of cells in the fluid domain were 30000. To control the size of cells near the wall, control edge sizing technique was used with a bias factor of 5 resulting in grid size near the wall of 0.025 mm as shown in Figure 3.20 [26].

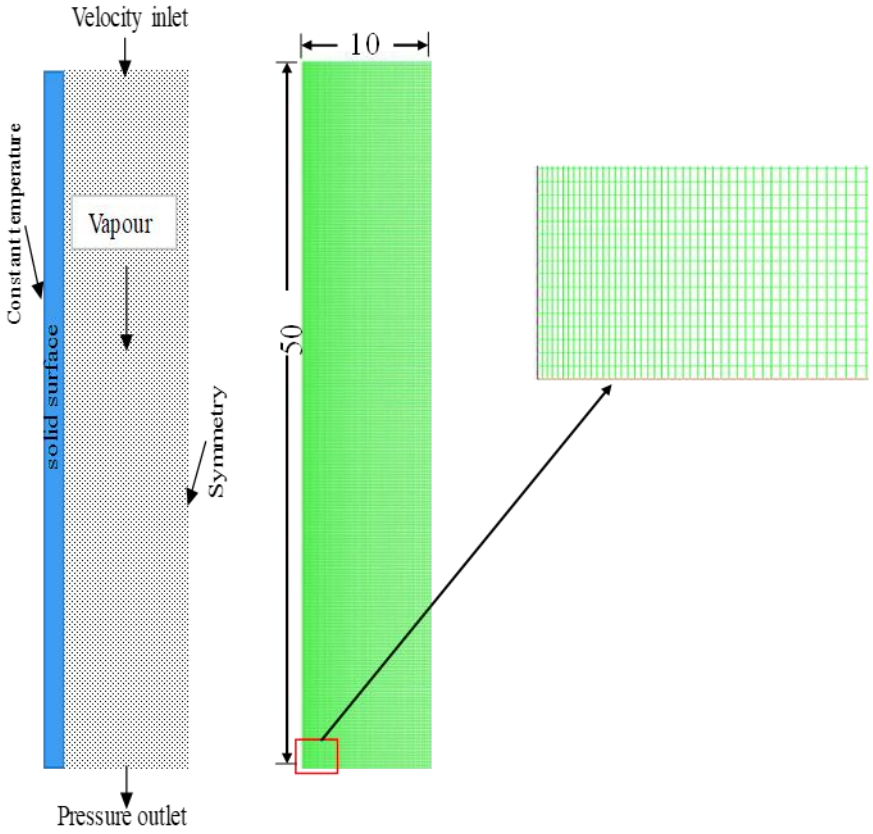

Figure 3.20 Geometry and mesh of vertical flat plate [26]

The VOF multiphase model was used with transient solver to model the vapour condensation on a vertical surface. The SIMPLE algorithm was used for pressure-velocity coupling and PRESTO discretization was utilised to determine the pressure. To calculate, momentum and energy, a first order upwind scheme was used whereas for modelling of the volume fraction, Geo-Reconstruct discretization was chosen [26]. The solution was considered reaching the steady state when flow field residuals were reduced to the 10^{-4} and energy residual to 10^{-6} as well as when no important change in the value of total heat flux was observed. In addition, the vapour was considered as the secondary phase; thereby the volume fraction equation (3.3) was solved only for the vapour phase. Furthermore, boundary conditions of inlet velocity and pressure outlet were applied at the top and bottom of the flat plate, respectively, whereas constant temperature and symmetry boundary conditions are imposed at the wall and the middle axis, respectively [26].

3.7.3.2. Results and Discussion

Vapour condensation process on a flat plate was modelled to investigate the effect of different surface characteristics in terms of the contact angle on the condensation heat transfer enhancement at different subcooled temperatures using Ansys Fluent [26].

3.7.3.2.1. Validation of CFD Results

To test the capability of Ansys Fluent software to model the enhancement in the condensation performance, the CFD solution is validated using two steps. The first step is to validate the condensation of the vapour on a smooth surface and the second step is to validate the vapour condensation process on the modified surface with different contact angles.

Validation of Condensation Process

To validate the CFD solution of a pure vapour condensation over a vertical surface, CFD results were compared with experimental data carried out by Yi et al [176] in terms of condensation heat transfer coefficient. Figure 3.21 compares the condensation heat transfer coefficient predicted by the present CFD results and those obtained from [176] and calculated from Nusselt theory. It presents the variation of condensation heat transfer coefficient with subcooled temperature (10, 20, 30, 40, 50 and 60 K) and the same trend was achieved in which heat transfer coefficient decreases as subcooled temperature increases. Figure 3.21 also shows a good agreement between the CFD simulation and Yi experimental work with a maximum deviation of 5% [26]. This deviation is within the uncertainty in the condensation heat transfer coefficient of 12.57% reported in the same experimental work [176].

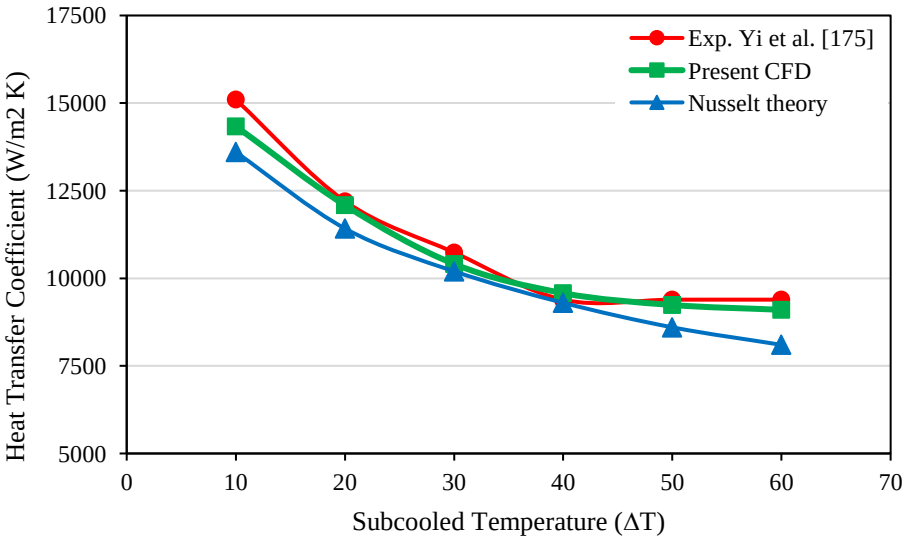

Figure 3.21 Comparison between CFD result and Yi experimental data [26]

Validation of the Effect of Contact Angle

To show the capability of CFD modelling to predict the influence of contact angle on condensation heat transfer, a comparison between CFD results of a coated surface with a certain contact angle and Qi experimental work [175] was performed as illustrated in Figure 3.22. It shows the variation of total heat flux with subcooled temperature (1, 2, 3, 4, 5, 6 and 7 K) at two different contact angles namely, 128.6^{o} and 159.3^{o}. A similar trend was attained where the heat flux increases as the subcooled temperature increases. In addition, the CFD solution showed a good agreement with experimental data with maximum deviation of 9.9% and 8.5% corresponding to contact angles of 128.6 and 159.3, respectively [26].

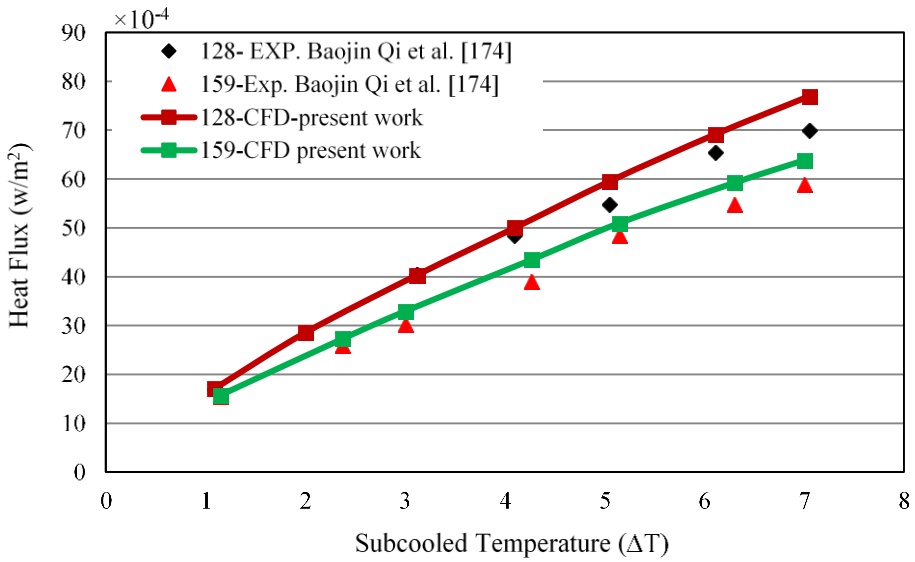

Figure 3.22. Comparison between Present CFD result and Qi experimental work [26]

3.7.3.2.2 Effect of Contact Angle

Figure 3.23 illustrates the variation of heat flux with the contact angle at two different subcooled temperatures of 3 and 7 K. It shows that condensation heat flux increases as the contact angle increases to attain its maximum value at a contact angle of 140° (hydrophobic surface) for both subcooled temperatures 3 and 7 K and this value is more than 3 times that the value of heat flux at a contact angle of 90° (plain surface). After that, it decreases at contact angles of 150° and 160° (superhydrophobic surface), but their values are still greater than that for plain surface (90°) (similar trend as [175]). This can be attributed to the formation of relatively large drops in case of contact angles of 150° and 160° [175] which reduces the contact surface area thus, the drops nucleation density decreases and, hence, reduces the heat flux [26].

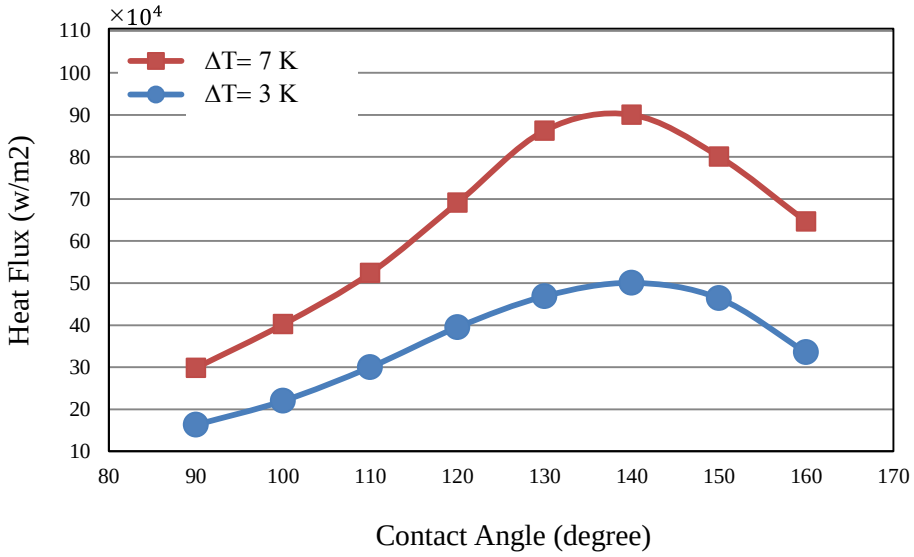

Figure 3.23 Heat flux versus contact angle at subcooled temperatures of 3 and 7 K [26]

The variation of the heat flux with the subcooled temperature of the wall is illustrated in Figure 3.24 at three different contact angles 90, 140 and 160º. It is clear that the heat flux increases as the temperature difference between wall and vapour increases for the three contact angles. It is also shown that the contact angle of 140º produces the highest value of heat flux for all values of subcooled temperatures which is about 3 times compared with that at a contact angle of 90º. In addition, the difference between them is much higher at subcooled temperature of 7 compared with that at 1, thus, changing the surface wettability by changing the contact angle produces a high enhancement in condensation heat transfer [26].

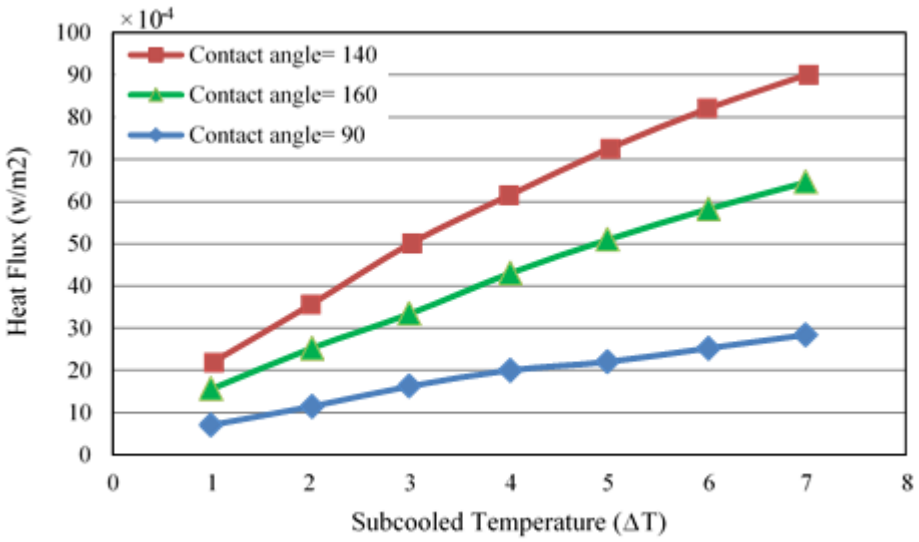

Figure 3.24 Heat flux varsus subcooled temperature for different contact angles [26]

3.7.4 Modelling of a Thermosyphon heat pipe

3.7.4.1 Geometry and Mesh

Ansys was employed to generate a geometry of a 2D vertical TPCT. The dimensions of the TPCT are 200 mm in total height with evaporator and condenser length of 100 mm each, outside diameter of 12.7 mm and wall thickness of 1.6 mm as shown in Figure.3.25. These dimensions have been adopted from the present experimental work that will be discussed in detail in chapter 5 in order to validate the CFD solution. Same method was used in meshing the geometry as in section 3.6.1.1.

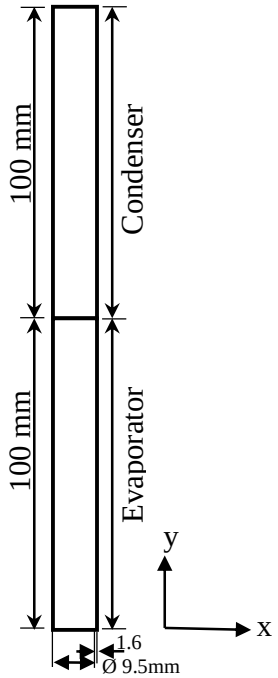

Figure.3.25 The TPCT geometry and dimensions

3.74.2 Initial and Boundary Conditions

The temperatures of evaporator wall, evaporator liquid and condenser vapour were set initially to be slightly above the boiling point and the initial condenser wall temperature was set as a condenser mean cooling temperature. In addition, the saturation temperature and operating pressure were obtained from the present experimental work as illustrated Table 3.1 in at each heat input.

A non-slip boundary condition was applied at the internal walls of the evaporator and condenser. Also, to define the heat added to the TPCT, a constant heat flux was chosen at the evaporator outer wall. Different values of heat flux which correspond to different values of heat input were used to represent those employed in the experimental work as listed in Table 3.1. A convection boundary condition was imposed at the outer wall of the condenser to simulate the heat sink at the condenser where the convection heat transfer coefficient between cooling water and the condenser's wall was calculated from equation (3.21). The $T_{cw,av}$ is obtained using the following equation:

$$T_{cw,av} = \frac{T_{13} + T_{16} + T_{19}}{3} \quad 3.35$$

Where, T_{13}, T_{16} and T_{19} are the temperature readings at the condenser section at 0.13, 0.16 and 0.19 m, respectively which were also adopted from the experimental work.

The temperature dependent polynomial eq. 3.24 was used to calculate the surface tension for water at any temperature which is included in the *Fs* term eq. (3.8) by activating the CSF in Fluent software. Also, the liquid density can be obtained using eq. (3.25) at any temperature, whereas the vapour density can be chosen as saturated vapour density value at the saturation temperature for any heat input which depends on the experimental data listed in Table 3.1.

Table 3.1 Initial and operating parameters from experimental work

Heat input (W)	Heat flux (W/m^2)	P_{sat} (kPa)	T_{sat} (K)	T_m (K)	ρ_v (kg/m^3)	Latent heat kJ/kg
80	20051.02	57	357.77	299.085	0.3432	2297.51
100	25063.77	61	359.45	300.325	0.3718	2291.93
120	30076.52	65	361.143	301.555	0.3945	2287.72
140	35089.28	70	363.082	302.13	0.4229	2282.74
160	40102.03	76	365.261	302.93	0.4567	2277.11

3.7.4.3 Solution Methods and Techniques

Same solution techniques and strategies as in section 3.6.1.3 were used to model the two-phase flow inside the TPCT in this section.

3.7.4.4 Results and Discussion

3.7.4.4.1 Validation of CFD Solution

Same geometry as that used in the present experimental work was adopted in the CFD simulation employing the same operating condition to validate the CFD solution. Thus, the wall temperature distribution and thermal resistance of the TPCT obtained from the CFD

results have been compared with the experimental data at five different heat loads (80, 100, 120, 140 and 160W).

Figure 3.26a and Figure 3.26b compares the wall temperature distribution predicted by CFD solution and the experimental data at heat inputs of 80, 120 and 160W, and 100 and 140W, respectively. It is seen that the CFD model predicts well the experimental data with a maximum deviation of about 1.9% and provides the same trend. Also, less deviation between the two results is observed at the condenser section compared with that at the evaporator which generally increases as the heat load increases.

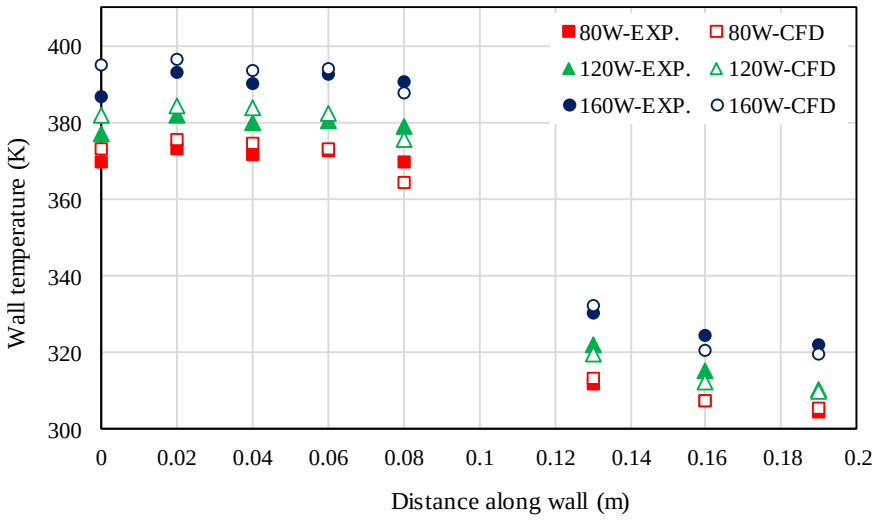

Figure 3.26a Comparison of wall temperature distribution of thermosyphon between experimental data and CFD results at heat loads of 80, 120 and 160W

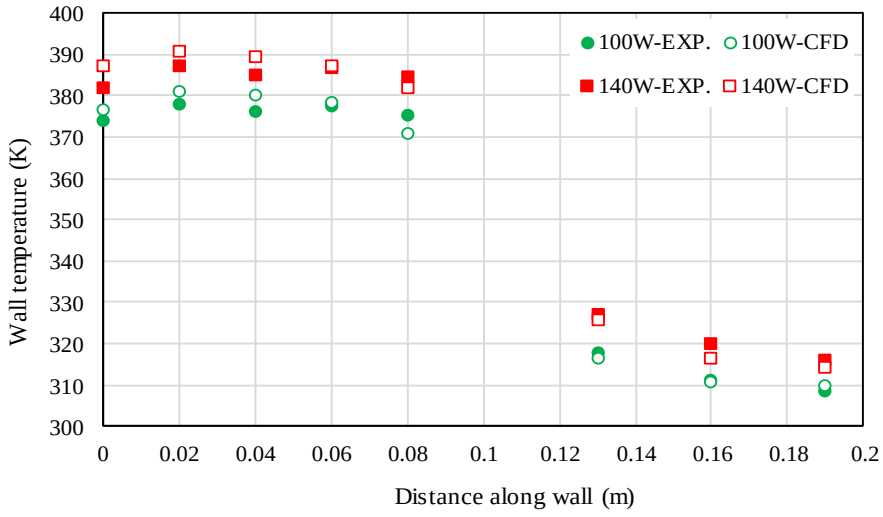

Figure 3.26b Comparison of wall temperature distribution of thermosyphon between experimental data and CFD results at heat loads of 100 and 140W

A comparison of the TPCT thermal resistance against the heat input between the CFD results and the experimental data is shown in Figure 3.27. It is observed that a good agreement between the two results is achieved with a maximum difference of about 6.6% at a heat load of 160W. In addition, the same trend is obtained in which the thermal resistance decreases with the increasing of the heat input.

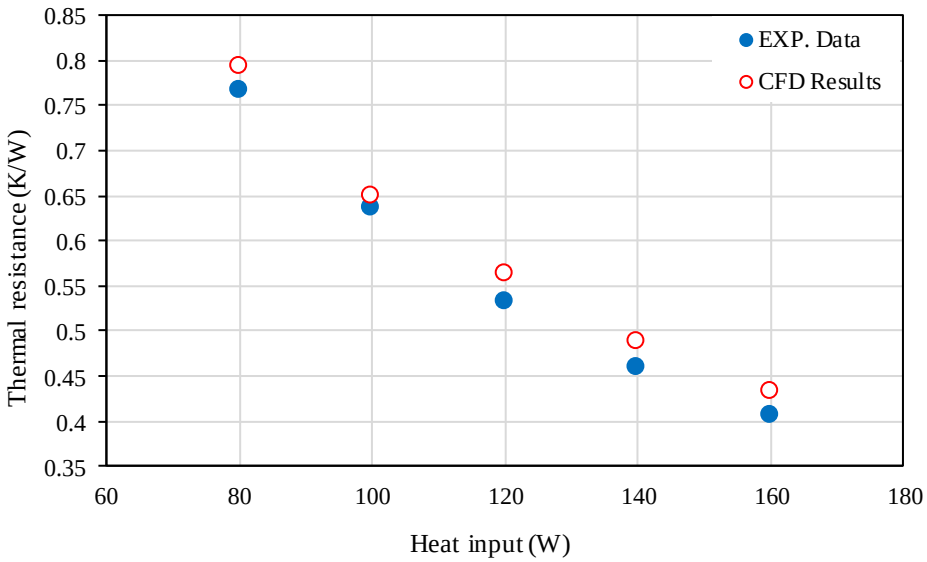

Figure 3.27 comparison of variation of thermal resistance with heat input between CFD and experimental data

3.7.4.4.2 Visualisation of Effect of Contact Angle

To show the capability of the model to simulate different surface wettabilities corresponding to different contact angles, a visualisation of volume fractions of liquid (blue colour) and vapour (red colour) is employed. Figure 3.28a and Figure 3.28b compare the variation of vapour volume fraction with time at a heat input of 80 W for a plain TPCT (contact angle 90^o in both sections) and a TPCT with contact angles of 40^o and 140^o in the evaporator and condenser, respectively. It is observed that at time 0.1 second, heat is transferred to the liquid pool by convection only due to low superheat in both thermosyphons, but as the volume fraction contours show, more heat is transferred to the liquid pool in the case of the TPCT with 40^o and 140^o contact angles compared with the plain TPCT. This can be seen from a

larger light blue colour referring to a mixture of liquid and vapour indicating that more heat is transferred. Then, at time 0.2 second, bubbles start forming indicating the bubbly flow due to further increase in the temperature difference between the heated surface and liquid pool in both TPCTs. However, it is obvious that a larger number of bubbles are formed in the TPCT with a low contact angle (40^o) than that in TPCT with an angle of 90^o due to a larger number of nucleation sites resulting from the coated surface. This bubbly regime is quickly diminished at a time of about 0.3 second to form vapour jackets attached to the wall in the case of the plain TPCT, while this bubbly regime continues in the case of the TPCT with 40^o contact angle where bubbles escape instantly from the heated surface to the liquid pool due to the wettable characteristics of this surface (40^o contact angle) until a time of 1 second. After this time, the detached bubbles gather to form a slug flow where the slug size increases as the time increases until reaching the steady state. A similar behaviour is observed from Figure 3.29a and Figure 3.29b at a higher heat load of 160 W in the two thermosyphons, but the bubbles start forming earlier due to a higher heat flux. Also, a higher number of vapour jackets attached to the surface of the plain TPCT compared with that at the heat load of 80 W are observed. On the other hand, for the TPCT with the contact angle of 40^o, larger bubbles and slugs are noticed at a heat load of 160 W compared with that at 80 W.

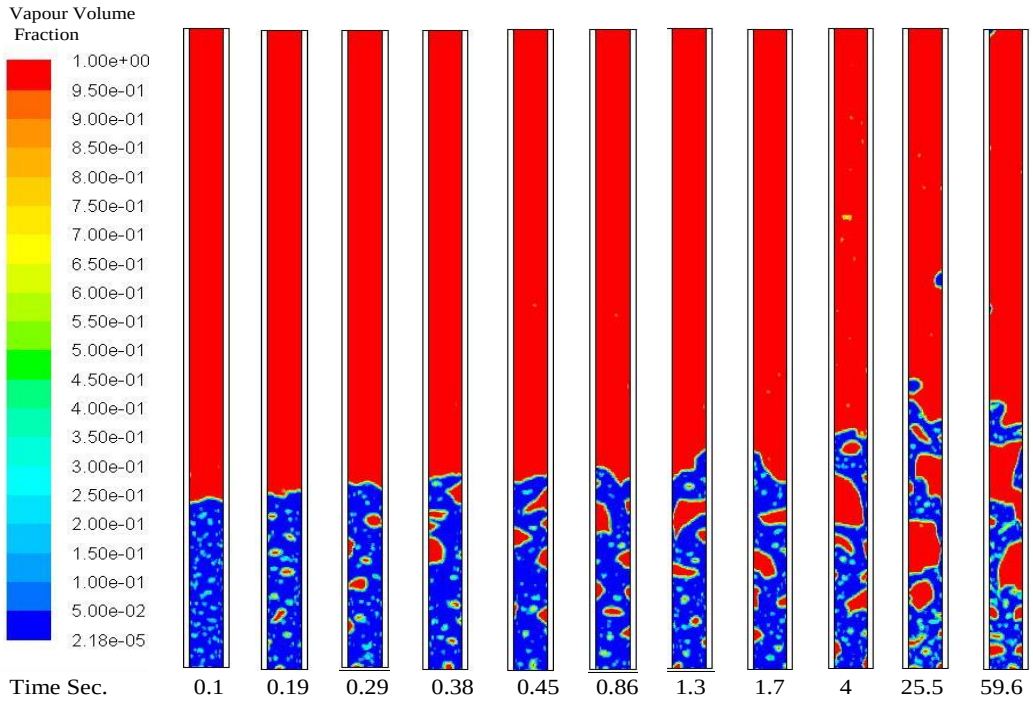

Figure 3.28a Vapor volume fraction for different times and contact angle of 90º at heat input of 80 W.

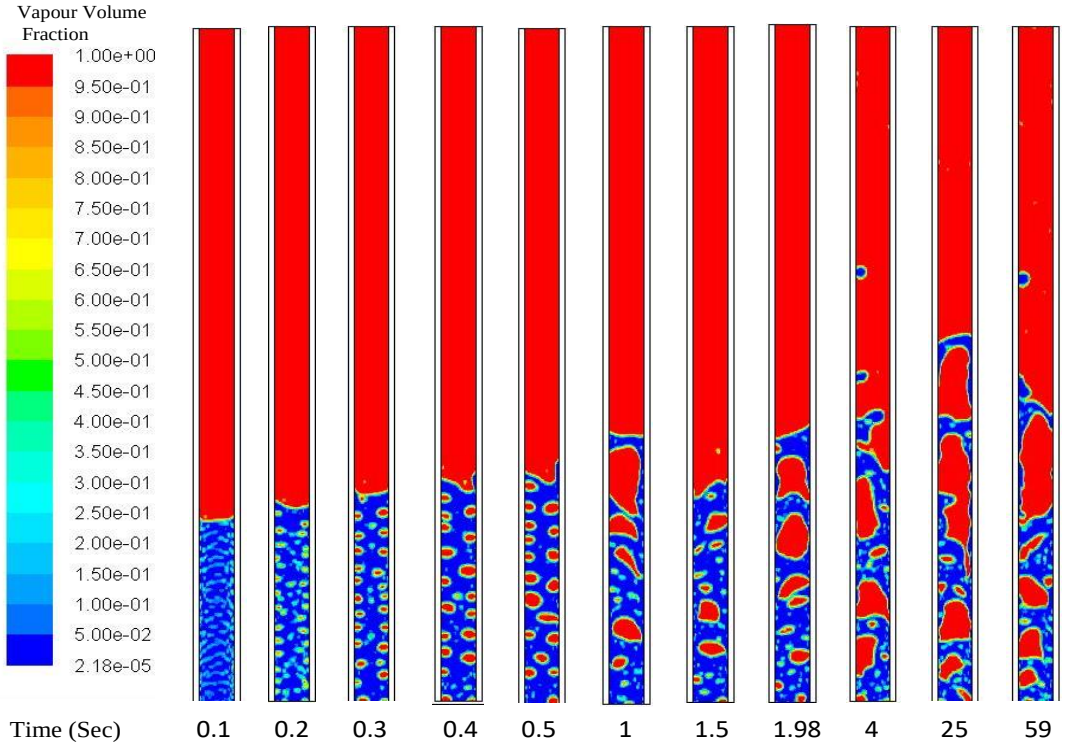

Figure 3.28b Vapor volume fraction for different times and contact angles of 40º and 140º at heat input of 80 W

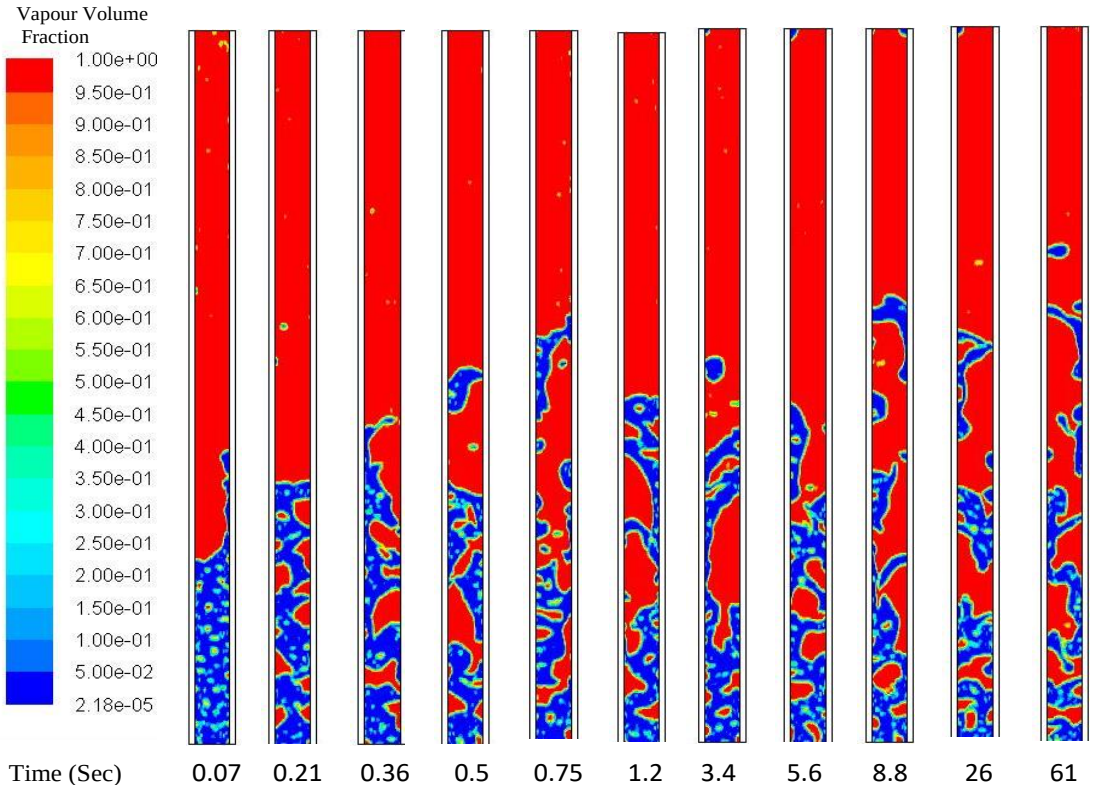

Figure 3.29a Vapor volume fraction for different times and contact angle of 90º at heat input of 160 W

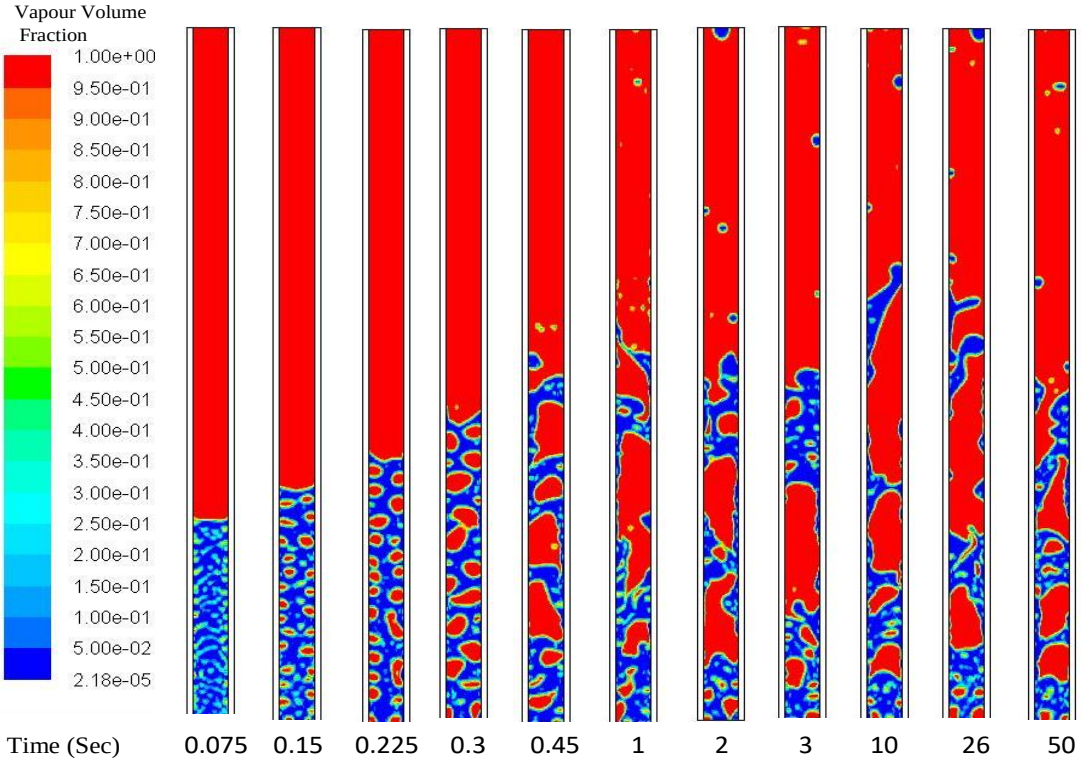

Figure 3.29b Vapor volume fraction for different times and contact angles of 40º and 140º at heat input of 160 W

Figure 3.30a and Figure 3.30b show the condensation and drop shapes in the condenser section for the plain TPCT and the TPCT with a contact angle of 140^o at a heat load of 160 W. It is observed that the model can visualise the shape of drops according to their interaction with different surface characteristics where contact angles are shown as 90^o and 140^o for the plain and the hydrophobic condensers, respectively. It is Also seen that although the hydrophobic condenser (contact angle 140^o) seems to have more liquid content, less contact area between the droplets and the condenser wall (Figure 3.30b) is obtained due to non-wettable features of the surface while the droplets sepread on a wider surface area in the case of the plain surface (as shown in zoomed picture in Figure 3.30a) with contact angle of 90^o.

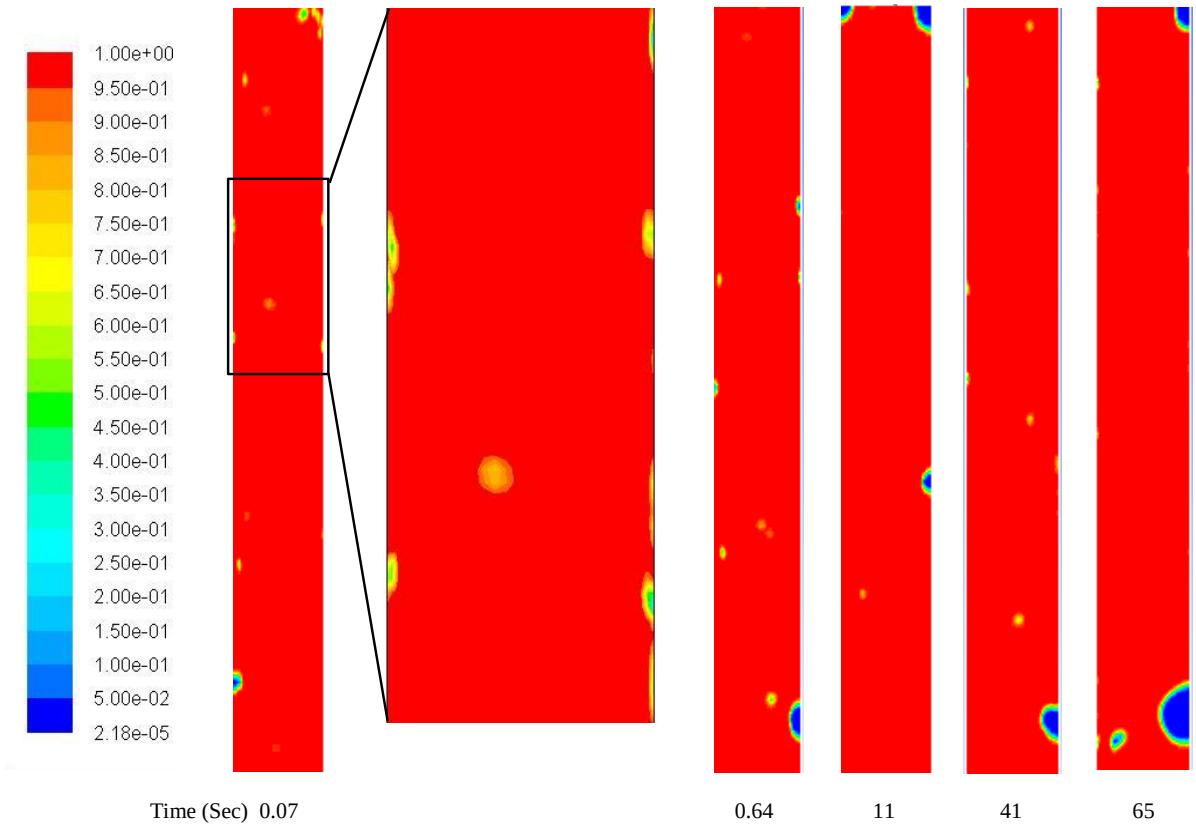

Figure 3.30a Visualisation of drops and condensation in condenser section for contact angle of 90^o and at heat load of 160W

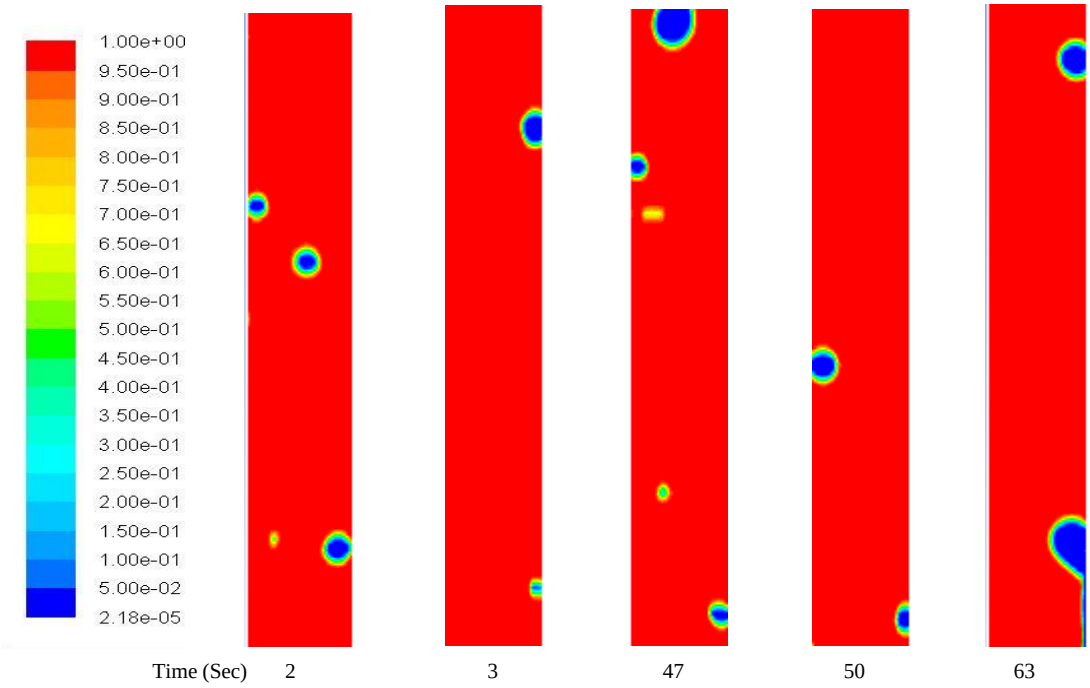

Figure 3.30b Visualisation of drops and condensation in condenser section for contact angle of 140° and at heat load of 160W

3.7.4.4.3 Effect of contact angle on Temperature Distribution

Comparison of the temperature distribution on the TPCT wall between two thermosyphons, one with contact angles of 40° and 140° for the evaporator and condenser sections, respectively, and another TPCT with a contact angle of 90° is illustrated in Figure 3.31 (a, b, c, d and e) at heat inputs of 80, 100, 120, 140 and 160 W, respectively. A noticeable decrease in the evaporator and increase in condenser temperatures of the TPCT with 40° and 140° contact angles are observed for all heat loads compared with the TPCT with 90°. This reduction and increase in temperature of the TPCT result from a wettable surface characteristic for the evaporator and non-wettable surface characteristic of the condenser which are represented by low and high contact angles, respectively. It is also noticed that the difference in the wall temperature of the two TPCTs increases as the heat input increases. However, after the heat input of 120 W, no obvious increase in temperature difference in the evaporator is observed because even though the surface has a high wettability, a vapour film

starts attaching to the surface due to a high heat input. This also can be seen from the visualisation of vapour volume fraction [2].

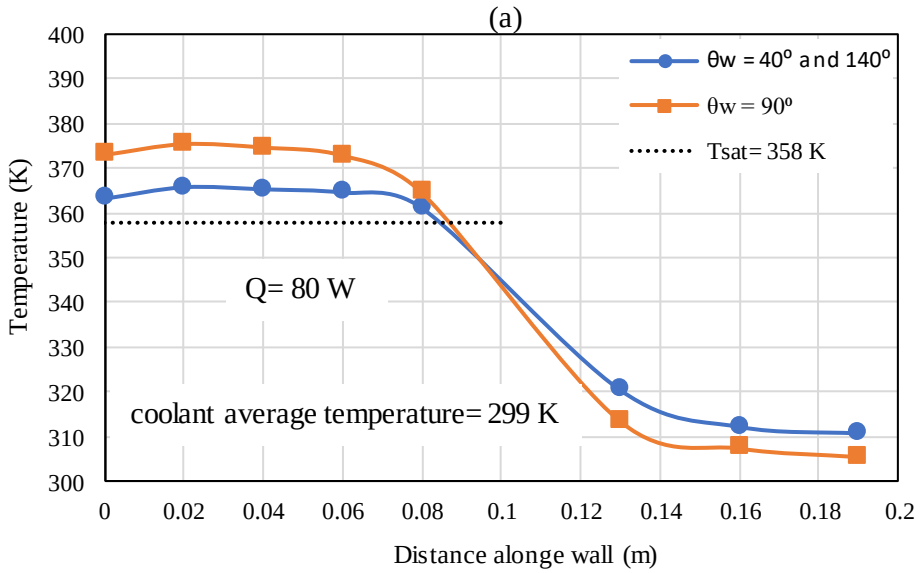

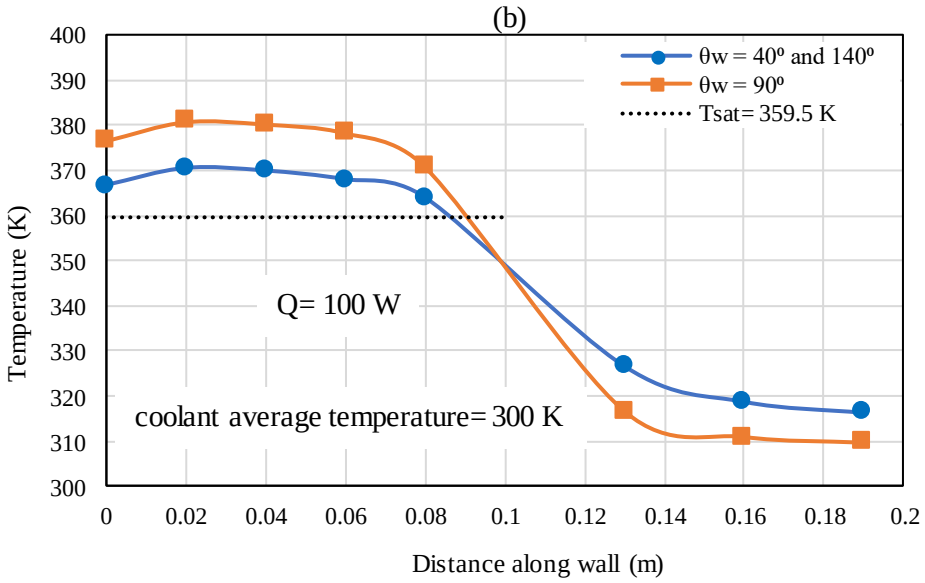

(c)

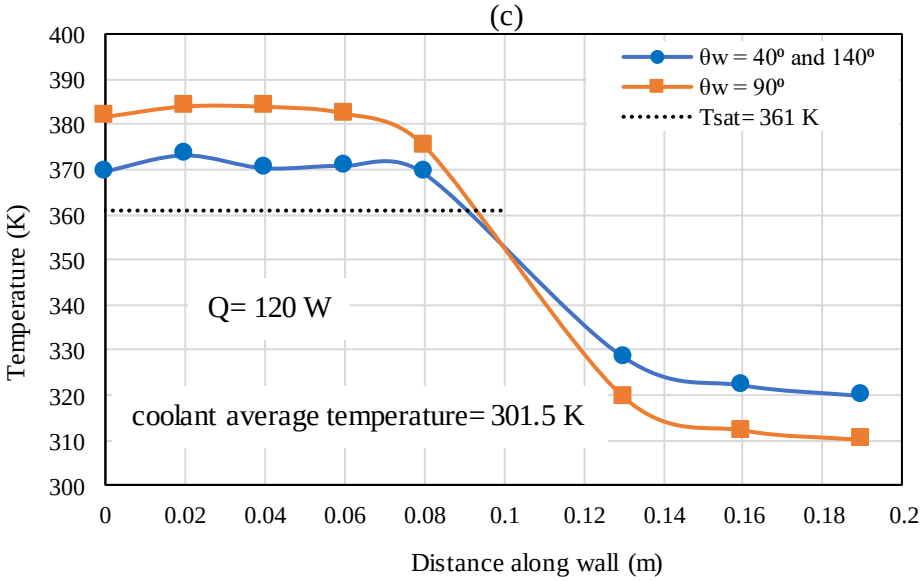
θw = 40º and 140º
θw = 90º
Tsat= 361 K
Q= 120 W
coolant average temperature= 301.5 K
Temperature (K)
Distance along wall (m)
400
390
380
370
360
350
340
330
320
310
300
0
0.02
0.04
0.06
0.08
0.1
0.12
0.14
0.16
0.18
0.2

(d)

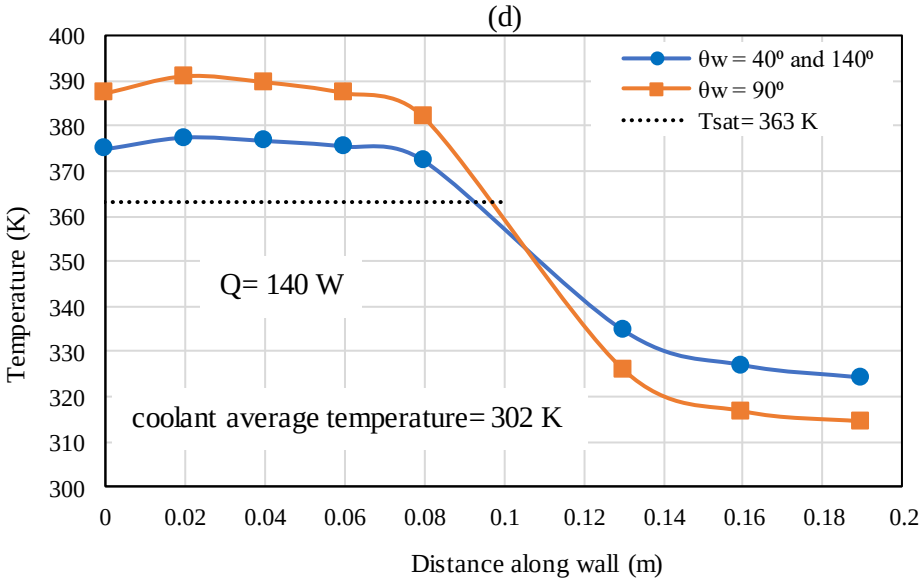
θw = 40º and 140º
θw = 90º
Tsat= 363 K
Q= 140 W
coolant average temperature= 302 K
Temperature (K)
Distance along wall (m)
400
390
380
370
360
350
340
330
320
310
300
0
0.02
0.04
0.06
0.08
0.1
0.12
0.14
0.16
0.18
0.2

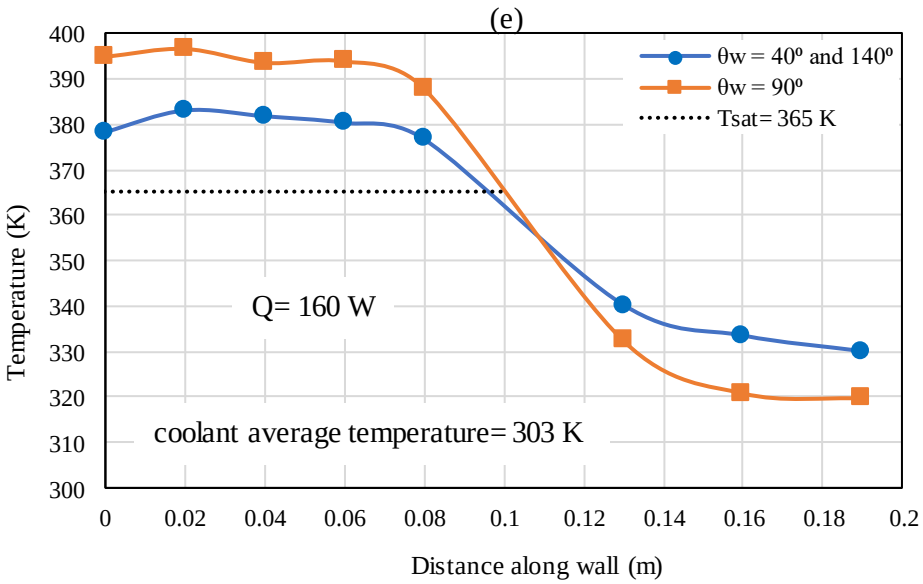

Figure 3.31 Comparison of temperature distribution between two TPCTs at different heat loads

3.7.4.4.4 Effect of Contact Angle on Thermal Performance of TPCT

Figure 3.32 compares the thermal resistance for the two TPCTs with two surface wettability features at different heat inputs. The thermal resistance generally reduces as the heat input increases for the two thermosyphons. In addition, a maximum decrease of about 34% in the thermal resistance of the TPCT with contact angles of 40º and 140º is obtained due to different surface wettabilities in terms of the contact angle. This reduction in the thermal resistance of the TPCT results from lower and higher wall temperatures in the evaporator and condenser, respectively. The higher wall temperature in the condenser section as confirmed by figures 3.31(a-e) results from a larger vapour-condenser wall contact area and quick removal of the condensate liquid due to the non-wettable surface characteristics (hydrophobic). This allow more amount of hot vapour to be in direct contact with the condenser surface (Figure 3.30b) thereby increases the condenser wall temperature and enhances the condenser performance.

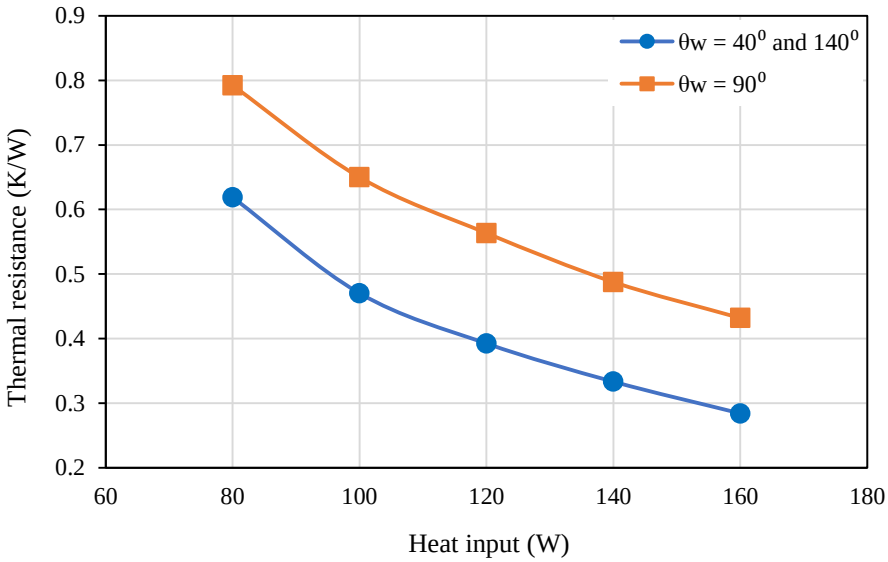

Figure 3.32 Comparison of thermal resistance between two TPCTs at different heat loads

3.8 Summary

Numerical CFD simulation using Fluent software was conducted to investigate the two-phase flow and phase-change process inside a TPCT. The developed model was validated using published work and then used to model the effect of inclination angle and fill ratio in the TPCT at different heat inputs and to visualise the complex phase-change phenomena during the boiling process for different fill ratios and inclinations. In addition, a new CFD model was developed to simulate the condensation process on a plain flat plate and a flat plate with different surface characteristics in terms of contact angle [26]. Then, the optimum contact angle was used in a model to investigate the effect of contact angle on the thermal performance of the TPCT. This model was also employed to visualised different boiling regimes and the shape of drops during the condensation process. The following outcomes were concluded from this chapter:

- Developed CFD simulation was successfully used to model the TPCT and investigate the effect of fill ratio and inclination angle on its thermal performance. This proved by comparing the wall temperature distribution and thermal resistance for three input energies at fill ratio of 65% with published experimental data, and maximum

deviations from experimental of 4.2% and 8.1% have been reported, respectively. Regarding inclination angle, the predicted thermal resistance for inclination angles of 50, 60, 70, 80 and 90^o at heat input 109 W and a fill ratio of 65% was compared with published experimental results and a maximum deviation of 1.3% was obtained.

- The model was also employed for the first time to visualise the complex two-phase process for the inclined TPCT and visualised the pool boiling for different fill ratios. Visualisation of the boiling process proved that the lower thermal performance of the TPCP at a low inclination results from the accumulation of a vapour film on the inner surface of the evaporator due to low inclination from the horizontal orientation.
- Heat transfer limit is reached when the volume of the charged liquid is small at fill charge ratios of 25% and 35%. This is observed when a considerable increase in evaporator wall temperature takes place, especially at higher energy input.
- The lowest evaporator average wall temperature and thermal resistance are achieved at a fill ratio of 65% and an angle of 90^o whereas the highest at 25% and 10^o due to the effect of small fill ratio and inclination, respectively. This effect is higher as heat input increases.
- The best fill ratio and inclination angle regarding the thermal performance for this case were found to be 65% and 90^o, respectively.
- In terms of the effect of contact angle, the VOF multiphase model in Fluent was successfully utilised to simulate the vapour condensation process on different surface features in terms of contact angle [26]. This model was also applied on the TPCT to simulate the effect of contact angle on the performance of the TPCT and visualise the phase change process during evaporation and condensation process.
- For the flat plate model, a good agreement was achieved between CFD results and the published experimental data with a maximum deviation of 5% for simulation of

vapour condensation process and 9.9% for the effect of contact angle. On the other hand, for the TPCT model, maximum deviations of 1.9% and 6.6% in the temperature distribution and thermal resistance were found, respectively.

- It is found for the flat plate model that a contact angle of 140^{o} exhibits the highest condensation thermal performance. Therefore, this contact angle was employed in the model of the TPCT to investigate the enhancement in its thermal performance.
- The TPCT model has successfully visualised different boiling regimes, convection, bubbly and slug regimes in both TPCTs of contact angles 90^{o} and 40^{o}. It is shown that a vapour film forms on the heated surface in the case of TPCT with contact angle of 90^{o}, while vapour bubbles detach away from the heated surface of the TPCT with a contact angle of 40^{o} which leads to enhancing the heat transfer performance. The model also has a capability to visualise different drop shapes for contact angles 90^{o} and 140^{o} in the condenser.
- A reduction in thermal resistance of 34% was obtained due to the use of a TPCT with a low and high contact angles of (40^{o}) and (140^{o}) in the evaporator and condenser, respectively, compared to the plain TPCT (contact angle 90^{o}).

Chapter 4

4. Experimental Study of geyser Boiling Phenomena Inside a TPCT

4.1 Introduction

Boiling is a phase change phenomenon which plays an important role in affecting the thermal performance of heat pipes. As has been reported in the literature review, even though numerous experimental investigations have been carried out to test the effect of various parameters affecting the thermal performance of the wickless heat pipe, challenges related to the two-phase phenomena still need to be investigated [25], [8].

Geyser boiling is a complex phenomenon which may occur in heat pipes causing high temperature and pressure oscillation leading to noticeable vibration. Geyser phenomenon occurs when a vapour gathering at the lower part of the evaporator inside the thermosiphon forming a large bubble size occupying the whole inside diameter. This bubble collapses causing liquid at the evaporator pushing severely up to the condenser section and may result in vibration of the TPCT [112]. Thus, heat pipes' thermal performance can be greatly affected by the occurrence of geyser boiling. Therefore, understanding of such a process is essential to improve heat pipes thermal performance [8], [2].

This chapter is divided into two main sections in terms of experimental results. Section 1 aims to provide a deep understanding and explanation of the characteristics of the geyser phenomenon, thereby the temperature oscillation behaviour in the TPCT under influence of various parameters which are important in optimizing the TPCT [8]. Consequently, the aim of section 2 is to investigate comprehensively the effect of the occurrence of geyser boiling on the thermal performance of the TPCT in terms of the temperature distribution and thermal resistance. This is carried out by testing the thermal characteristics of the TPCT before and after the occurrence of the geyser boiling phenomenon at different parameters [2].

4.2 Description of Experimental Apparatus

4.2.1 Experiment setup

A test rig was developed to study the transient and stable behaviour of wickless heat pipes. The characteristics of the geyser boiling under the effect of various parameters such as inclination and fill ratio at different operating conditions were investigated. In addition, the effect of the occurrence of the geyser boiling on the thermal performance of the TPCT at all tested parameters was also examined. A schematic diagram of the experimental system is illustrated in Figure 4.1 [8].

Three standard copper tubes with three different amounts of water as a working fluid were employed to represent three wickless heat pipes with fill ratios 25%, 65% and 100% of the evaporator volume as shown in Figure 4.2 [8]. The three thermosyphon heat pipes were evacuated to about 5×10^{-2} Torr (6.65 pa) to eliminate any non-condensable gases, charged with a certain amount of working fluid and sealed (S&P Coil Products Ltd, Leicester). Each TPCT has dimensions of 400 mm height, 22 mm diameter and a thickness of 0.9 mm. The TPCT consists of two parts: the lower part is the evaporator and the upper is the condenser with 200 mm length each. In addition, a copper tube with a diameter of 28 mm and 200 mm height is employed as a water jacket to eliminate heat from the condenser side [2].

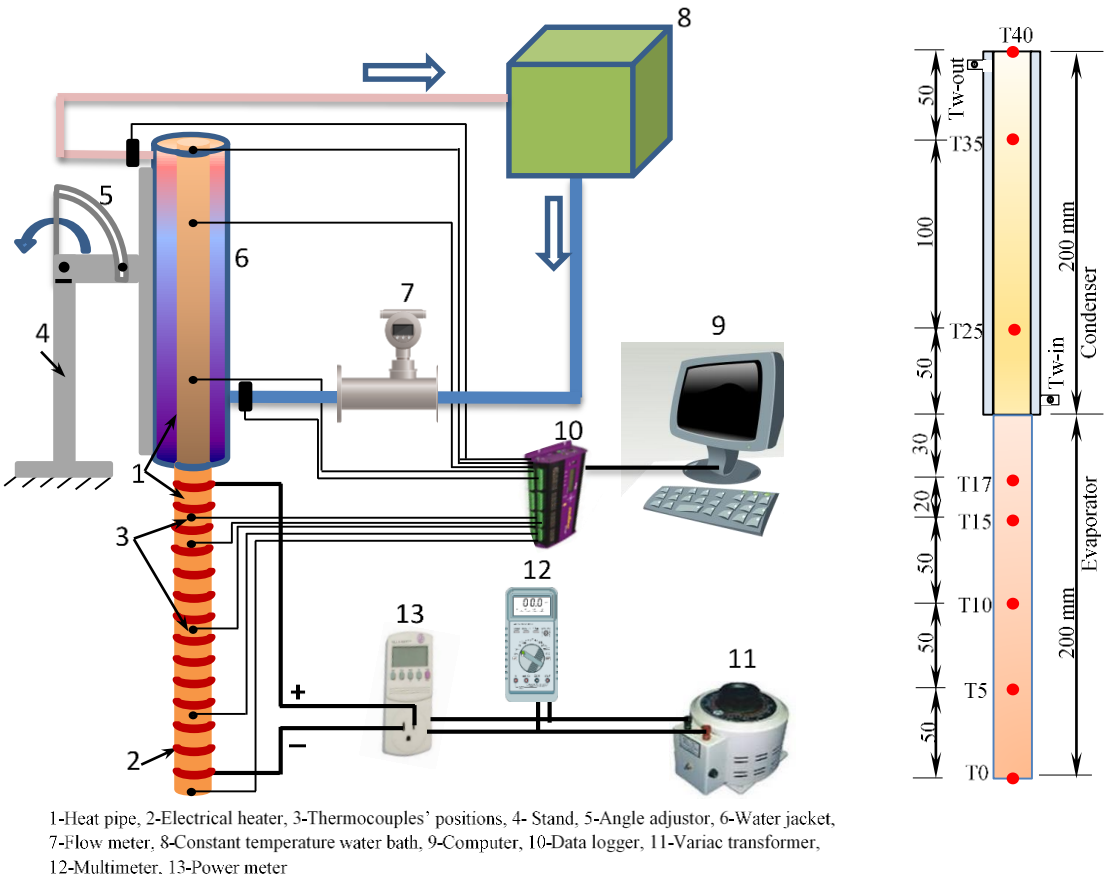

1-Heat pipe, 2-Electrical heater, 3-Thermocouples' positions, 4- Stand, 5-Angle adjustor, 6-Water jacket, 7-Flow meter, 8-Constant temperature water bath, 9-Computer, 10-Data logger, 11-Variac transformer, 12-Multimeter, 13-Power meter

Figure 4.1: (a)- graphic illustration of experimental system and (b)- Thermocouples' positions and dimensions of TPCT [8]

Furthermore, Ten T-type thermocouples were employed to monitor the temperature at various positions from which eight were surface thermocouples fixed on the surface of the heat pipe, five on the evaporator side and three on the condenser side, and the other two were probe thermocouples put in the outlet and inlet coolant flow to measure the inlet and the outlet coolant temperature at the condenser side. The dimensions of the thermosiphon heat pipe and thermocouple positions are shown in Figure 4.1.b [8].

Figure 4.2 Three TPCT with three different fill ratios

An electrical heater of 400 W wrapped around the outer surface of the evaporator was used as a heat source, Figure 4.3. Different values of heat input were applied to the evaporator section by changing the input voltage using a variable transformer and were measured using a multimeter and a wattmeter. This can be achieved by adjusting the transformer to a specified voltage which corresponds to the required heat input [2].

Figure 4.3 heat pipe with AC rope heater

To reduce the heat losses from the thermosiphon, 50 mm of high-temperature superwool blanket insulation was employed. The thermosyphon was fixed on a movable stand to adjust the inclination to the desired angle from the horizontal to vertical orientation. In addition, to measure the mass flow rate of the cooling water at the condenser section, a rotameter was used. The flow rate was controlled at the desired value using a valve just at the entrance of the flow meter. Also, a constant temperature water bath (CU-700) produced by the Betta-Tech company (see Figure 4.4) was utilised to maintain the inlet temperature of the cooling water at the required temperature to ensure that the same value is used for every run. The thermocouples were connected to a data logger to transfer their readings to a computer to be stored and analysed. A photograph of the test rig is shown in Figure 4.5 [2].

Figure 4.4 Constant temperature water bath

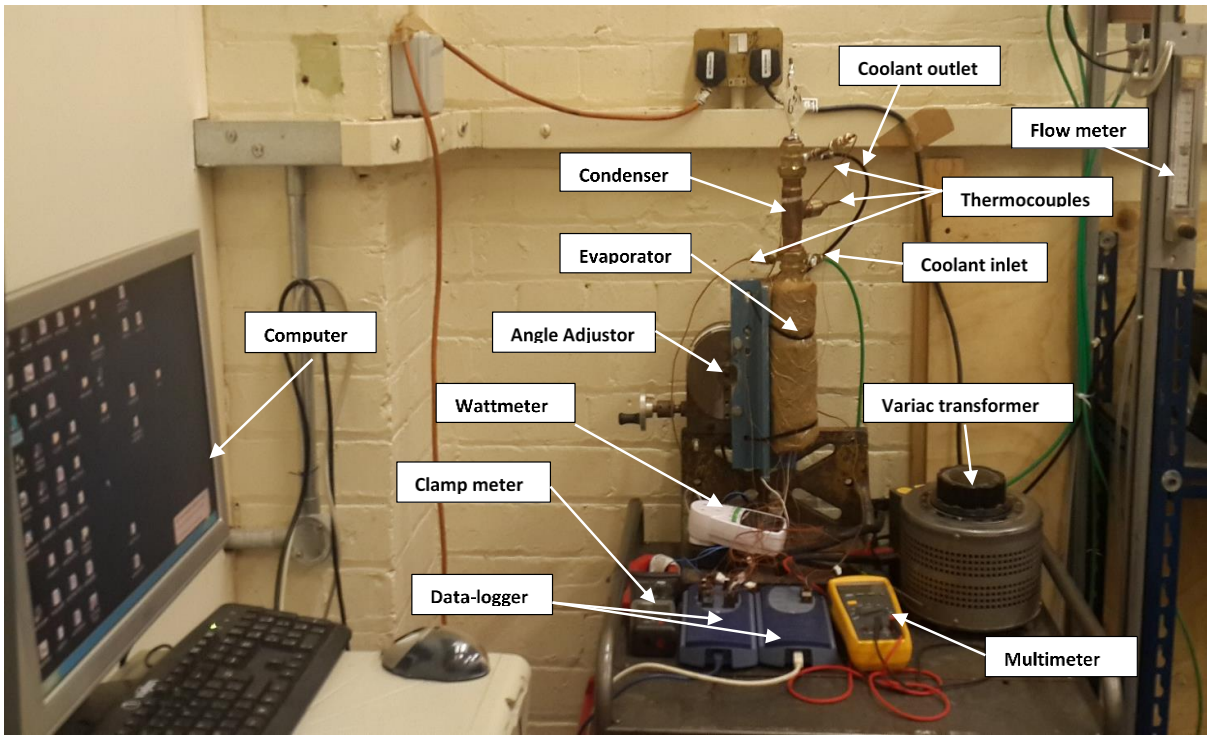

Figure 4.5 A picture of the test rig

4.2.2 Instrumentation

A number of measuring devices were used to measure temperature, flow rate and heat input to allow investigating the thermal behaviour and performance of the TPCT.

4.2.2.1 Thermocouples

To measure the surface temperature at different locations of the TPCT's wall, surface thermocouples of T-type were employed. Omega Engineering Ltd T-type thermocouples with a specification code of 5TC-TT-TI-30-1M were used in this work. This means a T-type thermocouple with PFA (Perfluoroalkoxy) insulation, 0.25 mm sheath diameter and one meter length of the extension wire. A thermal tape was used to fix the surface thermocouples on the outer surface of the TPCT as shown in Figure 4.6. On the other hand, the cooling water inlet and outlet temperatures were measured using probe thermocouples at the water jacket of the condenser section. T-type probe thermocouples with a code number of TJC1–CPSS–M050G-100 from Omega Engineering Ltd were selected. This code denotes T-type with one meter extension wire, stainless steel probe sheath material with 0.5 mm diameter and 100 mm length grounded junction type. These probes were inserted in the pipe to reach the centre of the pipe.

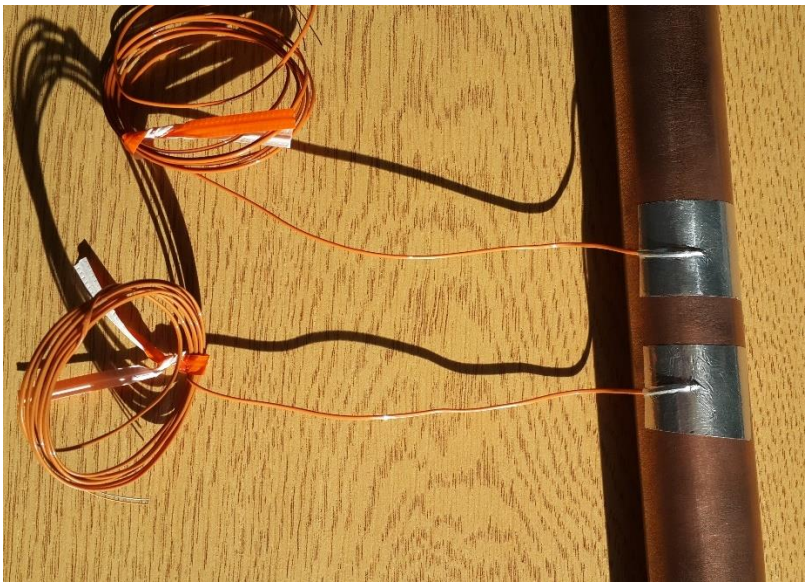

Figure 4.6 Fixing surface thermocouples on the TPCT wall

4.2.2.2 Flow Meter

CT Platon type water rotameter was used to measure the mass flow rate of the cooling water entering the water jacket at the condenser side. This flow meter has a measuring range of 0-800 cm^3/min (0-0.8 L/min) which is suitable for absorbing the heat from such size of a TPCT. It has a valve at its bottom to control the amount of the coolant when different coolant mass flow rates need to be investigated as shown in Figure 4.7 .

Figure 4.7 Platon water flow meter

4.2.2.3 Power Supply

The input power to the rope AC heater was regulated employing a variable transformer as shown in Figure 4.5. The maximum energy output of the AC heater is 400 W where heat from 0 to 400 W can be obtained by adjusting the transformer voltage from 0 to 240 V. Any power input can be selected by adjusting the variable transformer to change the output voltage and current and using these two values to obtain the heat input applied on the evaporator wall.

Also, the amount of any required heat input can be read directly from the reading of a digital power meter.

4.2.2.4 Data Logging

For interpreting thermocouples signals to temperature readings, a pico-logger type TC-08 was used. This temperature logger is connected to a personal computer where temperature readings is presented. Each logger contains eight channels, so two pico-loggers were used in this work to connect all the ten thermocouples as shown in Figure 4.5. On the other hand, readings of the flow rate, voltage and current were read and recorded manually for each run.

4.2.3 Calibration of Measuring Devices

Standard methods were used to calibrate and evaluate the measurement uncertainties of different measuring devices before being inserted in the test rig to obtain accurate results. To test the accuracy of the thermocouples, all thermocouples used in the experiment were put in a constant water temperature bath to compare their readings to a Resistance Temperature Detector (RTD) reading. The RTD type was used due to its high accuracy of 0.03^{o}C according to the manufaturer's data. The same accuracy was also reperted by [77] who did a calibration for the RTD. The calibration temperature range starts from the ambient temperature (about 18^{o}C) and gradually increased to reach the boiling temperature. At every desired temperature, the thermocouples were left to reach the steady state and the resulting temperature readings were sent to the pico-loggers and recorded in the computer. Figure 4.8 shows readings of one surface thermocouple (at the bottom of the evaporator, T0) versus the RTD readings and presents the obtained R-squared value and fitting equation [8].

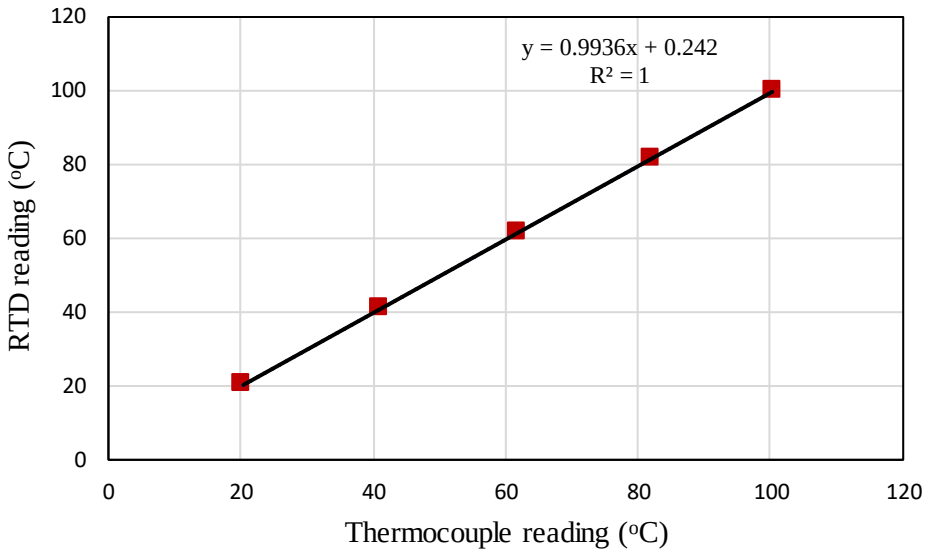

Figure 4.8 A surface thermocouple calibration curve

To calibrate the flow meter, a graduated cylinder was used to collect the amount of water from the rotameter for a time of one minute. This was achieved by adjusting the float of the flow meter to a certain value of flow rate and collect the flowing water in the cylinder for one minute and recording the two values. This was carried out eight times for a flow rate ranging from 100 to 800 cm^3/min with an increment of 100 cm^3/min. The flow meter readings against the collected volume per one minute were shown in Figure 4.9.

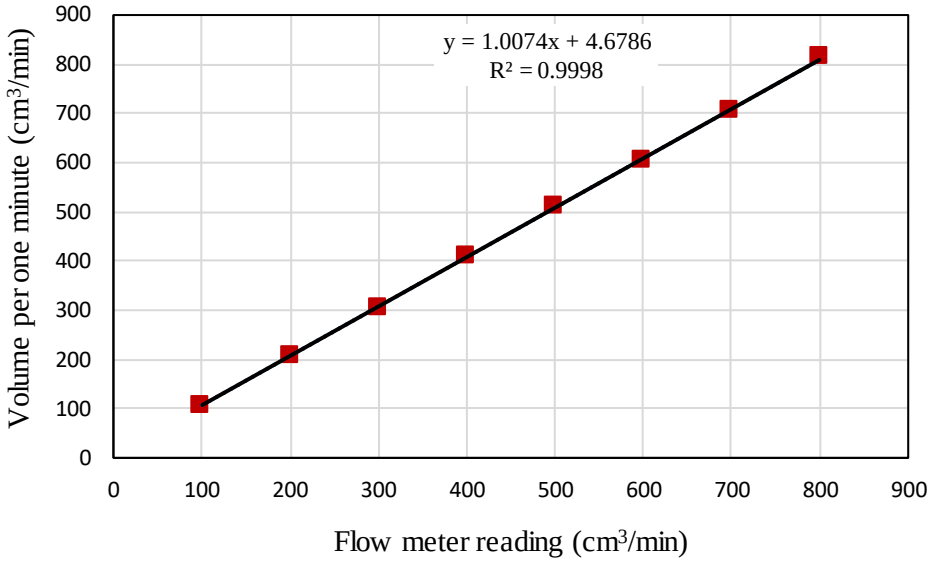

Figure 4.9 Flow meter calibration curve

4.2.4 Experimental Procedure

After the test rig was set up, it was ready to start the test. Firstly, the constant water bath was set to a specified inlet cooling water temperature. Then, the flow meter valve was opened to set the water flow rate to a certain value and allow the cooling water to circulate through the condenser water jacket. The temperature readings of the inlet and outlet temperature were monitored until they reached approximately the adjusted inlet temperature from the water bath and all other temperature readings were close to this temperature, to ensure that all thermocouple readings are at the same temperature. The tilt angle of the TPCT was adjusted to the desired angle. After that, the variable transformer was set to a certain voltage which corresponds to the required heat load and the transformer is switched on to apply the heat on the evaporator surface. Then, all temperature readings were monitored until they reached the steady state, then saved. At this time, the transformer was switched off to prepare for the next run [2].

The measured quantities are the heat input, cooling water flow rate and inlet and outlet cooling water temperatures, as well as the wall temperatures in the evaporator and condenser parts. All temperature readings were recorded every one second [8].

4.2.4.1 Measurement Uncertainty

Engineering tests can involve some errors resulting from test facilities and human. These errors are classified into two main types, systematic and random. Unlike the systematic error, the random error varies from one run to another. Therefore, the measuring device error can be corrected using a proper calibration, whereas uncertainty analysis can eliminate the human's error [77].

Root Sum Squared (RSS) method is used to evaluate the overall uncertainty encountered in different measurements [77], [177]:

$$U_{ov} = \pm\sqrt{U_{sys}^2 + U_{rand}^2} \quad 4.1$$

where U_{ov} is the overall uncertainty and U_{sys} and U_{rand} are systematic and random uncertainties. Systematic errors comprise data acquisition, calibration and hysteresis errors and can be expressed as follow:

$$U_{sys} = \sqrt{\sum_{j=1}^{L} U_{j,sys}^2} \quad 4.2$$

where j is the number of systematic uncertainty which can be obtained from manufacturer's information or calibration test.

To evaluate the random uncertainty which is a statistical error, the following equation is used [77]:

$$U_{rand} = t_{n-1,95\%} S_{\bar{x}} \quad 4.3$$

where $t_{n-1,95\%}$ is the Student's t-distribution which depends on the number of data samples (n). $S_{\bar{x}}$ is standard error of the mean and expressed as:

$$S_{\bar{x}} = \frac{1}{\sqrt{n}} \sqrt{\sum_{i=1}^{n} \frac{\left(X_i - \bar{X}\right)}{n-1}} \quad 4.4$$

4.2.4.1.1 Uncertainty in Temperature Measurement

Calibration of surface and probe thermocouples used to measure the temperature in this work showed a small deviation from the RTD reading for all surface and probe thermocouples. The overall uncertainty in temperature measurement is a combination of uncertainty in RTD reading, data logger and the thermocouple. According to manufacturer's data, the uncertainty in RTD and data logger readings are 0.03 and 0.025^{o}C, respectively. These values are negligible compared to the thermocouple uncertainty (obtained from curve fitting). Thus, the overall uncertainty in probe and surface thermocouples readings are 0.4^{o}C and 0.24^{o}C, respectively. Detailed calculations of the overall uncertainty in a thermocouple reading is reported in the appendix A.

4.2.4.1.2 Uncertainty in Flow Rate Measurement

Uncertainties of ±2.88 cm^3/min and ±2.635 cm^3/min were obtained for curve fitting and volume collection methods, respectively. Therefore, an overall uncertainty of 3.9 cm^3/min in the flow meter reading is produced from the squared sum of these two uncertainties. The flow rate uncertainty detailed calculations are presented in the appendix A.

4.2.4.1.3 Uncertainty in Heat Input Measurement

The uncertainty in the heat input U_Q is determined based on the uncertainties of the voltage (±0.1 V) and the current (±0.01A) using eq. 4-2 in terms of voltage and current as in the following equation [8]:

$$U_Q = \pm Q\sqrt{\left(\frac{\Delta V}{V}\right)^2 + \left(\frac{\Delta I}{I}\right)^2} \qquad 4.5$$

where, U_Q is the uncertainty in the heat input, Q is the heat input, V and I are the circuit voltage and current and ΔV and ΔI are the uncertainty in the voltage and current, respectively. The resulting uncertainty for each heat input are listed in Table 4.1, where the maximum uncertainty is 2.3% at the lowest heat input of 20 W [8].

Table 4.1: Heat input uncertainty

Q	V	I	U_Q	U_Q
W	V	A	W	%
20	45.7	0.4375	±0.46	±2.30
30	55.92	0.536	±0.56	±1.87
40	64.5	0.62	±0.65	±1.62
50	72	0.695	±0.72	±1.44
60	78.8	0.7625	±0.79	±1.32
70	85.2	0.8225	±0.86	±1.22
80	91	0.88	±0.91	±1.14

90	96.6	0.935	±0.97	±1.07
100	101.5	0.985	±1.02	±1.02
200	144	1.4	±1.45	±0.72
300	175.7	1.7075	±1.77	±0.59
400	202.7	1.975	±2.03	±0.51

4.3 Experimental Results

This section has been published in [8].

4.3.1 Validity of Experimental results

Casarosa and Latrofa [121] proposed a correlation to predict the heat transfer coefficient for the geyser phenomena in the circular TPCT. They tested a wide range of heat fluxes and vapour pressures in the range of the occurrence of the geyser boiling and linked the heat transfer coefficient to the heat flux and vapour pressure using the following eqution:

$$h = 2.925\, p_v^{0.18} q^{2/3} \quad (4.6)$$

where h is the heat transfer coefficient during the geyser boiling, p_v is the vapour pressure inside the TPCT and q is the heat flux at the evaporator.

For experimental work, h can be calculated as a mean heat transfer cofficient of the TPCT [112] using the following equation:

$$h = \frac{Q}{A_i(T_{e,av} - T_{c.av})} \quad (4.7)$$

where Q is the heat load, A_i is the evaporator internal surface area and $T_{e,av}$ and $T_{c,av}$ denote evaporator and condenser average wall temperatures, respectively.

To validate the experimental results obtained during the occurrence of the geysering in the TPCT, a comparison between the pridicted h (Eq. 4.6) and h obtained from the experimental

results using Eq. 4.7 is presented in Figure 4.10 for a fill ratio of 100% and vertical orientation. The comparison shows a good agreement within 20% bound and most point within 12% where the correlation overpredicts the measured data in most points.

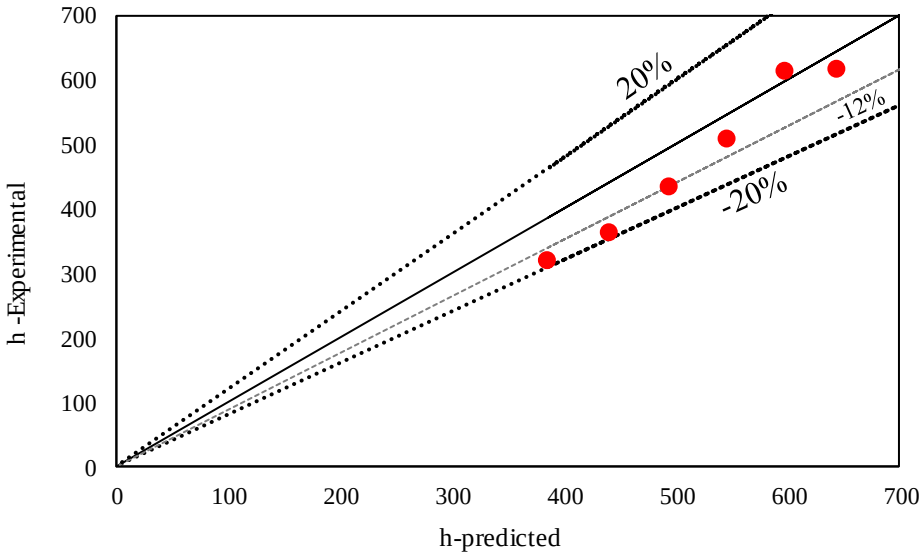

Figure 4.10 Predicted and measured *h* comparison during geyser boiling in TPCT

4.3.1 Effect of different parameters on geyser boiling characteristics inside the TPCT

Effect of the combination of different fill ratios and inclination angles at different input energies, mass flow rates and inlet temperatures of cooling water on the geyser boiling phenomenon inside the TPCT was tested experimentally. Table 4.2 illustrates the tested parameters [8].

Table 4.2: Factors investigated in present work [8]

Item	Values
Heat input (W)	20, 30, 40, 50, 60, 70, 80, 90, 100, 200, 300, 400.
Inclination angle (^{o})	10, 30, 60, 90.
Fill ratio (%)	25, 65, 100.
Coolant flow rate (kg/s)	0.0025, 0.00667, 0.01333 (0.00667 and 0.0133 only at 200 W).
Coolant inlet temperature (^{o}C)	15, 20, 25 (15 and 25 only at 200 W).

Effect of three fill ratios and four inclinations were studied at each heat input listed in Table 4.2 and only at coolant mass flow rate of 0.0025 kg/s and inlet temperature of 20^{o}C, whereas

the effect of mass flow rate and the inlet temperature of the cooling water were investigated for all fill ratios and inclination angles, but only at a heat input of 200W. In this work, values of thermocouples at the evaporator section are represented from the bottom of the evaporator by T0, T5, T10, T15, and T17 and at the condenser section by T25, T35, and T40, while the inlet and outlet cooling water temperatures are represented by Tw-in and Tw-out, respectively as demonstrated in Figure 4.1.b [8].

4.3.1.1 Effect of Heat Inputs at different inclinations and fill ratios

It is important to present the variation of the temperature with time to show the change in the temperature oscillation and the first occurrence of the geyser boiling for every single fill ratio, inclination and heat load. However, this may be difficult to achieve due to a large number of figures. Therefore, for the variation of temperature with time, only results at angles of 90^o and 10^o will be presented in this work, while results at angles 30^o and 60^o will be reported in the Appendix B. However, results at all inclinations (90, 60, 30 and 10^o) will be discussed [8].

Figure 4.11-(1-3) show the variation of the surface temperature along the wall of TPCT with time at three different fill ratios and an angle of 90^o for a range of heat input, 20^oC coolant inlet temperature and 0.0025 kg/s cooling water flow rate. It is observed that no geyser boiling occurs at the heat input of 20 W (Figure 4.11-1a) for the three fill ratios. It is also seen that the temperatures of T10, T15, T17 for the fill ratio 25% and T15 and T17 for the fill ratio 65% exhibit the highest temperature readings at the beginning due to their location outside the liquid pool, then decreased considerably to become the lowest when the condensate starts dropping down from the condenser. On the other hand, T10 for the fill ratio 65% and T10, T15 and T17 for 100% fill ratio increase normally with time to reach the steady state because they are covered with the liquid pool in the evaporator due to a higher amount of working fluid corresponding to a higher fill ratio compared with 25%. At a heat input of 30 W and for a fill ratio of 100%, the geyser boiling occurs, but it did not happen for fill ratios 25% and

65% at the same heat input. After that, the geyser phenomenon occurred at heat inputs 60 and 70 W (Figure 4.11-2a and b) for fill ratios 65% and 25%, respectively. This can be explained by the fact that at a small fill ratio, the amount of vapour which evaporates from the liquid is higher compared to that at a large fill ratio for the same heat input. This leads to a higher pressure inside the TPCT delaying the occurrence of the geyser boiling until reaching a higher superheat condition at a higher heat input to overcome the effect of the pressure. In addition, it is observed that the time at which the geyser boiling firstly occurring decreases as the heat input increases for the three fill ratios. Figure 4.11-(1-3) also show that unlike other temperature readings in the evaporator, the value of T17 for fill ratios 25% and 65% rises at the moment of the geysering occurrence due to its position which is outside the liquid pool and near the cold condenser section. Therefore, it is relatively at a lower temperature compared with the hot liquid mass pushed from the evaporator due to the geyser effect. However, this behaviour of T17 does not happen in the case of the fill ratio 100% in which all temperature readings in the evaporator drop at the occurrence of the geyser boiling due to their positions within the liquid pool. This behaviour of T17 changes to drop instead of rising at heat inputs of 200, 300 and 400 W due to high input energy. Also, alike T17, all temperature readings in the condenser section sharply rise at the geyser effect occurrence for all fill ratios and all heat inputs. Furthermore, Figure 4.11-3 shows that the geyser boiling tends to disappear at high heat inputs (200, 300 and 400 W) for the three fill ratios [8].

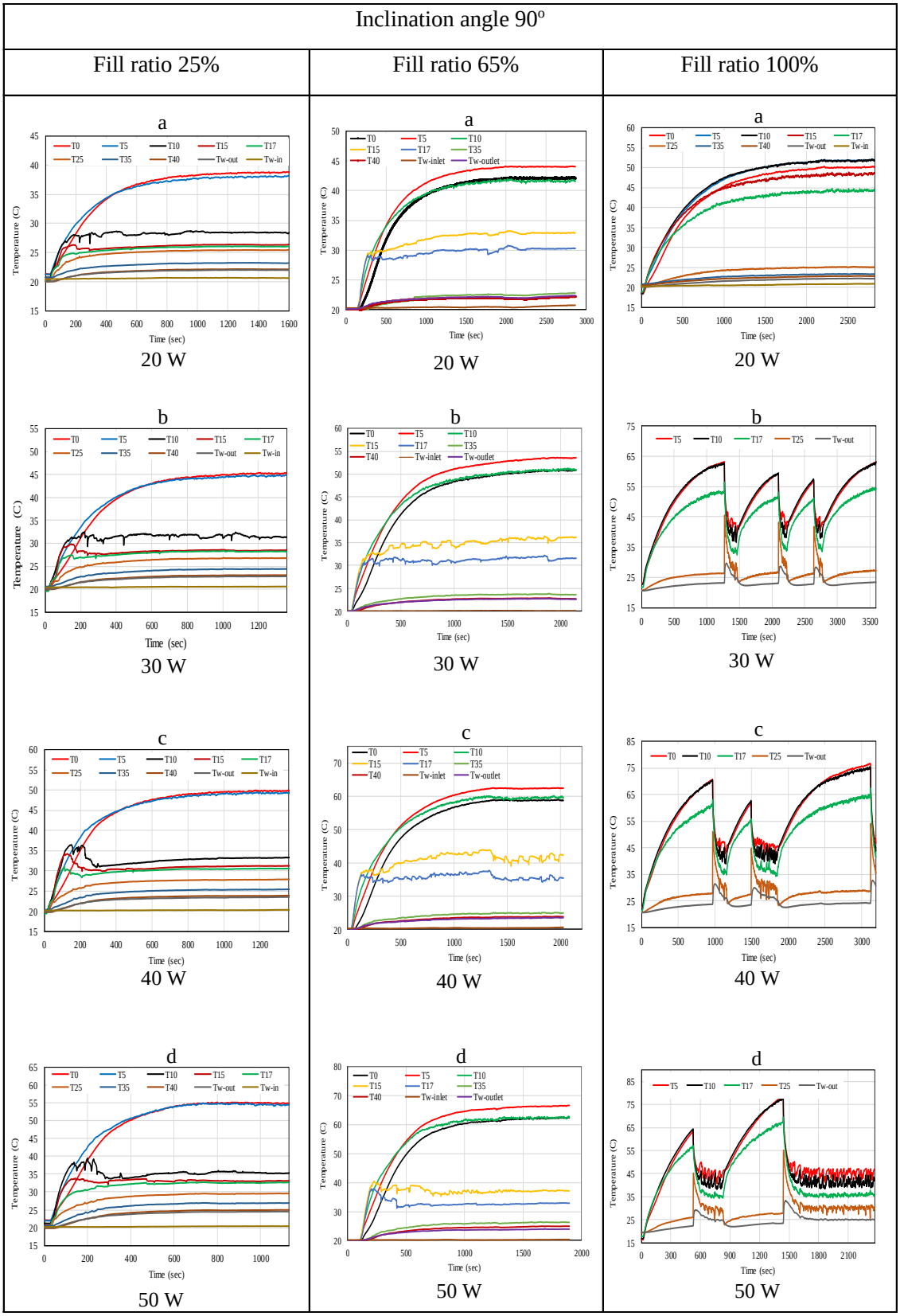

Figure 4.11-1 Time dependent wall temperature at angle of 90° and three liquid charges at heat loads (20, 30, 40 and 50W), (20°C , 0.0025 kg/s) [8].

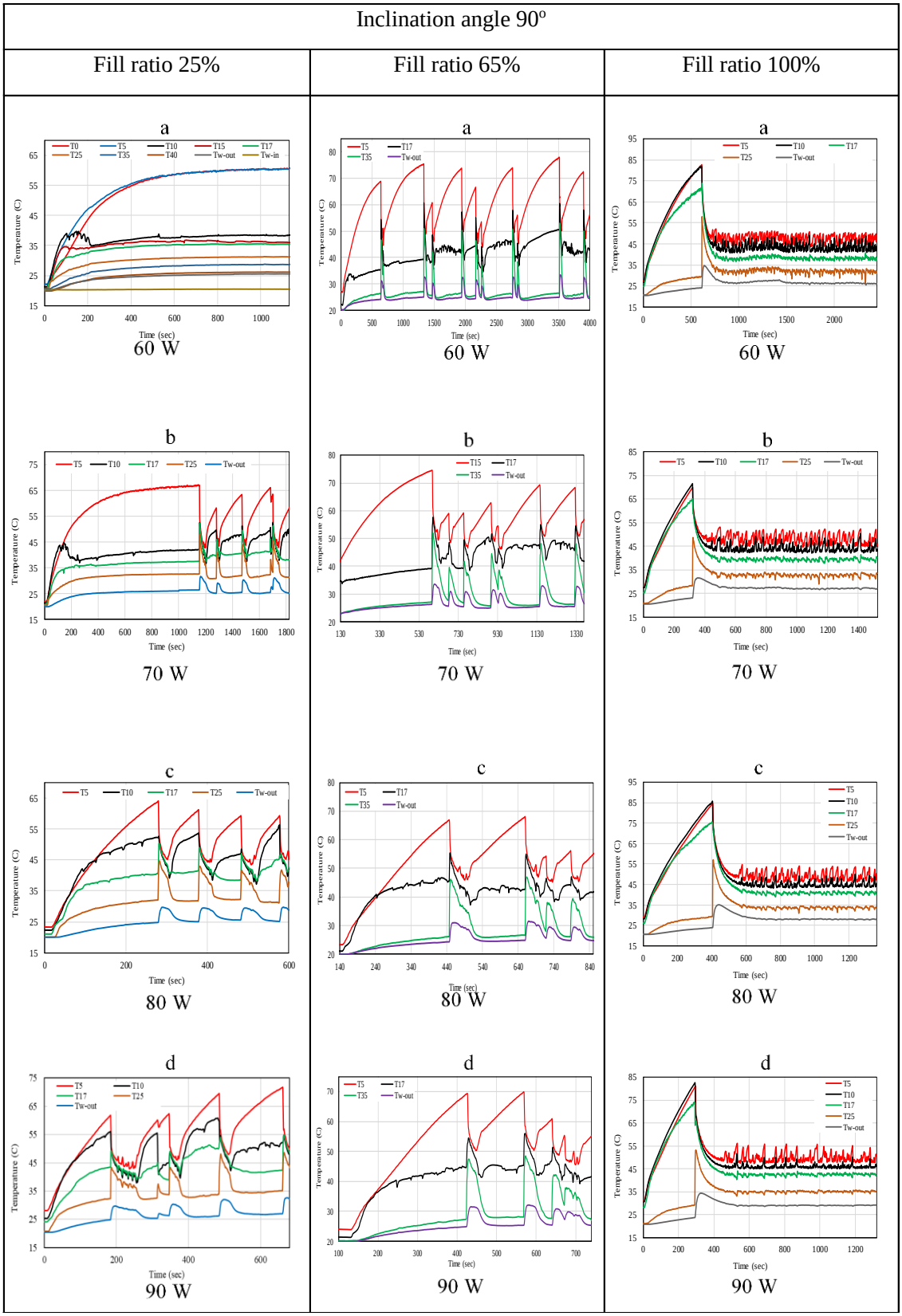

Figure 4.11-2 Time dependent wall temperature at angle of 90° and three liquid charges at heat loads (60, 70, 80 and 90 W), (20°C, 0.0025 kg/s) [8].

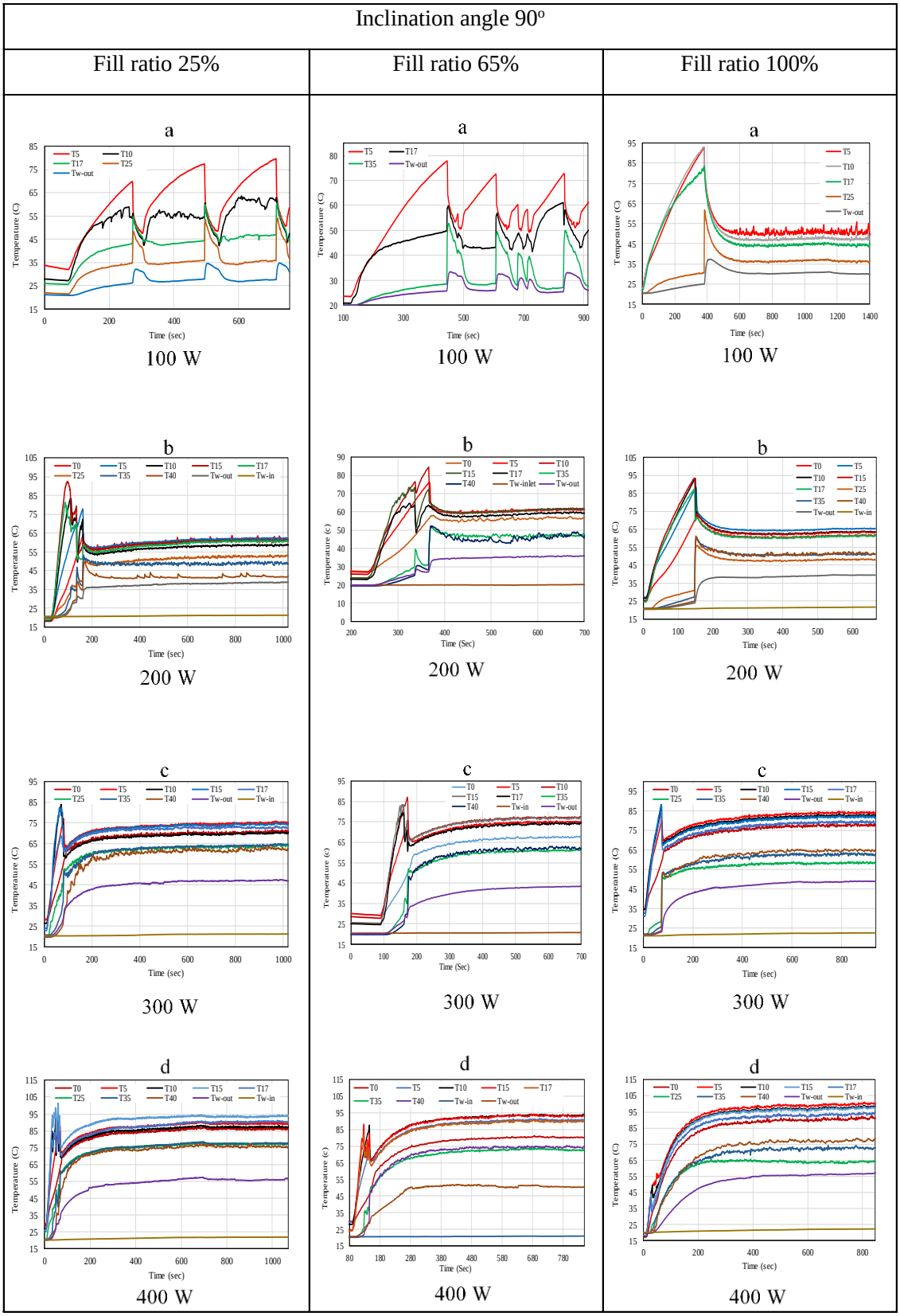

Figure 4.11-3 Time dependent wall temperature at angle of 90º and three liquid charges at heat loads (100, 200, 300 and 400 W), (20ºC, 0.0025 kg/s) [8].

At an angle of 60^{o} (Figure 4.12-(1-3)) , it is observed that the geyser boiling does not happen at heat inputs of 20 and 30 W for the three fill ratios. Then, the geyser effect starts to occur at a heat input of 40 W for the fill ratio 100%, whereas for fill ratios 25% and 65%, it occurs at a heat input of 50 W. It is also seen that the starting time of the geyser effect varies as the heat input and fill ratio change at the same inclination angle. For example, at a heat input of 50 W, the geyser boiling starts at about 1600, 650 and 1000 seconds for fill ratios 25%, 65% and 100%, respectively, while at a heat input of 60 W, it starts at about 470, 840, 770 seconds for the three fill ratios, respectively. In addition, the oscillation in the temperature occurs continuously and severely at input energies 60, 70, 80, 90 and 100 W for all fill ratios and it decreases as the heat input increases. Similar to the case of angle 90^{o}, the geyser effect almost disappears at heat inputs of 200, 300 and 400 W [8].

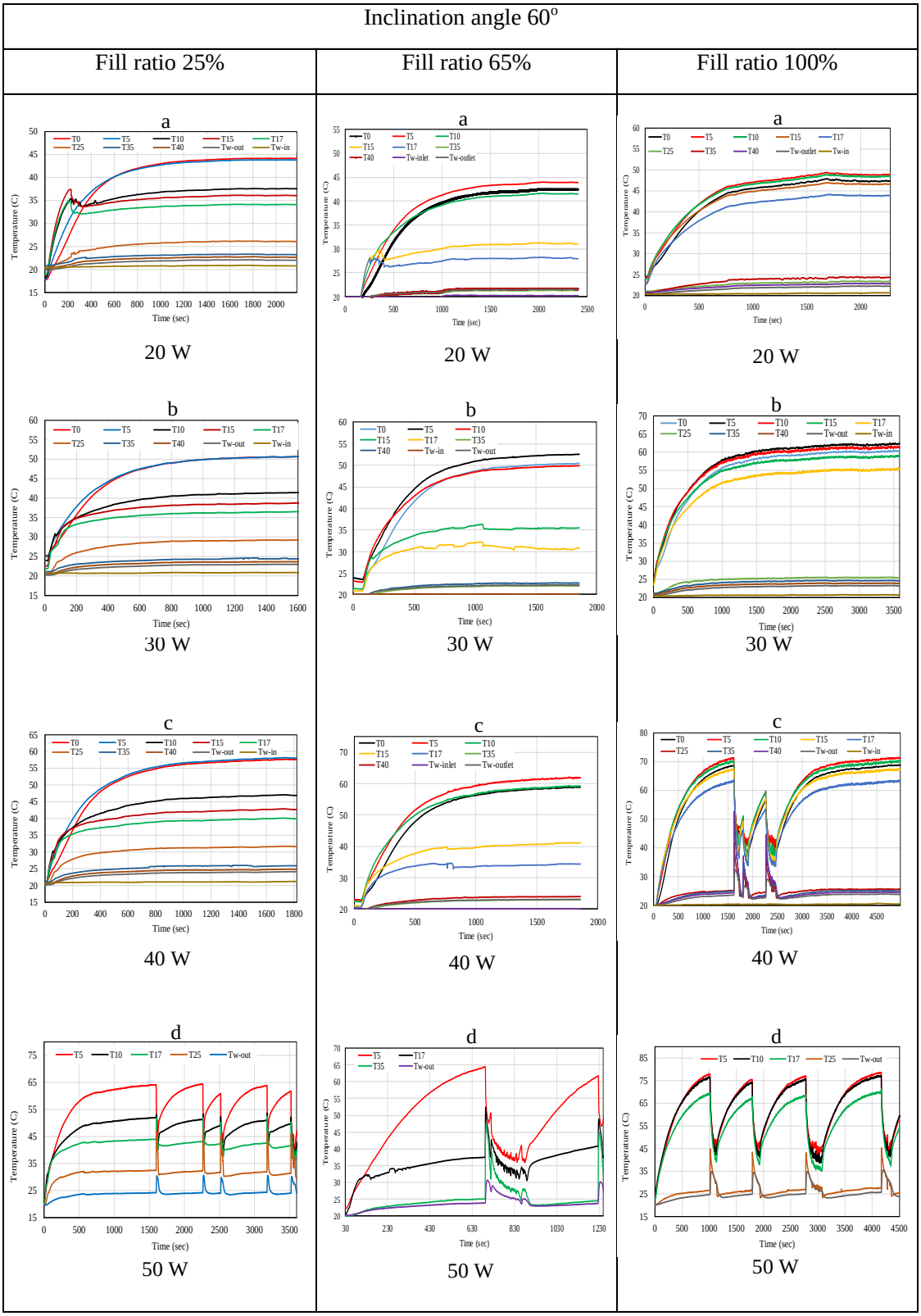

Figure 4.12-1 Time dependent wall temperature at angle of 60º and three liquid charges at heat loads (20, 30, 40 and 50W), (20ºC , 0.0025 kg/s) [8].

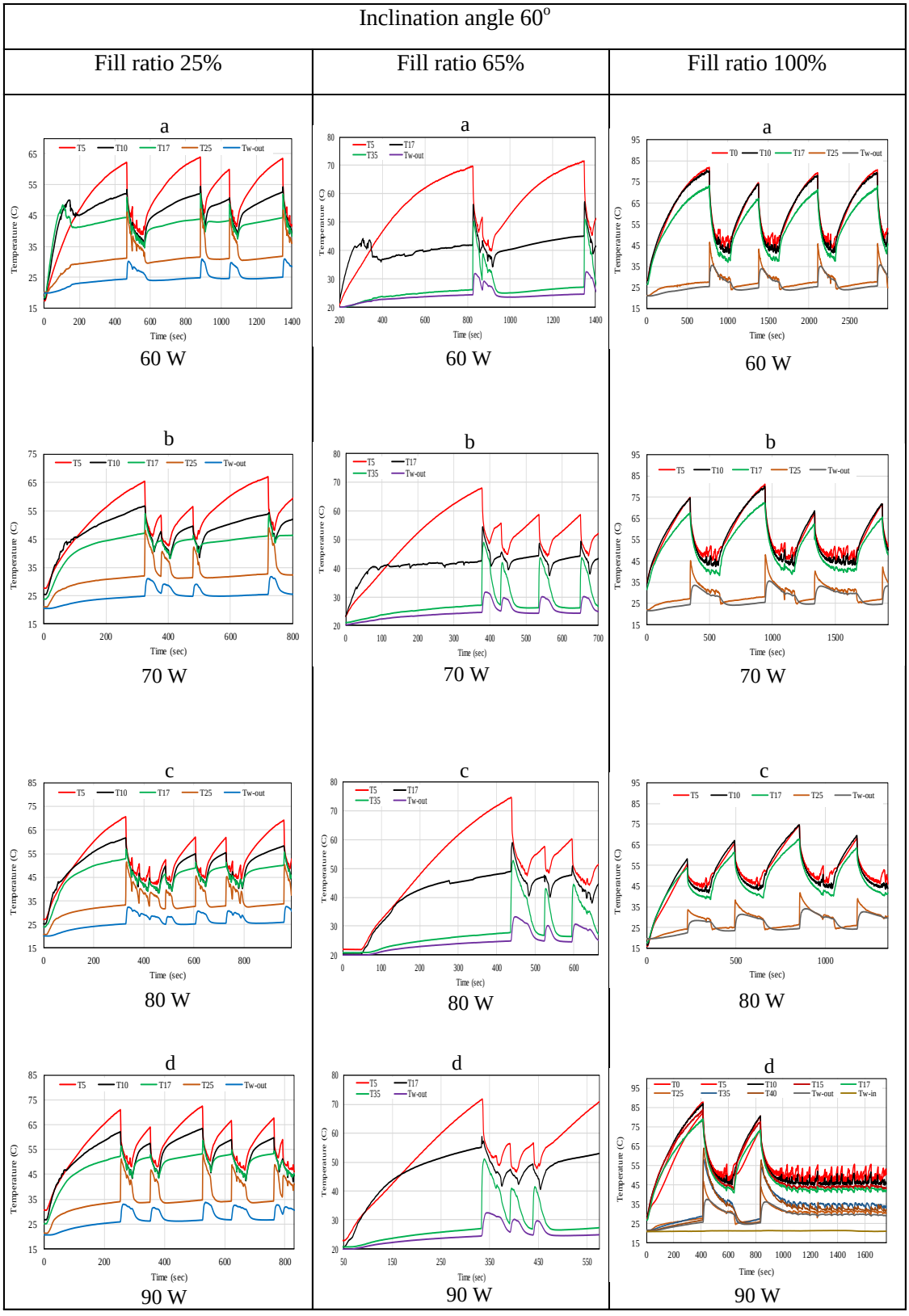

Figure 4.12-2 Time dependent wall temperature at angle of 60º and three liquid charges at heat loads (60, 70, 80 and 90 W), (20ºC, 0.0025 kg/s) [8].

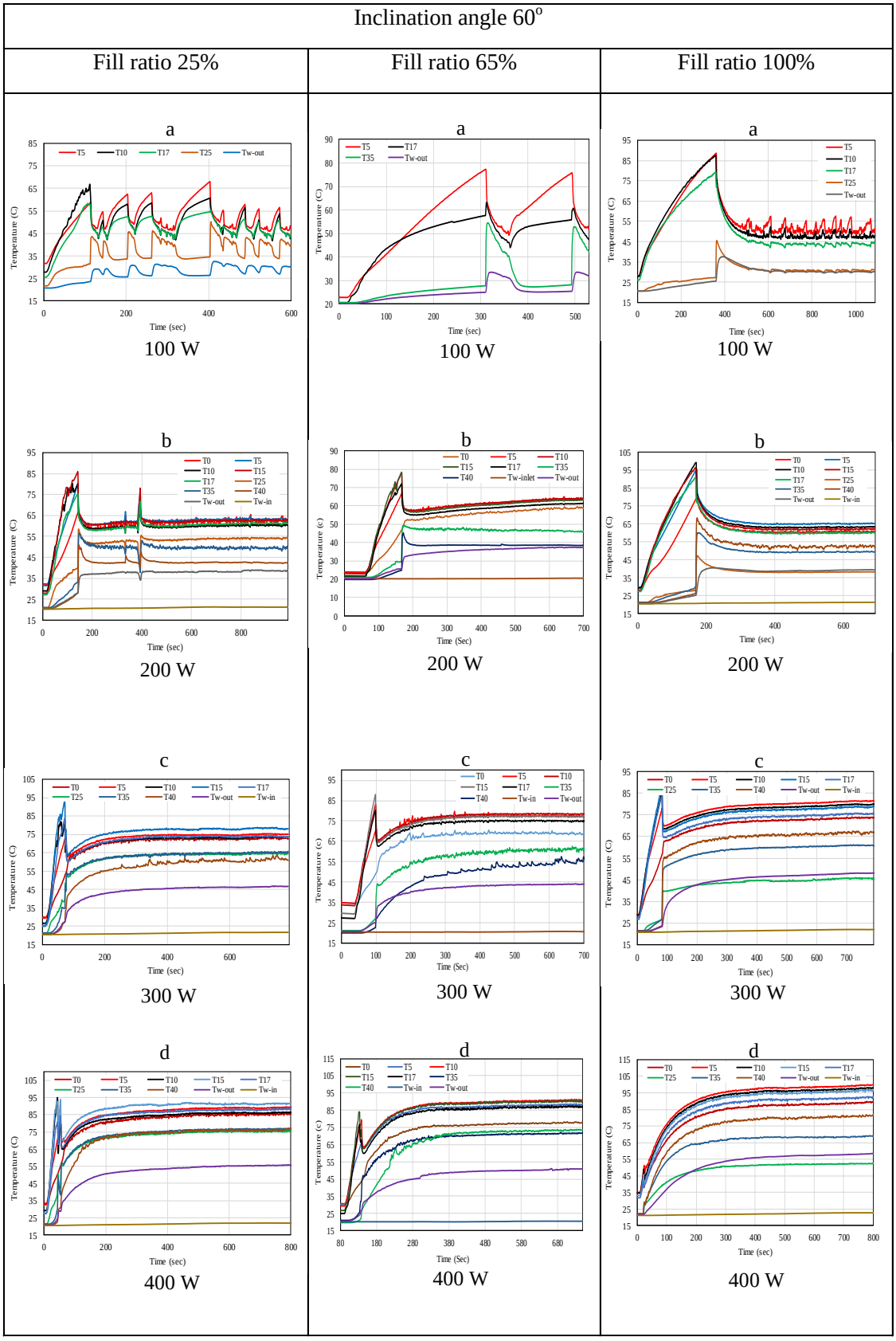

Figure 4.12-3 Time dependent wall temperature at angle of 60º and three liquid charges at heat loads (100, 200, 300 and 400 W), (20ºC, 0.0025 kg/s) [8].

At an inclination angle of 30^o (Figure 4.13-(1-3)), it is observed that at a fill ratio of 100%, the geyser boiling starts earlier at a heat input of 20 W instead of 30 and 40 W for angles of 90^o and 60^o, respectively, but it disappears afterwards at the same input energy, 20 W. Then, at the same fill ratio and a heat input of 30 W, the geyser boiling does not occur, whereas it occurs again at a heat input of 40 W, but again it does not continue. After that, at a heat input of 50 W, it does not happen, then it occurs at 60 W and continues repeatedly. This may be attributed to the change in superheat condition and pressure of the growing bubble due to change in the heat input at an angle of 30^o and 100% fill ratio. On the other hand, the geyser effect starts at 60 and 70 W for fill ratios of 65% and 25%, respectively and continues repeatedly. Also, for 100% fill ratio, lower temperature oscillation is observed at heat inputs 60, 70, 80, 90 and 100 W and tends to disappear at 200, 300 and 400 W compared with those for fill ratios 25% and 65%. Furthermore, unlike for the cases of angles 60^o and 90^o, at angle 30^o, high oscillation in the temperature readings is noticed at heat inputs 200, 300 and 400 W and fill ratios of 25% and 65%. The reason behind that can be the decrease in the force applied on the growing bubble by the liquid column as a result of a low inclination from the horizontal at the angle 30^o for lower fill ratios (25% and 65%) leading the bubble pressure to overcome the pressure applied by the upper liquid and pushing up the liquid easier. This effect was not observed when the fill ratio is 100% due to a large amount of working fluid [8].

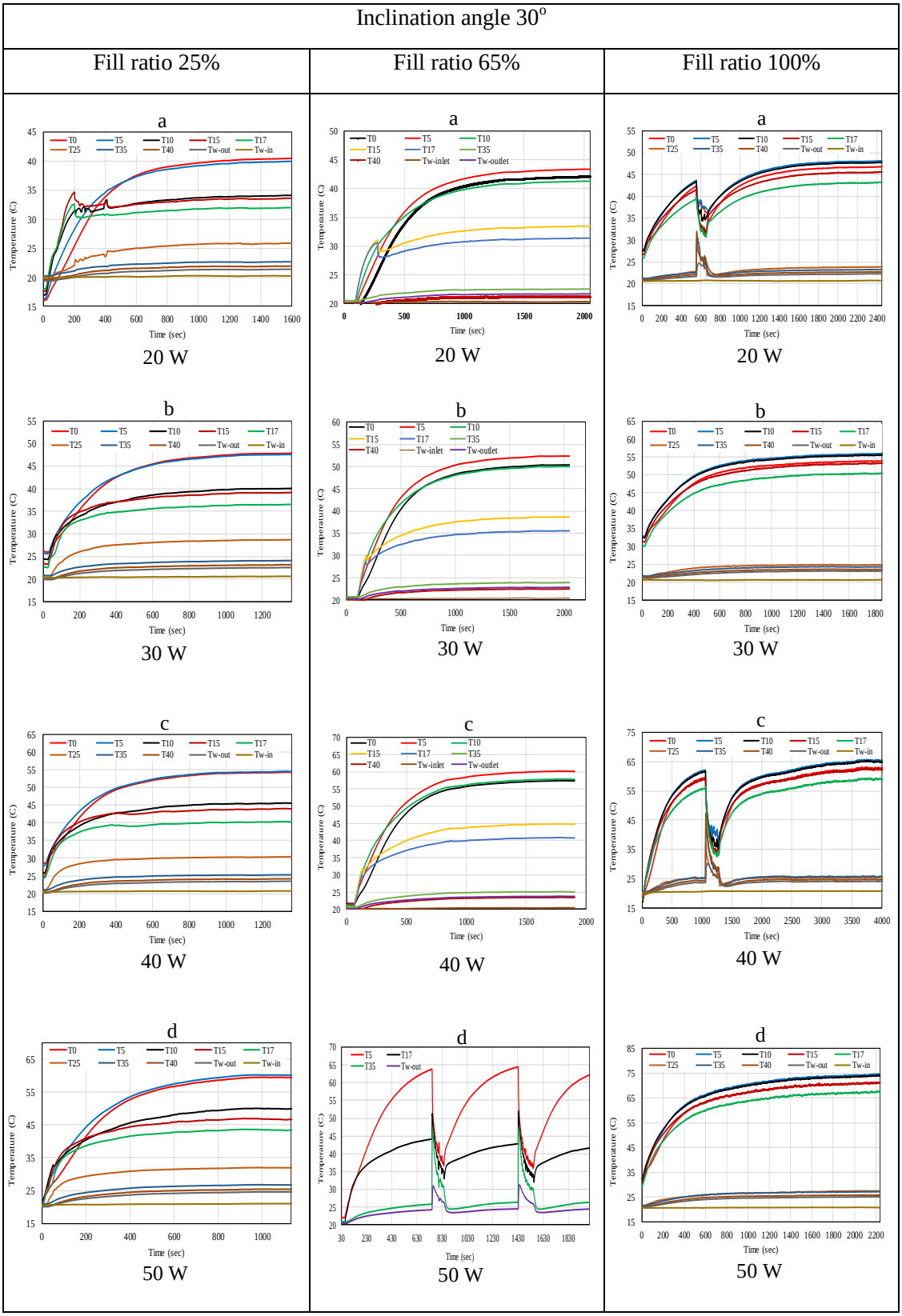

Figure 4.13-1 Time dependent wall temperature at angle of 30º and three liquid charges at heat loads (20, 30, 40 and 50W), (20ºC , 0.0025 kg/s) [8].

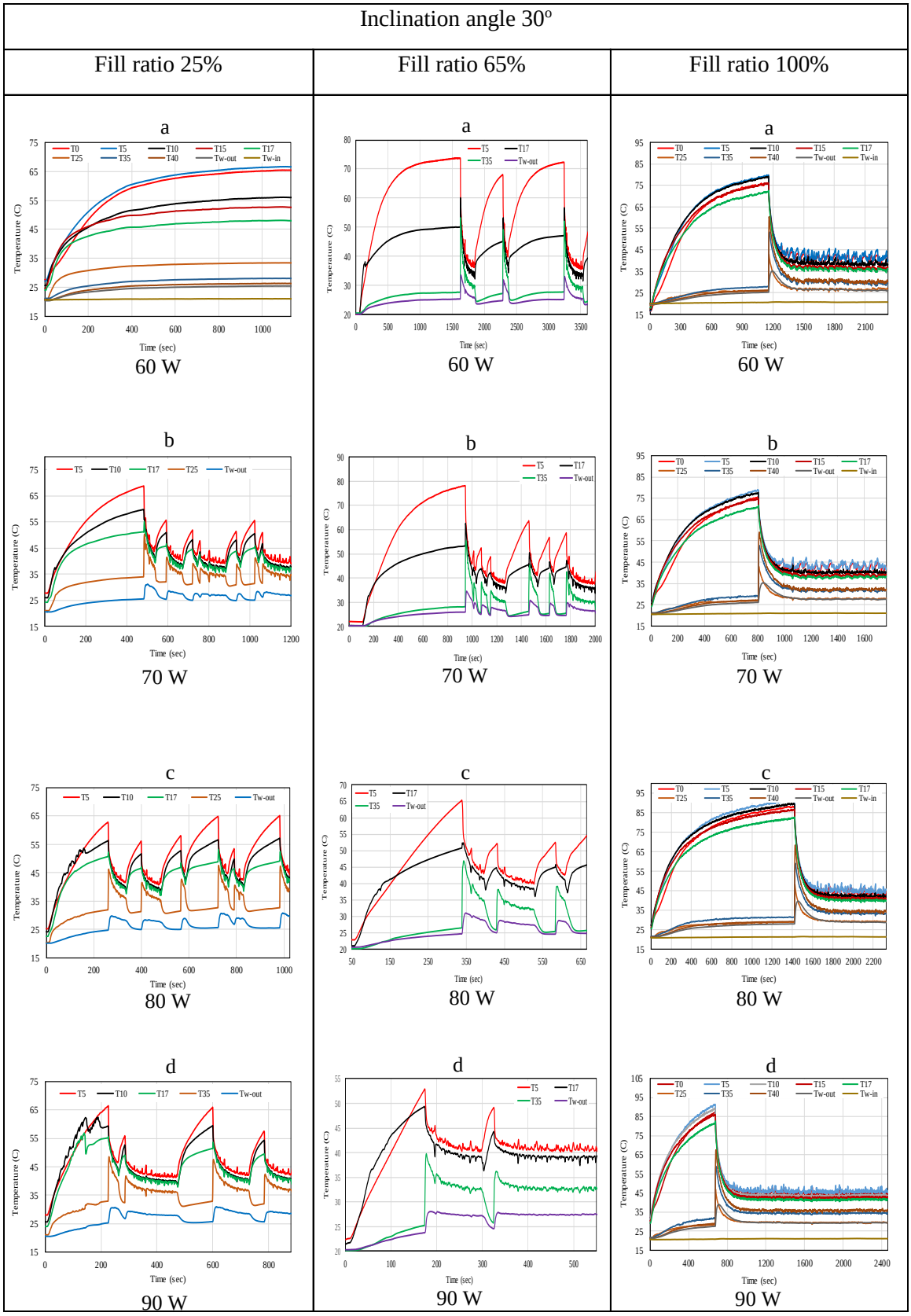

Figure 4.13-2 Time dependent wall temperature at angle of 30º and three liquid charges at heat loads (60, 70, 80 and 90 W), (20ºC, 0.0025 kg/s) [8].

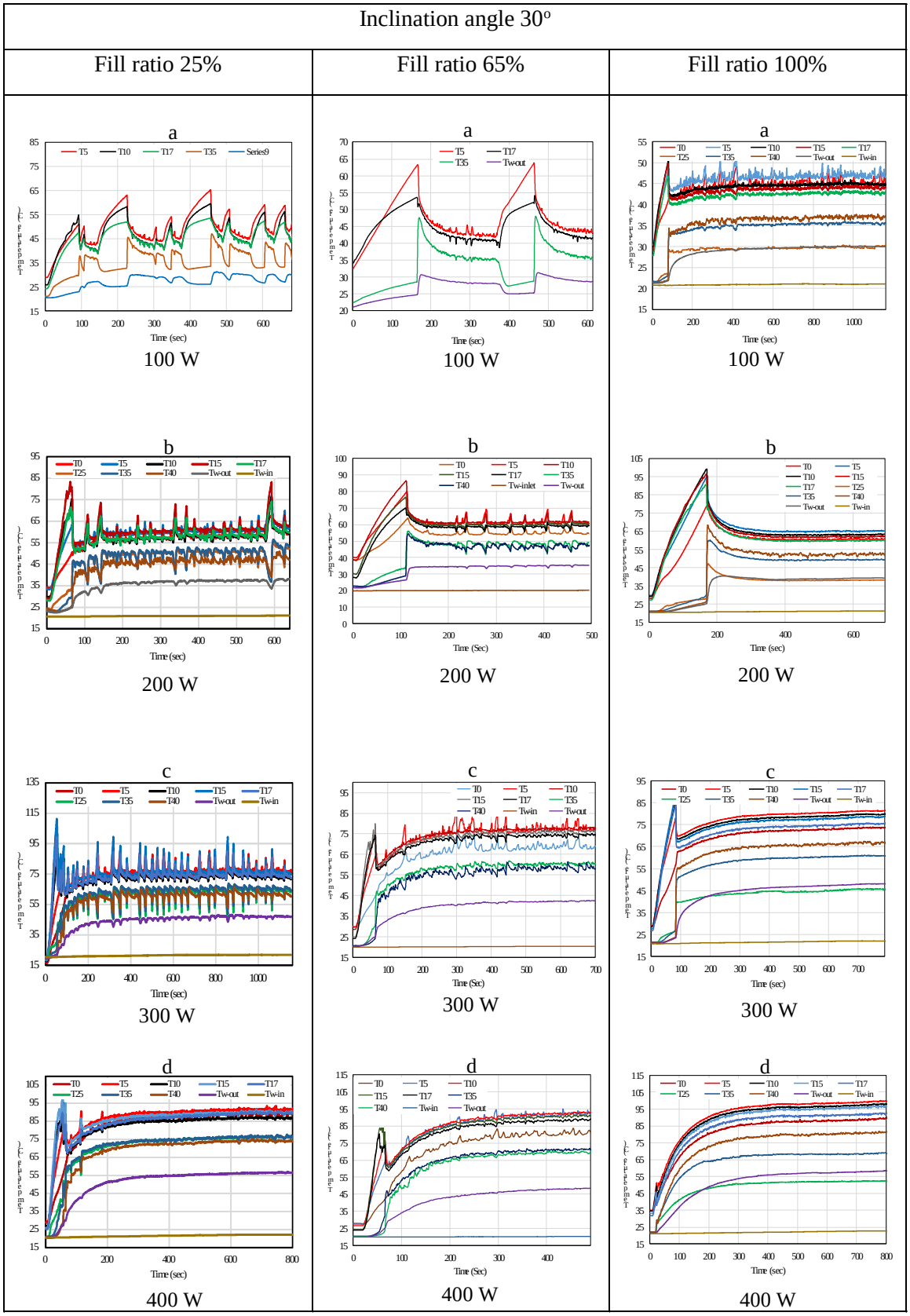

Figure 4.13-3 Time dependent wall temperature at angle of 30º and three liquid charges at heat loads (100, 200, 300 and 400 W), (20ºC, 0.0025 kg/s) [8].

Figure 4.14-(1-3) illustrate the temperature variation with time for three different fill ratios and an inclination angle of 10^o at various heat inputs. It is observed that no geyser boiling happens at heat inputs 20, 30, 40, 50 and 60 W (Figure 4.14-1(a-d) and Figure 4.14-2a) for all the three fill ratios. After that at a heat input of 70 W, the geysering firstly occurs only at the fill ratio 100%, whereas it occurs at 90 W for the fill ratio 65% and no geyser effect happens at the fill ratio 25% up to 100 W (Figure 4.14-3a). It is shown that at fill ratio 100%, the geyser boiling disappears after its occurrence at 70 W up to 100 W, whereas it continues for fill ratio 65% after its occurrence at 90 W. This delay in the occurrence of the geyser phenomenon at the angle 10^o may be attributed to high inclination from the vertical orientation at 10^o which may prevent the growing bubble to reach the superheat condition. Therefore, this leads to reduction in the pressure inside the bubble, thus delaying the occurrence of the geyser boiling even at the fill ratio 100%. On the other hand, at high heat inputs 200, 300 and 400 (Figure 4.14-3(c-d)), the fluctuation in the temperature increases for fill ratios 25% and 65% as in the case of angle 30^o for the same reason. In addition, unlike the cases of 30^o, 60^o and 90^o, higher temperature oscillation is observed at the fill ratio 100% and heat inputs 200, 300 and 400 due to the orientation of the TPCT which is close to the horizontal position [8].

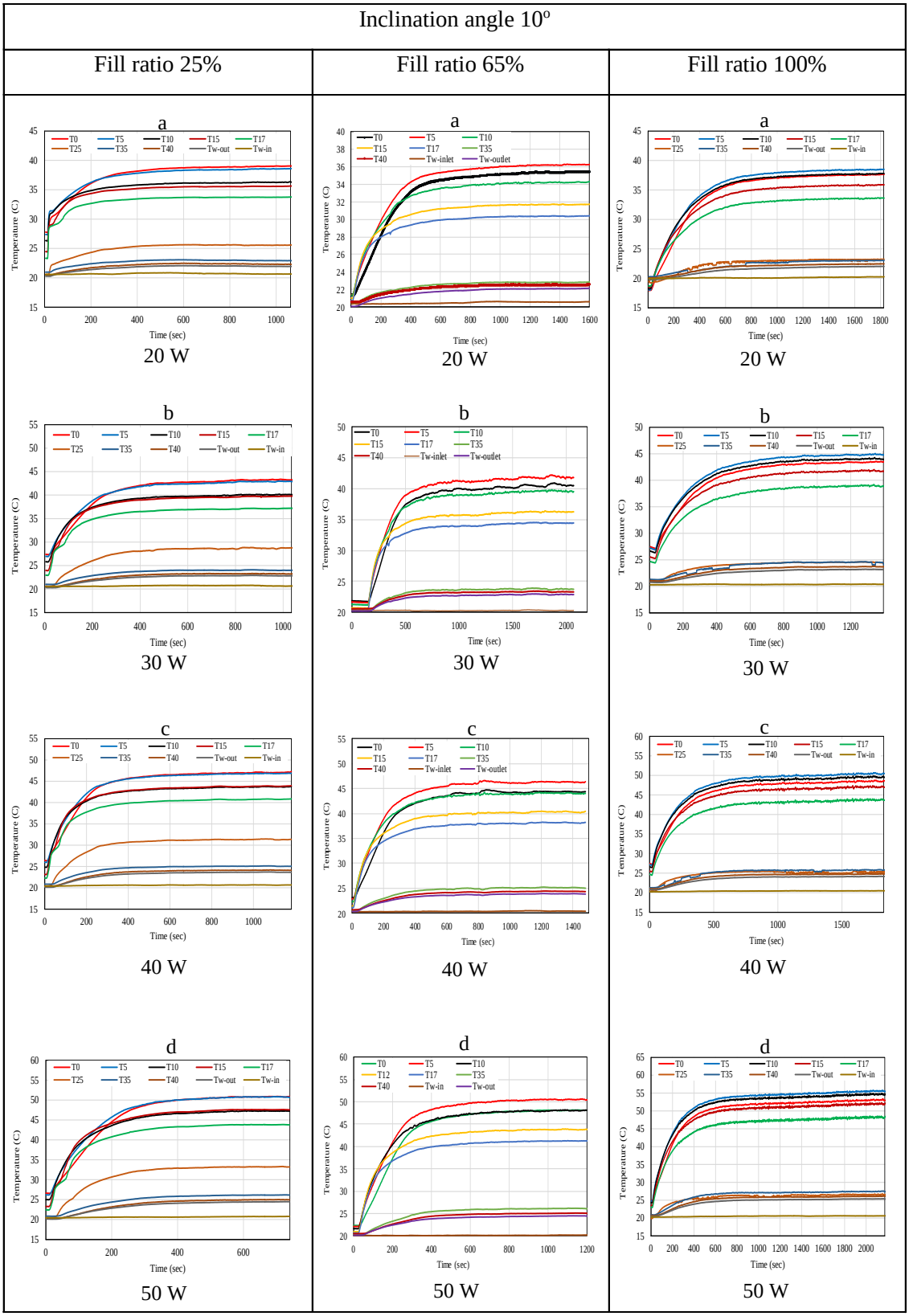

Figure 4.14-1 Time dependent wall temperature at angle of 10° and three liquid charges at heat loads (20, 30, 40 and 50 W), (20°C, 0.0025 kg/s) [8].

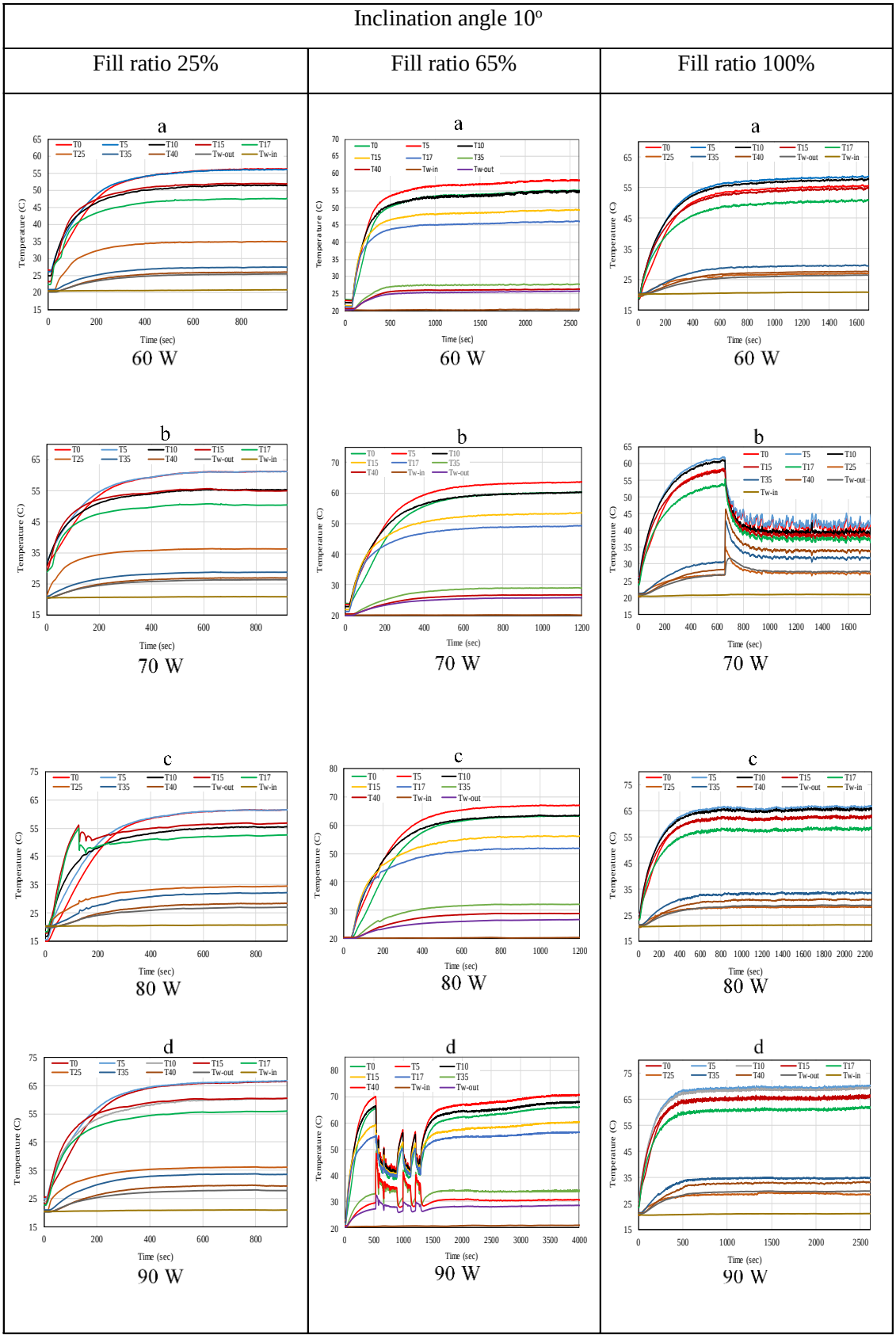

Figure 4.14-2 Time dependent wall temperature at angle of 10º and three liquid charges at heat loads (60, 70, 80 and 90 W), (20ºC, 0.0025 kg/s) [8].

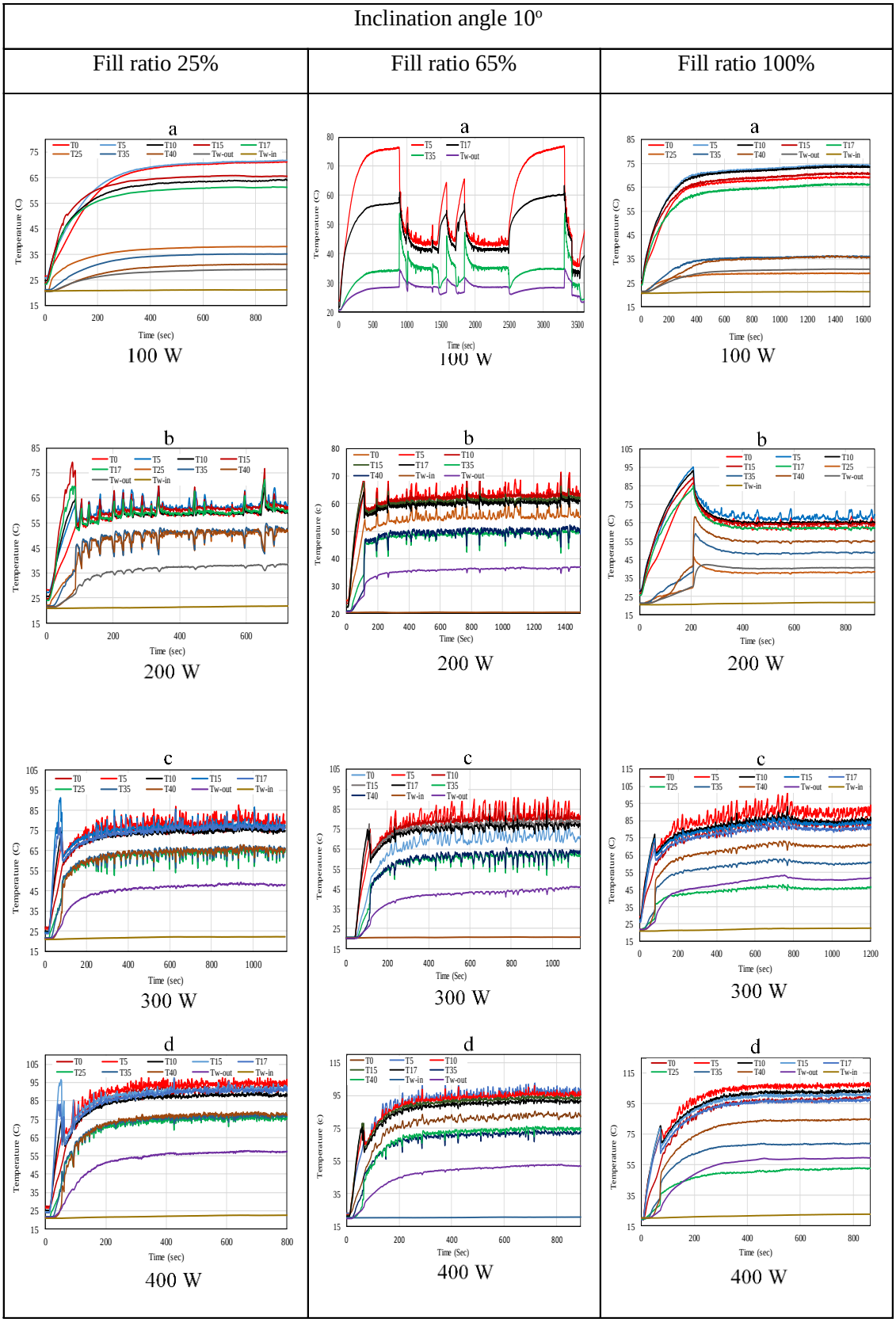

Figure 4.14-3 Time dependent wall temperature at angle of 10º and three liquid charges at heat loads (100, 200, 300 and 400 W), (20ºC, 0.0025 kg/s) [8].

4.3.1.2 Effect of Heat Load on Geyser Boiling Period

The period of geyser boiling is defined as the duration of the temperature oscillation where it is determined in this work by calculating the time between two oscillating pecks as shown in Figure 4.15.

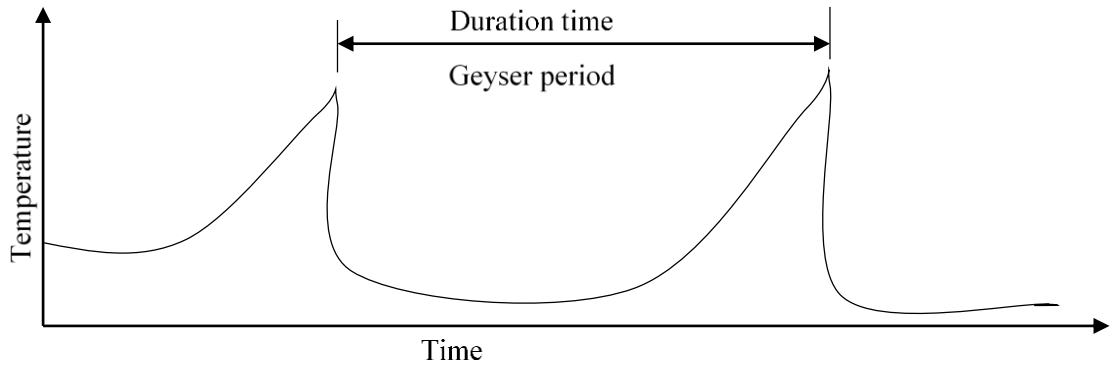

Figure 4.15 Meaning and estimation of the geyser period

Variation of the geyser boiling period with the heat input at three fill ratios, namely 25%, 65% and 100% are shown in Figure 4.16, Figure 4.17, Figure 4.18 and Figure 4.19 for inclination angles 90^o, 60^o, 30^o and 10^o, respectively. A semi-log plot is used due to a significant difference between the period values at low and high heat inputs. Figure 4.16 shows that the lowest geyser boiling is obtained at a fill ratio of 100% except at a heat input of 400 W where it is higher compared with the two other fill ratios for the angle 90^o. This could be explained by the earlier occurrence of the geyser effect at a lower heat input (30 W) for the fill ratio 100% compared with 60 and 70 W at fill ratios of 65% and 25%, respectively (Figure 4.11-(1-2)). This early occurrence makes the period for the fill ratio 100% to be lower at a higher heat input, for example at 70 W. At the same heat input, the geyser boiling just occurs for 25% fill ratio and it happened before only 10W for 65%. It is also observed that a high period is attained at a relatively low heat inputs (70, 80, 90 and 100 W), whereas it tends to disappear at high heat inputs (200, 300 and 400 W) due to the high pressure which forces the growing bubble to collapse before it reaches a larger size. In addition, at heat inputs of 60,70, 80, 90

and 100 W the period may increase as the heat input increases and this varies depending on the fill ratio. Figure 4.16 can also be interpreted by Figure 4.11-(1-3) [8].

For the inclination angle of 60^o, Figure 4.17 shows that the period of the geyser boiling decreases as the heat input increases for all fill ratios. It is also seen that at heat inputs of 50, 60, 70 and 80 W, 100% fill ratio exhibits the highest period due to a low superheat of the bubble resulting from a large amount of the working fluid which leads to a longer period. Further increase in heat input leads to increasing the growing bubble superheat and, hence, shorten the period. In addition, the period at high heat inputs (200, 300 and 400W) is still short as in the case of the angle 90^o [8].

Figure 4.18 shows (angle 30^o) that similar to the inclination angle of 90^o, the lowest geyser period is observed at the fill ratio 100% for the same reason. A noticeable increase in the period is observed at high heat inputs (200, 300 and 400W) and fill ratios 25% and 65% compared with that at angles of 60 and 90^o, while it is still short at the fill ratio 100%. This may result from the high inclination from the vertical orientation at an angle of 30^o which does not affect the period for the 100% case due to the large amount of the working fluid which prevents creating a gap between the evaporator surface and the working fluid at this orientation [8].

Figure 4.19 illustrates the period of the geyser effect at an inclination angle of 10^o. It shows that no period is presented for 25% fill ratio up to a heat input of 100W, while for 65% only at 90 and 100W and for 100% only at 70W. This can be clearly seen in Figure 4.14-(1-3) where the geyser boiling does not occur at the mentioned heat inputs and fill ratios. Also, as in the case of angle 30^o, a significant increase in the geysering period is observed at input energies of 200, 300 and 400 not only at fill ratios 25% and 65%, but also at 100%. This again may be attributed to a very low inclination from the horizontal orientation which makes parts of the inner evaporator surface unoccupied with the liquid and decreases the liquid height above the

growing bubble. Therefore, the void causes a decrease in the static pressure of the liquid in the evaporator, and the lower liquid height reduces the pressure applied on the bubble, thereby increasing the liquid superheat and bubble pressure resulting in the period to be longer instead of collapcing due to higher liquid pressure and lower superheat. This can also be confirmed by Figure 4.14-1(b-d) [8].

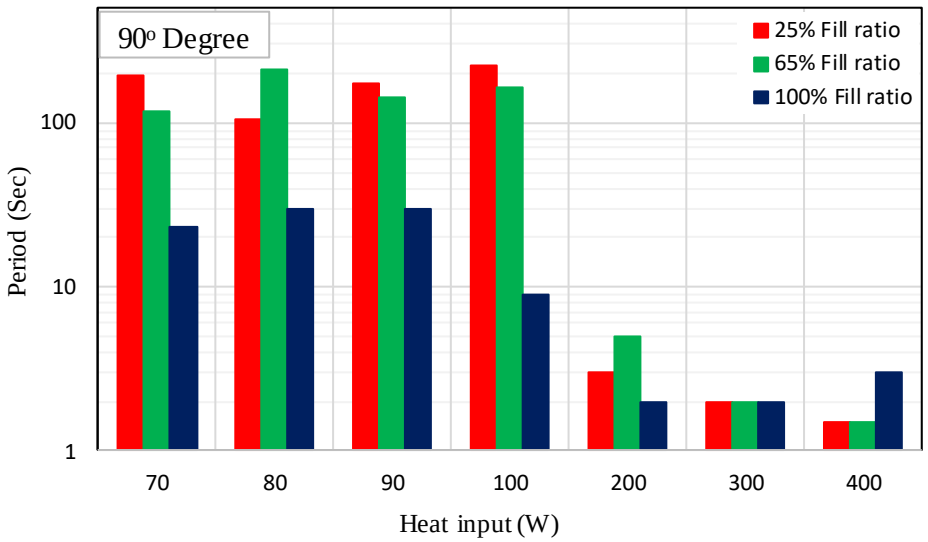

Figure 4.16 Variation of geyser boiling period with heat load at inclination of 90º for three fill ratios (20ºC, 0.0025 Kg/s) [8]

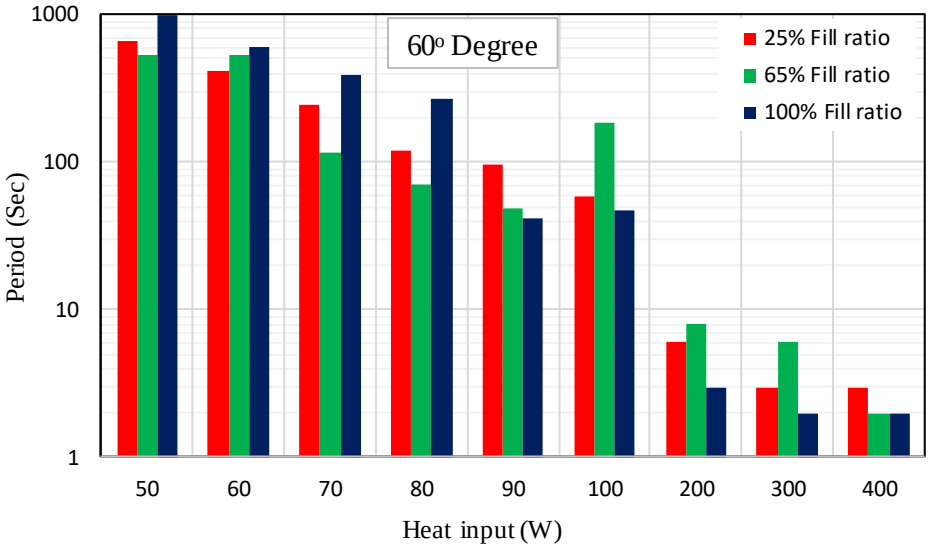

Figure 4.17 Variation of geyser boiling period with heat load at inclination of 60º for three fill ratios (20ºC, 0.0025 Kg/s) [8]

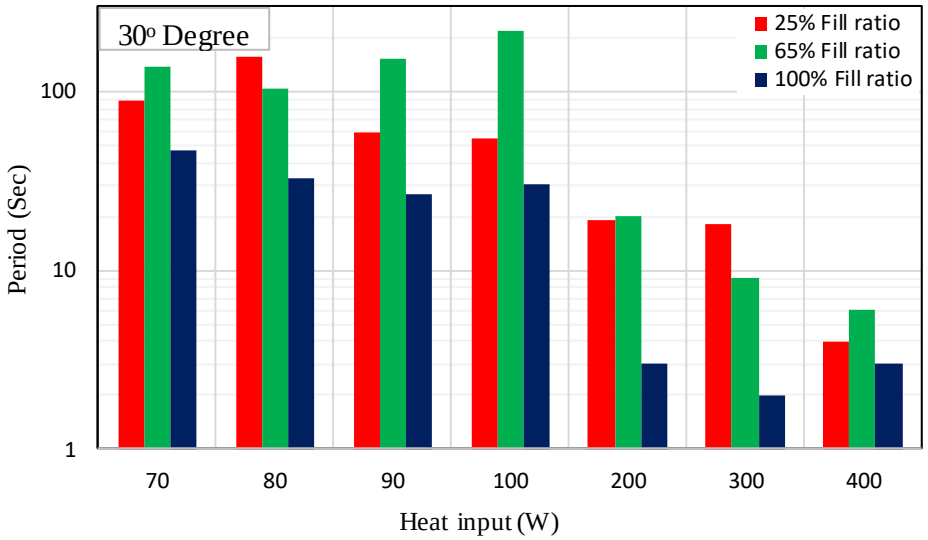

Figure 4.18 Variation of geyser boiling period with heat load at inclination of 30º for three fill ratios (20ºC, 0.0025 Kg/s) [8]

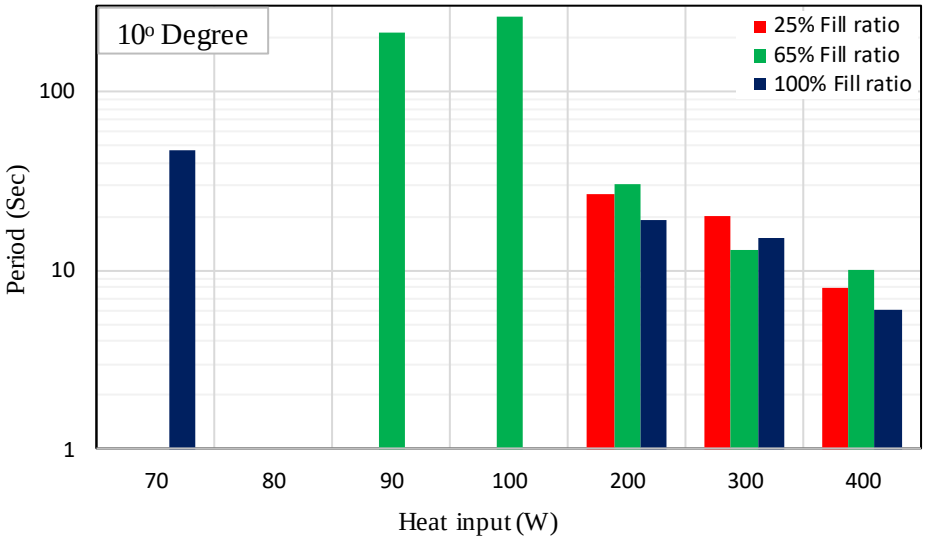

Figure 4.19 Variation of geyser boiling period with heat load at inclination of 10º for three fill ratios (20ºC, 0.0025 Kg/s) [8]

4.3.1.3 Effect of Cooling Water Mass Flow Rate

Effect of the flow rate of the cooling water on the geysering at three different fill ratios, heat input of 200 W and 20ºC cooling water inlet temperature was investigated at four angles 90º, 60º, 30º and 10º as shown in Figure 4.20-1,Figure 4.20-2, Figure 4.20-3 and Figure 4.20-4, respectively. At an angle of 90º (Figure 4.20-1), it is observed that the temperature oscillation is not affected by the change in cooling flow rate at the fill ratio of 100%. For 25% and 65% fill ratios, however, the temperature fluctuation is affected considerably by the change in the flow rate, especially at high flow rate. Similar to the case of the angle 90º, no obvious change in temperature behaviour is reported at the angle 60º (Figure 4.20-2) for the fill ratio 100%. On the other hand, a small change is noticed at 65%, whereas a significant change is obtained at the fill ratio of 25%. At the angle 30º (Figure 4.20-3), again the temperature readings are not affected by the increase in flow rate for 100% fill ratio, while the effect reverses for fill ratio of 65% compared with that at 90º and 60º. Also, higher temperature oscillation is observed at fill ratio of 25% compared with that at angles 60º and 90º. At the angle of 10º (Figure 4.20-4), the highest fluctuation in the temperature is found to be at a low flow rate for all fill ratios. In addition, a higher oscillation in the temperature is observed at 100% fill ratio compared with that at angles of 30º, 60º, and 90º. However, the temperature oscillation is lower for fill ratio 25% compared with that at angles of 30º, 60º, and 90º [8].

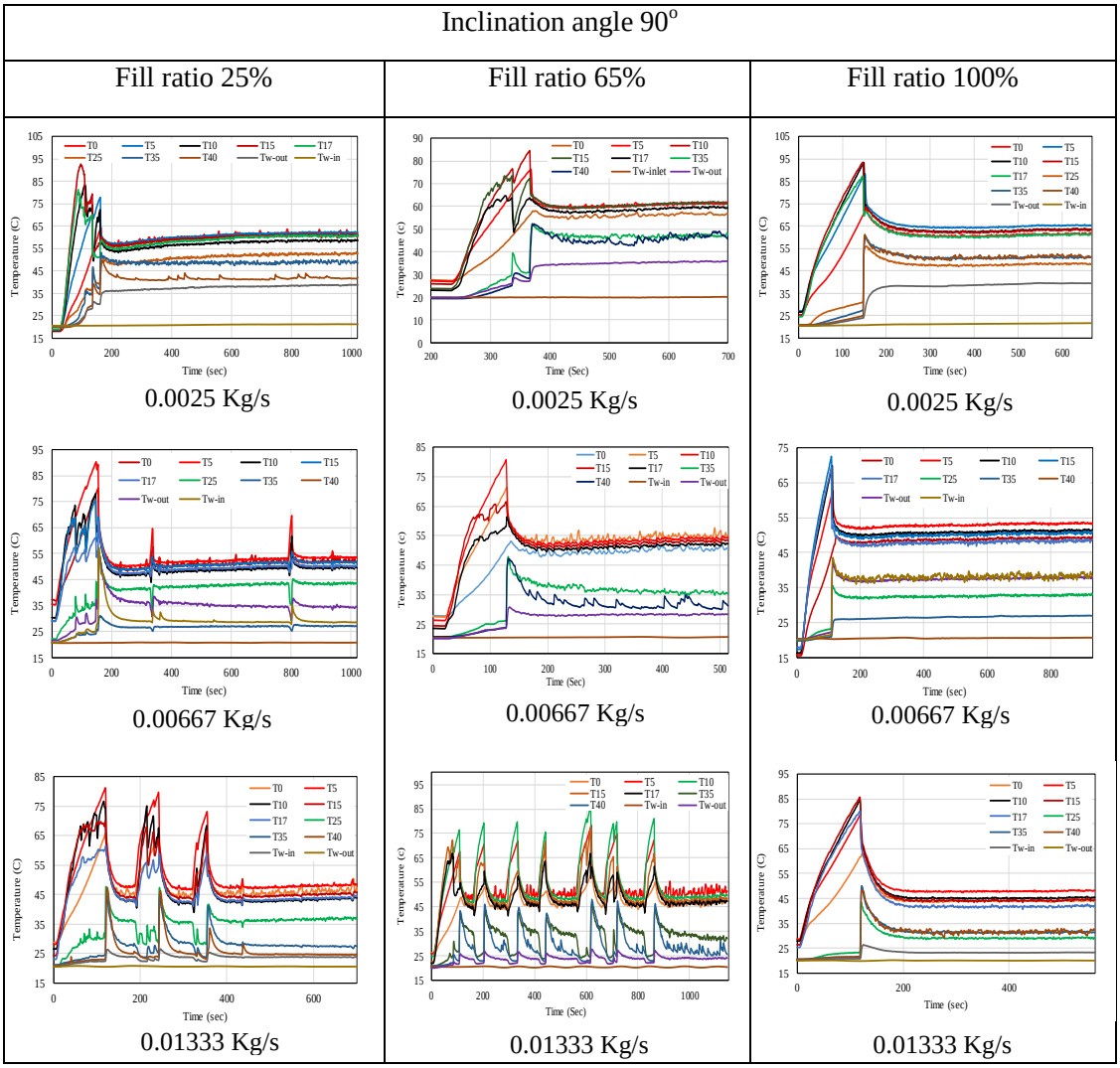

Figure 4.20-1 Time dependent wall temperature at different mass flow rates of cooling water, angle of 90º and three liquid charges (200 W, 20ºC)

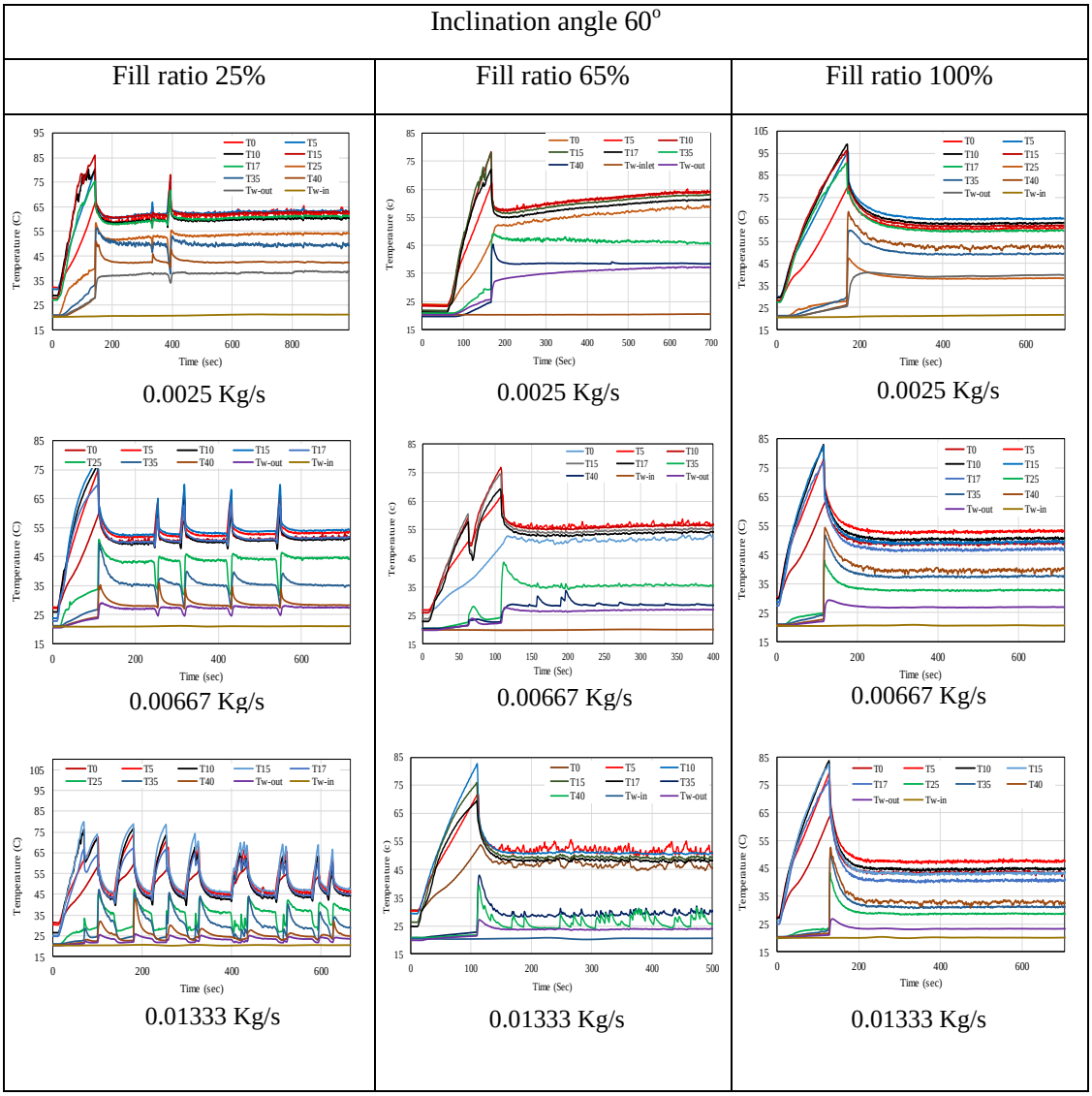

Figure 4.20-2 Time dependent wall temperature at different mass flow rates of cooling water, angle of 60º and three liquid charges (200 W, 20ºC)

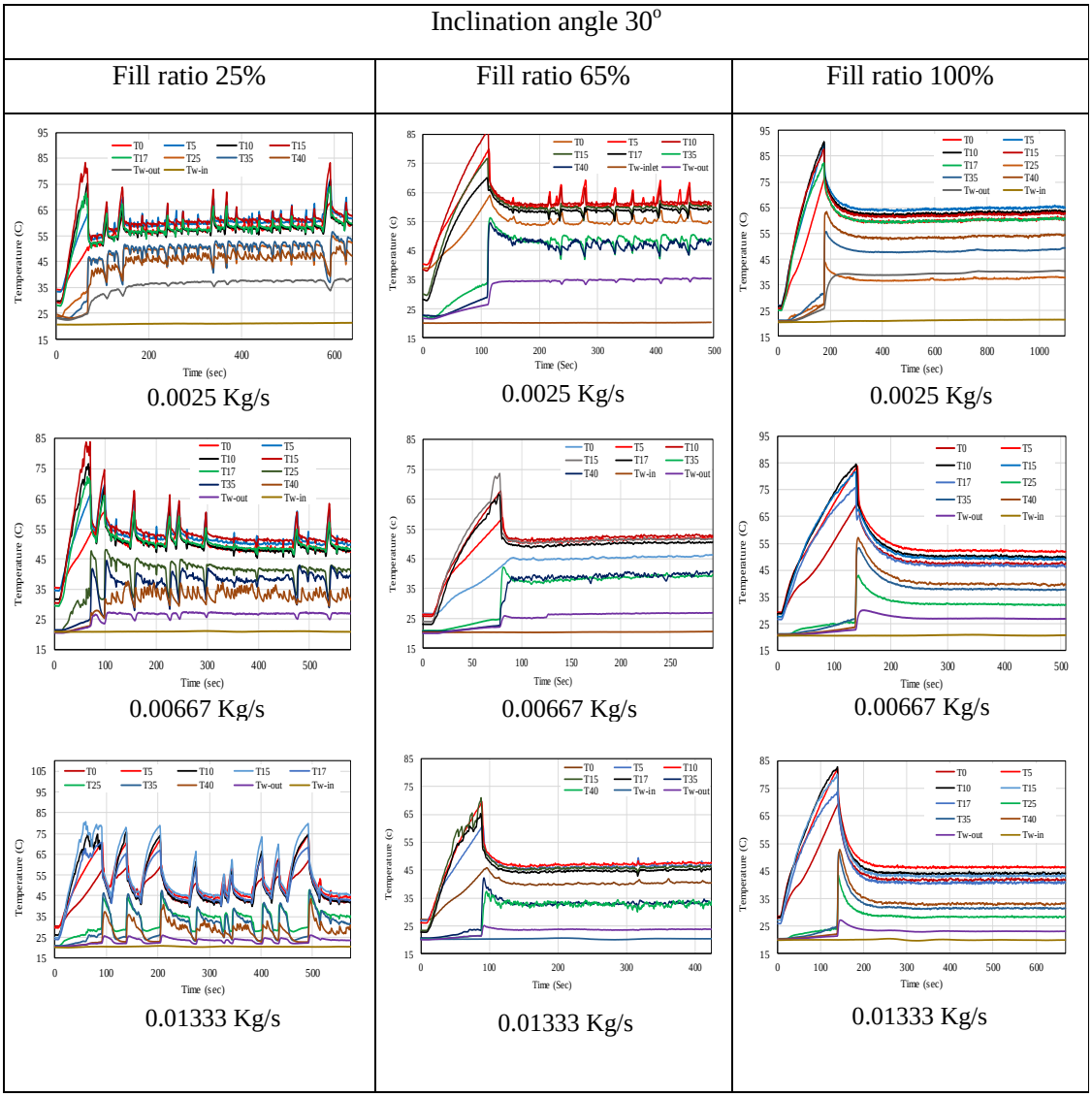

Figure 4.20-3 Time dependent wall temperature at different mass flow rates of cooling water, angle of 30º and three liquid charges (200 W, 20ºC)

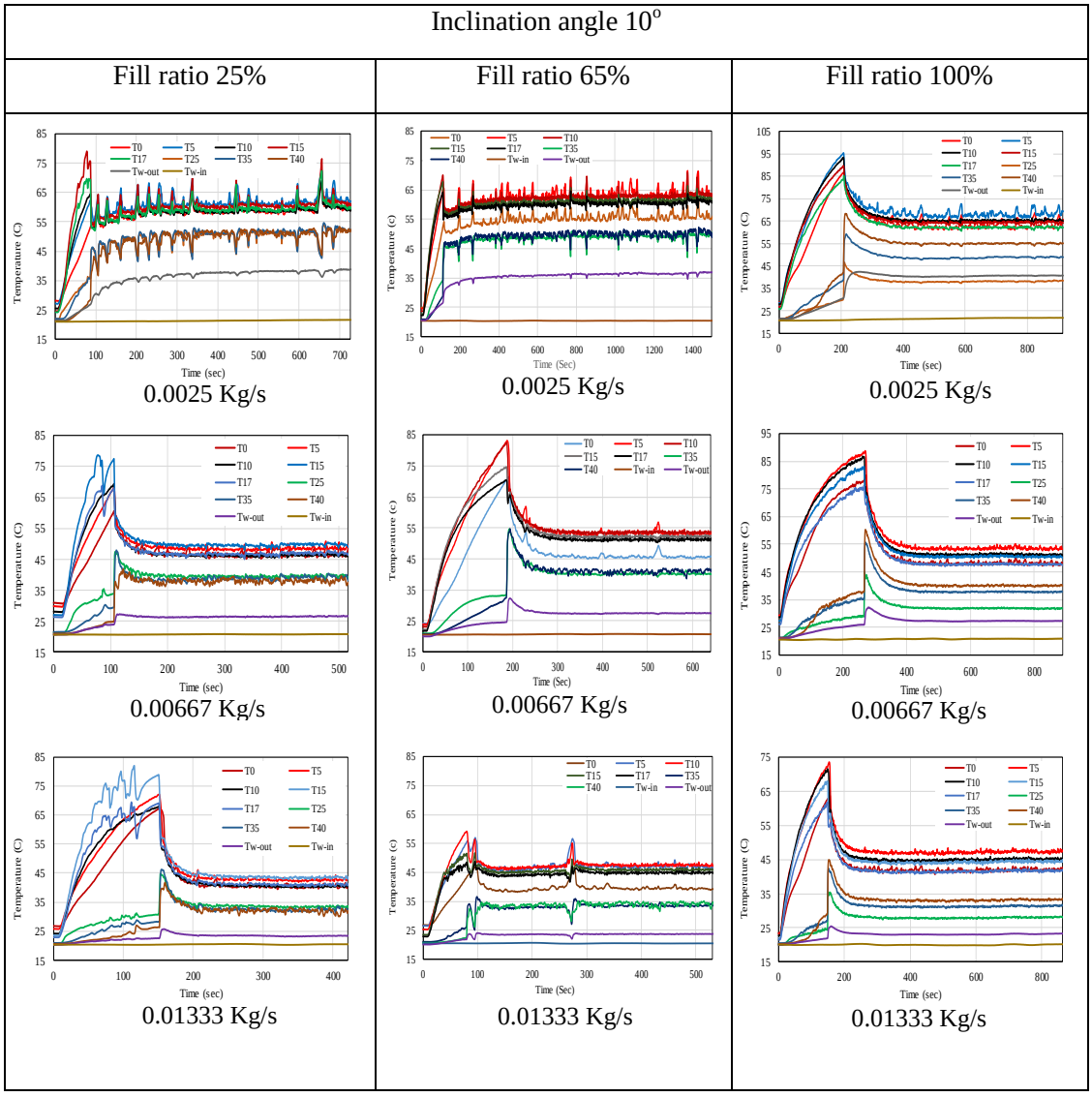

Figure 4.20-4 Time dependent wall temperature at different mass flow rates of cooling water, angle of 10° and three liquid charges (200 W, 20°C)

The geyser boiling period variation with the coolant mass flow rate at three different fill ratios, heat input of 200 W and inlet temperature of 20°C is presented in Figure 4.21, Figure 4.22, Figure 4.23 and Figure 4.24 for angles of 90, 60, 30 and 10°, respectively. Figure 4.21 shows that the lowest period is obtained at a fill ratio of 100% for the three values of the coolant flow rate and no change in the period is noticed at the three coolant flow rates. However, a relatively large change in the period is observed for fill ratios 25% and 65% and the period increases as the flow rate increases for both fill ratios. This may be attributed to the high liquid height in case of the 100% fill ratio due to a large amount of the charging liquid

which applies higher pressure on the growing bubble, thereby forcing the growing bubble to collapse before it reaches a larger size and mitigating the effect of the geyser boiling. In contrast, in the case of fill ratios 25% and 65%, the lower amount of the working fluid and the increase in the flow rate at a constant heat input which decreases the pressure inside the TPCT reduce the force on the growing bubble, thereby allowing the bubble to develop into a larger size resulting in a longer geyser period [8].

Figure 4.22 shows the same trends as in Figure 4.21 in which the period increases as the flow rate increases for fill ratios of 25% and 65%. However, a slight increase in the period is observed at fill ratio 100% and a flow rate of 0.0025 kg/s. Figure 4.23 demonstrates that the trend at angle 30^o is reversed for the fill ratio 65% where the period decreases as the coolant flow rate increases, while the same trend is shown for fill ratios 25% and 100% as in the case of angle 60^0. This may be explained as follow: due to a low degree of inclination from the horizontal position, an amount of liquid may cover a part of the condenser and this amount depends on the quantity of the working fluid (fill ratio). Therefore, at a high coolant mass flow rate, the effect of cooling transfers to the evaporator which reduces the liquid superheat and causes the growing bubble to collapse before it reaches a larger size resulting in a lower period despite the pressure reduction. Further inclination toward the horizontal orientation at angle 10^o causes the trend of the period at fill ratio 25% to be reversed compared with that at angles of 90, 60 and 30^o as shown in Figure 4.24. From Figure 4.24, it can be understood that the period of the geyser boiling decreases as the mass flow rate increases for all fill ratios (25%, 65% and 100%) [8].

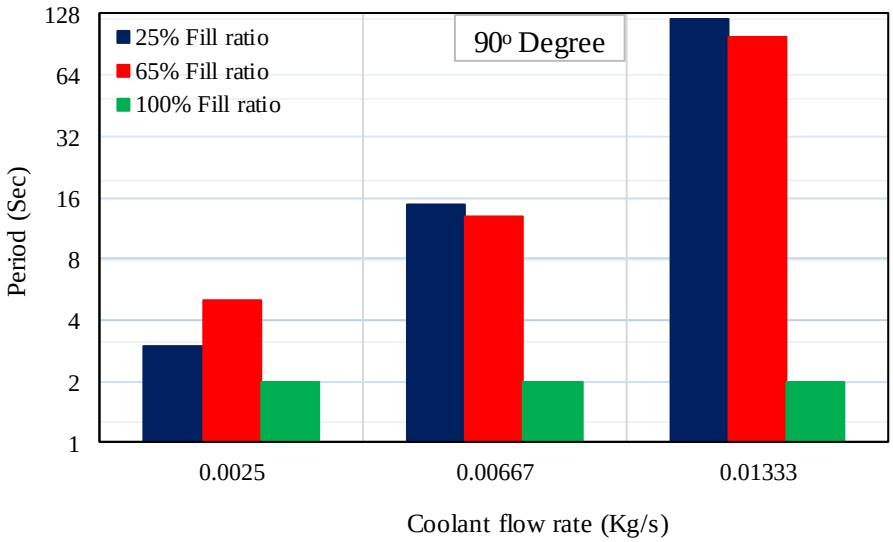

Figure 4.21 Variation of geyser boiling period with coolant flow rate at inclination of 90º for three fill ratios (200 W, 20ºC) [8]

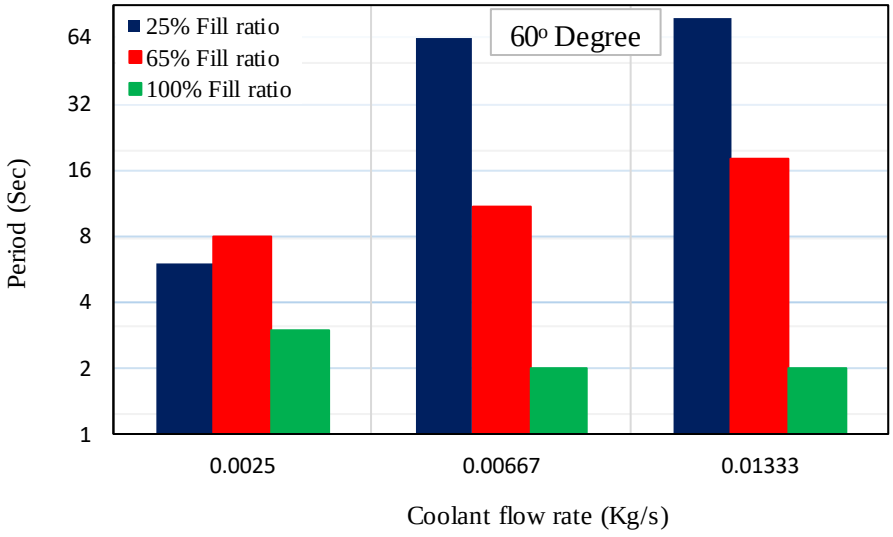

Figure 4.22 Variation of geyser boiling period with coolant flow rate at inclination of 60º for three fill ratios (200 W, 20ºC) [8]

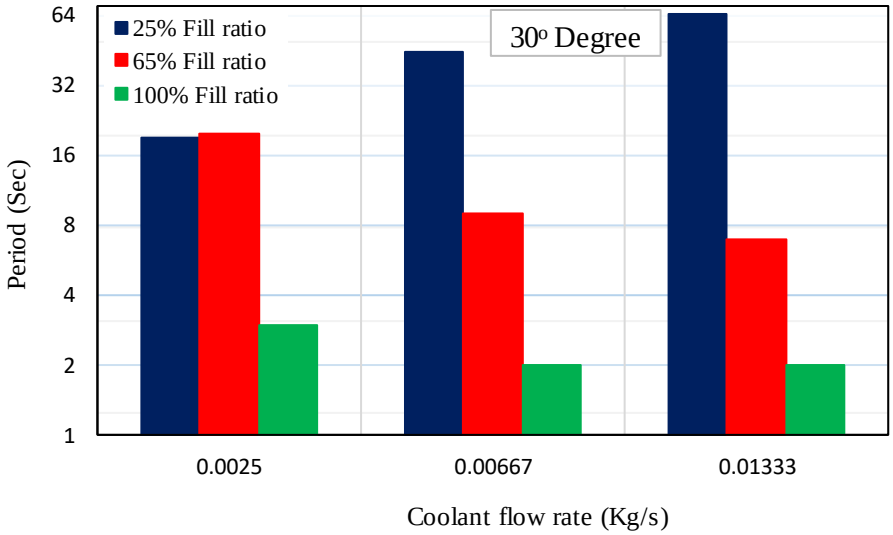

Figure 4.23 Variation of geyser boiling period with coolant flow rate at inclination of 30º for three fill ratios (200 W, 20ºC) [8]

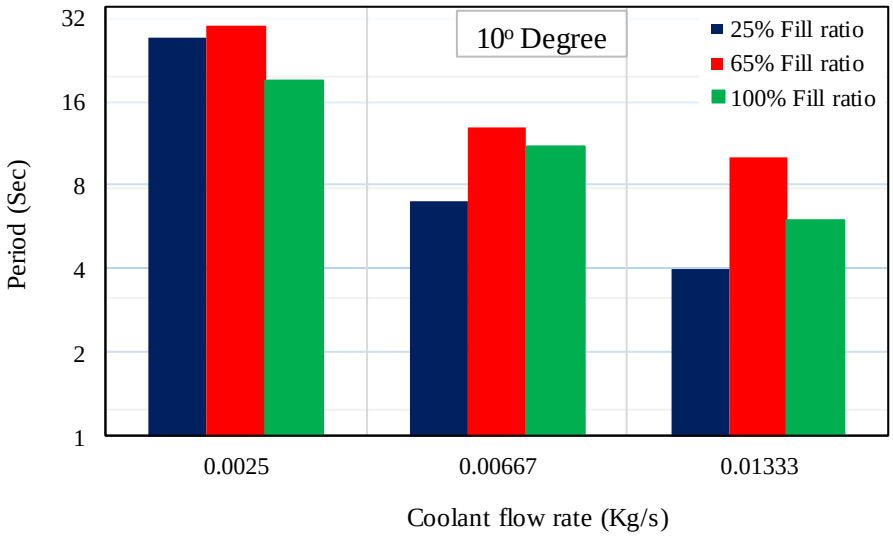

Figure 4.24 Variation of geyser boiling period with coolant flow rate at inclination of 10º for three fill ratios (200 W, 20ºC) [8]

4.3.1.4 Effect of cooling water inlet temperature

Effect of the inlet temperature of the cooling water on the geyser boiling at three different fill ratios, heat input of 200 W and 0.0025 kg/s coolant flow rate was tested at inclination angles of 90º, 60º, 30º and 10º as shown in Figure 4.25-1, Figure 4.25-2, Figure 4.25-3 and Figure 4.25-4, respectively. At angles of 90º and 60º (Figure 4.25-1 and Figure 4.25-2), no significant effect of the coolant inlet temperature on the temperature oscillation is observed for the three fill ratios except at the fill ratio of 25% and inlet temperature of 15ºC where higher oscillation in the temperature is noticed for both angles (60º and 90º). This effect is higher at an angle of 60º than that at 90º. It is also observed that the fluctuation in the temperature is higher at the condenser section, especially at the fill ratio 65%. At an angle of 30º (Figure 4.25-3), the inlet temperature considerably affects the temperature behaviour at fill ratios of 25% and 65% due to the relatively lower amount of the working fluid and low inclination from the horizontal position. However, at fill ratio of 100% and the same angle, no obvious effect is observed due to a higher amount of the working fluid. On the other hand, at an angle of 10º (Figure 4.25-4), a higher temperature oscillation is observed, especially, compared with that at an angle of 90º and 60º for all the three fill ratios resulting from a further inclination toward the horizontal position [8].

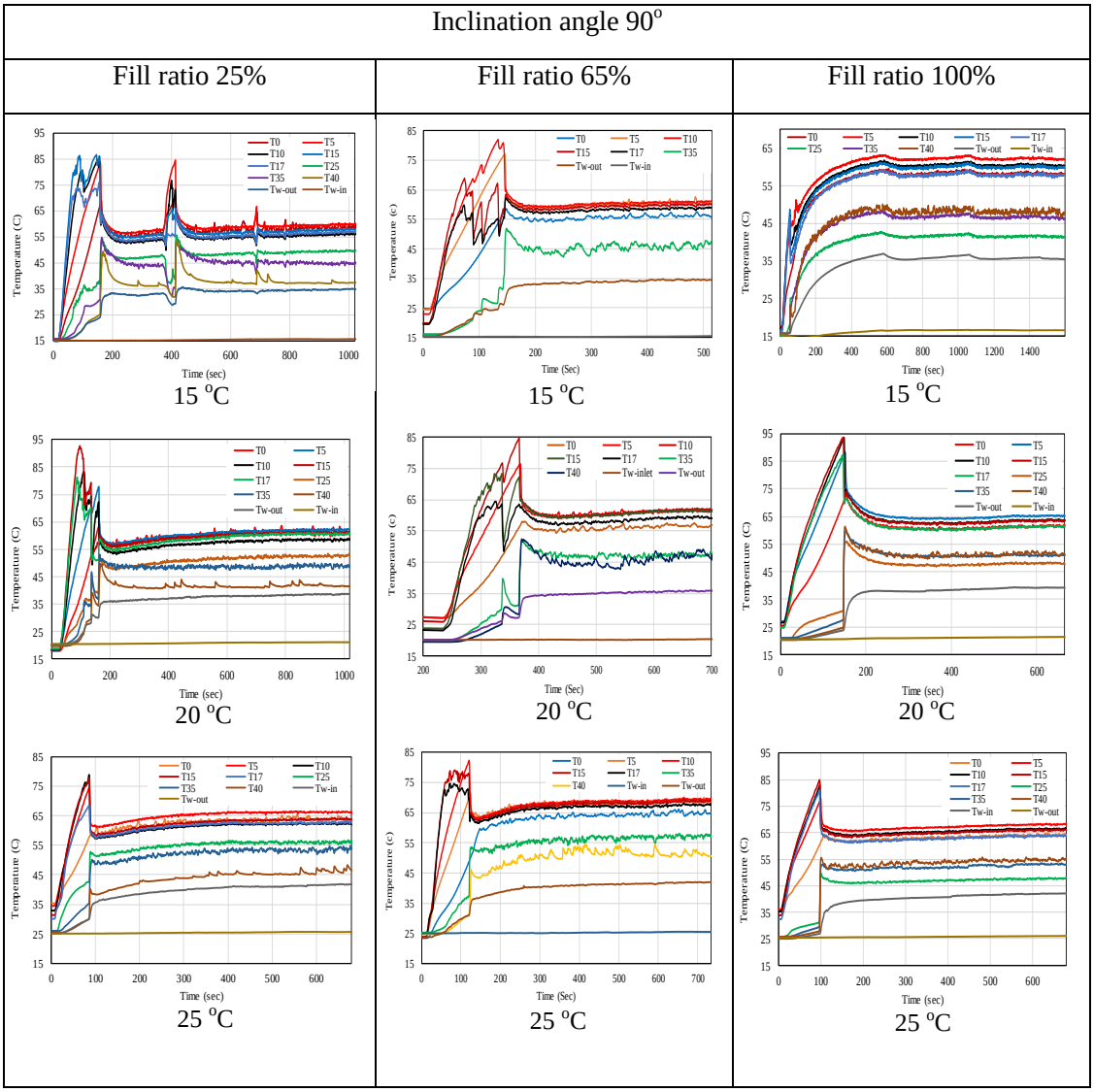

Figure 4.25-1 Time dependent wall temperature at different inlet tempertures of cooling water, angle of 90° and three liquid charges (200 W, 0.0025 kg/s)

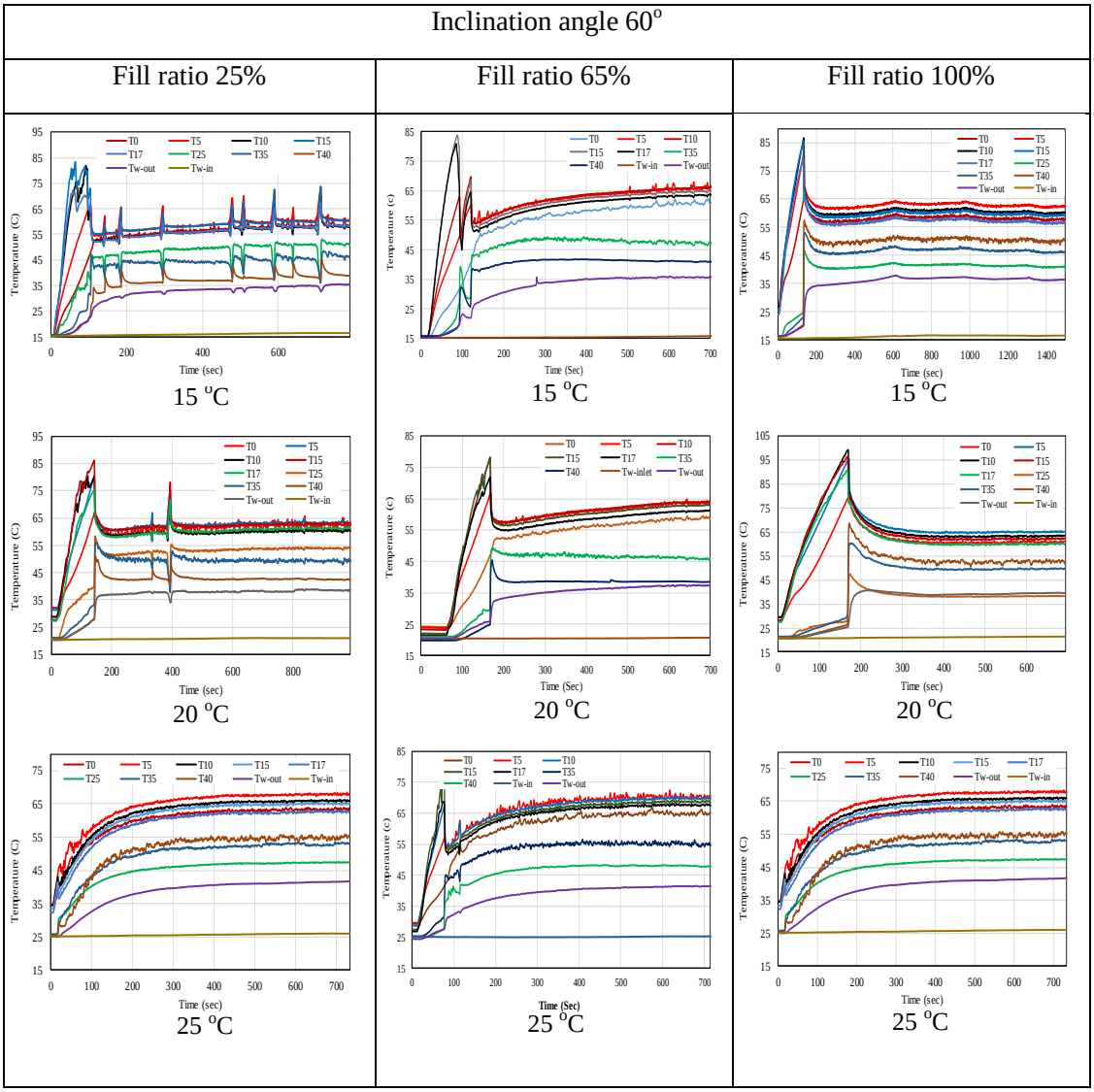

Figure 4.25-2 Time dependent wall temperature at different inlet tempertures of cooling water, angle of 60° and three liquid charges (200 W, 0.0025 kg/s)

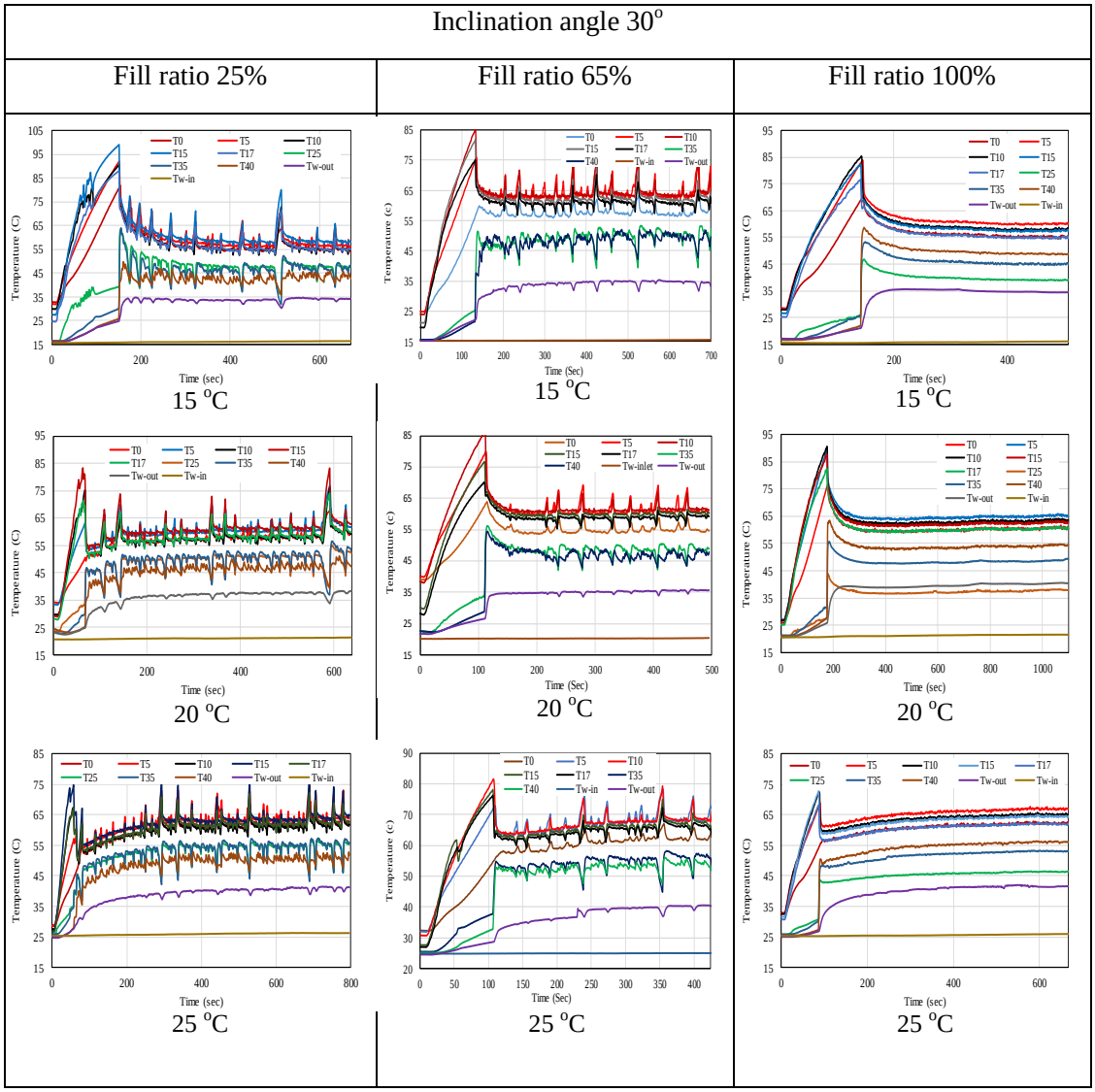

Figure 4.25-3 Time dependent wall temperature at different inlet tempertures of cooling water, angle of 30° and three liquid charges (200 W, 0.0025 kg/s)

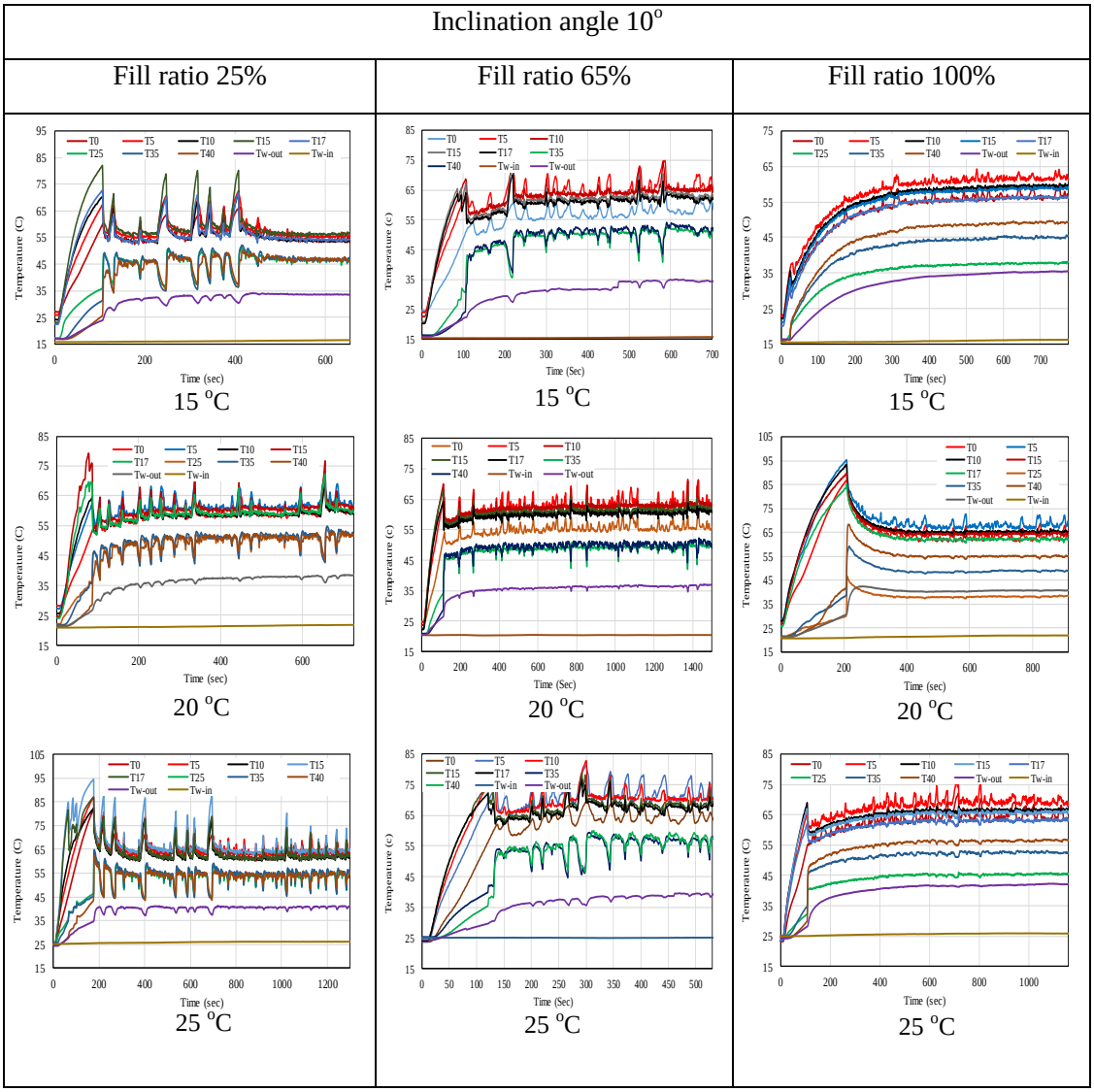

Figure 4.25-4 Time dependent wall temperature at different inlet tempertures of cooling water, angle of 10° and three liquid charges (200 W, 0.0025 kg/s)

Variation of the geyser boiling period with the inlet temperature of cooling water at three fill charges, namely 25%, 65% and 100%, heat load of 200 W and a mass flow rate of 0.0025 kg/s is presented in Figure 4.26, Figure 4.27, Figure 4.28 and Figure 4.29 for angles of 90°, 60°, 30° and 10°, respectively. Figure 4.26 shows that the period decreases as the coolant inlet temperature increases for fill ratios of 25% and 100%, while for the fill ratio of 65%, it increases as the inlet temperature increases. The highest period is observed at 25% and 15°C and the second highest period at 65% and 25°C, whereas the lowest period is noticed at 100% for all inlet temperatures where almost no change in the period is shown at this fill ratio. This

is also true for Figure 4.27 and Figure 4.28, but the period is higher as the inclination angle is lower except for 100% where a small change is seen for these three figures (Figure 4.26, Figure 4.27 and Figure 4.28). On the other hand, at angle of 10º, Figure 4.29 shows that the trend is reversed for fill ratios 25% and 100% where the period increases as the coolant inlet temperature increases, while for the fill charge of 65% the same trend is kept as that for angles 90º, 60º and 30º. In addition, again the value of the period for angle 10º is higher compared with that at angles of 90º, 60º and 30º for all fill ratios. It also noticed that a considerable increase in the period is obtained at the fill 100% compared with that at other angles due to the high inclination at the angle 10º [8]. This may result from low inclination near the horizontal orientation which allows to generate more vapour leading to increase the pressure inside the TPCT. This needs more time for the pressure inside the forming bubble to overcome the external applied pressure (outside the bubble) thereby increasing the period in this case.

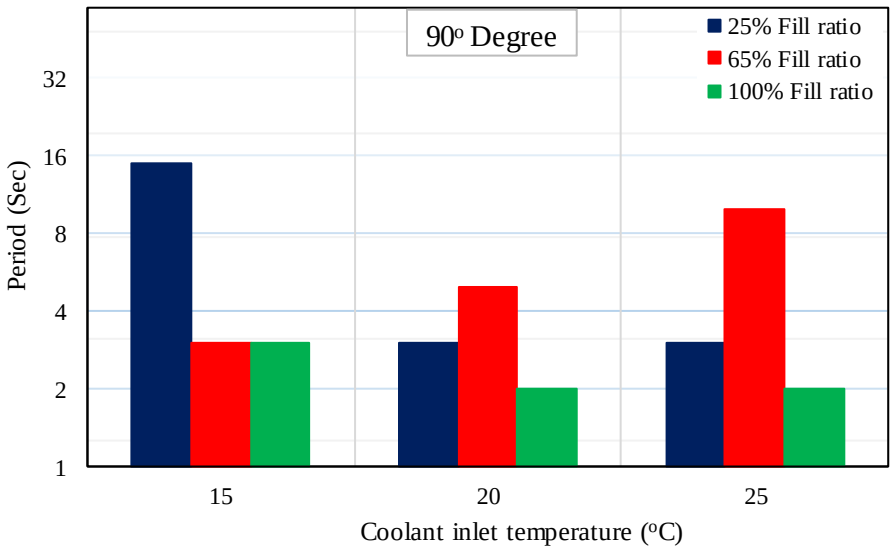

Figure 4.26 Variation of geysering period with coolant inlet temperature at inclination of 90º for three fill ratios (0.0025 kg/s, 200 W) [8]

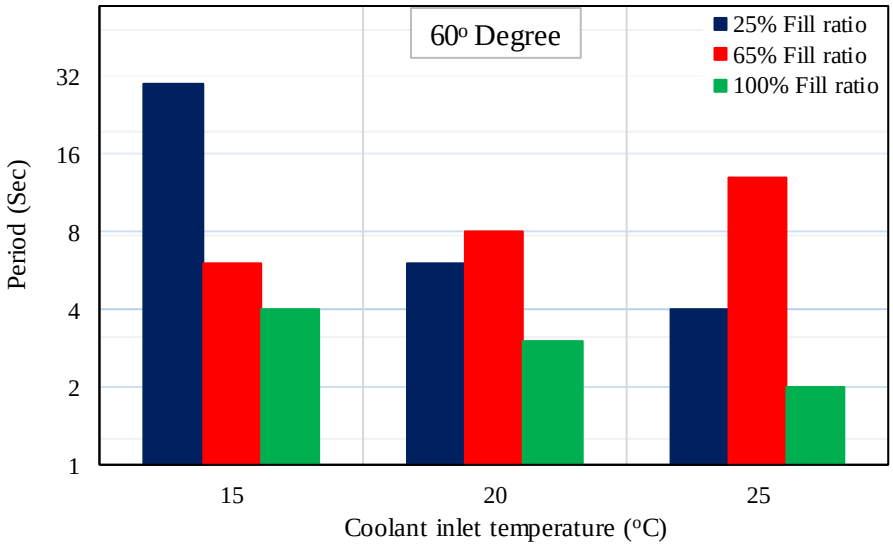

Figure 4.27 Variation of geysering period with coolant inlet temperature at inclination of 60º for three fill ratios (0.0025 kg/s, 200 W) [8]

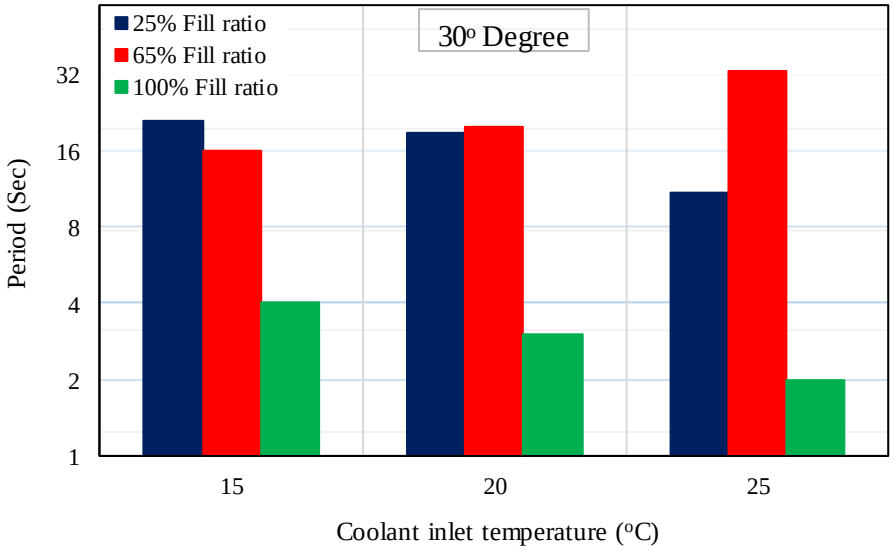

Figure 4.28 Variation of geysering period with coolant inlet temperature at inclination of 30º for three fill ratios (0.0025 kg/s, 200 W) [8]

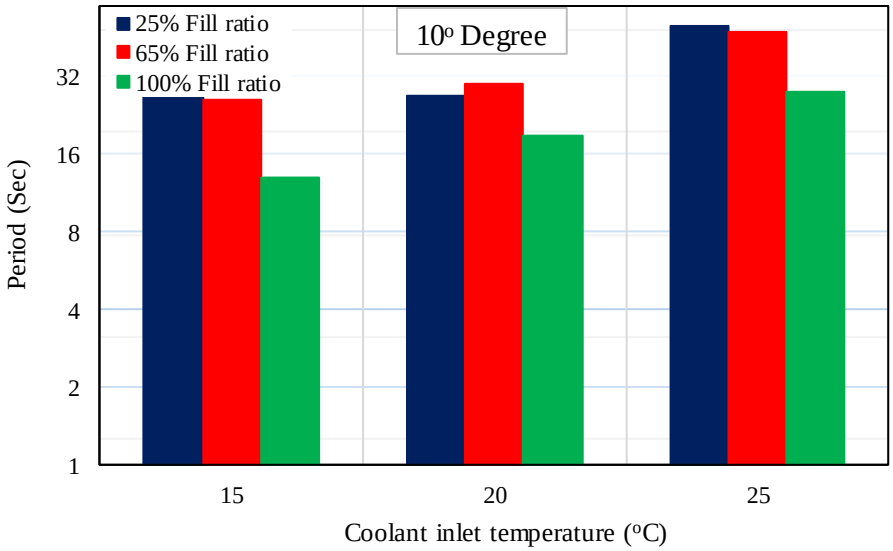

Figure 4.29 Variation of geysering period with coolant inlet temperature at inclination of 10º for three fill ratios (0.0025 kg/s, 200 W) [8]

4.3.2 Geyser Boiling Influence on Thermal Performance of TPCT [2]

The influence of geyser boiling on the heat transfer performance of a TPCT was investigated experimentally under the effect of different fill ratios and inclination angles at a wide range of input energies. This section is published in [2]. The following parameters were considered:

Heat input: 20-400 W

Inclination angle: 10^o, 30^o, 60^o, 90^o

Fill ratio: 25%, 65%, 100%

Coolant mass flow rate: 0.0025 kg/s

Same as in the last section, the symbols T0, T5, T10, T15, and T17 represent the values of thermocouple locations at the evaporator section from the bottom of the evaporator to the top, respectively; and T25, T35, and T40 characterise the values of thermocouples at the condenser section as demonstrated in Figure 4.1.b [2].

4.3.2.1 Geyser Boiling Effect on Temperature Distribution of TPCT Wall [2]

4.3.2.1.1 Fill Ratio 25%

The temperature distribution along the wall of the TPCT at a fill ratio of 25% and a range of heat inputs is shown in Figure 4.30.a, Figure 4.30.b, Figure 4.30.c and Figure 4.30.d at inclinations of 90^o, 60^o, 30^o and 10^o, respectively. It is observed that at an angle of 90^o (Figure 4.30.a), there is a large difference between the temperature values at the bottom of the evaporator (T0 and T5) and those at the top part (T10, T15 and T17) at low heat loads (20, 30, 40, 50 and 60 W). This can be attributed to a low amount of working fluid at a fill ratio of 25% where T0 and T5 are located within the liquid pool; while T10, T15 and T17 are positioned outside the liquid pool so that they are affected by a relatively cold liquid film dropping down from the condenser. This difference decreases as the inclination decreases towards the horizontal orientation, owing to the top part of the evaporator becoming covered with more hot liquid due to a decrease in the inclination, where the lowest difference is noticed at an angle of 10^o [2].

On the other hand, at high heat inputs (200, 300 and 400 W), the trend is reversed at angles of 90^o and 60^o where temperatures of the evaporator's top part T15 and T17 are higher than those at the bottom part, due to the presence of film boiling resulting from high superheat at these positions. This does not happen at angles of 30^o and 10^o because these locations are covered with the liquid pool due to a low inclination angle. It is also seen that the occurrence of the geyser boiling affects the temperature values at the evaporator where they decrease and become more uniform after the geyser effect [2].

For instance, at an angle of 90^o (Figure 4.30.a), after the occurrence of the geyser boiling (occurring at 70 W, the temperature distribution at heat load of 70 W and other heat loads is not plotted in the graph because of the high temperature oscillation), the temperature values of the evaporator's bottom (T0 and T5) at a heat load of 200 W decrease to become equal to

those at a heat input of 60 W; whereas at an angle of 30° (Figure 4.30.c) they decrease to become equal to those at 50 W and less than those at 60 W. In addition, at an angle of 10° (Figure 4.30.d), all evaporator temperatures at 200 W decrease to become approximately equal to those at 70 and 80 W and less than the evaporator temperatures at 90 and 100 W after the occurrence of the geyser boiling [2] .

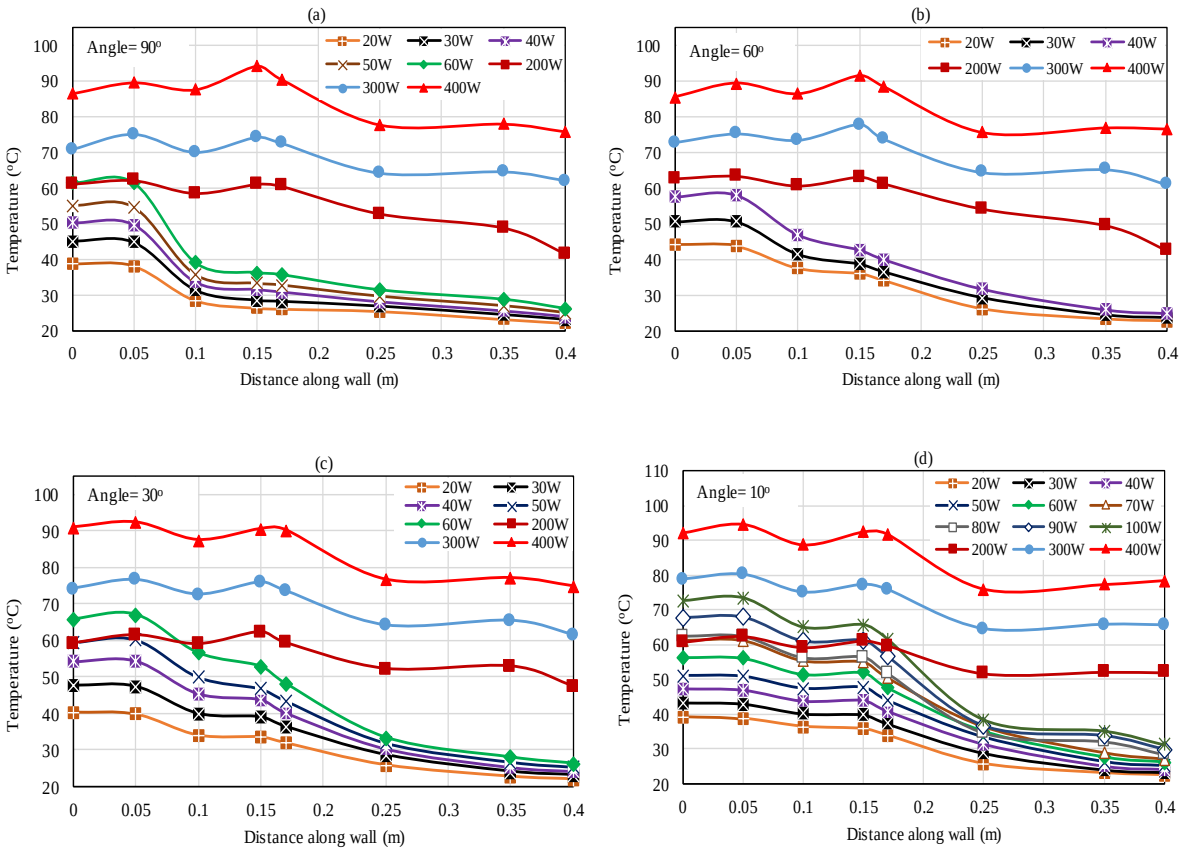

Figure 4.30 Temperature distribution on TPCT's wall at different inclinations and heat loads for a liquid charge 25% [2]

4.3.2.1.2. Fill Ratio 65% [2]

The temperature variation with distance along the wall of the TPCT at a fill ratio of 65% and a range of heat inputs is illustrated in Figure 4.31.a, Figure 4.31.b, Figure 4.31.c and Figure 4.31.d at inclinations of 90, 60, 30 and 10°, respectively. Unlike at a fill ratio of 25%, for low heat inputs, T10 exhibits the same high temperature value as T0 and T5 because of their location within the liquid pool, resulting from the higher amount of the working fluid at a fill

ratio of 65% for all the four angles; while T15 and T17 still show low-temperature values due to their positions away from the liquid pool. Also, at low heat loads, the same temperature trend is observed at the condenser section, as in the case of the fill ratio of 25%. However, at high heat inputs and an angle of 90^{o} (Figure 4.31.a), T40 and T35 exhibit a higher temperature than T25 due to the large thickness of the condensate film resulting from the high evaporation rate. This is also true at angle 60^{o} (Figure 4.31.b) and 400 W and at angle 10^{o} (Figure 4.31.d) and 300 and 400 W. Regarding the effect of geyser boiling, Figure 4.31.a shows that the evaporator temperature at 200 W decreases to become less than that at heat inputs 40 and 50 W after the occurrence of the geysering (occurs at 60 W). Also, at an angle of 30^{o} (Figure 4.31.c), the evaporator temperature at 200 W declines to become equal to that at 40 W after the geyser boiling (occurs at 50 W); whereas at an angle of 10^{o} (Figure 4.31.d), it decreases to become equal to that at 70 W and less than that at 80 W [2].

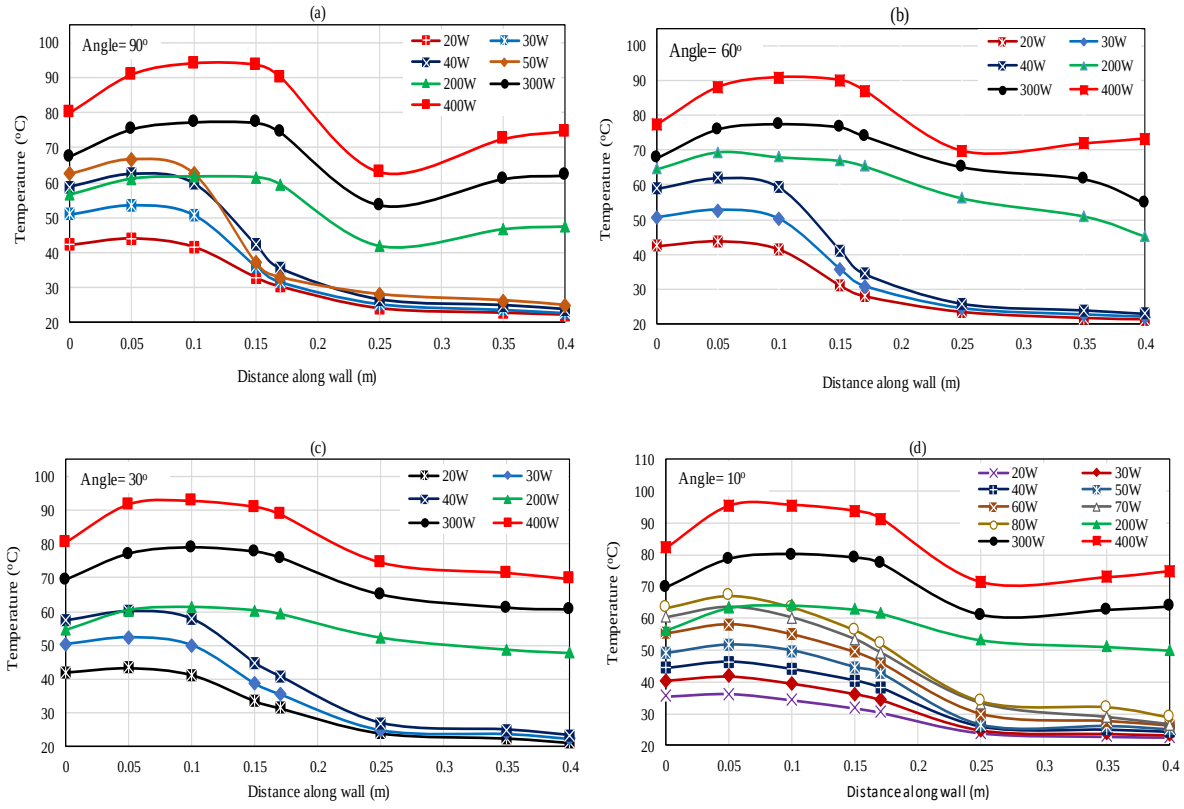

Figure 4.31 Temperature distribution on TPCT's wall at different inclinations and heat loads for a liquid charge 65% [2]

4.3.2.1.3. Fill Ratio 100% [2]

The variation of the wall temperature with distance along the wall of the TPCT at a fill ratio of 100% and a range of heat inputs is presented in Figure 4.32.a, Figure 4.32.b, Figure 4.32.c and Figure 4.32.d at inclinations of 90, 60, 30 and 10^o, respectively. Unlike the cases of fill ratios 25% and 65%, a more uniform temperature distribution at the evaporator is observed for the fill ratio of 100% at low heat loads because T0, T5, T10, T15 and T17 are all located within the liquid pool, where at this fill ratio a higher amount of working fluid is used. However, for the condenser section, a large difference is noticed between the temperature at the end of the condenser (T40) and the temperature at the bottom of the condenser (T25), especially at high heat loads. Figure 4.32.a shows that a significant drop in evaporator temperature is observed after the occurrence of the geyser boiling (occurs at 40 W). This is clearly seen from the lower evaporator temperature at heat inputs 50, 60, 70, 80, 90 and 100 W than that at heat loads of 20 and 30 W, despite the high increase in input energy from 20 to 100 W [2].

At an angle of 60^o (Figure 4.32.b), the reduction in the evaporator temperature can also be seen at heat loads of 90 and 100 W compared with 30 and 40 W due to geyser boiling occurrence (occurs at 50 W). In addition, at an angle of 30^o (Figure 4.32.c), the geyser effect happened at 60 W, thus a lower evaporator temperature is obtained at heat loads 60, 70, 80, 90 and 100 W compared with those at 20, 30, 40 and 50 W. However, at an angle of 10^o (Figure 4.32.d), the geyser effect occurred at 70 W and then disappeared at 80, 90, and 100 W. Therefore, a lower evaporator temperature is obtained only at 70 W compared with those at 30, 40, 50, 60, 80, 90 and 100 W; whereas the evaporator temperature at 200 W becomes lower than that at 90 and 100 W due to occurrence of the geyser boiling again at 120W [2].

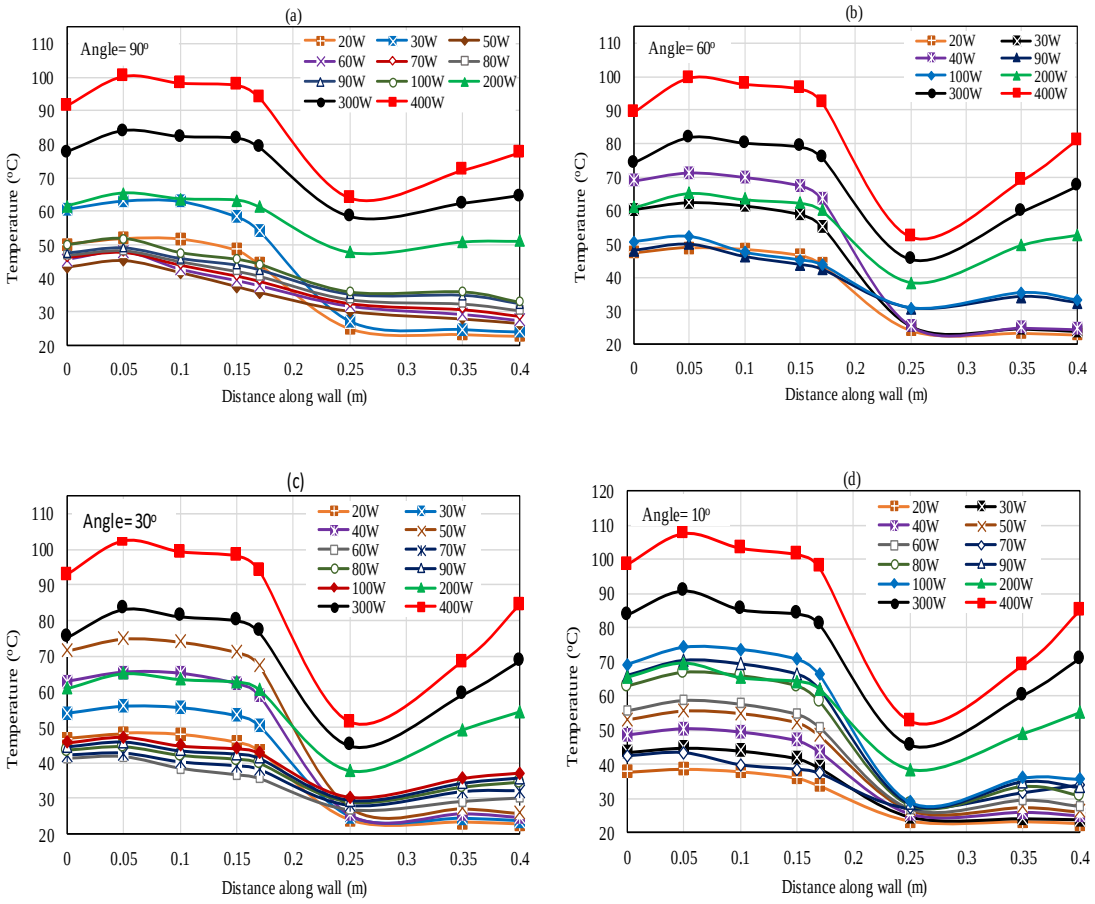

Figure 4.32 Temperature distribution on TPCT's wall at different inclinations and heat loads for a liquid charge 100% [2]

Figure 4.33 shows the effect of the geyser boiling occurrence on the temperature distribution along the wall of thermosiphon at three fill ratios, a heat input of 50 W and an angle of 90º. It presents the temperature profile at fill ratios of 25% and 65% where the geyser boiling still does not occur and after its occurrence at a fill ratio of 100%. It is shown that a significant decrease in the evaporator temperature is obtained at a fill ratio of 100% after the occurrence of the geyser effect (occurs at 40 W) compared with that at fill ratios 25% and 65% at the same heat load. It is also seen that a more uniform temperature distribution in the evaporator is achieved after the occurrence of the geysering at a fill ratio of 100%. In addition, a higher temperature is obtained at the condenser section for the fill ratio of 100% compared with 25% and 65% due to the occurrence of the geyser boiling [2].

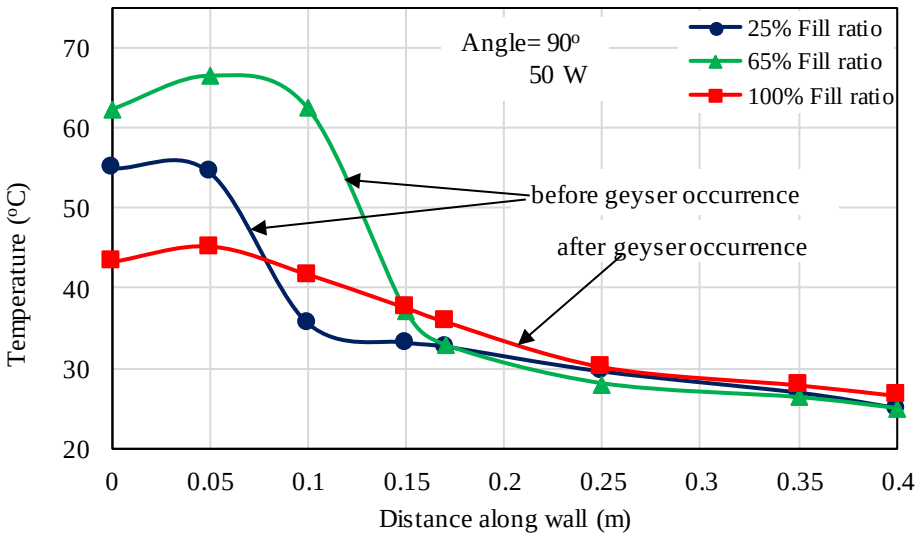

Figure 4.33 Temperature distribution on TPCT's wall at different liquid charges (50 W, 90º) [2]

The influence of the occurrence of the geyser phenomenon on the wall temperature distribution for two fill ratios of 25% and 100% is presented in Figure 4.34 at a heat load of 60 W and an angle of 30º. The wall temperature distribution for the fill ratio of 65% is not shown in Figure 4.34 because of a high oscillation in the thermosiphon wall temperature at 60 W so that the temperature distribution cannot be obtained. Figure 4.34 shows that a considerable reduction in the evaporator temperature is observed for a fill ratio of 100% due to the occurrence of the geyser boiling compared with that at a fill ratio of 25% where the geysering does not occur at a heat load of 60 W. As in Figure 4.33 and Figure 4.34, Figure 4.35 shows the effect of the geyser boiling on the evaporator wall temperature at a heat input of 70 W and an angle of 10º for three different fill ratios. Similar to Figure 4.33 and Figure 4.34, the occurrence of the geyser boiling produces a lower evaporator temperature at a fill ratio of 100% compared with that at fill ratios of 25% and 65% where no geysering occurs. Also, higher condenser wall temperatures are obtained for T35 and T40, while a lower temperature is attained for T25 compared with that at fill ratios of 25% and 65% [2].

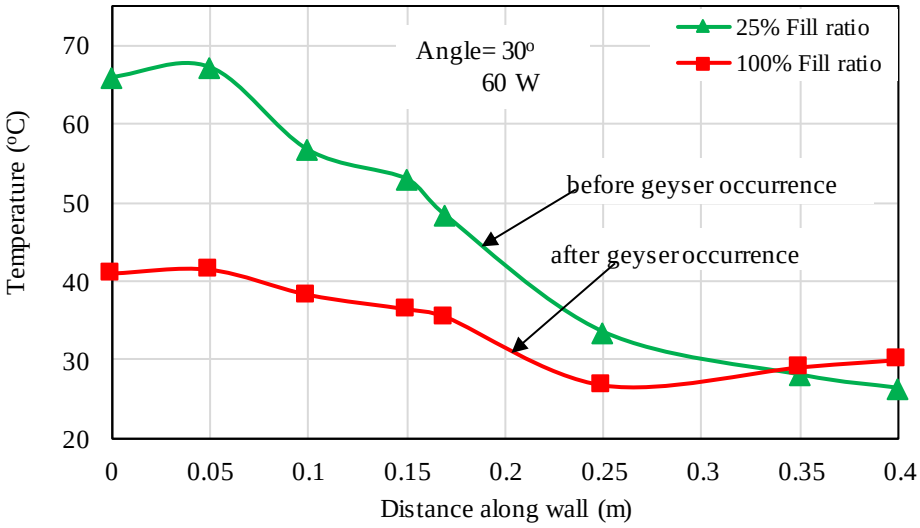

Figure 4.34 Temperature distribution on TPCT's wall at different liquid charges (60 W, 30º) [2]

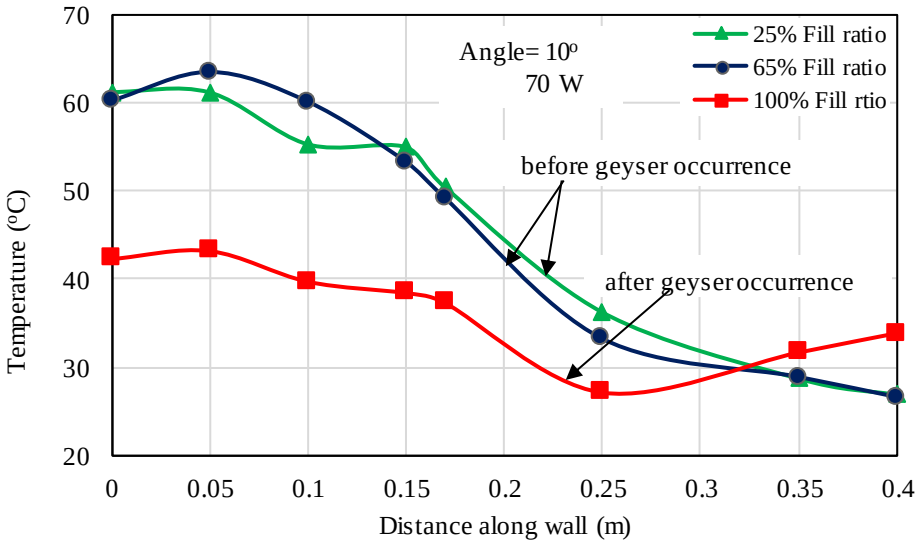

Figure 4.35 Temperature distribution on TPCT's wall at different liquid charges (70 W, 10º) [2]

From the variation of temperature distribution at different fill ratios, inclinations and heat loads a more uniform temperature is achieved after the occurrence of geyser boiling. At fill ratios of 25% and 65%, this uniform temperature distribution can be obtained at high heat inputs, especially, at 200 W and tilt angles of 30 and 10º. On the other hand, at a fill ratio of 100%, the uniformity of the wall temperature is achieved at medium heat loads, 50, 60, 70, 80, 90 and 100 W at an angle of 90º; at 90 and 100 W at an angle of 60º; at 60, 70, 80, 90 and

100 W at an angle of 30°; and 70 W at an angle of 10° [2]. This uniform distribution in the wall temperature of the TPCT plays an important role in improving the thermal performance of the solar water collector, especially with the flat plate type where the uniform surface temperature reduces the heat losses significantly; thereby this increases the heat gain and thermal efficiency of the collector [11].

4.3.2.2 Effect of Geyser Boiling on Thermal Resistance [2]

The total thermal resistance of the TPCT can be determined using the following equations:

$$R_{th} = \frac{T_e - T_c}{Q_{in}} \quad 4.7$$

$$T_e = \frac{T0 + T5 + T10 + T15 + T17}{5} \quad 4.8$$

$$T_c = \frac{T25 + T35 + T40}{3} \quad 4.9$$

And

$$Q_{in} = VI \quad 4.10$$

Where R_{th} is the total thermal resistance of the TPCT; T_c and T_e and are the condenser and evaporator average wall temperatures, respectively; Q_{in} is the heat input; and V and I are the circuit voltage and current, respectively [2].

Thermal Resistance

The variation of the total thermal resistance of the TPCT with the heat load for three different fill ratios is illustrated in Figure 4.36.a, Figure 4.36.b, Figure 4.36.c and Figure 4.36.d at inclination angles of 90, 60, 30 and 10°, respectively. Figure 4.36.a shows that the fill ratio of 100% exhibits the highest thermal resistance at heat inputs 20 and 30 W, and 65% is the second highest at heat loads of 20, 30, and 40 W; whereas the lowest thermal resistance is shown for the fill ratio of 25% at heat inputs 20, 30 and 40 W, where all these values represent the thermal resistance before the occurrence of the geyser boiling [2]. However,

after the geyser boiling occurs, the thermal resistance for the fill ratio of 100% drops significantly from about twofold that at a fill ratio of 25% to become the lowest thermal resistance at heat inputs 50, 60, 70, 80, 90 and 100 W which are enclosed by a circle. Then, at high heat loads (300 and 400 W), the thermal resistance for the fill ratio 100% returns to being higher than that for 25% and 65% where the geysering almost disappears [2].

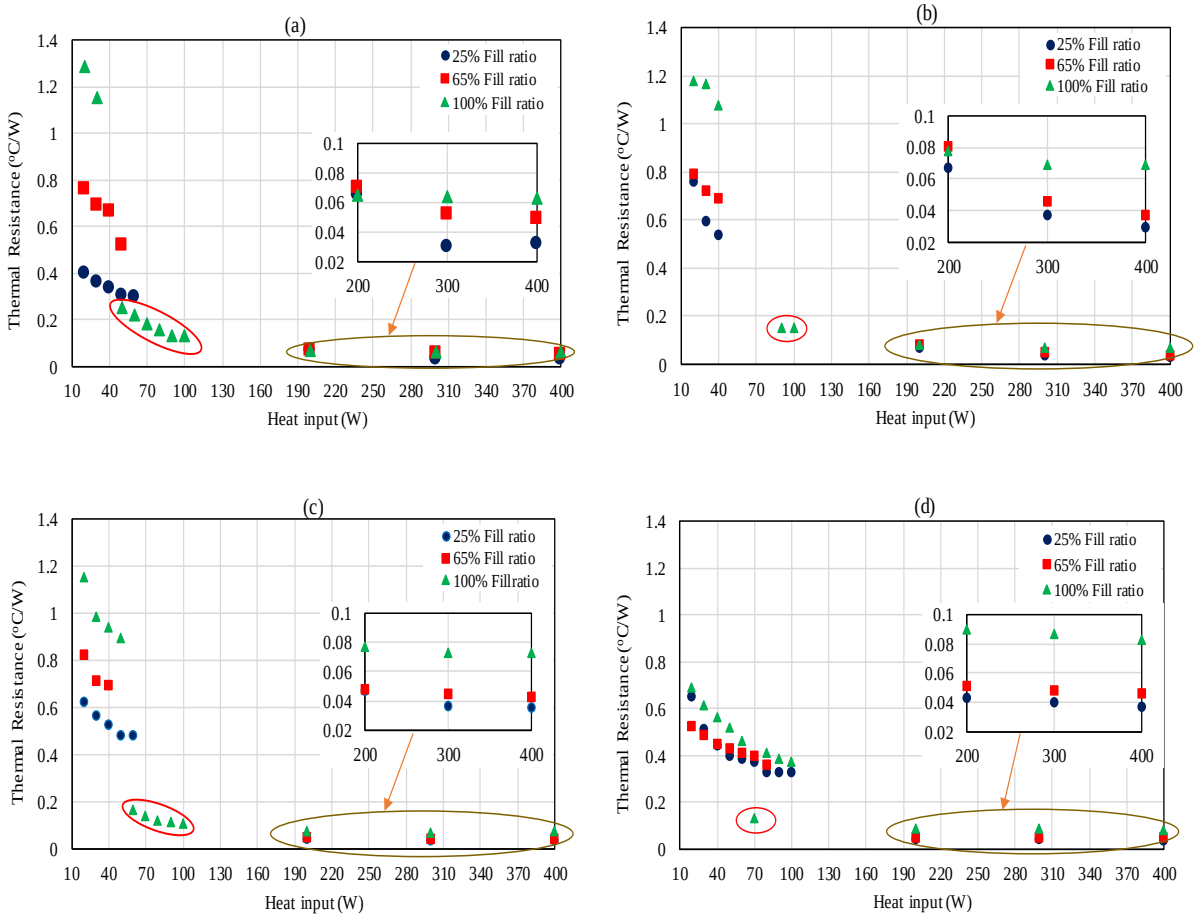

Figure 4.36 Thermal resistance against heat input at three liquid charges and different angles: (a)-90º, (b)-60º, (c)-30º and (d)-10º [2]

At an angle of 60º, greater thermal resistance is observed for the fill ratio of 25% compared with that at angle of 90º as shown in Figure 4.36.b. Figure 4.36.b also shows a higher thermal resistance for the fill ratio of 100% compared with that at 25% and 65% at low heat inputs 20, 30 and 40 W before the occurrence of the geyser boiling. However, after the occurrence of the geyser effect, at fill ratio of 100%, a significant reduction in the thermal resistance at heat

loads 90 and 100 W is obtained (enclosed by a circle). When the geysering almost disappears at heat inputs 300 and 400 W, the thermal resistance for the fill ratio of 100% again becomes higher than those at 25% and 65%. The same trend is noticed at an angle of 30^{o} (Figure 4.36.c), but the highest thermal resistance for the fill ratio of 100% is obtained at input energies 20, 30, 40 and 50 W; while it exhibits significantly lower thermal resistance at heat inputs 60, 70, 80, 90 and 100 W, after the geyser boiling occurs [2].

At an angle of 10^{o}, Figure 4.36.d shows that the thermal resistance for the fill ratio of 25% is higher than that for the fill ratio of 65% at low heat loads 20 and 30 W [2]. Also, less difference in thermal resistance is observed between the three fill ratios than that at angles 90, 60 and 30^{o}, due to the low inclination from the horizontal orientation. Figure 4.36 also shows a significant decrease in the thermal resistance at a heat input of 70 W and 100% fill ratio due to the occurrence of the geyser boiling. Then, when the geysering disappears at a heat input of 80 W, the thermal resistance for the fill ratio of 100% returns to its trend before the geysering to become the highest, despite another occurrence of the geyser boiling at 120 W. It is also seen that for the fill ratio of 25% and the angle 10^{o,} the thermosyphon reaches its heat transfer limit (boiling heat transfer limit which represents the critical heat flux) at a heat load of 90 W before the occurrence of the geyser phenomenon. This is shown by the increase in the thermal resistance as the heat load increases at 90 and 100 W. However, this heat transfer limit is improved considerably at higher heat loads after the occurrence of geyser boiling. In addition, unlike at angles 90 and 60^{o}, at a heat input of 200 W, the difference in thermal resistance between the fill ratio of 100% and that for 25% and 65% increases due to the low inclination where some liquid is expected to cover the condenser wall at the point T25 [2].

Figure 4.36 (a-d) also show that for the fill ratio of 100%, the thermal resistance decreases as the tilt angle decreases at low heat loads, while it increases as the angle decreases at high heat loads. This may be explained by the decrease in liquid depth as the inclination decreases,

which allows the generation of more vapour leading to the removal of more heat and a reduction in the evaporator wall temperature, thereby decreasing the thermal resistance [2]. On the other hand, at a high heat input, the wall temperature increases as the angle decreases because some parts of the evaporator wall are not occupied by liquid at a low inclination, causing poor heat transfer from the wall at high heat input and thus, higher thermal resistance. For the fill ratio of 65%, no obvious difference in thermal resistance is observed at angles of 90, 60 and 30^o at low heat inputs; while a lower thermal resistance is obtained at an angle of 10^o compared with other angles [2]. However, the fill ratio of 25% shows an opposite trend to other fill ratios, where at low heat loads, the lowest thermal resistance is observed at the vertical orientation; and at the angle of 10^o, the thermal resistance is higher than that for the fill ratio of 65% [2]. In addition, at high heat inputs, lower thermal resistance is achieved at all inclinations compared with fill ratios 65% and 100% owing to the higher evaporation rate obtained with a small amount of working fluid which increases the vapour pressure; thereby enhancing the evaporation heat transfer coefficient [110].

Therefore, the obtained significant reduction in the thermal resistance just after the occurrence of geyser boiling, especially at the fill ratio of 100% and medium heat loads can considerably increase the heat transfer capacity and reduce heat losses of the TPCT. This will also guarantee prevention of the occurrence of the dry-out issue due to a large amount of working fluid (100% fill ratio). Thus, this can be utilised in suitable applications to greatly improve its heat transfer performance [2].

Evaporator Wall Temperature

The variation of the evaporator's average wall temperature with heat input for three fill ratios is presented in Figure 4.37.a, Figure 4.37.b, Figure 4.37.c and Figure 4.37.d at inclination ingles of 90^o, 60^o, 30^o and 10^o, respectively. At some heat inputs where the geysering just occurs, the evaporator average wall temperature cannot be calculated due to a very high temperature oscillation, so these data points do not appear in the graphs. Figure 4.37.a shows that the evaporator temperature increases with heat load for the three fill ratios at low heat inputs before the occurrence of the geyser boiling, where the fill ratio of 100% exhibits the highest temperature [2]. However, after the occurrence of the geysering, at a heat load of 50 W (the evaporator average wall temperature can not be calculated at heat input 40 W due to a very high temperature oscillation) , the evaporator temperature for the fill ratio of 100% decreases from 60^oC to 40^oC despite the increase in the heat load from 30 to 50 W. On the other hand, for the fill ratios of 25% and 65%, the evaporator temperature continues increasing abruptly until the geyser boiling occurs at 60 and 70 W (missing data points), respectively. Subsequently, the rate of increase of the evaporator temperature decreases due to the occurrence of the geyser boiling. Consequently, at high heat loads, the evaporator temperature for the fill ratio of 100% again becomes higher than that for 25% and 65% due to geysering disappearance [2].

At an angle of 60^o (Figure 4.37.b), the evaporator temperature for the three fill ratios increases with the heat input at low heat loads of 20, 30 and 40 W; again the temperature for the fill ratio of 100% is higher than for the others. Then, the geyser boiling occurs at 50 W for the three fill ratios, so the evaporator temperature for 100% drops noticeably from about 68^oC at 40 W to about 45^oC at 90 W, regardless of a 50 W increase in input energy; whereas it is difficult to report the evaporator temperature at fill ratios of 25% and 65% due to sever temperature oscillation (missing data points) [2].

Figure 4.37.c shows that the evaporator temperature for the fill ratio of 100% and at 50 W is higher than that for 25% by about 20^{o}C before the geyser boiling; while after the geysering occurs at 60 W, the temperature for the fill ratio of 100% becomes lower by about 20^{o}C than that for 25%, where the geyser effect did not happen yet. At an angle of 10^{o} (Figure 4.37.d), for heat inputs from 20 to 100 W, the geyser boiling only occurs at 70 W and a fill ratio of 100%; thereby the evaporator temperature decreases by about 18^{o}C compared with that at 25% and 65%. Also, after the heat input of 100 W, the geyser boiling occurs causing a reduction in the evaporator temperature at a heat load of 200 W for the three fill ratios and then increases again with the heat load [2].

Additionally, Figure 4.37(a-d) show that for the fill ratio of 100% and heat inputs of 20 and 30 W, the evaporator average temperature decreases as the inclination decreases. For a higher heat input, the change of average temperature with the inclination depends on a heat input at which the geyser effect occurs. Generally, geyser boiling occurs at a higher heat input as the inclination angle decreases. This causes a large difference in the average evaporator temperature at a certain heat input as the inclination decreases for the same fill ratio (100%) [2]. For instance, at angle 90^{o}, geysering occurs at a heat load of 40 W and the corresponding average temperature is about 40^{o}C, while at angle 60^{o}, it does not occur at 40 W, so, the average temperature increases to about 68^{o}C. Similarly, at angles 30^{o} and 10^{o}, it delayed in to 60 and 70 W, so that the average temperature at 40 W are 62 and 48^{o}C respectively, which are higher compared with that at an angle of 90^{o}. On the other hand, for high heat inputs (200, 300 and 400 W) and all inclinations, the average evaporator temperature for a fill ratio of 100% is higher compared with that for 25% and 65%. In addition, for fill ratios of 25% and 65%, no obvious difference in the average temperature is observed between them at high heat loads for all angles [2].

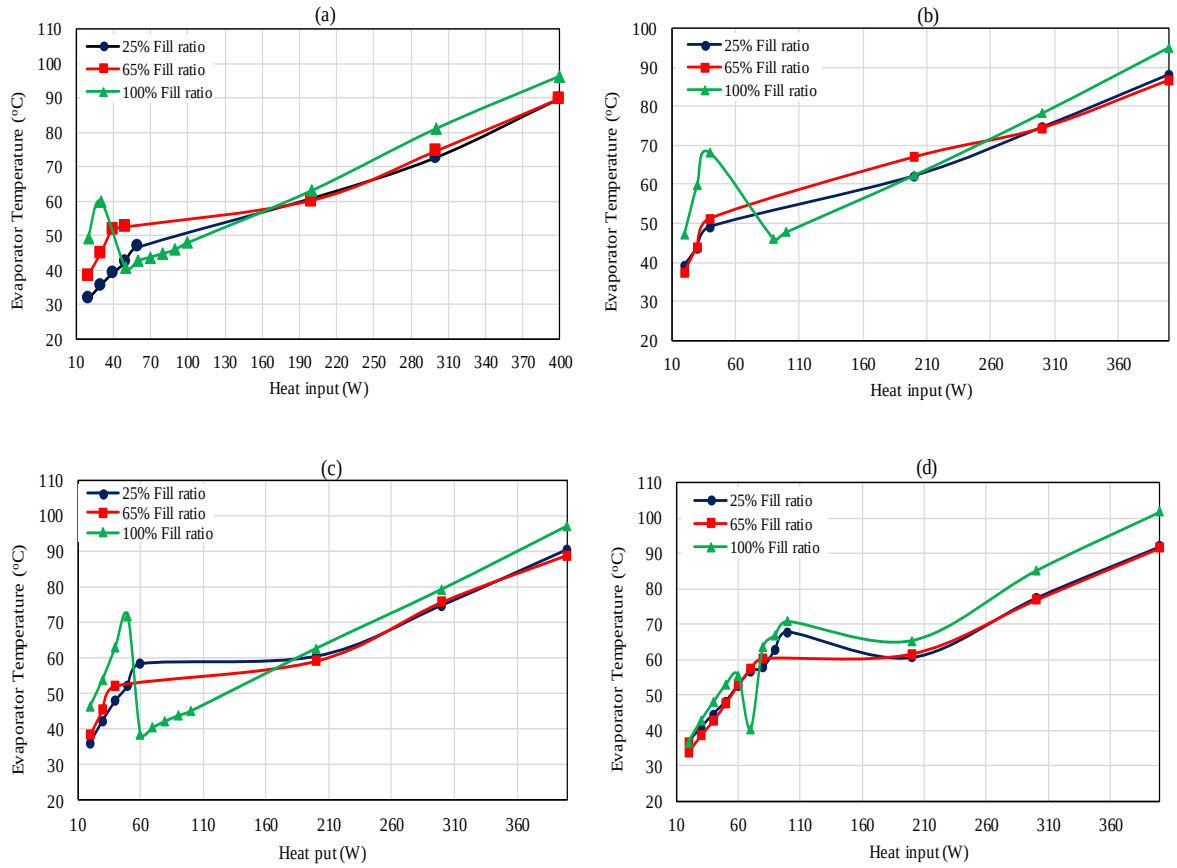

Figure 4.37 Variation of thermal resistance with evaporator average wall temperature at three liquid charges and different angles: (a)-90º, (b)-60º, (c)-30º and (d)-10º [2]

Condenser Wall Temperature

The variation of the condenser's average wall temperature with heat input for three fill ratios is shown in Figure 4.38.a, Figure 4.38.b, Figure 4.38.c and Figure 4.38.d at tilt angles of 90º, 60º, 30º and 10º, respectively. It is observed that the wall temperature of the condenser increases as the heat load increases for all fill ratios and inclination angles. Figure 4.38.(a-d) also show that the difference in the condenser's wall temperature between the three fill ratios is larger at high heat inputs compared to that at low heat loads [2]. Regarding the effect of the geyser boiling, it is concluded from Figure 4.38.(a-d) that there is no clear effect of geysering on the condenser wall temperature where it almost increases linearly with the heat load after the occurrence of the geyser boiling for all fill ratios and inclinations. Therefore, the effect of the geyser boiling on the performance of the thermosiphon heat pipe is produced from the

significant change in the evaporator's wall temperature, rather than the condenser's wall temperature [2].

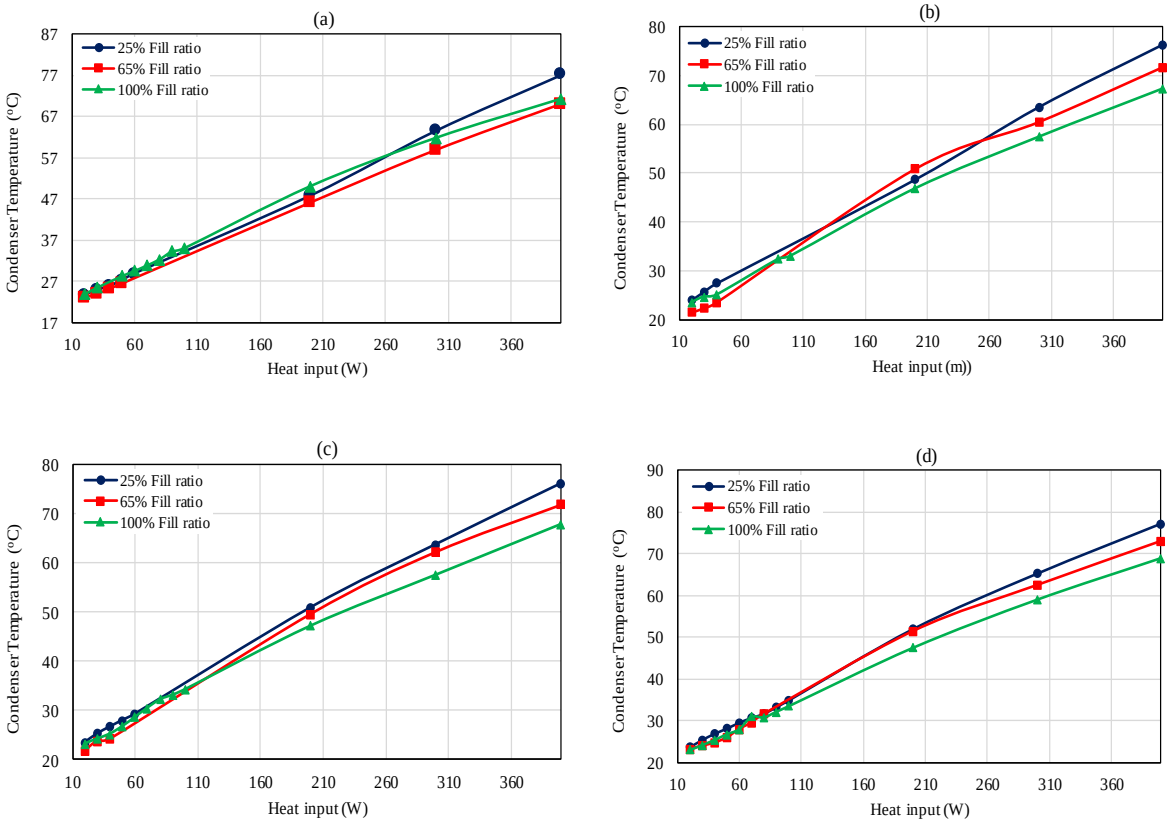

Figure 4.38 Variation of thermal resistance with condenser average wall temperature at three liquid charges and different angles: (a)-90°, (b)-60°, (c)-30° and (d)-10° [2]

4.4 Summary

An experimental test rig was developed to test three TPCTs with three different fill ratios (25%, 65% and 100%). Each TPCT was examined at four different inclinations (10°, 30°, 60° and 90°) and at every inclination, the TPCT was tested at a wide range of heat inputs (20-400 W). Also, the test was carried out at various coolant flow rates and inlet temperatures for all inclinations and fill ratios and a heat load of 200 W. These tests were conducted to investigate the geyser boiling, a two-phase phenomenon under influence of all mentioned parameters to report the temperature oscillation and the occurrence and period of the geysering inside the TPCT which is important in optimising of such adevice. Then, the heat transfer characteristics of the TPCT was investigated during the occurrence of the geyser boiling. Consequently, the

TPCT's thermal performance was compared before and after the occurrence of the geysering. The following outcomes can be given:

4.4.1 Effect of Different Parameters on Geyser Boiling [8]

1- The occurrence of the geyser boiling at any heat input highly depends on the fill ratio and the orientation of the TPCT. Generally, for fill ratio 100%, it occurs at a lower heat load compared with smaller fill ratios (25% and 65%) for all inclination angles. On the other hand, the geyser effect occurs at a higher heat input for the orientation near the horizontal (10^o) than that at the vertical position [8].

2- At heat loads of 200, 300 and 400W, the geyser effect almost disappears at angles of 90 and 60^o for the three fill ratios as well as at 30^o only for 100%, while it still occurs at angle of 30^o for filling charges of 25% and 65%, and at 10^o for the three fill ratios [8].

3- Generally, the period of geyser boiling decreases as the heat input increases for all inclination angles and fill ratios. However, at relatively medium heat inputs (60,70, 80, 90, and 100W) the period may increase and then decrease with increasing the heat load, which varies as the fill ratio and inclination angle varies [8].

4- At angles of 90^o, 30^o and 10^o, a lower period is observed for the fill ratio 100% at almost all heat inputs compared with that for fill ratios of 25% and 65%. On the other hand, at the angle 60^o, a higher period is obtained for the liquid charge of 100% at heat inputs of 50, 60, 70 and 80W and lower for higher heat inputs compared with that for fill ratios of 25% and 65% [8].

5- At high heat loads (200, 300 and 400W), a very low period is found at angles of 90 and 60^o for fill ratios of 25% and 65% and at angles of 90^o, 60^o and 30^o for 100%. However, a significant increase in the period is observed at angles of 30 and 10^o for liquid charges of 25% and 65% and at 10^o for 100% [8].

6- At angles of 90^o and 60^o, the period increases as the coolant mass flow rate increases for fill ratios 25% and 65%, whereas for fill ratio of 100%, the period is not affected by the

change in the flow rate. In addition, at the angle 30^o, the same trend is obtained for fill ratios of 25% and 100%, while for the fill ratio 65%, the trend is reversed in which the period decreases with increasing the flow rate. On the other hand, at the angle 10^o, a reversed trend is obtained for the fill ratio 25% where the period decreases with the increase of the flow rate for all the three fill ratios [8].

7- Regarding the effect of the inlet temperature of the cooling water, for the fill ratio 65%, the period increases with increasing the inlet temperature at all the four angles. This is also true for fill ratios of 25% and 100% at the angle 10^o only. However, at angles of 90^o, 60^o and 30^o and for fill ratios of 25% and 100%, the period decreases as the inlet temperature increases. In addition, for fill ratio of 25% and 100%, a small period is obtained at angles of 90 and 60^o and inlet temperatures of 20 and 25^{o}C. This is also true for the fill ratio 100% at the angle 30^o [8].

4.4.2 Effect of Geyser Boiling on Thermal performance of the TPCT [2]

1- More uniform temperature distribution is obtained after the occurrence of the geyser boiling [2].

2- A significant drop in the evaporator's temperature is obtained after the occurrence of the geyser boiling in which a lower temperature is attained despite the increase in the heat load. This reduction in the evaporator's temperature depends on the orientation and the fill ratio [2].

3- It is observed that a fill ratio of 100% exhibits the highest thermal resistance before the occurrence of the geyser effect at low heat inputs. However, after the occurrence of the geyser boiling, the thermal resistance drops considerably to become lower than that for 25%. This reduction in the thermal resistance can also be seen at other inclinations, but at different heat loads and at different rates [2].

4- Before the occurrence of the geyser phenomenon, at an angle of 10^o and a fill ratio of 25%, the thermosyphon reaches its heat transfer limit. After its occurrence, however, the heat transfer limit of the TPCT improves remarkably [2].

5- The reduction in the thermosyphon thermal resistance due to the occurrence of the geyser boiling results from the significant change in the evaporator's wall temperature rather than the condenser's wall temperature [2].

Chapter 5

5. Enhancing the TPCT Thermal Performance by changing Surface Characteristics

5.1 Introduction

Energy demand has increased rapidly worldwide due to inefficient use and conversion of energy in different applications. Therefore, reduction of losses and enhancing heat transfer processess in energy systems have become an essential area of research in recent years. Heat pipes offer an effective way to transfer thermal energy by utilising the latent heat of the working fluid by means of evaporation and condensation passively in a closed container.

Several research works have been carried out to investigate enhancing the thermal performance of heat pipes using two different techneques as reviewed in chapter 2. The first technique employs addition of nano metalic particles of the working fluid to increase its thermal conductivity and the heat pipe performance. The second method has focused on modifying the inner surface characteristics of the evaporator and condenser either mechanically or chemically to augment the heat transfer performance of the heat pipe. As has been concluded from the review of the previous work, some of these methods suffer from some difficulties and disadvantages related to time and cost of the manufacturing process.

Therefore, in this chapter, a new method is employed to enhance the thermal characteristics of the TPCT and tested experimentally. This method involves making roughness on the internal surface of the TPCT using Electrical Discharge Machine (EDM) to enhance the phase-change characteristics, thereby enhancing the performance of the TPCT. This is carried out by comparing the internally resurfaced copper thermosyphon performace with a normal copper thermosyphon at two different initial sub-atmospheric pressures and a range of heat inputs.

5.2 Experimental Work

5.2.1. Manufacture of the Rough Surface [178]

Electrical Discharge Machining (EDM) or Spark Erosion Machining (SEM) was used to make a surface roughness inside a tube with a 200 mm length, 12.7 mm outside diameter and 1.6 mm thickness. This machine generates an electrical spark between a cutting wire (electrode) and a sample material. The spark indicates the flowing of the electrical power through the wire. Thus, the material (workpiece) starts melting due to the intensively produced heat which produces a very high temperature of 8000 to 12000 ^{o}C. The spark is controlled and positioned cautiously in order to machine only the material surface as shown in Figure 5.1. Deionized water is always used as a dielectric medium for the spark in the case of the wire EDM. Water not only functions as a coolant but also to remove the eroded material away from the surface. The wire diameter is between 0.1-0.3 mm and is made either from brass or copper. Also, the electrode (wire) must not be in direct contact with the sample material and the workpiece must be electrically conductive. The minimum eroded thickness is 0.00254 mm and the maximum is 0.051 mm per one pass [179], [178].

Figure 5.1 Working principles of EDM [179]

5.2.2 Measurement of Surface Roughness

The resulting roughness was measured using Mitutoyo Surftest SJ-310 tester in terms of two parameters. The first is the arithmetical mean roughness value Ra which represents the average distance between the valleys and peaks and the deviation from the mean line throughout the surface and along the length of the surface. The second is the mean roughness depth Rz which represents the average of five sampling lengths by indicating the vertical

distance between the deepest valley and highest peak for each sampling length [178]. The two roughness parameters Ra and Rz are illustrated in Figure 5.2a and b, respectively [180]. For heat transfer enhancement of the boiling process, values of individual valleys and peaks are considered important because they increase the density of nucleation sites and the heat transfer area. Therefore, the importance of the surface roughness in such a case is indicated by Rz more than Ra which almost ignores the effect of individual peaks and valleys due to its dependence on the mean value of the entire shape.

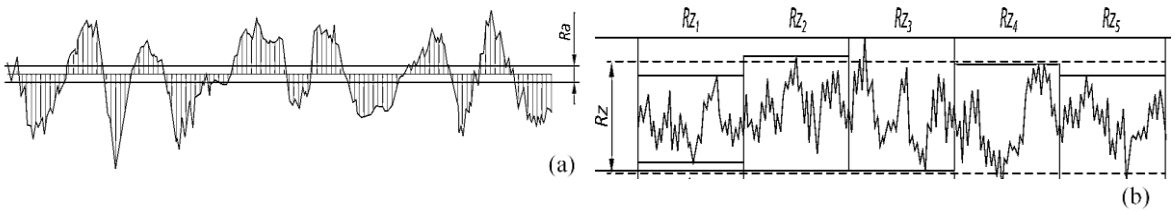

Figure 5.2 -(a) Ra and (b) Rz [180]

The surface roughness was measured at five different positions on the sample surface for a rough and plain surfaces. Table 5.1 illustrates values of Ra and Rz for the rough and plain surfaces. It can be seen that values of Ra and Rz for the rough surface are more than one order of magnitude greater than those of the plain surface [178].

Table 5.1 Values of Ra and Rz [178]

	Rough surface		Plain surface	
Item	Ra (µm)	Rz (µm)	Ra (µm)	Rz (µm)
1	2.935	15.256	0.289	1.89
2	3.658	22.268	0.278	1.764
3	3.675	20.460	0.275	1.687
4	3.664	21.568	0.275	1.67
5	3.639	21.376	0.281	1.82

Alicona infinitefocus machine (see Figure 5.3) is used to provide a three-dimensional micro picture for the plain and rough surfaces as shown in Figure 5.4 a and b, respectively. The measure sample length is 800 µm. Almost unlimited range of surface sizes can be measured using Alicona device due to the adjusting of LED ring light and employing of coaxial lighting. High accuracy, repeatability and resolution measurements can be achieved and accessed. Also, the device provides an automatic adjusment of optimal measuring parameters, so, there is no need to set these parameters after each use for different surface samples [181].

Figure 5.3: Alicona infinitefocus system

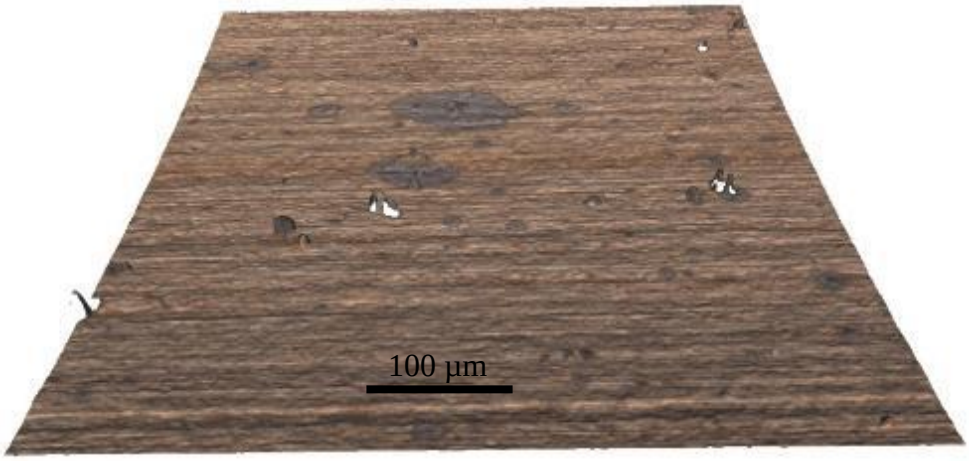

Figure 5.4-a: Plain surface

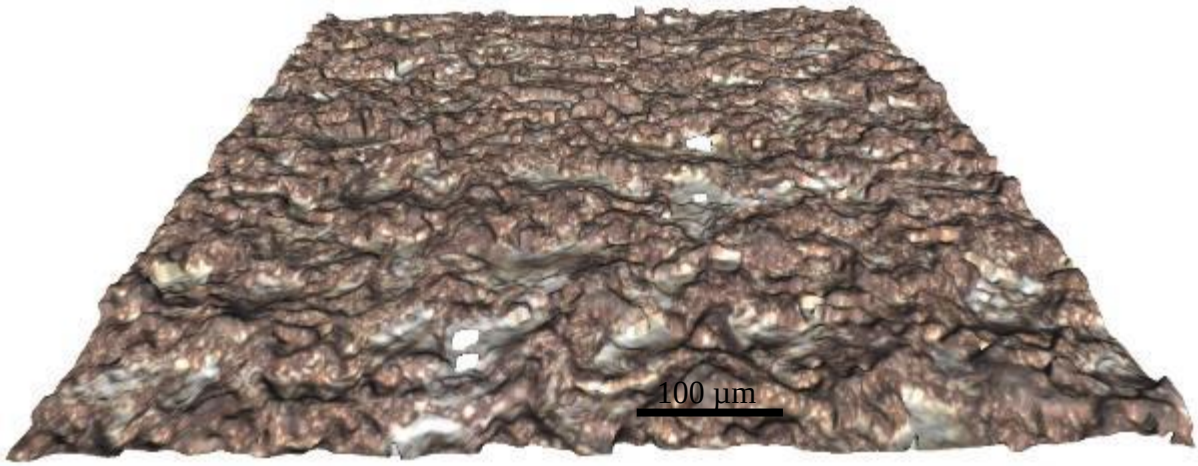

Figure 5.4-b: Rough surface

5.2.3 Measurement of Contact Angle

Two pieces of the rough and plain surfaces were used to measure their contact angles with water. The contact angle was measured using an optical tensiometer-contact angle meter as shown in Figure 5.5 [178]. This commonly used technique directly measures the tangent angle at the contact point of the three-phase (solid-liquid-air) on a sessile drop profile. The device consists of a micrometer pipette to form a liquid droplet, sample mounting stage to mount the sample, telescope and a lighting source. Also, a motorised syringe is used to add or remove the liquid used.

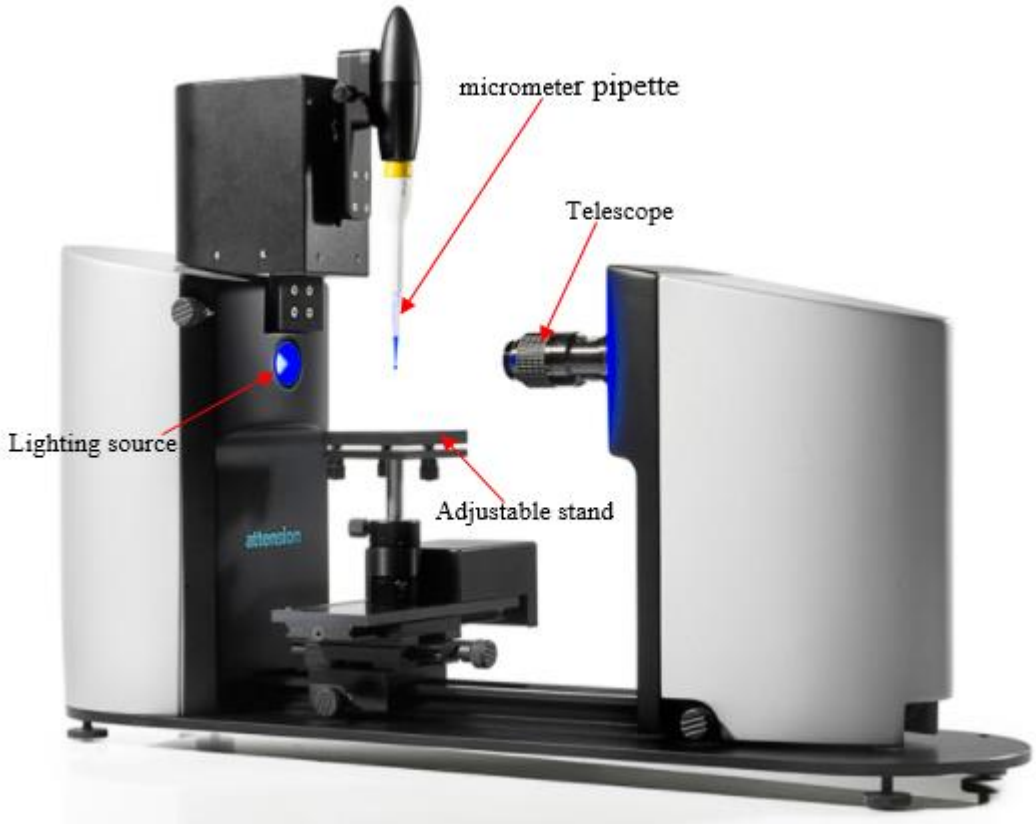

Figure 5.5 Optical tensiometer

The contact angle can be measured by adjusting the sessile drop tangent at the liquid-solid interface and read the resulting value. The maximum sample size is 200 mm in length and 45 mm in height including the stage height [173]. The measured contact angles for the rough and plain surfaces are shown in Figure 5.6 a and b, respectively.

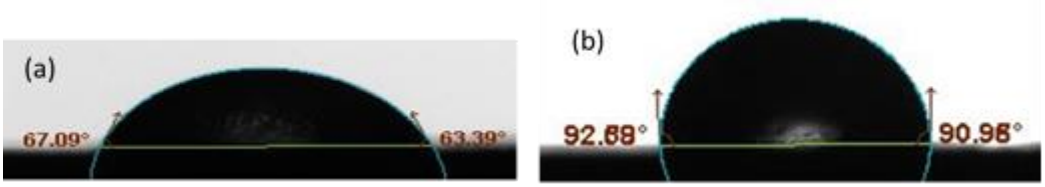

Figure 5.6 Measured contact angle for: (a) Rough and (b) plain copper surfaces [178]

5.2.3 Heat Pipe Fabrication

After the roughness was made on the entire internal wall of the tube, the resulting rough tube and another plain copper tube were employed to fabricate two thermosyphon heat pipes (TPCTs). The process starts by rinsing the two tubes many times with ethanol to remove any grease or other contaminants, then washing with deionised water to ensure that all ethanol was removed. Then, a three-way valve with a vacuum pressure gauge was welded to the condenser end of the TPCT to enable evacuating and charging as shown in Figure 5.7. To ensure that no contaminants remained due to the welding process, the two TPCTs were washed again with deionised water many times. Then the end cap of the evaporator was welded to form the closed TPCT [178].

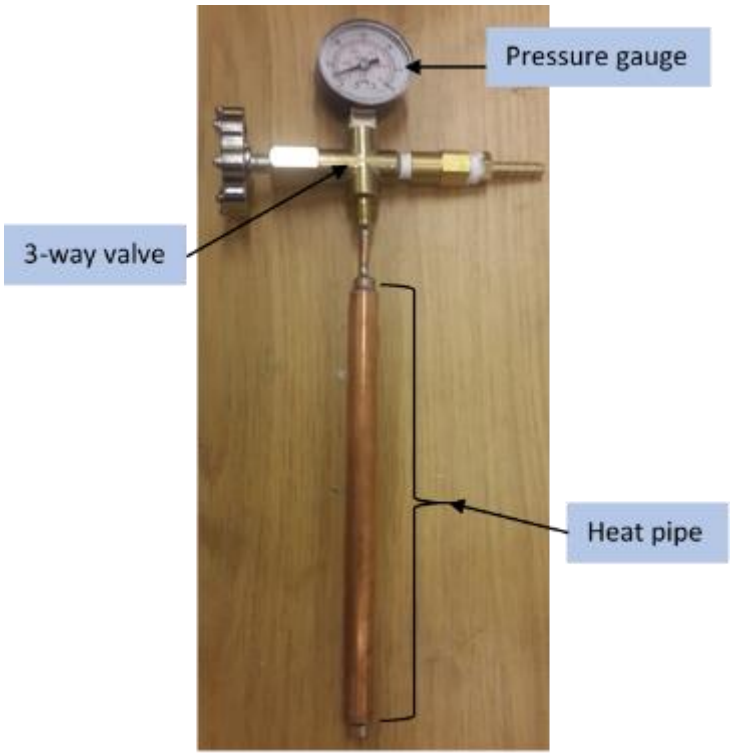

Figure 5.7 A TPCT with three-way valve and pressure gauge

The two proposed thermosyphons were evacuated to desired pressure (3 kPa or 30 kPa, these two initial pressures were used to examine the effect of the presence of non-condensable gases on the thermal performance of the TPCT) using a vacuum pump. A dual stage, oil lubricated vacuum pump, model ECVP 3400 with a capacity of 750 W (see Figure 5.8) was

connected to the third side of the 3-way valve to evacuate the TPCTs. Once the required initial pressure was reached, the vacuum pump was disconnected. Then, the deionised water was charged to the TPCT using a scaled syringe with a known amount of water to fill half of the evaporator (50%). The evacuated TPCTs were left 24 hours before using them in the test to ensure that the same vacuum degree is maitained.

Figure 5.8 Vacuum pump

5.2.5 Test facility Set up

A test apparatus was developed to investigate the effect of the surface roughness on the heat transfer performance of the TPCT at a range of heat inputs and two initial pressures. A schematic diagram of the test rig is shown in Figure 5.9a [178]. The resulting test rig consists of similar components as shown in Figure 4.5 in chapter 4 except the TPCT shown in Figure 5.7 and the vacuum pump in Figure 5.8

The thermosyphon is 200 mm long consisting of two sections, the evaporator and condenser with 100 mm long each, 12.7 mm outside diameter and 1.6 mm thickness. The condenser section is surrounded by a brass water jacket of 16 mm inside diameter and 28 mm outside diameter to remove the heat from the condenser using water as a cooling liquid (cooling water flowing through the anulus between 12.7 mm and 16 mm). Eight type T surface thermocouples were fixed on the outer surface of the TPCT to measure the wall temperature,

five thermocouples at the evaporator and three at the condenser. In addition, two type T probe thermocouples were fitted in the inlet and outlet of the water jacket to measure the inlet and outlet temperatures of the cooling water. Figure 5.9b illustrates the TPCT dimensions and the positions of thermocouples [178]. All thermocouples were fitted in a similar manner as described in chapter 4.

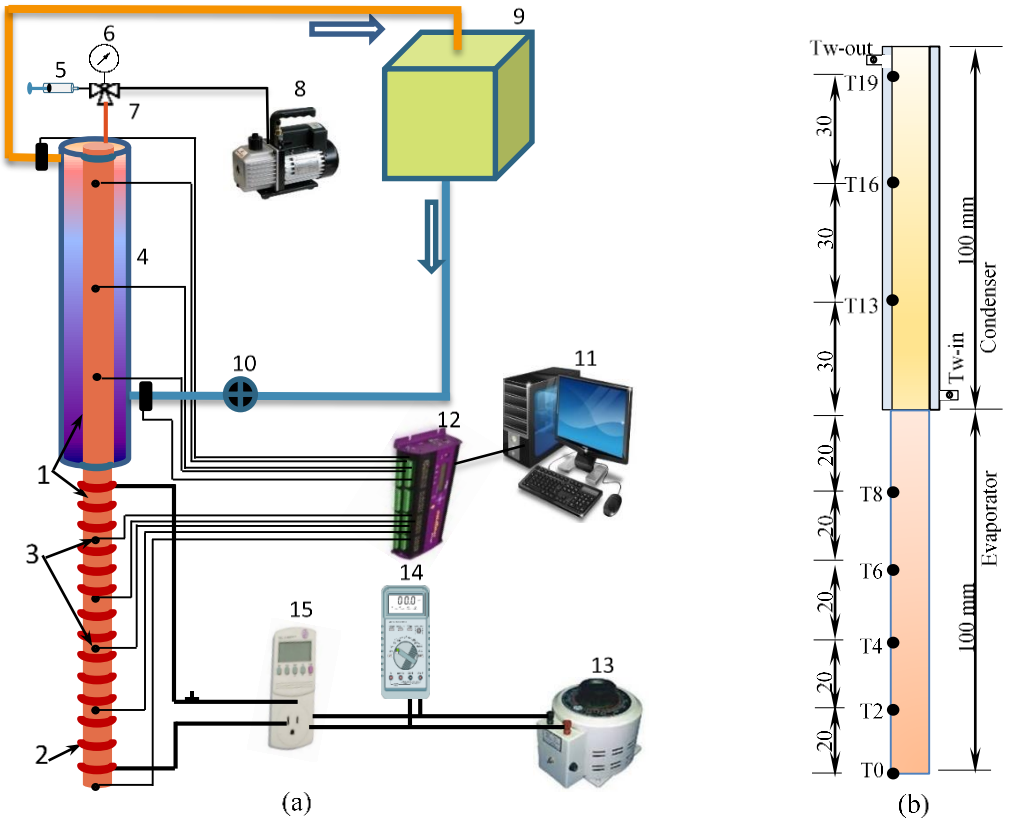

1-Heat pipe, 2-Electrical heater, 3-Thermocouples positions, 4- Water jacket, 5-Syringe, 6-Pressure gauge, 7-Three-way valve, 8-Vacuum pump, 9-Constant temperature water bath, 10- Flow meter 11-Computer, 12-Data logger, 13-Variable transformer, 14-Multimeter, 15-Power meter.

Figure 5.9: (a)-Test rig schematic diagram and (b)- Dimensions and Thermocouples positions [178]

An electrical heater with a maximum power of 160W was used to supply the heat to the evaporator section where it was wrapped evenly to distribute the heat input equally on the evaporator surface. Consequently, the value of the heat applied on the evaporator wall can be changed by changing the input voltage using a variable transformer. Also, a wattmeter and multimeter were used to measure the heat load. A high-temperature superwool blanket insulation of 50 mm thickness was used to reduce the thermal losses from the evaporator wall

of the TPCT, so, the heat losses were neglected. This was also proved by comparing the heat output to the heat input which was found to be more than 93% in all tests. Also, a rotameter was employed to measure the coolant mass flow rate at the condenser section. In addition, to ensure that all tests are performed at the same inlet temperature of the cooling water, a chiller was employed to maintain the coolant inlet temperature at the desired temperature. All thermocouples were connected to a data taker to send their temperature readings into a computer to be saved and analysed [8], [178].

5.2.6 Instrumentation

Same measuring devices were used in current experimental apparatus as those described in chapter 4, section 4.2.2, namely thermocouples, flow meter, power supply and data logger. The only new measuring instrument is the vacuum pressure gauge shown in Figure 5.10. The gauge is dry type with diameter of 50 mm and two pressure ranges, 0 to -1000 mbar and 0 to -30 inHg. The value of the operating pressure was recorded manually for each run at different heat inputs.

Figure 5.10 Pressure gauge

5.2.7 Calibration of Measuring Devices

As the flow meter and probe thermocouples were same as in the test rig described in chapter 4, the calibration data were also the same. Also, same type-T surface thermocouples were used, but new items were used on this TPCT, thus they were calibrated using the calibration

procedure explained in chapter 4, section 4.2.3. One of the surface thermocouples (T0, at the bottom of the evaporator, see Figure 5.9b) calibration curve is presented in Figure 5.11 versus the reading of the RTD including R-value and a curve fitting equation.

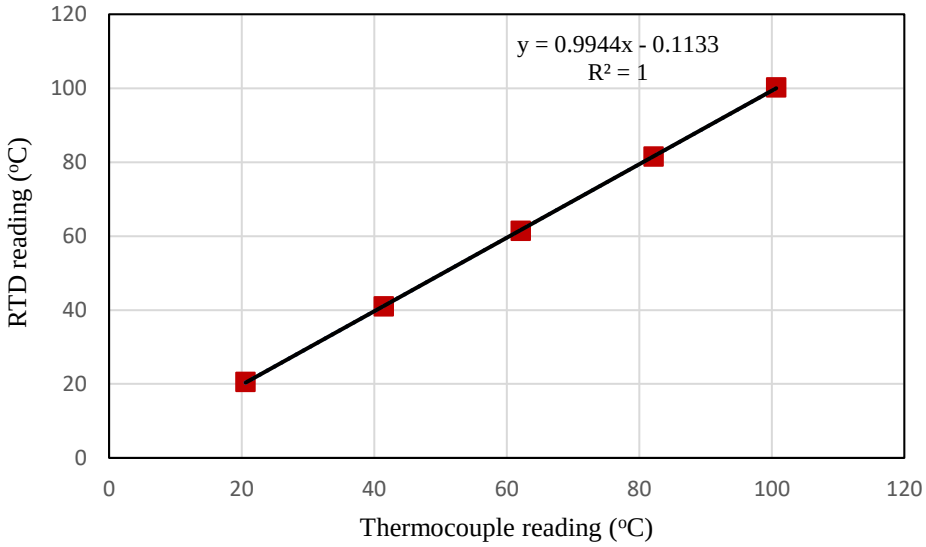

Figure 5.11 Calibration curve of T0 thermocouple

5.2.8 Experimental Procedure

After the test rig was built, it was ready to examine the TPCT performance using the following test procedure. Firstly, the chiller is set at a desired cooling temperature (20°C). Then, the globe valve before the rotameter is opened to allow the cooling water to circulate throughout the water jacket at the condenser section. Also, the rotameter is adjusted to a specified flow rate of 0.0025 kg/s using the globe valve to be fixed for all tests. Before power is supplied to the rope heater, enough time is provided to ensure that all thermocouples readings reach approximately a value of 20°C which is another proof of thermocouples consistancy and accuracy in temperature measurement. Then, the power is supplied to the electrical heater by adjusting the variable transformer to a certain value equivalent to the desired heat input to the evaporator section. This heat input can be obtained by multiplying the voltage times the current as well as the reading of the wattmeter. After all temperatures reach the steady state, the data is saved and the power is switched off [8]. Some runs were

repeated three times to prove the repeatability and accuracy of the test facility and the procedure used. The measured quantities are the heat load, operating pressure, coolant mass flow rate, inlet and outlet temperatures of the cooling water and wall temperatures of the evaporator and condenser sections [178].

5.2.8.1 Measurement Uncertainty

Explanation about types of uncertainties encountered in various measurements and the method and equations used in their calculations was reported in chapter 4, section 4.2.4.1. Consequently, uncertainty in the measurement of the flow meter and the probe thermocouples were the same. However, the uncertainty in the measurement of the surface thermocouples and the power supply was different although same type of the surface thermocouple (type-T) and same power supply components were used. This is because new surface thermocouples and different heater capacity demanding different voltages and current at each heat load were used. Therefore, the overall uncertainty in surface thermocouple reading (T0) obtained from curve fitting (Figure 5.11) was about 0.22^{o}C. Regarding the uncertainty of the vacuum pressure gauge reading, an accuracy of 2.5% (absolute uncertainty is 25 mbar of 1000 mbar) was obtained from the manufacturer's data.

The uncertainty in the heat input was determined from a combination of uncertainties in the measurement of the voltage (0.1 V) and the current (0.01 A) which were adopted from the manufacturer's data using Eq. 4-5 as detailed in chapter 4. Therefore, Table 5.2 illustrates the uncertainty in the measurement of heat input at different input energies.

Table 5.2 Heat input uncertainty in

Q	V	I	U_Q	U_Q
W	V	A	W	%
80	197.5	0.405	±1.98	±2.5
90	209.5	0.43	±2.09	±2.32
100	220	0.453	±2.21	±2.21
110	231.5	0.475	±2.32	±2.11
120	242	0.495	±2.42	±2.02
130	248.5	0.523	±2.49	±1.91
140	258.5	0.542	±2.58	±1.85
150	267.5	0.561	±2.67	±1.78
160	278.5	0.575	±2.78	±1.74

5.3- Results and discussion

A TPCT with internal wall roughness made using the EDM technique was tested and compared with a smooth TPCT to investigate the enhancement in the heat transfer at a range of heat loads (90-160 W) and two different initial pressures of 3 and 30 kPa. The two TPCT have the same dimensions and thermocouple positions as illustrated in Figure 5.9b [178].

5.3.1. Temperature distribution

The temperature distribution along the wall of the rough TPCT for all tested heat inputs (90-160 W) is shown in Figure 5.12 a and b at two initial pressures of 3 and 30 kPa, respectively. It is observed that the same trend is obtained at the evaporator section for all heat inputs and the two initial pressures (Figure 5.12 a and b). However, a higher flucuation and larger temperature difference among heat loads are observed at a preassure of 3 kPa compared with 30 kPa. This may be attributed to the higher increase in the saturation temperature (due to the

increase of the operating pressure with the heat load) at low pressures than that at relatively high pressure. On the other hand, at the condenser section, a different trend is noticed between the 3 and 30 kPa pressures for all heat inputs. The reason will be explained in the comparison between the two pressures in Figure 5.16. Also, a dip is observed in the temperature of the evaporator at a distance of 0.06 m and all heat loads. This may be attributed to the occurrence of dry-out condition at this point during the transient operation due to an insufficient amount of the working fluid. It is known that the dry out region quickly disappears and shows lower temperature when the thermosyphon heat pipe reaches the steady state condition.

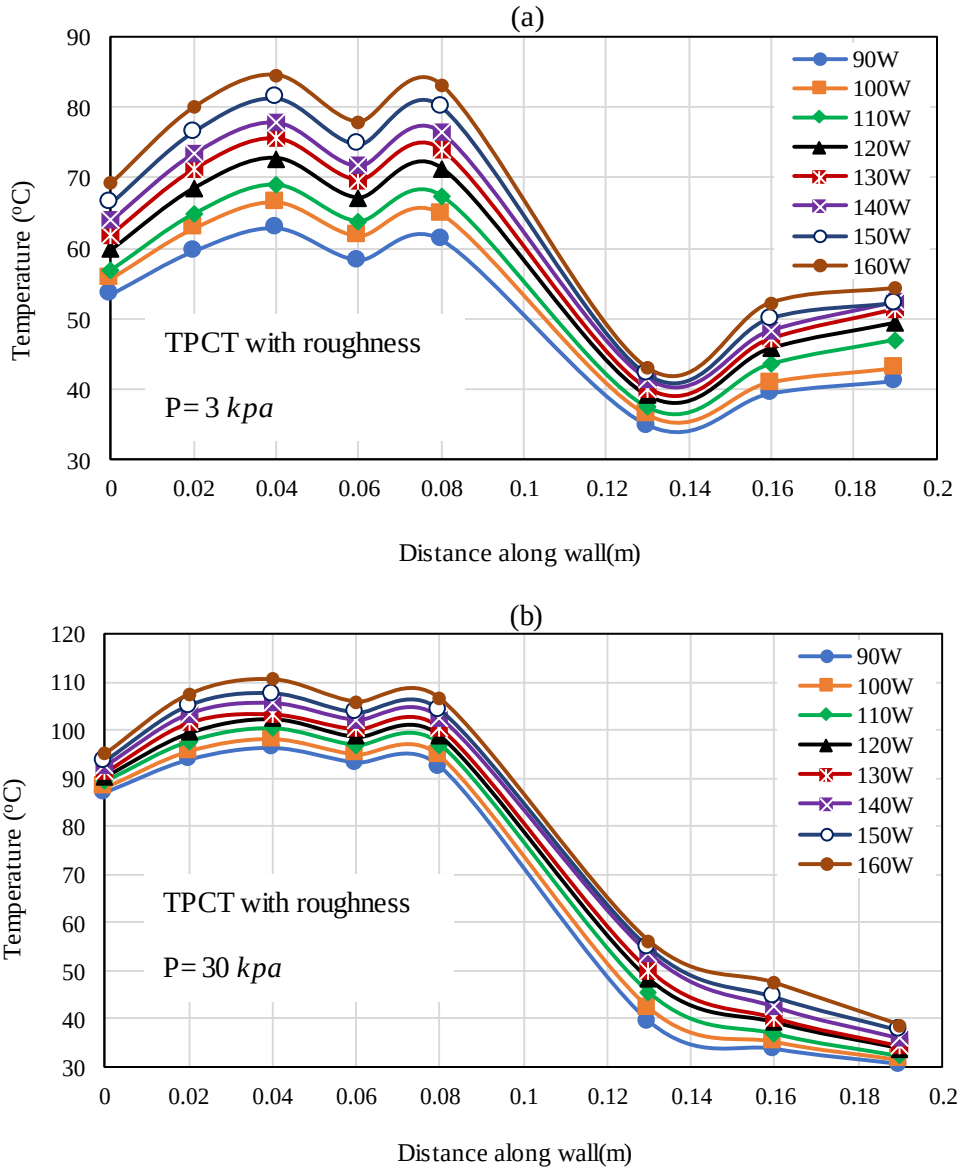

Figure 5.12 Temperature distriution on wall of rough TPCT for heat loads range of 90-160 W and two initial pressures: (a)- 3 kPa and (b)- 30 kPa

Effect of different heat loads on the wall temperature distribution of the plain TPCT at two pressures 3 and 30 kPa are shown, respectively in Figure 5.13 a and b. Almost same trends are observed for Figure 5.13 a and b as in Figure 5.12 a and b, respectively. However, higher wall temperatures are attained of the plain than those of the rough TPCT for both evaporator and condenser sections at the two initial pressures.

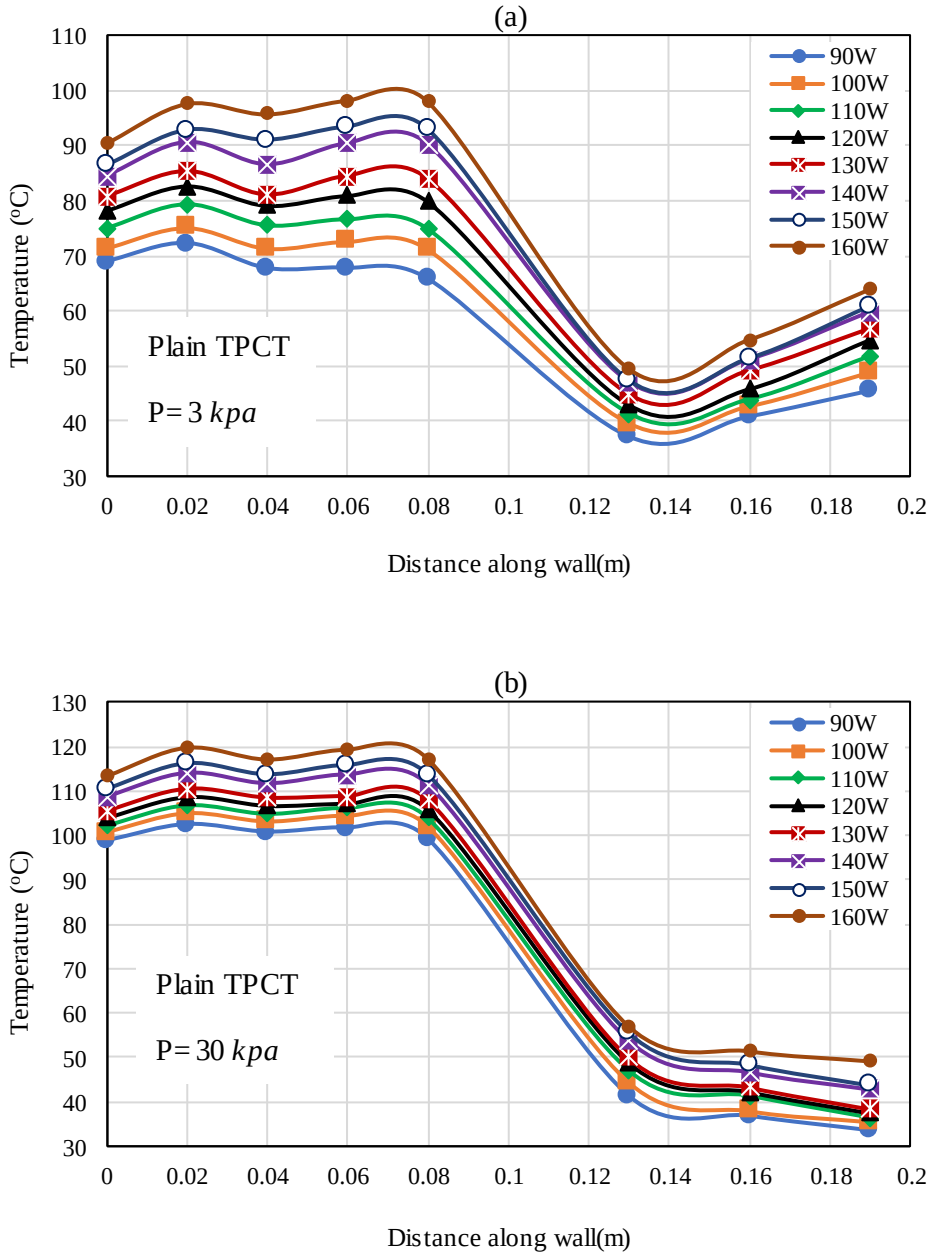

Figure 5.13 Temperature distriution on wall of plain TPCT for heat loads range of 90-160 W and two initial pressures: (a)- 3 kPa and (b)- 30 kPa

Variation of the wall temperature of the plain and rough thermosyphons with distance along the wall at a heat load of 100W is shown in Figure 5.14a and b for initial pressures of 3 and 30 kPa, respectively. Figure 5.14a shows that a significant reduction in the evaporator wall temperature is achieved for the TPCT with roughness compared to the plain TPCT. This can be explained by the increase in the nucleation sites density (as confirmed by Figure 5.4b), thereby increasing the frequency of bubbles generation [165] resulting from a rough surface, which transfers heat efficiently from the TPCT wall reducing noticeably the wall temperature. Another reason causing the decrease in the evaporator wall temperature is the hydrophilic characteristics of the modified wall [163], [165] which make the surface wetted with liquid instead of vapour as illustrated in Figure 5.6a [178].

However, in the condenser section, it is observed that the condenser wall temperature of the plain TPCT is higher than that for the TPCT with roughness, but the difference is much lower compared with the evaporator. This also may be attributed to the wettability feature of the rough surface which provides opposite effect on the condensation heat transfer in the condenser. This results in increasing the condensate film thickness which leads to additional heat transfer resistance, thereby lower condenser wall temperature [178].

Figure 5.14b presents a similar trend as Figure 5.14a in the evaporator section for both plain and modified TPCTs. However, a lower difference in evaporator temperature is obtained between the two thermosyphons due to the higher pressure. The reason behind that may be attributed to the activation of small surface cavities of the plain TPCT when the pressure increases [182] which reduces the wall temperature of the plain TPCT. On the other hand, most cavities of the rough surface are already activated, so the increase in pressure produces relatively less temperature reduction compared with the plain TPCT, but the evaporator wall temperature of the rough TPCT is still lower than that of the plain TPCT due to the roughness effect. Also, a different trend of the condenser wall temperature is observed at a pressure of

30 kPa compared with that at 3 kPa for both TPCTs. The reason will be explained in the discussion of Figure 5.16a and b [178].

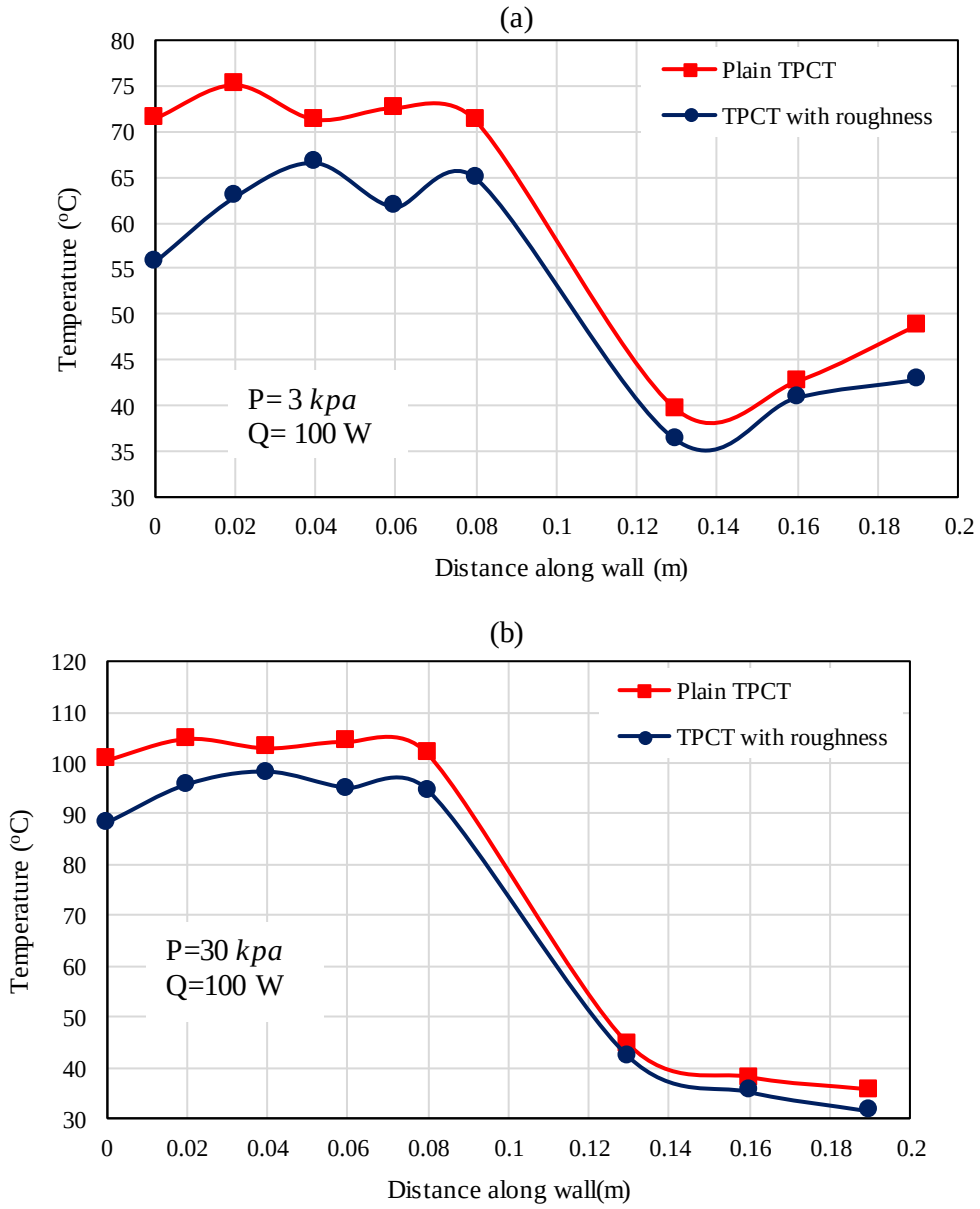

Figure 5.14 Comparison of wall temperature between plain and rough TPCT at heat load 100 W and initial pressures: (a)-3 kPa and (b)-30 kPa [178]

Figure 5.15a and b also show the temperature distribution along the wall of the two TPCTs at 3 and 30 kPa, respectively, but at a heat input of 160W. It is observed that the difference in the evaporator wall temperature between the plain and modified thermosyphons is higher compared with that at a heat load of 100W. This could be explained as: before reaching the critical heat flux which limits the boiling heat transfer in the TPCT, when the heat load

increases, the heat transfer mechanism is enhanced due to the generation of more bubbles transferring further heat from the hot wall to the liquid, thereby further reduces the evaporator wall temperature [178].

On the other hand, approximately the same difference in the condenser wall temperature as in the case of 100W is obtained when the pressure is 3 kPa (Figure 5.15a). However, when the pressure is 30 kPa (Figure 5.15b), a higher difference in the wall temperature of the condenser is noticed between the two TPTCs compared with that at 100W, especially at the upper part of the rough thermosyphon. This can be explained that the rate at which the vapour is generated at 160 W is higher than that at 100 W in both plain and rough TPCTs. Therefore, the rate of the condensate removal is smaller than the rate of droplets growth, which leads to thickening the condensate film thus reducing the condenser wall temperature [183]. This effect is higher in the case of the rough condenser due to the wettable characteristics of the rough surface compared with the smooth surface, so that the difference at 160 W is higher than that at 100 W [178].

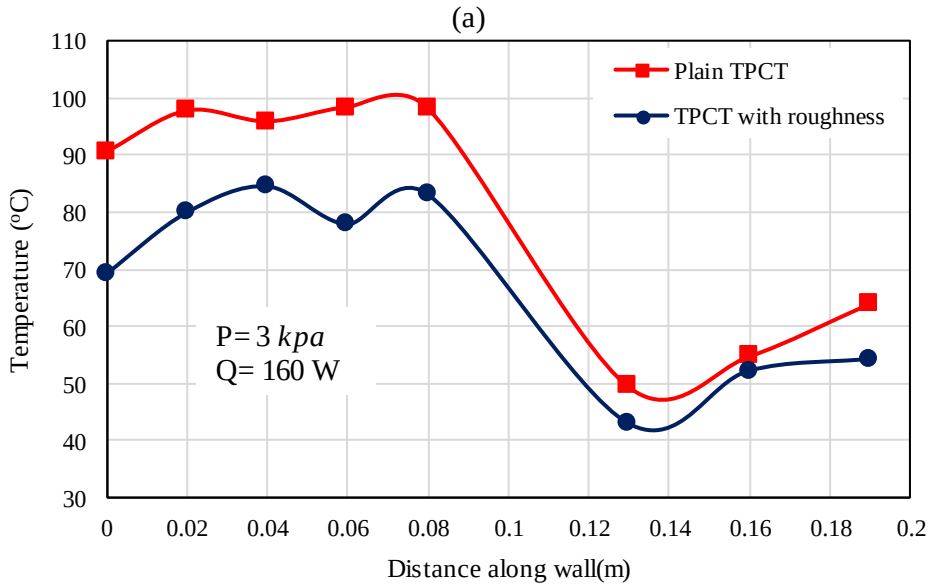

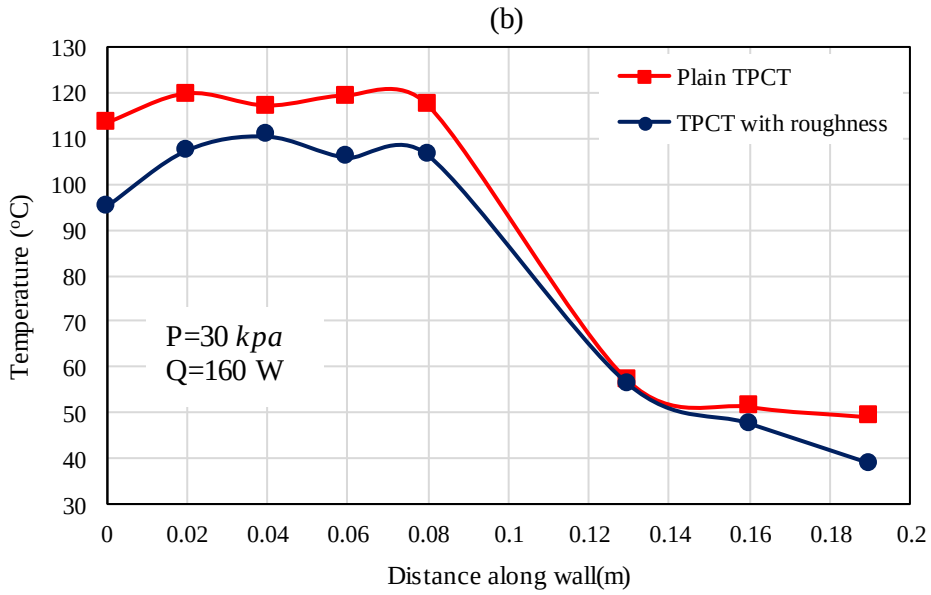

Figure 5.15 Comparison of wall temperature between plain and rough TPCT at heat load 160 W and initial pressures: (a)-3 kPa and (b)-30 kPa [178]

Effect of two initial pressures of 3 and 30 kPa on the wall temperature distribution is presented in Figure 5.16a and b for rough and plain thermosyphons, respectively, at a heat input of 160 W. It can be seen that for both TPCTs, using the pressure of 3 kPa provides a lower evaporator wall temperature compared with 30 kPa due to corresponding low saturation temperature which leads to earlier evaporation start-up, thereby a lower evaporator wall temperature [144]. On the other hand, a higher condenser wall temperature is obtained employing 3 kPa at the middle and upper parts of the condenser (T16 and T19), while it is lower at the lower part (T13). This may result from the rising of the saturated vapour to the upper part of the condenser and the small condensate film thickness, resulting in a low thermal resistance, thereby higher heat transfer coefficient between the hot vapour and the wall leading to a higher condenser wall temperature at the upper part compared with the lower part [66]. In contrast, in the case of 30 kPa, the upper part of the condenser wall exhibits a lower wall temperature compared with the lower part for both TPCTs. This may be attributed to the existence of non-condensable gases in the case of 30 kPa (as the TPCT is partially evacuated) which blocks the upper part of the condenser preventing the hot vapour to reach

this part and deteriorating the heat transfer mechanism leading to a lower condenser wall temperature compared with lower part at 3 kPa. Thus, a smaller condensate quantity is produced making the wall temperature of the lower part of the condenser (T13) for both TPCTs at 30 kPa higher than that at 3 kPa. In addition, the difference in the wall temperature between the two pressures is higher in the case of modified TPCT compared with plain one for the same reasons explained in the discussion of Figure 5.14(a-b) and Figure 5.15(a-b) [178].

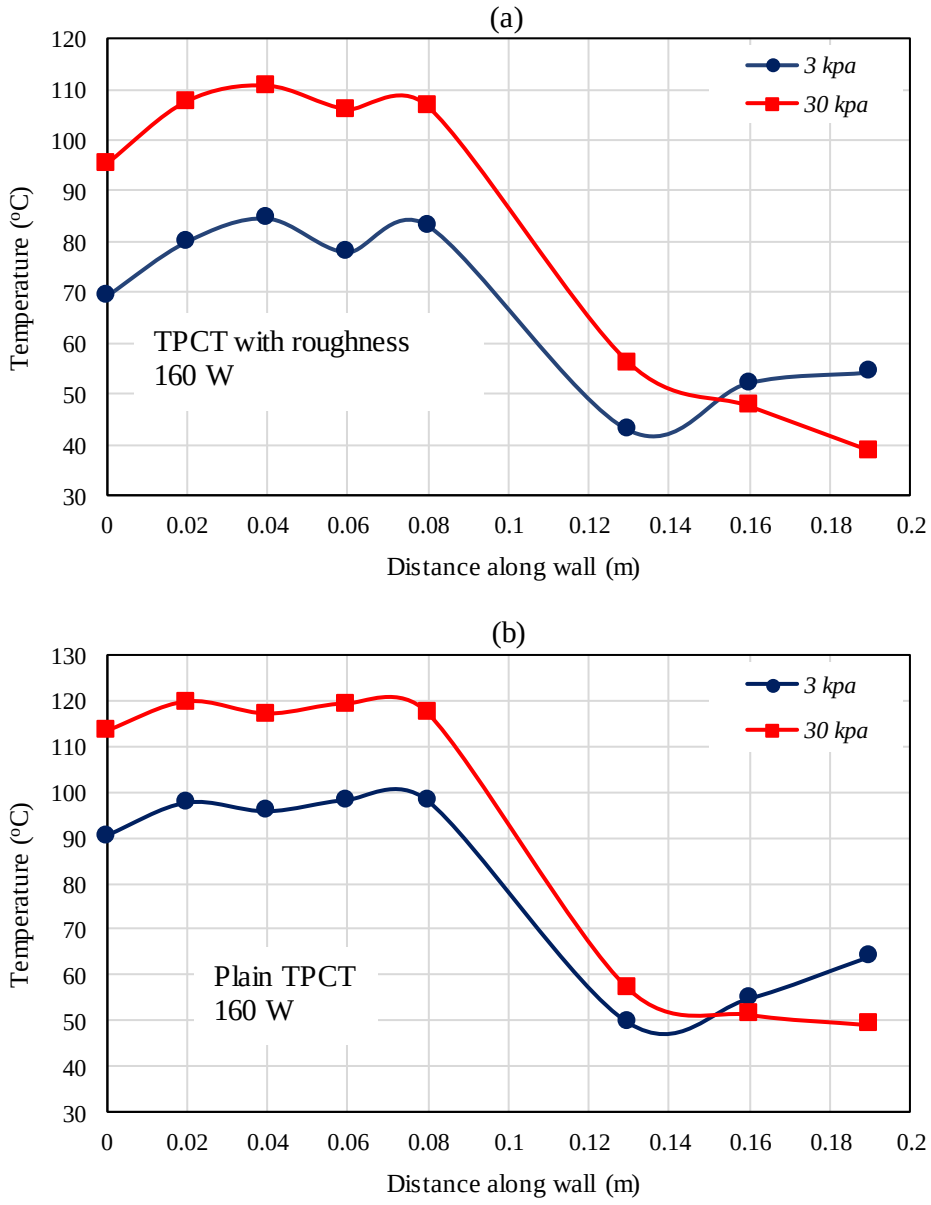

Figure 5.16 Comparison of wall temperature between initial pressures 3 and 30 kPa at heat load 160 W and: (a)-TPCT with roughness and (b)-Plain TPCT [178]

5.3.2. Thermal Performance of the Thermosyphon [178]

Parameters such as evaporator and condenser thermal resistances, total thermal resistance and the evaporator heat transfer coefficient need to be determined to obtain and compare the heat transfer characteristics of the plain and modified TPCTs.

The evaporator and condenser thermal resistances can be obtained from the following equations:

$$R_e = \frac{T_{e,av} - T_{sat}}{Q} \quad 5.1$$

$$R_c = \frac{T_{c,av} - T_{sat}}{Q} \quad 5.2$$

where R_e and R_c are the evaporator and condenser thermal resistances, respectively, T_{sat} is the saturation temperature which corresponds to operating pressure at each heat input, and Q is the heat input calculated from [178]:

$$Q = VI \quad 5.3$$

where V and I and denote the circuit voltage and current, respectively. $T_{c,av}$ and $T_{e,av}$ represent the average wall temperatures of the condenser and evaporator, respectively and can be obtained as follow:

$$T_{e,av} = \frac{T0 + T2 + T4 + T6 + T8}{5} \quad 5.4$$

$$T_{c,av} = \frac{T13 + T16 + T19}{3} \quad 5.5$$

Therefore the total thermal resistance of the TPCT can be calculated from:

$$R_t = \frac{T_{e,av} - T_{c,av}}{Q} \quad 5.6$$

Where R_t is the total thermal resistance of the thermosyphon.

The evaporator heat transfer coefficient can be obtained from the following equation:

$$h_e = \frac{Q}{\pi D_i L_e (T_{i,av} - T_{sat})} \quad 5.7$$

Where h_e is the evaporator heat transfer coefficient, D_i *and* L are the inside diameter and length of the evaporator and $T_{i,av}$ is the inside surface average temperature of the evaporator and can be determined from [178]:

$$\mathrm{T_{i,av}} = \mathrm{T_{e,av}} - \frac{\mathrm{Q}}{2\pi \mathrm{LK}} ln\left(\frac{D_o}{D_i}\right) \quad 5.8$$

Where D_o is the outside diameter of the evaporator and k is the solid thermal conductivity.

5.3.2.1 Thermal Resistance

5.3.2.1.1 Validation of Experimental Data

Different correlations have been proposed to predict the boiling heat transfer coefficient and hence, the thermal resistance of TPCT. Jouhara et al. [73] compared the validity of a number of these correlations and concluded that Kutateladze correlation [184] is the best among all correlation for the prediction of the evaporator thermal resistance of the TPCT when the thermal resistance is low. This is because Kutateladze correlation includes a wide range of parameters making them more general and accurate for different liquids and various boiling conditions. Thus, the following Kutateladze correlation was used to validate the experimental data in terms of evaporator thermal resistance:

$$h_e = 0.44\left(\frac{k_l}{l_b}\right)\left[\frac{10^{-4} qP}{g\rho_v h_{fg} \mu_l} \frac{\rho_l}{\rho_l - \rho_v}\right]^{0.7} (\mathrm{Pr}_l)^{0.35} \quad 5.9$$

Where,

$$l_b = \left(\frac{\sigma}{g(\rho_l - \rho_v)}\right)^{0.5} \quad 5.10$$

where q is the heat flux, P operating pressure, ρ_l and ρ_v are densities of liquid and vapour, h_{fg} latent heat, k_l liquid thermal conductivity, μ_l liquid viscosity, g acceleration of gravity, Pr_l Prantel number of liquid, σ surface tension and l_b is the bubble scale length.

Once h_e is calculated from Eq. 5-9, the predicted evaporator thermal resistance can be calculated using the following equation:

$$R_e = \frac{1}{\pi D_i L_e h_e} \qquad 5.11$$

A comparison of the evaporator thermal resistance for the plain TPCT between the predicted and measured results is shown in Figure 5.17. It shows that the experimental data agree with the predicted results within a band of 30% in which the correlation underpredicts the measured R_e. It can also be concluded that most of the points are within 15%. This may be considered as a reasonable result because of the complex nature of the boiling process which can not be fully represented by any correlation.

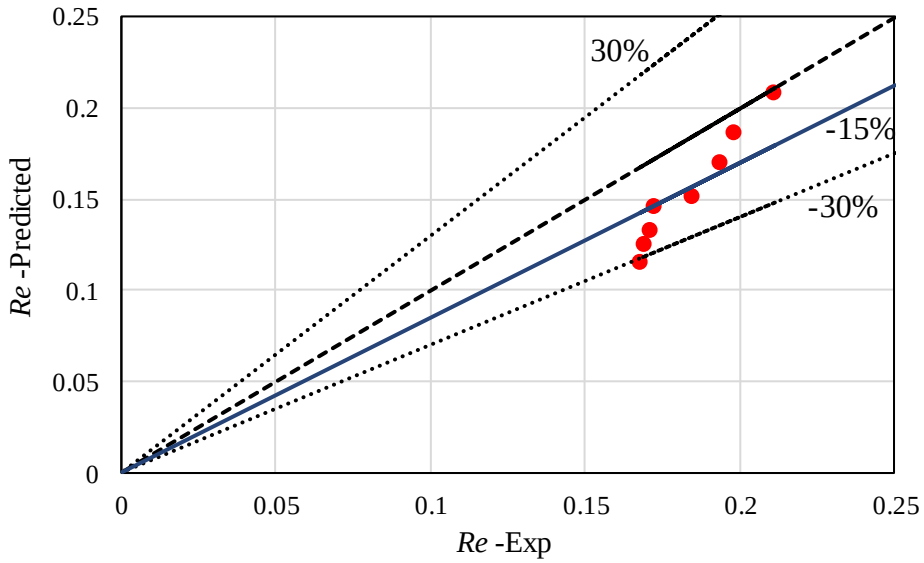

Figure 5.17 Comparison between predicted and measured R_e for plain TPCT

5.3.2.1.2 Thermal Resistance Results [178]

Variation of evaporator thermal resistance (R_e) with the heat load for the plain and rough TPCTs are shown in Figure 5.18a and b at two different initial pressures of 3 and 30 kPa, respectively. They show that a considerable decrease in the evaporator thermal resistance is achieved when the rough thermosyphon is compared with the plain one for both pressures. It is found that the reduction in the evaporator thermal resistance varies with the heat load from about 51-68% and from 68-115% for pressures of 30 and 3 kPa, respectively. The achieved reduction is higher than those reported in literature of 30.4% [148], 40% [162], 15.01% [165]. This reduction in R_e may result from the presence of the roughness in the evaporator wall which creates additional nucleation sites leading to generate more bubbles, thereby more heat is released from the evaporator internal surface. Also, the rough surface increases the wall wettability by decreasing the contact angle making the liquid in continuous contact with the evaporator wall removing the vapour away from the wall surface. In addition, at 3 kPa, it is observed that the R_e for the plain TPCT increases at a heat input of 140W, while for the TPCT with roughness, it increases at 150W [178]. Similarly, At 30 kPa, same trend is observed for the plain TPCT, while the R_e for rough TPCT continues decreasing as heat input increasing for the tested range of heat loads indicating an increase in the CHF for the rough TPCT.

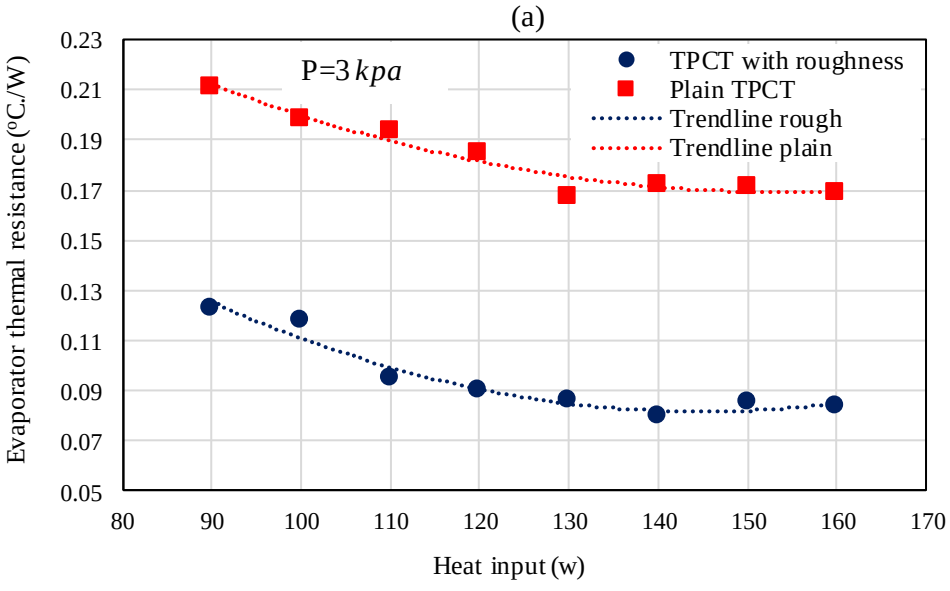

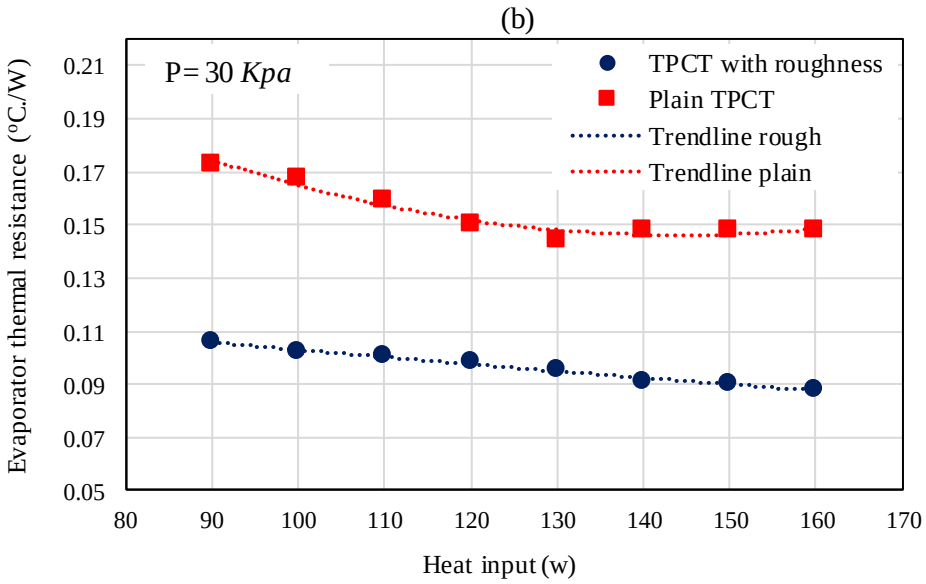

Figure 5.18 Comparison of evaporator thermal resistance versus heat input between plain and rough TPCTs at initial pressures: (a)-3 kPa and (b)-30 kPa [178]

However, Figure 5.19a and b show that the condenser thermal resistance (R_c) increases when the modified TPCT is employed compared with the plain one which worsens the heat transfer performance in the condenser section. Higher R_c for coated TPCT was also reported by [162] and no reduction in R_c for anodised TPCT was reported by [165]. This may be attributed to the fact that the high surface wettability produced from the rough surface can form a liquid film on the condenser wall which prevents the vapour to be in direct contact with the condenser inner wall resulting in additional thermal resistance. The maximum increase in the R_c is about 22% compared with plain TPCT. It is also seen from Figure 5.19a for initial pressure of 3 kPa that R_c of the rough and plain TPCTs decreases steadily with the heat load, while Figure 5.19b for initial pressure of 30 kPa shows that R_c of both TPCTs decreases sharply with the heat load. This may be explained by a larger amount of vapour generated at the low pressure compared with the high pressure. This increases the liquid film thickness, thereby the condenser thermal resistance reducing the effect of heat input on the thermal resistance at the low pressure. The film thickness on the rough wettable condenser wall is higher (at 3 kPa), so that a higher difference is noticed between the two thermal resistances at

a pressure of 3 kPa (Figure 5.19a) compared with that at 30 kPa (Figure 5.19b) and they both decreases with the input energy [178].

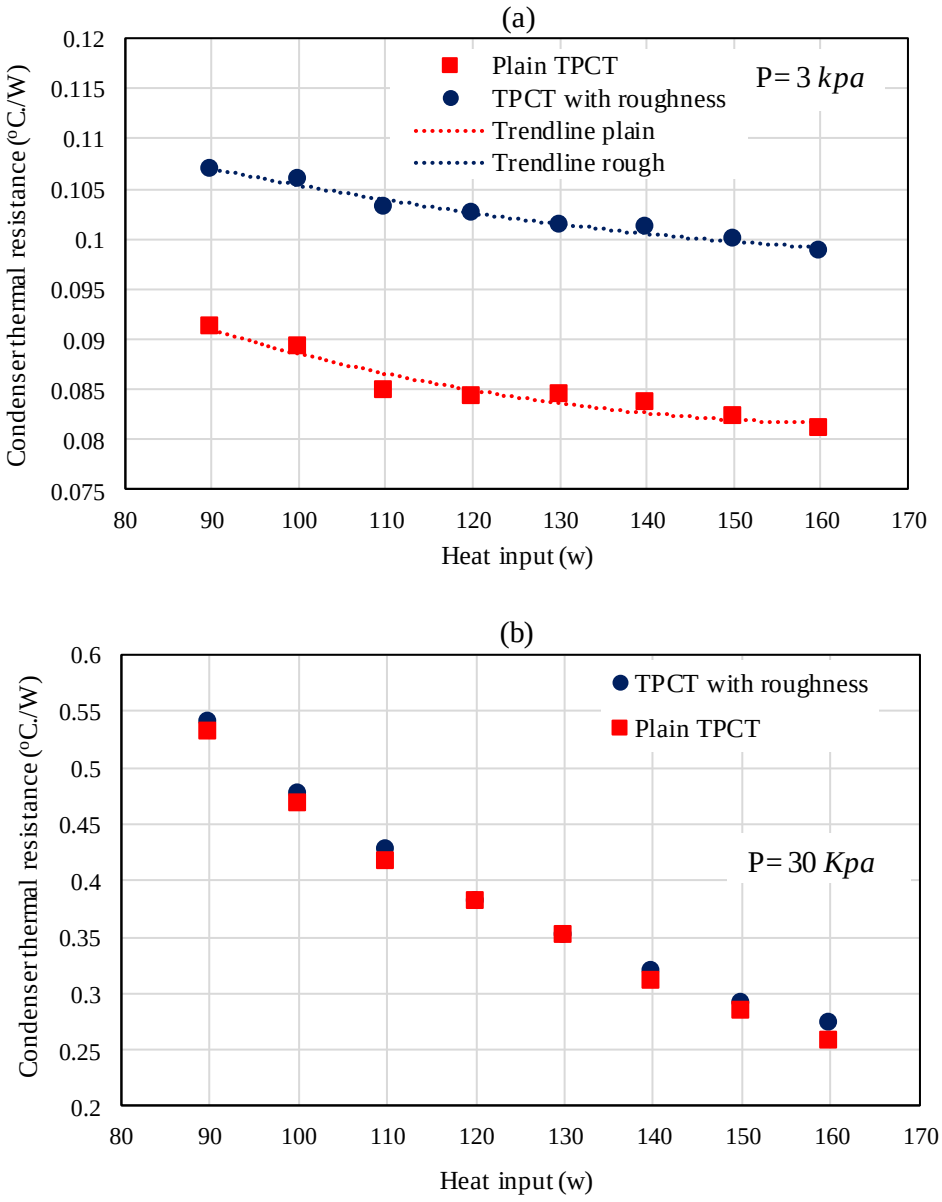

Figure 5.19 Comparison of condenser thermal resistance versus heat input between plain and rough TPCTs at initial pressures: (a)-3 kPa and (b)-30 kPa. [178]

Despite the increase in condenser thermal resistance for the rough TPCT, a noticeable decrease in the total thermal resistance (R_t) of the rough TPCT is shown in Figure 5.20a and b at 3 and 30 kPa, respectively, due to the high reduction in the evaporator thermal resistance. The reduction in the R_t varies with the input energy from about 9-13% and 28-42% compared with the plain TPCT at 30 and 3 kPa respectively. Reduction in the total thermal resistance of

18.2%, 19%, 125%, 15%, 26.1% and 35.48% was also obtained by [148], [162], [164], [165], [166] and [160], respectively. In addition, Figure 5.20a (3 kPa) shows the same trend as the R_e in Figure 5.18a, and almost the same rate of decrease in the R_t for both TPCTs with the heat load is observed at a pressure of 30 kPa (Figure 5.20b) [178].

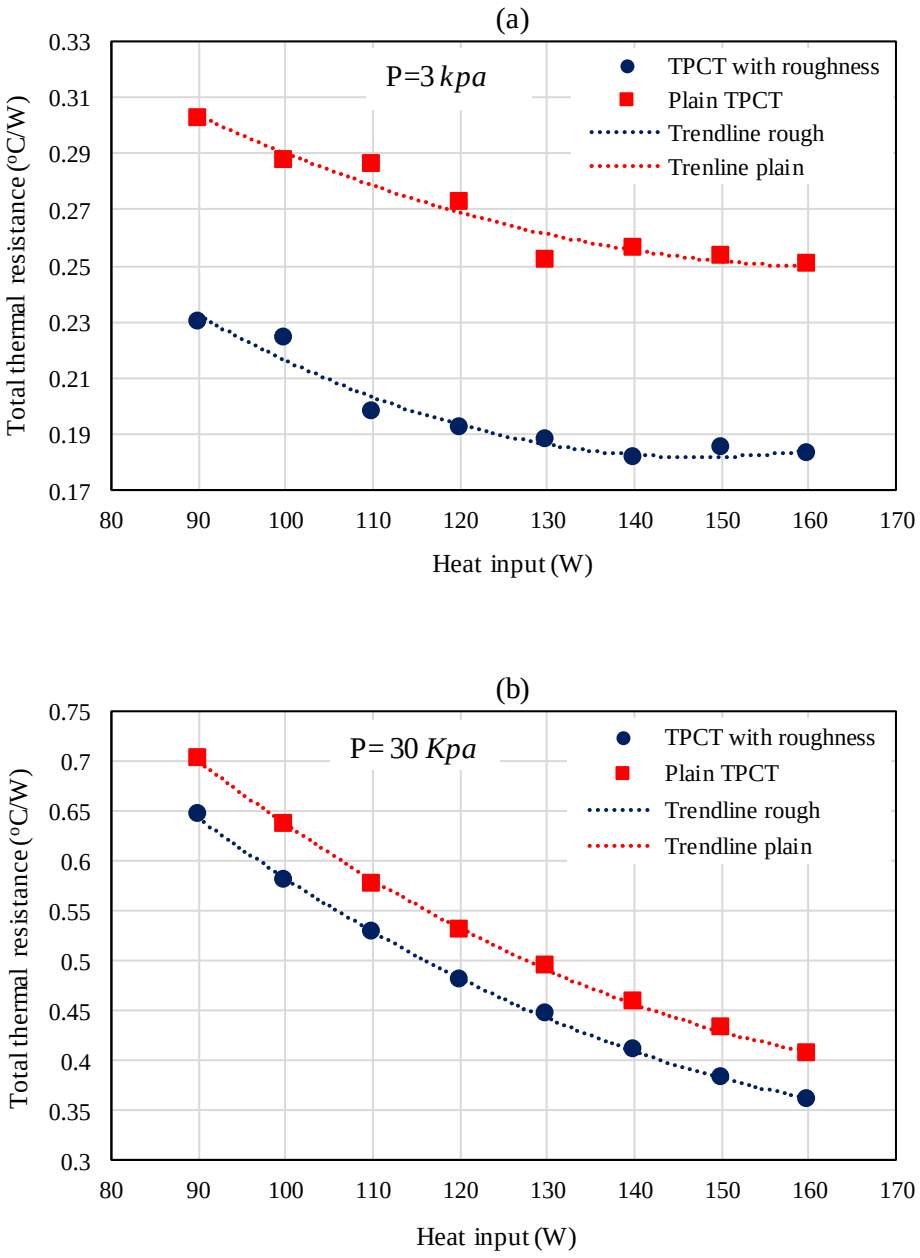

Figure 5.20 Comparison of total thermal resistance versus heat input between plain and rough TPCTs at initial pressures: (a)-3 kPa and (b)-30 kPa. [178]

5.3.2.2 Heat Transfer Coefficient [178]

Figure 5.21a and b show a significant enhancement in the evaporator heat transfer coefficient (h_e) for the TPCT with roughness at 3 and 30 kPa, respectively. The increase in the h_e is about 68-115% and 51-68% at 3 and 30 kPa, respectively. Enhancement in the h_e also reported by [162] (40%), [153] (50-100% for methanol and 30-50% for ethanol) and [159] (maximum of 116.87%). In addition, at a pressure of 3 kPa (Figure 5.21a), h_e generally increases as the heat load increases for both the TPCTs. However, the rate of increase in h_e is higher for the modified TPCT compared with the plain one and it becomes approximately constant after a heat load of 130W for the plain TPCT. Therefore, the difference in h_e between the two TPCTs increases as the input energy increases. This is also true at a pressure of 30 kPa (Figure 5.21b), but with a lower difference in h_e and a lower rate of increase for the rough TPCT [178].

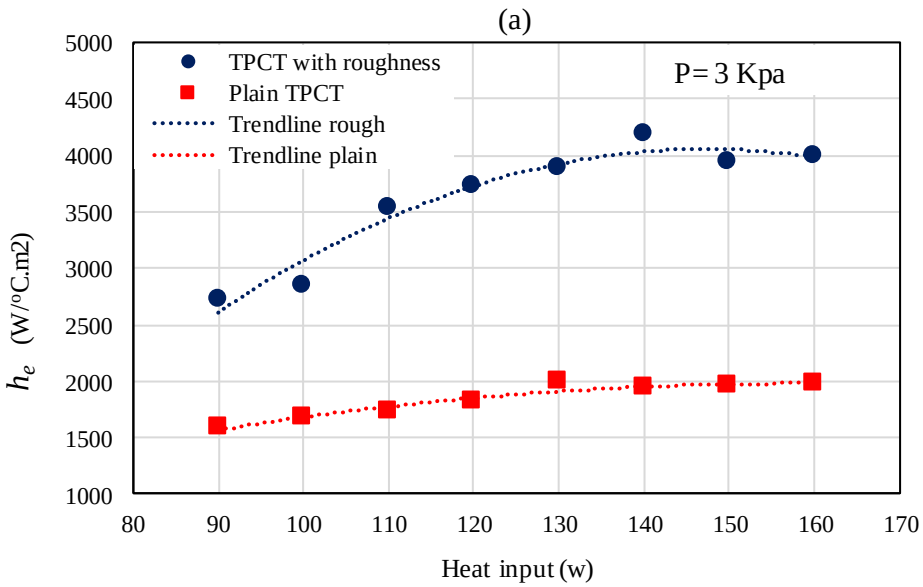

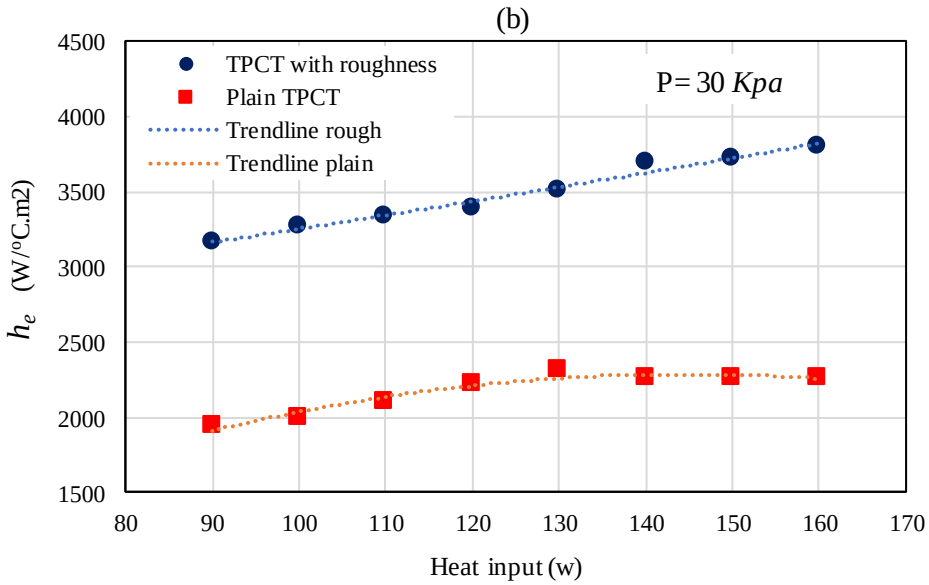

Figure 5.21 Comparison of evaporator heat transfer coefficient versus heat input between plain and rough TPCTs at initial pressures: (a)-3 kPa and (b)-30 kPa. [178]

5.4 Summary

Thermal performance of a TPCT with an internal surface roughness was tested to investigate the enhancement of heat transfer characteristics. The roughness was produced using advanced machining technique named as Electrical Discharge Machining (EDM). The performance was assessed by comparing the modified TPCT with a plain TPCT at various heat loads and two different initial pressures (sub-atmospheric pressures). The following outcomes were concluded:

- Making this type of the roughness increased the surface wettability by reducing the contact angle, and produced more nucleation sites.
- The evaporator wall temperature decreased significantly when the TPCT with the modified surface was used compared with the plain TPCT at both tested pressures. Also, it was observed that the enhancement increases as the heat load increases for the range used in this work.
- Regarding the effect of the initial pressure, a higher reduction in the wall temperature was achieved at a pressure of 3 kPa compared with that achieved at 30 kPa. Also, the

difference in evaporator average temperature between the two pressures was lower for the plain TPCT compared with the rough TPCT.

- An opposite trends of the wall temperature were noticed at the condenser section due to different initial pressures (3 and 30 kPa). At the 3 kPa, the condenser wall temperature increases as the distance toward the condenser end cap increases, while it decreases with the distance at the 30 kPa.
- A remarkable reduction and enhancement in the evaporator thermal resistance and heat transfer coefficient of 115% and 68% were obtained at pressures of 3 and 30 kPa, respectively.
- The resurfaced wall had a negative effect on the heat transfer process in the condenser section, where a lower condenser wall temperature was obtained in the rough TPCT compared with the plain one. Consequently, a higher condenser thermal resistance of the rough TPCT was produced. However, this was much lower than the enhancement in the evaporator section.
- Accordingly, the total thermal resistance of the rough TPCT was reduced by about 42% and 13% at 3 and 30 kPa, respectively, compared with the plain TPCT.

Chapter 6

6. Conclusions and Future Works

6.1 Introduction

Solar thermal heaters have been widely employed for tens of years all over the world to meet the needs of space cooling and heating, hot water and heat required for manufacturing processes. A substantial amount of thermal energy is consumed in hot water production, so that most of solar thermal systems are utilised in buildings. The main factor affecting the thermal performance of the thermal solar systems is the collector efficiency. It was concluded from the literature review that the efficiency of solar thermal collectors can be greatly increased by integrating heat pipes with solar collectors. Using heat pipes can also eliminate a number of drawbacks related to the operation of the conventional solar collectors. Thus, enhancing the thermal performance of heat pipes represents a vital aim to improve the performance of the solar hot water systems.

Therefore, a CFD model was developed to simulate the flow and phase-change process inside the Two-Phase Closed Thermosyphon (TPCT). This was carried out to investigate the effect of fill ratio and inclination angle on the thermal performance of the TPCT, and to visualise the phase change characteristics under the influence of the inclination and different fill ratios. Also, the surface wettability in terms of the contact angle was investigated to report their effect on the thermal characteristics of the TPCT and to visualise the phase-change characteristics inside the TPCT for different contact angles using Fluent Ansys. Furthermore, the effect of different parameters on the geyser boiling in the TPCT was investigated experimentally. Consequently, the influence of geyser effect on the TPCT thermal characteristics was examined experimentally under the effect of various liquid charges and angles of inclination at a broad range of input energy. Finally, advanced manufacturing

technique using wire EDM was employed to introduce a surface roughness in the internal wall of the TPCT, thereby enhancing the thermal performance of the thermosyphon heat pipe. This was achieved by comparing its thermal performance with a plain copper thermosyphon at two different initial sub-atmospheric pressures (3 and 30 kPa) and various heat loads.

6.2 Conclusions

A number of conclusions can be made for every research point described above as follow:

6.2.1 CFD Modelling

- Validating the CFD model, maximum deviations of 4.2% and 8.1% were obtained in wall temperature and thermal resistance, respectively. Also, a maximum deviation between the CFD modelling and the experimental results of 1.3% was achieved regarding the inclination angle.
- The complex boiling process was successfully visualised for the inclined TPCT and TPCTs with different fill ratios. This showed that as a result of low inclination with respect to the horizontal axis, a vapour film is formed on the evaporator internal surface leading to the increase in the evaporator thermal resistance.
- A considerable increase in the evaporator wall temperature was attained when small fill ratios of 25% and 35% were used at high heat loads indicating that the TPCT reached its heat transfer limit at these liquid charges.
- Angle of 90^{o} and a charged liquid ratio of 65% exhibited the highest thermal performance, while the lowest thermal performance was noticed at 10^{o} and 25%. This is due to the effect of the small charged liquid ratio and inclination, which were higher at higher heat loads.
- Regarding the contact angle effect, the vapour condensation on a flat surface with different contact angles was successfully modelled using the Volume Of Fluid (VOF)

approach in Fluent. Using the same model, the TPCT thermal performance and visualising of the phase-change process inside the TPCT were also investigated at different contact angle and heat inputs.

- Validating the flat plate CFD model, maximum deviations from published experimental data of 5% and 9.9% were obtained for the vapour condensation and the effect of the contact angle, respectively. Consequently, for the TPCT model, the wall temperature and thermal resistance deviated maximally by 1.9% and 6.6%, respectively.
- The highest condensation thermal performance was obtained at a contact angle of 140^{o} as was proved by the flat plate model. Therefore, this contact angle was adopted in the modelling of the TPCT.
- The TPCT CFD model was capable to visualise various droplet shapes in the condenser section for contact angles of 90^{o} and 140^{o}, and different boiling modes, convection, bubbly and slug regimes in the evaporator for 90^{o} and 40^{o}.
- Visualisation showed that in the case of the contact angle 90^{o}, the formed bubbles stay attached to the heating surface forming a vapour film, while in the case of 40^{o}, vapour bubbles continuously were removed to the liquid pool due to the wettable feature of the surface which justified the heat transfer enhancement.
- A reduction of 34% in the thermal resistance was obtained for the TPCT with contact angles of 40^{o} and 140^{o} in the evaporator and condenser, respectively, compared with that of contact angle 90^{o}.

6.2.2 Effect of Different Parameters on Geyser Boiling Characteristics

- At the moment that the geyser boiling occurs, a sharp increase is observed in thermocouple readings of the condenser side and those placed outside the liquid pool,

while a sharp drop is noticed in those placed within the liquid pool. This is also affected by the liquid level in the evaporator (charged liquid ratio).

- Liquid charge ratio and inclination angle affect significantly the first occurrence of the geysering which also depends on the heat load. Generally, it occurs at lower heat load as the inclination increases toward the vertical axis and as the fill ratio increases. Therefore, this study concluded that it is not a condition that geyser boiling occurs at low heat input.
- At a relatively high heat inputs (200, 300 and 400 W), high temperature oscillation is noticed for all liquid charges and at angle of 10^o. This is also observed for only 25% and 65% liquid charges at angle of 30^o. Previous studies reported that the geysering does not happen for inclinations lower than 30^o. This may be attributed to a narrow range of the tested heat loads at a certain value of fill ratio.

Period of Geyser Boiling

- Generally, for all inclinations and liquid charges, as the heat load increases, the period decreases. Accordingly, at medium heat loads (50, 60, 70, 80, 90 and 100 W) a very long period (600 seconds) is obtained, while at 200, 300 and 400 W, very short period (3 seconds at angles of 60 and 90^o) is observed.
- At heat inputs of 200, 300 and 400 W and angles of 30 and 10^o, the period increases considerably (40 seconds) compared with these at angles of 60 and 90^o. However, at angle of 30^o and liquid charge of 100%, the period is still short (3 seconds).

Effect of Coolant Flow Rate and Inlet Temperature

- At high fill ratio (100%) and angles of 60 and 90^o, it is found that the mass flow rate has no effect on the geysering period (this explains why some studies reported no effect of mass flow rate on the period), while at 25% and 65% liquid charges and same angles, the period decreases as the coolant flow rate decrease.

- For all liquid charges and angle of 10^o, the period increases as the coolant flow rate decreases. Also, for liquid charge 100% and the same angle, the period is effected by the change in the flow rate on contrast of that at 30, 60 and 90^o.
- For liquid charges of 25% and 100% and angles of 30, 60, and 90^o, the period increases with decreasing of the inlet temperature. However, fill charge of 65% provides an opposite trend at same angles.

6.2.3 Effect of Geyser boiling on TPCT's Thermal Performance

- After the geysering occurs, the temperature distribution of the TPCT's wall become more uniform.
- The evaporator's wall temperature decreased significantly after the geysering occurrence regardless of the increase in the input energy. This drop was greatly affected by the inclination and fill ratio.
- Before the occurrence of geysering at low heat loads, the highest thermal resistance corresponded to a fill ratio of 100% for all inclinations. However, this thermal resistance became the lowest compared with other fill ratios after the geyser boiling occurrence. The drop rate varies as the inclination and heat input vary as well as to the fill ratio.
- The TPCT reached its heat transfer limit at a fill ratio of 25% and an angle of 10^o before the geysering occurs. However, the heat transfer limit was improved considerably after the geysering occurrence.
- The considerable drop in the wall temperature of the evaporatore produces the reduction in the thermal resistance of the TPCT after the geysering occurrence rather than the wall temperature of the condenser.
- This work has shown that geyser phenomena can be beneficial at certain operating conditions in terms of improving the TPCT thermal ressistance and its temperature

distribution. Likewise, it can have deteremental effects on the TPCT performance under certain operating conditions. The result from this work allows the user to identify the range of operating conditions that can either improve the TPCT performance or to avoid the conditions that lead to the opposite effect.

6.2.4 Resurfaced TPCT

- More nucleation sites and lower contact angle were produced by changing surface features of the TPCT's internal wall as a result of introducing a surface roughness.
- A significant decrease in the evaporator wall temperature was achieved using the resurfaced TPCT at both initial pressures 3 and 30 kPa. This reduction increases as the input energy increases.
- Less reduction was obtained at a pressure of 30 kPa compared with 3 kPa and the difference in evaporator temperature between the two pressures for the rough TPCT was higher than that for the plain.
- At the condenser section, using two different initial pressures provided an opposite trend of the wall temperature. These wall temperatures increases and decreases with the height of the condenser at 3 kPa and 30 kPa, respectively.
- Accordingly, a considerable decrease in the evaporator thermal resistance and enhancement in the evaporator heat transfer coefficient of 115% and 68% were obtained at 3 and 30 kPa, respectively.
- The condenser wall temperature for the rough TPCT was noticed to be lower than that for the plain one. Likewise, the thermal resistance of the condenser section for the rough TPCT was higher, but the difference in the condenser was much lower than that at the evaporator.

- The total thermal resistance for modified TPCT was decreased by about 42% at a pressure of 3 kPa, whereas it is reduced by 13% at 30 kPa compared with the plain TPCT despite the increase in the condenser thermal resistance.

6.3 Future Works

For further enhancement in the thermal performance of the TPCT, some suggestions for future works are recommended as follow:

- Extend the CFD model to simulate other working fluids (such as acetone, methanol and ethanol) and compare their performance with water at different fill ratios and inclinations. This model can also be used to visualise and compare different liquid pools for different fluids.
- Develop a CFD model to simulate a thermosyphon heat pipe with micro-grooves to study their influence on the thermal performance of the TPCT.
- Investigate the effect of different initial pressures on the geyser boiling and accordingly on the thermal performance of the TPCT.
- Investigate the effect of using different working fluids on the geyser boiling characteristics inside the TPCT.
- Using one of the proved modified surfaces in the literature which enhanced the performance in the condenser rather than the rough surface (only in the condenser) for more enhancement in the total performance of the TPCT.
- Using a nanofluid such as Ti/H_2O which was proved to enhance the h_c by 2-3 times with the rough TPCT to achieve enhancement in both the condenser and evaporator.

Appendix A: Uncertainty calculations

1. Thermocouples

The overall uncertainty ($U_{T,ov}$) in thermocouples readings is calculated using the Root Square Sum (RSS):

$$U_{T,ov} = \pm\sqrt{(U_{st})^2 + (U_{c-f})^2 + (U_{DL})^2} \quad \text{A-1}$$

where $U_{T,ov}$ is the thermocouple overall uncertainty, U_{st} and U_{c-f} are the standard, curve-fit thermocouple uncertainties and U_{DL} data logger uncertainty.

From manufacturer's data, the uncertainties in RTD and data logger are 0.03 and 0.025°C, respectively, and the thermocouple curve-fit uncertainty is calculated using the following equation:

$$U_{c-f} = t_{n-1,95\%} S_{\bar{x}} \quad \text{A-2}$$

where $t_{n-1,95\%}$ is the student factor and $S_{\bar{x}}$ is the standard error of the mean.

Table A.1 illustrates calculations of the uncertainty associated with the curve fitting of one surface thermocouple.

Table A.1 Calculation of overall uncertainty of a type-T surface thermocouple

Data point	RTD reading (°C)	Thermocouple reading (°C)	Curve fitting equation Y=0.9936X-0.242 (°C)	Deviation squared
1	20.58248	20.262402	20.37472263	0.043161464
2	41.01263	41.127651	41.10643403	0.008799197
3	61.46811	61.842739	61.68894547	0.048768747
4	81.54824	81.959595	81.67705359	0.016592684
5	100.1954	100.35201	99.95175714	0.059381338
			Sum	0.1767
Dgree of freedom (n-1) = 4				
Standard deviation = 0.21				
$S_{\bar{x}}$ =0.094				
$t_{n-1,95\%}$= 2.57				
U_{c-f} = 0.24 K				

The uncertainties in RTD and data logger readings are negligible compared with the uncertainty of curve fitting. Therefore, the overall uncertainty of the type-T surface thermocouple is 0.24 K.

2. Flow Meter

Measuring of the flow rate has an overall uncertainty resulting from uncertainties associated with the water volume collection and the curve fitting which is calculated using equation:

$$U_{F,ov} = \pm\sqrt{(U_{VC})^2 + (U_{F,c-f})^2} \quad \text{A-3}$$

where $U_{F,ov}$ is the overall uncertainty in the flow rate measurement and U_{VC} *and* $U_{F,c-f}$ are water volume collection and curve fitting uncertainties.

The uncertainty associated with the flow rate of volume collection resulting from the uncertainty in the cylinder scale and the collection time which are ±2.5 cm^3 and ±0.5 second. Therefore, the uncertainty in the measuring of the flow rate 100 cm^3/min which represents the highest uncertainty percentage is:

$$U_{VC} = \pm 100\sqrt{\left(\frac{2.5}{100}\right)^2 + \left(\frac{0.5}{60}\right)^2} = \pm 2.635 \text{ cm}^3/\text{min}$$

While the curve fitting uncertainty is calculated statistically as illustrated in Table A.2.

Table A.2 Uncertainty in flow rate measurement calculated using curve fitting

Data point	Flow meter reading (cm^3/min)	Measured flow rate (cm^3/min)	Curve fitting equation Y=1.0074 X-4.6786	Deviation squared
1	100	105	105.4186	0.17522596
2	200	207	206.1586	0.70795396
3	300	305	306.8986	3.60468196
4	400	410	407.6386	5.57620996
5	500	512	508.3786	13.11453796
6	600	605	609.1186	16.96286596
7	700	705	709.8586	23.60599396
8	800	815	810.5986	19.37232196
			Sum	83.1198
Dgree of freedom (n-1) = 7				
Standard deviation (σ)= 3.446				
$S_{\bar{x}}$ =1.218				
$t_{n-1,95\%}$= 2.365				
$U_{F,c-f}$ = 2.88 cm^3/min				

The overall uncertainty associated with flow meter reading at a flow rate of 100 cm/min is obtained using equation (A.3):

$$U_{F,ov} = \pm\sqrt{(2.635)^2 + (2.88)^2} = \pm 3.9 \text{ cm}^3/\text{min} = \frac{\pm 3.9}{100} \times 100 = \pm 3.9\%$$

References

[1] W. Weiss, M. Spörk-Dür, and F. Mauthner, "Solar Heat Worldwide Global Market Development and Trends in 2016," *SHC, IEA*, p. 86, 2017.

[2] A. A. Alammar, R. K. Al-Dadah, and S. M. Mahmoud, "Experimental investigation of the influence of the geyser boiling phenomenon on the thermal performance of a two-phase closed thermosyphon," *J. Clean. Prod.*, vol. 172, pp. 2531–2543, 2017.

[3] L. M. Ayompe, a. Duffy, S. J. McCormack, and M. Conlon, "Validated TRNSYS model for forced circulation solar water heating systems with flat plate and heat pipe evacuated tube collectors," *Appl. Therm. Eng.*, vol. 31, no. 8–9, pp. 1536–1542, 2011.

[4] Z. Wang, Z. Duan, X. Zhao, and M. Chen, "Dynamic performance of a facade-based solar loop heat pipe water heating system," *Sol. Energy*, vol. 86, no. 5, pp. 1632–1647, 2012.

[5] D. Zhang, H. Tao, M. Wang, Z. Sun, and C. Jiang, "Numerical simulation investigation on thermal performance of heat pipe flat-plate solar collector," *Appl. Therm. Eng.*, vol. 118, pp. 113–126, 2017.

[6] B. Rassamakin, S. Khairnasov, V. Zaripov, A. Rassamakin, and O. Alforova, "Aluminum heat pipes applied in solar collectors," *Sol. Energy*, vol. 94, pp. 145–154, 2013.

[7] H. M. S. Hussein, H. H. El-Ghetany, and S. A. Nada, "Performance of wickless heat pipe flat plate solar collectors having different pipes cross sections geometries and filling ratios," *Energy Convers. Manag.*, vol. 47, no. 11–12, pp. 1539–1549, 2006.

[8] A. A. Alammar, R. K. Al-Dadah, and S. M. Mahmoud, "Effect of inclination angle and fill ratio on geyser boiling phenomena in a two-phase closed thermosiphon – Experimental investigation," *Energy Convers. Manag.*, vol. 156, no. October 2017, pp. 150–166, 2018.

[9] S. A. Nada, H. H. El-Ghetany, and H. M. S. Hussein, "Performance of a two-phase closed thermosyphon solar collector with a shell and tube heat exchanger," *Appl. Therm. Eng.*, vol. 24, no. 13, pp. 1959–1968, 2004.

[10] S. B. Riffat, X. Zhao, and P. S. Doherty, "Developing a theoretical model to investigate thermal performance of a thin membrane heat-pipe solar collector," *Appl. Therm. Eng.*, vol. 25, no. 5–6, pp. 899–915, 2005.

[11] M. Esen and H. Esen, "Experimental investigation of a two-phase closed thermosyphon solar water heater," *Sol. Energy*, vol. 79, no. 5, pp. 459–468, 2005.

[12] B. Abebe and K. Endalew, "Numerical Modelling and Experimental Validation of Heat Pipe Solar Collector for Water Heating," 2011.

[13] M. A. Ersoz and A. Yildiz, "Thermoeconomic analysis of thermosyphon heat pipes," *Renew. Sustain. Energy Rev.*, vol. 58, pp. 666–673, 2016.

[14] S. B. Riffat and X. Zhao, "A novel hybrid heat-pipe solar collector/CHP system-Part II: Theoretical and experimental investigations," *Renew. Energy*, vol. 29, no. 12, pp. 1965–1990, 2004.

[15] W. He, Y. Su, S. B. Riffat, J. Hou, and J. Ji, "Parametrical analysis of the design and performance of a solar heat pipe thermoelectric generator unit," *Appl. Energy*, vol. 88, no. 12, pp. 5083–5089, 2011.

[16] D. A. Reay, P. A. Kew, and R. J. McGlen, *Heat pipes Theory, Design and Applications*, (Sixth Ed). Butterworth-Heinemann, 2014.

[17] J. Danielewicz, M. A. Sayegh, B. Śniechowska, M. Szulgowska-Zgrzywa, and H. Jouhara, "Experimental and analytical performance investigation of air to air two phase closed thermosyphon based heat exchangers," *Energy*, vol. 77, pp. 82–87, 2014.

[18] A. Amini, J. Miller, and H. Jouhara, "An investigation into the use of the heat pipe technology in thermal energy storage heat exchangers," *Energy*, vol. 136, pp. 1–10,

2016.

[19] G. A. Longo, G. Righetti, C. Zilio, and F. Bertolo, "Experimental and theoretical analysis of a heat pipe heat exchanger operating with a low global warming potential refrigerant," *Appl. Therm. Eng.*, vol. 65, no. 1–2, pp. 361–368, 2014.

[20] K. S. Yang, T. Y. Yang, C. W. Tu, C. T. Yeh, and M. T. Lee, "A novel flat polymer heat pipe with thermal via for cooling electronic devices," *Energy Convers. Manag.*, vol. 100, pp. 37–44, 2015.

[21] X. Chen, H. Ye, X. Fan, T. Ren, and G. Zhang, "A review of small heat pipes for electronics," *Appl. Therm. Eng.*, vol. 96, pp. 1–17, 2016.

[22] H. Jouhara, A. Chauhan, T. Nannou, S. Almahmoud, B. Delpech, and L. C. Wrobel, "Heat pipe based systems - Advances and applications," *Energy*, vol. 128, pp. 729–754, 2017.

[23] K. Grissa, A. M. Benselama, C. Romestant, Y. Bertin, K. Grissa, Z. Lataoui, and A. Jemni, "Performance of a cylindrical wicked heat pipe used in solar collectors: Numerical approach with Lattice Boltzmann method," *Energy Convers. Manag.*, vol. 150, pp. 623–636, 2017.

[24] G. P. Peterson, *An Introduction to Heat Pipes Modeling, Testing, and Application*. John Wiley & Sons, Inc., 1994.

[25] D. Jafari, A. Franco, S. Filippeschi, and P. Di Marco, "Two-phase closed thermosyphons: A review of studies and solar applications," *Renew. Sustain. Energy Rev.*, vol. 53, pp. 575–593, 2016.

[26] A. A. Alammar, R. K. Al-Dadah, and S. M. Mahmoud, "Effect of hydrophobicity on enhancement of condensation heat transfer-numerical investigation," in *2016 International Conference for Students on Applied Engineering, ICSAE 2016*, 2017.

[27] W. Chun, Y. Heack, H. Youl, and Y. Soo, "An experimental study of the utilization of

heat pipes for solar water heaters," *Appl. Therm. Eng.*, vol. 19, pp. 807–817, 1999.

[28] C. I. Ezekwe, "Thermal performance of heat pipe solar energy systems," *Sol. Energy*, vol. 7, no. 4, pp. 349–354, 1990.

[29] H. M. S. Hussein, M. A. Mohamad, and A. S. El-Asfouri, "Theoretical analysis of laminar-film condensation heat transfer inside inclined wickless heat pipes flat-plate solar collector," *Renew. Energy*, vol. 23, no. 3–4, pp. 525–535, 2001.

[30] M. Esen, "Thermal performance of a solar cooker integrated vacuum-tube collector with heat pipes containing different refrigerants," *Sol. Energy*, vol. 76, no. 6, pp. 751–757, 2004.

[31] K. A. Joudi and A. A. Al-tabbakh, "Computer simulation of a two phase thermosyphon solar domestic hot water heating system," *Energy Convers. Manag.*, vol. 40, no. 7, pp. 775–793, 1999.

[32] E. Mathioulakis and V. Belessiotis, "A new heat-pipe type solar domestic hot water system," *Sol. Energy*, vol. 72, no. 1, pp. 13–20, 2002.

[33] H. M. S. Hussein, "Theoretical and experimental investigation of wickless heat pipes flat plate solar collector with cross flow heat exchanger," *Energy Convers. Manag.*, vol. 48, no. 4, pp. 1266–1272, 2007.

[34] H. M. S. Hussein, M. A. Mohamad, and A. S. El-Asfouri, "Transient investigation of a thermosyphon flat-plate solar collector," *Appl. Therm. Eng.*, vol. 19, no. 7, pp. 789–800, 1999.

[35] E. Azad, "Theoretical and experimental investigation of heat pipe solar collector," *Exp. Therm. Fluid Sci.*, vol. 32, no. 8, pp. 1666–1672, 2008.

[36] X. Zhao, Z. Wang, and Q. Tang, "Theoretical investigation of the performance of a novel loop heat pipe solar water heating system for use in Beijing, China," *Appl. Therm. Eng.*, vol. 30, no. 16, pp. 2526–2536, 2010.

[37] K. S. Ong, W. L. Tong, and K. Low, "System Performance of Heat Pipe Solar Water Heaters," vol. 15, no. 2, pp. 261–266, 2011.

[38] D. A. G. Redpath, S. N. G. Lo, and P. C. Eames, "Experimental investigation and optimisation study of a direct thermosyphon heat-pipe evacuated tube solar water heater subjected to a northern maritime climate," *Int. J. Ambient Energy*, vol. 31, no. 2, pp. 91–100, 2010.

[39] M. Arab, M. Soltanieh, and M. B. Shafii, "Experimental investigation of extra-long pulsating heat pipe application in solar water heaters," *Exp. Therm. Fluid Sci.*, vol. 42, pp. 6–15, 2012.

[40] P. Gang, F. Huide, Z. Tao, and J. Jie, "A numerical and experimental study on a heat pipe PV/T system," *Sol. Energy*, vol. 85, no. 5, pp. 911–921, 2011.

[41] P. Gang, F. Huide, Z. Huijuan, and J. Jie, "Performance study and parametric analysis of a novel heat pipe PV/T system," *Energy*, vol. 37, no. 1, pp. 384–395, 2012.

[42] P. Gang, F. Huide, J. Jie, C. Tin-Tai, and Z. Tao, "Annual analysis of heat pipe PV/T systems for domestic hot water and electricity production," *Energy Convers. Manag.*, vol. 56, pp. 8–21, 2012.

[43] M. A. Islam, M. A. R. Khan, and M. A. R. Sarkar, "Performance of a Two-Phase Solar Collector in Water Heating," vol. 4, pp. 117–123, 2005.

[44] B. R. Chen, Y. W. Chang, W. S. Lee, and S. L. Chen, "Long-term thermal performance of a two-phase thermosyphon solar water heater," *Sol. Energy*, vol. 83, no. 7, pp. 1048–1055, 2009.

[45] A. Samanci and A. Berber, "Experimental investigation of single-phase and two- phase closed thermosyphon solar water heater systems," vol. 6, no. 4, pp. 688–693, 2011.

[46] N. Z. Aung and S. Li, "Numerical investigation on effect of riser diameter and inclination on system parameters in a two-phase closed loop thermosyphon solar water

heater," *Energy Convers. Manag.*, vol. 75, pp. 25–35, 2013.

[47] M. Arab and A. Abbas, "Model-based design and analysis of heat pipe working fluid for optimal performance in a concentric evacuated tube solar water heater," *Sol. Energy*, vol. 94, pp. 162–176, 2013.

[48] L. Wei, D. Yuan, D. Tang, and B. Wu, "A study on a flat-plate type of solar heat collector with an integrated heat pipe," *Sol. Energy*, vol. 97, pp. 19–25, 2013.

[49] J. Li, F. Lin, and G. Niu, "An insert-type two-phase closed loop thermosyphon for split-type solar water heaters," *Appl. Therm. Eng.*, vol. 70, no. 1, pp. 441–450, 2014.

[50] A. Jahanbakhsh, H. R. Haghgou, and S. Alizadeh, "Experimental analysis of a heat pipe operated solar collector using water-ethanol solution as the working fluid," *Sol. Energy*, vol. 118, pp. 267–275, 2015.

[51] M. A. Ersöz, "Effects of different working fluid use on the energy and exergy performance for evacuated tube solar collector with thermosyphon heat pipe," *Renew. Energy*, vol. 96, pp. 244–256, 2016.

[52] A. E. Kabeel, M. M. Khairat Dawood, and A. I. Shehata, "Augmentation of thermal efficiency of the glass evacuated solar tube collector with coaxial heat pipe with different refrigerants and filling ratio," *Energy Convers. Manag.*, vol. 138, pp. 286–298, 2017.

[53] S. Ghorai and K. D. P. Nigam, "CFD modeling of flow profiles and interfacial phenomena in two-phase flow in pipes," *Chem. Eng. Process. Process Intensif.*, vol. 45, no. 1, pp. 55–65, 2006.

[54] Z. Yang, X. F. Peng, and P. Ye, "Numerical and experimental investigation of two phase flow during boiling in a coiled tube," *Int. J. Heat Mass Transf.*, vol. 51, no. 5–6, pp. 1003–1016, 2008.

[55] H. L. Wu, X. F. Peng, P. Ye, and Y. Eric Gong, "Simulation of refrigerant flow boiling

in serpentine tubes," *Int. J. Heat Mass Transf.*, vol. 50, no. 5–6, pp. 1186–1195, 2007.

[56] S. C. K. De Schepper, G. J. Heynderickx, and G. B. Marin, "CFD modeling of all gas-liquid and vapor-liquid flow regimes predicted by the Baker chart," *Chem. Eng. J.*, vol. 138, no. 1–3, pp. 349–357, 2008.

[57] S. C. K. De Schepper, G. J. Heynderickx, and G. B. Marin, "Modeling the evaporation of a hydrocarbon feedstock in the convection section of a steam cracker," *Comput. Chem. Eng.*, vol. 33, no. 1, pp. 122–132, 2009.

[58] C. Fang, M. David, A. Rogacs, and K. Goodson, "Volume of Fluid Simulation of Boiling Two-Phase Flow in a Vapor-Venting Microchannel," *Front. Heat Mass Transf.*, vol. 1, no. 1, 2010.

[59] D. L. Sun, J. L. Xu, and L. Wang, "Development of a vapor-liquid phase change model for volume-of-fluid method in FLUENT," *Int. Commun. Heat Mass Transf.*, vol. 39, no. 8, pp. 1101–1106, 2012.

[60] H. Ganapathy, a. Shooshtari, K. Choo, S. Dessiatoun, M. Alshehhi, and M. Ohadi, "Volume of fluid-based numerical modeling of condensation heat transfer and fluid flow characteristics in microchannels," *Int. J. Heat Mass Transf.*, vol. 65, pp. 62–72, 2013.

[61] A. Dehbi, F. Janasz, and B. Bell, "Prediction of steam condensation in the presence of noncondensable gases using a CFD-based approach," *Nucl. Eng. Des.*, vol. 258, pp. 199–210, 2013.

[62] Z. Yin, Y. Guo, B. Sunden, Q. Wang, and M. Zeng, "Numerical Simulation of Laminar Film Condensation in a Horizontal Minitube with and Without Non-Condensable Gas by the VOF Method," *Numer. Heat Transf. Part A*, vol. 68, no. 9, pp. 958–977, 2015.

[63] J. De Li, "CFD simulation of water vapour condensation in the presence of non-condensable gas in vertical cylindrical condensers," *Int. J. Heat Mass Transf.*, vol. 57,

no. 2, pp. 708–721, 2013.

[64] B. Fadhl, L. C. Wrobel, and H. Jouhara, "Numerical modelling of the temperature distribution in a two-phase closed thermosyphon," *Appl. Therm. Eng.*, vol. 60, no. 1–2, pp. 122–131, 2013.

[65] M. Zhang, Z. Liu, G. Ma, and S. Cheng, "Numerical simulation and experimental verification of a flat two-phase thermosyphon," *Energy Convers. Manag.*, vol. 50, no. 4, pp. 1095–1100, 2009.

[66] A. Alizadehdakhel, M. Rahimi, and A. A. Alsairafi, "CFD modeling of flow and heat transfer in a thermosyphon," *Int. Commun. Heat Mass Transf.*, vol. 37, no. 3, pp. 312–318, 2010.

[67] K. Kafeel and A. Turan, "Axi-symmetric simulation of a two phase vertical thermosyphon using Eulerian two-fluid methodology," *Heat Mass Transf.*, vol. 49, no. 8, pp. 1089–1099, 2013.

[68] K. Kafeel and A. Turan, "Simulation of the response of a thermosyphon under pulsed heat input conditions," *Int. J. Therm. Sci.*, vol. 80, no. 1, pp. 33–40, 2014.

[69] G. Huminic and A. Huminic, "Numerical study on heat transfer characteristics of thermosyphon heat pipes using nanofluids," *Energy Convers. Manag.*, vol. 76, pp. 393–399, 2013.

[70] R. S. Nair and C. Balaji, "Synergistic analysis of heat transfer characteristics of an internally finned two phase closed thermosyphon," *Appl. Therm. Eng.*, vol. 101, pp. 720–729, 2015.

[71] H. Shabgard, B. Xiao, A. Faghri, R. Gupta, and W. Weissman, "Thermal characteristics of a closed thermosyphon under various filling conditions," *Int. J. Heat Mass Transf.*, vol. 70, pp. 91–102, 2014.

[72] Q. Baojin, Z. Li, X. Hong, and S. Yan, "Heat transfer characteristics of titanium/water

two-phase closed thermosyphon," *Energy Convers. Manag.*, vol. 50, no. 9, pp. 2174–2179, 2009.

[73] H. Jouhara and A. J. Robinson, "Experimental investigation of small diameter two-phase closed thermosyphons charged with water, FC-84, FC-77 and FC-3283," *Appl. Therm. Eng.*, vol. 30, no. 2–3, pp. 201–211, 2010.

[74] Y. W. Kuang, W. Wang, R. Zhuan, and C. C. Yi, "Simulation of boiling flow in evaporator of separate type heat pipe with low heat flux," *Ann. Nucl. Energy*, vol. 75, pp. 158–167, 2015.

[75] B. Fadhl, L. C. Wrobel, and H. Jouhara, "CFD modelling of a two-phase closed thermosyphon charged with R134a and R404a," *Appl. Therm. Eng.*, vol. 78, pp. 482–490, 2015.

[76] H. Jouhara, B. Fadhl, and L. C. Wrobel, "Three-dimensional CFD simulation of geyser boiling in a two-phase closed thermosyphon," *Int. J. Hydrogen Energy*, vol. 41, no. 37, pp. 16463–16476, 2015.

[77] B. Abdullahi, "Development and Optimization of heat pipe based Compound Parabolic Collector," University of Birmingham, 2015.

[78] W. Lian, W. Chang, and Y. Xuan, "Numerical investigation on flow and thermal features of a rotating heat pipe," *Appl. Therm. Eng.*, vol. 101, pp. 92–100, 2016.

[79] Z. Xu, Y. Zhang, B. Li, C.-C. Wang, and Y. Li, "The influences of the inclination angle and evaporator wettability on the heat performance of a thermosyphon by simulation and experiment," *Int. J. Heat Mass Transf.*, vol. 116, pp. 675–684, 2018.

[80] Z. Xu, Y. Zhang, B. Li, C.-C. Wang, and Q. Ma, "Heat performances of a thermosyphon as affected by evaporator wettability and filling ratio," *Appl. Therm. Eng.*, vol. 129, pp. 665–673, 2018.

[81] Y. Kim, J. Choi, S. Kim, and Y. Zhang, "Effects of mass transfer time relaxation

parameters on condensation in a thermosyphon," *J. Mech. Sci. Technol.*, vol. 29, no. 12, pp. 5497–5505, 2015.

[82] Z. Xu, Y. Zhang, B. Li, and J. Huang, "Modeling the phase change process for a two-phase closed thermosyphon by considering transient mass transfer time relaxation parameter," *Int. J. Heat Mass Transf.*, vol. 101, pp. 614–619, 2016.

[83] L. Xia, D. Dong, H. Zhang, and C. Yu, "Numerical simulation of wickless gravity-assisted two-phase cooling system used in heavy duty extrusion pelleting line," *Int. J. Heat Mass Transf.*, vol. 111, pp. 540–550, 2017.

[84] S. E. D. Fertahi, T. Bouhal, Y. Agrouaz, T. Kousksou, T. El Rhafiki, and Y. Zeraouli, "Performance optimization of a two-phase closed thermosyphon through CFD numerical simulations," *Appl. Therm. Eng.*, vol. 128, pp. 551–563, 2018.

[85] M. R. Sarmasti Emami, S. H. Noie, and M. Khoshnoodi, "Effect of Aspect Ratio and Filling Ratio on Thermal Performance of an Inclined Two-Phase Closed Thermosyphon," *Iran. J. Sci. Technol.*, vol. 32, no. February 2008, pp. 39–51, 2008.

[86] B. Jiao, L. M. Qiu, X. B. Zhang, and Y. Zhang, "Investigation on the effect of filling ratio on the steady-state heat transfer performance of a vertical two-phase closed thermosyphon," *Appl. Therm. Eng.*, vol. 28, no. 11–12, pp. 1417–1426, 2008.

[87] T. Sukchana and C. Jaiboonma, "Effect of Filling Ratios and Adiabatic Length on Thermal Efficiency of Long Heat Pipe Filled with R-134a," *Energy Procedia*, vol. 34, pp. 298–306, 2013.

[88] A. A. Chehade, H. Louahlia-Gualous, S. Le Masson, I. Victor, and N. Abouzahab-Damaj, "Experimental investigation of thermosyphon loop thermal performance," *Energy Convers. Manag.*, vol. 84, pp. 671–680, 2014.

[89] J.-S. Chen and J.-H. Chou, "Cooling performance of flat plate heat pipes with different liquid filling ratios," *Int. J. Heat Mass Transf.*, vol. 77, pp. 874–882, 2014.

[90] D. Yin, H. Rajab, and H. B. Ma, "Theoretical analysis of maximum filling ratio in an oscillating heat pipe," *Int. J. Heat Mass Transf.*, vol. 74, pp. 353–357, 2014.

[91] Z. Lataoui and A. Jemni, "Experimental investigation of a stainless steel two-phase closed thermosyphon," *Appl. Therm. Eng.*, vol. 121, pp. 721–727, 2017.

[92] R. Manimaran, K. Palaniradja, N. Alagumurthi, and K. Velmurugan, "An Investigation of Thermal Performance of Heat Pipe Using Di-water," *Sci. Technol.*, vol. 2, no. 4, pp. 77–80, 2012.

[93] R. Manimaran, K. Palaniradja, and N. Alagumurthi, "Effect of filling ratio on thermal characteristics of circular heat pipe using nanofluid," *Front. Heat Pipes*, vol. 3, no. 2, pp. 1–5, 2012.

[94] E. Sadeghinezhad, M. Mehrali, M. A. Rosen, A. R. Akhiani, S. Tahan Latibari, M. Mehrali, and H. S. C. Metselaar, "Experimental investigation of the effect of graphene nanofluids on heat pipe thermal performance," *Appl. Therm. Eng.*, vol. 100, pp. 775–787, 2016.

[95] M. Ghanbarpour, N. Nikkam, R. Khodabandeh, and M. S. Toprak, "Thermal performance of inclined screen mesh heat pipes using silver nanofluids," *Int. Commun. Heat Mass Transf.*, vol. 67, pp. 14–20, 2015.

[96] M. Ghanbarpour, N. Nikkam, R. Khodabandeh, and M. S. Toprak, "Improvement of heat transfer characteristics of cylindrical heat pipe by using SiC nanofluids," *Appl. Therm. Eng.*, vol. 90, pp. 127–135, 2015.

[97] Z. Xue and W. Qu, "Experimental study on effect of inclination angles to ammonia pulsating heat pipe," *Chinese J. Aeronaut.*, vol. 27, no. 5, pp. 1122–1127, 2014.

[98] R. Senthilkumar, S. Vaidyanathan, and B. Sivaraman, "Effect of inclination angle in heat pipe performance using copper nanofluid," *Procedia Eng.*, vol. 38, pp. 3715–3721, 2012.

[99] M. Nazarimanesh, T. Yousefi, and M. Ashjaee, "Experimental study on the effects of inclination situation of the sintered heat pipe on its thermal performance," *Exp. Therm. Fluid Sci.*, vol. 68, pp. 625–633, 2015.

[100] T. Sukchana and N. Pratinthong, "A two-phase closed thermosyphon with an adiabatic section using a flexible hose and R-134a filling," *Exp. Therm. Fluid Sci.*, vol. 77, pp. 317–326, 2016.

[101] E. Gedik, "Experimental investigation of the thermal performance of a two-phase closed thermosyphon at different operating conditions," *Energy Build.*, vol. 127, pp. 1096–1107, 2016.

[102] H. Tang, Y. Tang, B. Zhuang, G. Chen, and S. Zhang, "Experimental investigation of the thermal performance of heat pipes with double-ended heating and middle-cooling," *Energy Convers. Manag.*, vol. 148, pp. 1332–1345, 2017.

[103] S. H. Noie, "Heat transfer characteristics of a two-phase closed thermosyphon," *Appl. Therm. Eng.*, vol. 25, no. 4, pp. 495–506, 2005.

[104] P. Amatachaya and W. Srimuang, "Comparative heat transfer characteristics of a flat two-phase closed thermosyphon (FTPCT) and a conventional two-phase closed thermosyphon (CTPCT)," *Int. Commun. Heat Mass Transf.*, vol. 37, no. 3, pp. 293–298, 2010.

[105] J. Seo and J. Y. Lee, "Length effect on entrainment limitation of vertical wickless heat pipe," *Int. J. Heat Mass Transf.*, vol. 101, pp. 373–378, 2016.

[106] A. K. Mozumder, A. F. Akon, M. S. H. Chowdhury, and S. C. Banik, "Performance of Heat Pipe for Different working fluids and fill ratios," *J. Mech. Eng.*, vol. 41, no. 2, pp. 96–102, 2010.

[107] L. Ma, L. Shang, D. Zhong, and Z. Ji, "Experimental Performance of a Two-phase Closed Thermosyphon Charged with Hydrocarbons and Freon Refrigerants for

Renewable Energy Applications," *Energy Procedia*, vol. 105, pp. 5147–5152, 2017.

[108] H. Jouhara, Z. Ajji, Y. Koudsi, H. Ezzuddin, and N. Mousa, "Experimental investigation of an inclined-condenser wickless heat pipe charged with water and an ethanol-water azeotropic mixture," *Energy*, vol. 61, pp. 139–147, 2013.

[109] S. Liu, J. Li, and Q. Chen, "Visualization of flow pattern in thermosyphon by ECT," *Flow Meas. Instrum.*, vol. 18, no. 5–6, pp. 216–222, 2007.

[110] N. Putra, R. Sahmura Ramadhan, W. N. Septiadi, and Sutiarso, "Visualization of the boiling phenomenon inside a heat pipe using neutron radiography," *Exp. Therm. Fluid Sci.*, vol. 66, pp. 13–27, 2015.

[111] D. Jafari, P. Di Marco, S. Filippeschi, and A. Franco, "An experimental investigation on the evaporation and condensation heat transfer of two-phase closed thermosyphons," *Exp. Therm. Fluid Sci.*, vol. 88, pp. 111–123, 2017.

[112] T. F. Lin, W. T. Lin, Y. L. Tsay, J. C. Wu, and R. J. Shyu, "Experimental investigation of geyser boiling in an annular two-phase closed thermosyphon," *Int. J. Heat Mass Transf.*, vol. 38, no. 2, pp. 295–307, 1995.

[113] I. Khazaee, R. Hosseini, and S. H. Noie, "Experimental investigation of effective parameters and correlation of geyser boiling in a two-phase closed thermosyphon," *Appl. Therm. Eng.*, vol. 30, no. 5, pp. 406–412, 2010.

[114] K. Negishi and T. Sawada, "Heat transfer performance of an inclined two-phase closed thermosyphon," *Int. J. Heat Mass Transf.*, vol. 26, no. 8, pp. 1207–1213, 1983.

[115] H. Kuncoro, Y. F. Rao, and K. Fukuda, "An experimental study on the mechanism of geysering in a closed two-phase thermosyphon," *Int. J. Multiph. Flow*, vol. 21, no. 6, pp. 1243–1252, 1995.

[116] G. Xia, W. Wang, L. Cheng, and D. Ma, "Visualization study on the instabilities of phase-change heat transfer in a flat two-phase closed thermosyphon," *Appl. Therm.*

Eng., vol. 116, pp. 392–405, 2017.

[117] S. H. Noie, M. R. Sarmasti Emami, and M. Khoshnoodi, "Effect of Inclination Angle and Filling Ratio on Thermal Performance of a Two-Phase Closed Thermosyphon under Normal Operating Conditions," *Heat Transf. Eng.*, vol. 28, no. January 2015, pp. 365–371, 2007.

[118] S. L. Abreu and S. Colle, "An experimental study of two-phase closed thermosyphons for compact solar domestic hot-water systems," *Sol. Energy*, vol. 76, no. 1–3, pp. 141–145, 2004.

[119] M. R. S. Emami, S. H. Noie, M. Khoshnoodi, M. T. H. Mosavian, and A. Kianifar, "Investigation of Geyser Boiling Phenomenon in a Two-Phase Closed Thermosyphon," *Heat Transf. Eng.*, vol. 30, no. 5, pp. 408–415, 2009.

[120] D. Jafari, S. Filippeschi, A. Franco, and P. Di Marco, "Unsteady experimental and numerical analysis of a two-phase closed thermosyphon at different filling ratios," *Exp. Therm. Fluid Sci.*, vol. 81, pp. 164–174, 2017.

[121] C. Casarosa, E. Latrofa, and A. Shelginski, "The geyser effect in a two-phase thermosyphon," *Int. J. Heat Mass Transf.*, vol. 26, no. 6, pp. 933–941, 1983.

[122] C. Tecchio, J. L. G. Oliveira, K. V. Paiva, M. B. H. Mantelli, R. Galdolfi, and L. G. S. Ribeiro, "Geyser boiling phenomenon in two-phase closed loop-thermosyphons," *Int. J. Heat Mass Transf.*, vol. 111, pp. 29–40, 2017.

[123] A. S. Dalkilic and S. Wongwises, "Intensive literature review of condensation inside smooth and enhanced tubes," *Int. J. Heat Mass Transf.*, vol. 52, no. 15–16, pp. 3409–3426, 2009.

[124] N. A. Patankar, "Supernucleating surfaces for nucleate boiling and dropwise condensation heat transfer," *R. Soc. Chem.*, vol. 6, pp. 1613–1620, 2010.

[125] S. Vemuri, K. J. Kim, B. D. Wood, S. Govindaraju, and T. W. Bell, "Long term testing

for dropwise condensation using self-assembled monolayer coatings of n-octadecyl mercaptan," *Appl. Therm. Eng.*, vol. 26, no. 4, pp. 421–429, 2006.

[126] P. Zhang and F. Y. Lv, "A review of the recent advances in superhydrophobic surfaces and the emerging energy-related applications," *Energy*, vol. 82, pp. 1068–1087, 2015.

[127] C. Fang, J. E. Steinbrenner, F.-M. Wang, and K. E. Goodson, "Impact of wall hydrophobicity on condensation flow and heat transfer in silicon microchannels," *J. Micromechanics Microengineering*, vol. 20, no. 4, p. 45018, 2010.

[128] S. Lee, K. Cheng, V. Palmre, M. M. H. Bhuiya, K. J. Kim, B. J. Zhang, and H. Yoon, "Heat transfer measurement during dropwise condensation using micro/nano-scale porous surface," *Int. J. Heat Mass Transf.*, vol. 65, pp. 619–626, 2013.

[129] A. Chatterjee, M. M. Derby, Y. Peles, and M. K. Jensen, "Condensation heat transfer on patterned surfaces," *Int. J. Heat Mass Transf.*, vol. 66, pp. 889–897, 2013.

[130] M. M. Derby, A. Chatterjee, Y. Peles, and M. K. Jensen, "Flow condensation heat transfer enhancement in a mini-channel with hydrophobic and hydrophilic patterns," *Int. J. Heat Mass Transf.*, vol. 68, pp. 151–160, 2014.

[131] A. Chatterjee, M. M. Derby, Y. Peles, and M. K. Jensen, "Enhancement of condensation heat transfer with patterned surfaces," *Int. J. Heat Mass Transf.*, vol. 71, pp. 675–681, 2014.

[132] M. Roudgar and J. De Coninck, "Condensation heat transfer coefficient versus wettability," *Appl. Surf. Sci.*, vol. 338, pp. 15–21, 2015.

[133] H. W. Hu, G. H. Tang, and D. Niu, "Experimental investigation of condensation heat transfer on hybrid wettability finned tube with large amount of noncondensable gas," *Int. J. Heat Mass Transf.*, vol. 85, pp. 513–523, 2015.

[134] H. W. Hu, G. H. Tang, and D. Niu, "Experimental investigation of convective condensation heat transfer on tube bundles with different surfacewettability at large

amount of noncondensable gas," *Int. J. Heat Mass Transf.*, vol. 85, pp. 513–523, 2015.

[135] K. Cheng, S. Kim, S. Lee, and K. J. Kim, "Internal dropwise condensation: Modeling and experimental framework for horizontal tube condensers," *Int. J. Heat Mass Transf.*, vol. 83, pp. 99–108, 2015.

[136] P. S. Mahapatra, A. Ghosh, R. Ganguly, and C. M. Megaridis, "Key design and operating parameters for enhancing dropwise condensation through wettability patterning," *Int. J. Heat Mass Transf.*, vol. 92, pp. 877–883, 2016.

[137] Y. Takata, S. Hidaka, M. Masuda, and T. Ito, "Pool boiling on a superhydrophilic surface," *Int. J. Energy Res.*, vol. 27, no. 2, pp. 111–119, 2003.

[138] Y. Takata, S. Hidaka, and T. Uraguchi, "Boiling feature on a super water-repellent surface," *Heat Transf. Eng.*, vol. 27, no. 8, pp. 25–30, 2006.

[139] A. R. Betz, J. Jenkins, C. J. Kim, and D. Attinger, "Boiling heat transfer on superhydrophilic, superhydrophobic, and superbiphilic surfaces," *Int. J. Heat Mass Transf.*, vol. 57, no. 2, pp. 733–741, 2013.

[140] H. Jo, S. Kim, H. Kim, J. Kim, and M. Kim, "Nucleate boiling performance on nano/microstructures with different wetting surfaces," *Nanoscale Res. Lett.*, vol. 7, no. 1, p. 242, 2012.

[141] B. J. Suroto, M. Tashiro, S. Hirabayashi, S. Hidaka, M. Kohno, and Y. Takata, "Effects of Hydrophobic-Spot Periphery and Subcooling on Nucleate Pool Boiling from a Mixed-Wettability Surface," *J. Therm. Sci. Technol.*, vol. 8, no. 1, pp. 294–308, 2013.

[142] M. Zupančič, M. Steinbücher, P. Gregorčič, and I. Golobič, "Enhanced pool-boiling heat transfer on laser-made hydrophobic/superhydrophilic polydimethylsiloxane-silica patterned surfaces," *Appl. Therm. Eng.*, vol. 91, pp. 288–297, 2015.

[143] M. Yamada, B. Shen, T. Imamura, S. Hidaka, M. Kohno, K. Takahashi, and Y. Takata, "Enhancement of boiling heat transfer under sub-atmospheric pressures using biphilic

surfaces," *Int. J. Heat Mass Transf.*, vol. 115, pp. 753–762, 2017.

[144] X. F. Yang, Z.-H. Liu, and J. Zhao, "Heat transfer performance of a horizontal micro-grooved heat pipe using CuO nanofluid," *J. Micromechanics Microengineering*, vol. 18, p. 35038, 2008.

[145] Z. H. Liu, Y. Y. Li, and R. Bao, "Thermal performance of inclined grooved heat pipes using nanofluids," *Int. J. Therm. Sci.*, vol. 49, no. 9, pp. 1680–1687, 2010.

[146] R. K. Cheedarala, E. Park, K. Kong, Y.-B. Park, and H. W. Park, "Experimental study on critical heat flux of highly efficient soft hydrophilic CuO–chitosan nanofluid templates," *Int. J. Heat Mass Transf.*, vol. 100, pp. 396–406, 2016.

[147] S. H. Noie, S. Z. Heris, M. Kahani, and S. M. Nowee, "Heat transfer enhancement using Al2O3/water nanofluid in a two-phase closed thermosyphon," *Int. J. Heat Fluid Flow*, vol. 30, no. 4, pp. 700–705, 2009.

[148] W. I. A. Aly, M. A. Elbalshouny, H. M. Abd El-Hameed, and M. Fatouh, "Thermal performance evaluation of a helically-micro-grooved heat pipe working with water and aqueous Al2O3 nanofluid at different inclination angle and filling ratio," *Appl. Therm. Eng.*, vol. 110, pp. 1294–1304, 2017.

[149] T. Paramatthanuwat, S. Boothaisong, S. Rittidech, and K. Booddachan, "Heat transfer characteristics of a two-phase closed thermosyphon using de ionized water mixed with silver nano," *Heat Mass Transf.*, vol. 46, pp. 281–285, 2010.

[150] G. Huminic, A. Huminic, I. Morjan, and F. Dumitrache, "Experimental study of the thermal performance of thermosyphon heat pipe using iron oxide nanoparticles," *Int. J. Heat Mass Transf.*, vol. 54, no. 1–3, pp. 656–661, 2011.

[151] M. Shanbedi, S. Z. Heris, M. Baniadam, A. Amiri, and M. Maghrebi, "Investigation of Heat-Transfer Characterization of EDA-MWCNT / DI-Water Nanofluid in a Two-Phase Closed Thermosyphon," *Ind. Eng. Chem. Res.*, vol. 51, pp. 1423–1428, 2012.

[152] R. Sureshkumar, S. T. Mohideen, and N. Nethaji, "Heat transfer characteristics of nanofluids in heat pipes: A review," *Renew. Sustain. Energy Rev.*, vol. 20, pp. 397–410, 2013.

[153] K. Han and D.-H. Cho, "Effect of micro groove on the performance of condensing heat transfer of the micro grooved thermosyphon," *Int. J. Air-Conditioning Refrig.*, vol. 10, no. 4, pp. 184–191, 2002.

[154] K. Han and D.-H. Cho, "A comparison of the heat transfer performance of thermosyphon using a strait groove and a hilical groove," *J. Mech. Sci. Technol.*, vol. 19, no. 12, pp. 2296–2302, 2005.

[155] A. J. Jiao, R. Riegler, H. B. Ma, and G. P. Peterson, "Thin film evaporation effect on heat transport capability in a grooved heat pipe," *Microfluid. Nanofluidics*, vol. 1, no. 3, pp. 227–233, 2005.

[156] A. J. Jiao, H. B. Ma, and J. K. Critser, "Evaporation heat transfer characteristics of a grooved heat pipe with micro-trapezoidal grooves," *Int. J. Heat Mass Transf.*, vol. 50, no. 15–16, pp. 2905–2911, 2007.

[157] F. Lefèvre, R. Rullière, G. Pandraud, and M. Lallemand, "Prediction of the temperature field in flat plate heat pipes with micro-grooves – Experimental validation," *Int. J. Heat Mass Transf.*, vol. 51, no. 15–16, pp. 4083–4094, 2008.

[158] T. Yong, C. Ping, and W. Xiaowu, "Experimental investigation into the performance of heat pipe with micro grooves fabricated by Extrusion-ploughing process," *Energy Convers. Manag.*, vol. 51, no. 10, pp. 1849–1854, 2010.

[159] X. Wang, G. M. Xin, F. Z. Tian, and L. Cheng, "Effect of Internal Helical Microfin on Condensation Performance of Two-Phase Closed Thermosyphon," *Adv. Mater. Res.*, vol. 516–517, pp. 9–14, 2012.

[160] Y. Naresh and C. Balaji, "Experimental investigations of heat transfer from an

internally finned two phase closed thermosyphon," *Appl. Therm. Eng.*, vol. 112, pp. 1658–1666, 2017.

[161] S. C. Wong and Y. C. Lin, "Effect of copper surface wettability on the evaporation performance: Tests in a flat-plate heat pipe with visualization," *Int. J. Heat Mass Transf.*, vol. 54, no. 17–18, pp. 3921–3926, 2011.

[162] A. B. Solomon, K. Ramachandran, and B. C. Pillai, "Thermal performance of a heat pipe with nanoparticles coated wick," *Appl. Therm. Eng.*, vol. 36, pp. 106–112, 2012.

[163] Y. Hu, J. Cheng, W. Zhang, R. Shirakashi, and S. Wang, "Thermal performance enhancement of grooved heat pipes with inner surface treatment," *Int. J. Heat Mass Transf.*, vol. 67, pp. 416–419, 2013.

[164] M. Rahimi, K. Asgary, and S. Jesri, "Thermal characteristics of a resurfaced condenser and evaporator closed two-phase thermosyphon," *Int. Commun. Heat Mass Transf.*, vol. 37, no. 6, pp. 703–710, 2010.

[165] A. B. Solomon, A. Mathew, K. Ramachandran, B. C. Pillai, and V. K. Karthikeyan, "Thermal performance of anodized two phase closed thermosyphon (TPCT)," *Exp. Therm. Fluid Sci.*, vol. 48, pp. 49–57, 2013.

[166] C. Hsu, D. Yang, L. Kuo, and P. Chen, "Thermal Performance Improvement of a Cylindrical Thermosyphon with Modified Wettability on both Evaporator and Condenser Sections," *Am. J. Heat Mass Transf.*, vol. 1, no. 2, pp. 81–89, 2014.

[167] A. A. Alammar, R. K. Al-dadah, and S. M. Mahmoud, "Numerical investigation of effect of fill ratio and inclination angle on a thermosiphon heat pipe thermal performance," *Appl. Therm. Eng.*, vol. 108, pp. 1055–1065, 2016.

[168] Ansys Southpointe, *Ansys Fluent Theory Guide*, vol. 15317, no. November. 2013.

[169] D. Sun, J. Xu, and Q. Chen, "Modeling of the evaporation and condensation phase-change problems with FLUENT," *Numer. Heat Transf. Part B Fundam.*, vol. 66, no. 4,

pp. 326–342, 2014.

[170] J. . Brackbill, D. . Kothe, and C. Zemach, "A continuum method for modeling surface tension," *J. Comput. Phys.*, vol. 100, pp. 335–354, 1992.

[171] ANSYS Southpointe, "ANSYS Fluent User's Guide 15.0," vol. 15317, no. February, pp. 724–746, 2013.

[172] C. Y. Lee, H. H. Huang, S. M. Lee, and K. Ouyang, "Numerical simulation of the heat transfer characteristics of low-watt thermosyphon influence factors," *J. Appl. Sci. Eng.*, vol. 17, no. 4, pp. 423–428, 2014.

[173] G. Bracco and B. Holst, *Surface Science Techniques: Chapter 1: Contact Angle and Wetting Properties*, vol. 51, no. 1. 2013.

[174] W. H. Lee, "A Pressure Iteration Sheme for Two-Phase Flow Modeling," *Multiph. Transp. Fundam. React. Safety, Appl.*, pp. 407–431, 1980.

[175] B. Qi, J. Wei, L. Zhang, and H. Xu, "A fractal dropwise condensation heat transfer model including the effects of contact angle and drop size distribution," *Int. J. Heat Mass Transf.*, vol. 83, pp. 259–272, 2015.

[176] Q. Yi, M. Tian, W. Yan, X. Qu, and X. Chen, "Visualization study of the influence of non-condensable gas on steam condensation heat transfer," *Appl. Therm. Eng.*, vol. 106, pp. 13–21, 2016.

[177] K. Cheatle, *Fundamentals of test measurement instrumentation*. ISA-Instrumentation, Systems, and Automation Society, 2006.

[178] A. A. Alammar, F. N. Al-Mousawi, R. K. Al-Dadah, S. M. Mahmoud, and R. Hood, "Enhancing thermal performance of a two-phase closed thermosyphon with an internal surface roughness," *J. Clean. Prod.*, vol. 185, pp. 128–136, 2018.

[179] Johnson Waukesha, "How EDM works." [Online]. Available: https://www.xactedm.com/edm-capabilities/how-edm-works/. [Accessed: 21-Dec-

2017].

[180] Mitutoyo, “Quick Guide to Surface Roughness Measurement: Reference guide for laboratory and workshop,” 1984.

[181] Alicona, “Optical 3D Surface Metrology InfiniteFocus.” [Online]. Available: www.alicona.com. [Accessed: 05-Jan-2018].

[182] R. Khodabandeh and B. Palm, “Influence of system pressure on the boiling heat transfer coefficient in a closed two-phase thermosyphon loop,” vol. 41, pp. 619–624, 2002.

[183] D. Attinger, C. Frankiewicz, A. R. Betz, T. M. Schutzius, R. Ganguly, A. Das, C.-J. Kim, and C. M. Megaridis, “Surface engineering for phase change heat transfer: A review,” *MRS Energy Sustain.*, vol. 1, p. E4, 2014.

[184] S. S. Kutateladze, *Heat Transfer and Hydrodynamic Resistance*. Moscow, Russia: Energoatomizdat Publishing House, 1990.